Input Admittance Modeling and Passivity-Based Stabilization of Digitally Current-Controlled Grid-Connected Converters

Von der Fakultät für Elektrotechnik, Informationstechnik, Physik
der Technischen Universität Carolo-Wilhelmina zu Braunschweig

zur Erlangung des Grades eines Doktors
der Ingenieurwissenschaften (Dr.-Ing.)

genehmigte Dissertation

von Florian Hans, M. Sc.

aus Neunkirchen (Saar)

eingereicht am: 19.11.2020

mündliche Prüfung am: 25.06.2021

1. Referent: Prof. Dr.-Ing. Walter Schumacher
2. Referent: Prof. Dr.-Ing. habil. Dipl.-Math. Bernd Meinerzhagen

Druckjahr: 2021

Preface

This dissertation was developed during my work as a research and teaching assistant at the Institute of Control Engineering at Technische Universität Braunschweig.

First, I would like to express my special thanks to my supervisor, Prof. Dr. -Ing. Walter Schumacher, for his support of my doctoral phase, for the technical discussions and the contribution of his practical know-how, as well as for the freedom he gave me in designing this thesis. I would also like to thank Prof. Dr. -Ing. Bernd Meinerzhagen for agreeing to be my second reviewer and for his professional advice on this thesis. I would also like to thank Prof. Dr. -Ing. Markus Henke for taking over the chair of the doctoral committee.

Of course, my thanks also go to my colleagues at the Institute of Control Engineering, who have contributed in various ways to the success of my work. Here I would especially like to thank my office colleague, Steffen Lampke, for the help and the great teamwork during our time at the Institute, and also Malte Thielmann for the numerous fruitful conversations during and far beyond our coffee breaks. At this point I want also mention my colleague Dr. -Ing. Marcus Grobe and Prof. Dr. -Ing. Bernd Lichte from the Ostfalia, University of Applied Science, who gave me the right impulses for thinking when solving some tricky mathematical problems. Furthermore, I would like to thank Professor Xiongfei Wang and Shih-Feng Chou from Aalborg University for their time, the practical support and for becoming co-authors of two of my publications.

Last but not least, I want to thank my parents Marika and Gerhard Hans for their loving support and for helping me with all my decisions and following me on my path through life.

Florian Hans, Braunschweig, July 2021

Contents

Notation, List of Symbols, Commonly used Indices, and Abbreviations

Notation

Symbol	*Description*
X	Physical quantity or (pulse) transfer function
x	Normalized scalar quantity
$\boldsymbol{X}^t$	Physical three-phase quantity in the (a, b, c)-domain
$\boldsymbol{X}, \boldsymbol{x}$	Physical and normalized complex space vector in the stationary (α, β)-domain
$\boldsymbol{X}^{dq}, \boldsymbol{x}^{dq}$	Physical and normalized complex space vector in a synchronous rotating (d, q)-reference frame
$\tilde{X}$	Transfer function of a synthetic system
X^*	Pulse transfer function in the Laplace-domain
$\boldsymbol{x}^*$	Normalized complex space vector of impulse-sampled signal in the stationary (α, β)-domain
X'	Alternative representation of discrete system in the Laplace-domain
$\boldsymbol{x}'$	Alternative representation of normalized complex space vector of sampled signal in the Laplace-domain
$\underline{\underline{X}}$	Multiple-input multiple-output transfer function matrix
$\underline{X}$	Column vector with transfer functions
$\underline{x}, \underline{\boldsymbol{x}}$	Column vector with scalars and vector with normalized complex space vectors in the (α, β)-domain

Symbols

Symbol	*Description*	*Unit*
a_m	Amplitude modulation index	-

α	Selected angular frequency	rad/s
β	Alignment factor	-
C	Capacitance	F
δ	Dirac impulse or damping ratio	-
Δ	Dynamic uncertainty	-
D_0	Averaged PWM duty-cycle	-
E, e	Voltage at synthetic point of common coupling	V
f	Frequency	Hz
F	Reference filter transfer function	-
G	Transfer function	-
g	Impulse response	-
g_{m}	Gain margin	-
Γ	Auxiliary (scaling) transfer function	-
γ	Harmonic weightings	-
h_i	Harmonic number	-
H	Active filter transfer function	-
I, i	Current	A
j	Imaginary number	-
k	Normalized gain or Running index	-
κ	Scaling factor	-
L	Inductance	H
$\underline{\lambda}$	Minimum eigenvalue of a matrix	-
m	Number of resonators	-
n	Running index	-
ν	Input feed-forward passivity index	-
o	Offset factor	-
P	Active power	W
ϕ	Phase angle	rad
Φ_{m}	Phase margin	-
q	Running index	-
Q	Reactive power	Var
R	Resistance	Ω
ρ	Output feedback passivity index	-
s	Complex Laplace variable	1/s

s_λ	Pole of a transfer function	1/s
S	Complex power	VA
$\sigma, \overline{\sigma}$	Step function or maximum singular value	-
t	Time	s
T	Time constant	s
V, v	Voltage	V
ω	Angular frequency	rad/s
x	General quantity	-
Y	Admittance	$1/\Omega$
Z	Impedance	Ω
z	Complex variable	-

Commonly used indices

Symbol	*Description*
b	Base/Nominal
c	Capacitive, converter, carrier, cut-off, or computation
cl	Closed-loop
crit	Critical
d	Delay, damping, or disturbance
DC	Direct current
fb	Feedback
fc	Filter on converter side
ff	Feed-forward
fg	Filter on grid side
g	Grid
H	Active part
h_i	Harmonic number
i, i	Inner/input or running index
I	Integral
l	Inductance
m	Highest resonator
N	Nyquist
o	Open-loop

r	Resonance
ref	Reference
p	Primary frequency or pulse
P	Proportional
PR	Proportional-resonant
PWM	Pulsewidth modulation
s	Switching

Abbreviations

Symbol	*Description*
AC	Alternating current
AVC	Alternating voltage control
DC	Direct current
DVC	Direct voltage control
FFT	Fast Fourier Transformation
IFP	Input feed-forward passivity
LCL	Inductive-capacitive-inductive
MIMO	Multiple-input multiple-output
OFP	Output feedback passivity
PCC	Point of common coupling
PI	Proportional-integral
PLL	Phase-locked-loop
PR	Proportional-resonant
PWM	Pulsewidth modulation
RES	Renewable energy sources
ROGI	Reduced-order generalized integrator
SISO	Single-input single-output
SOGI	Second-order generalized integrator
SSI	Sinusoidal signal integrator
TSO	Transmission System Operator
VSC	Voltage-source converter
ZOH	Zero-order hold

Kurzfassung

Aufgrund der immer größer werdenden Anzahl von erneuerbaren Energieanlagen im elektrischen Energieversorgungsnetz gewinnt der Einsatz von leistungselektronischen Schaltungen, wie z. B. Spannungszwischenkreisumrichter, immer mehr an Bedeutung. Obwohl die verwendeten Technologien die Abkehr von fossilen Brennstoffen ermöglichen und eine Vielzahl neuer Möglichkeiten eröffnen, ist seit längerem bekannt, dass Wechselwirkungen von einem oder mehreren Umrichtern mit Resonanzen im Netz zu schlecht gedämpften Schwingungen führen und damit die Stabilität von Teilen des Energienetzes gefährden können.

Im Laufe der Jahre hat sich die Passivitätstheorie als besonders wirkungsvoll erwiesen, um solche Situationen zu verhindern. Demnach kann die Stabilität des Stromnetzes bereits in der Designphase ohne Detailkenntnis des Systems gewährleistet werden, indem alle Komponenten passiv wirken. Das bedeutet, dass alle aktiven Verbraucher und einspeisenden Umrichter eine Eingangsadmittanz mit nicht negativem Realteil besitzen. Geht man, wie in den meisten Forschungsarbeiten, von einem quasi-analogen Betrieb der Umrichter aus, so ist eine vollständige Passivierung der Eingangsadmittanzen relativ einfach mit Hilfe von passiven oder aktiven Dämpfungsstrategien zu erreichen. Grundsätzlich werden hierbei jedoch die digitale Implementierung des Regelalgorithmus sowie reale Effekte, die bei der Abtastung von hochfrequenten Harmonischen entstehen, vernachlässigt. Eine korrekte Abbildung ist aber gerade bei der Stabilitätsanalyse von Netzen mit einer Vielzahl von leistungselektronischen Schaltungen von zentraler Bedeutung.

Ziel dieser Dissertation ist es daher, den kompletten Modellierungs-, Analyse- und Regler- sowie Filterentwurfsprozess von digital-stromgeregelten, netzgebundenen Umrichtern zu überprüfen und zu erweitern. Nach der Herleitung zweier bekannter Eingrößenmodelle werden die

resultierenden Eingangsadmittanzen ausführlich hinsichtlich ihrer Passivitätseigenschaften untersucht. Darauf aufbauend werden Verfahren für die Auslegung einer passiven Dämpfung bzw. einer aktiven Vorsteuerung vorgeschlagen und es wird diskutiert, welche Aspekte bei der Implementierung der Filter zu berücksichtigen sind.

Da sich die verwendeten Eingrößenmodelle jedoch nur zur anfänglichen Analyse eignen und sich nicht alle Alias-Effekte abbilden lassen, wird im weiteren Teil der Arbeit ein Mehrgrößen-Umrichtermodell entwickelt. Der Fokus liegt hierbei auf der Modellierung des Abtastprozesses sowie der Pulsweitenmodulation. Es zeigt sich, dass die Spiegelung hochfrequenter Signalanteile auf niederfrequente Anteile prinzipiell durch eine dynamische Unsicherheit beschrieben werden kann, die das Grundfrequenzverhalten der Umrichter beeinflusst. Mit dieser neuen Erkenntnis lassen sich eine Reihe wichtiger Schlussfolgerungen über den Entwurf und die Integration von Anlagen mit Spannungszwischenkreisumrichter in schlecht gedämpften Netzen ziehen. Insbesondere wird deutlich, welche Kriterien passive oder aktive Filter erfüllen sollten, um den oft negativen Spiegeleffekten der digitalen Regelung gezielt entgegenzuwirken. Schlussendlich wird demonstriert, dass eine robuste Passivierung der Umrichter-Eingangsadmittanz das Entstehen kritischer Oszillationen und somit eine Destabilisierung des Energienetzes durch Harmonische verhindern kann. Die vorgestellte Theorie und der erarbeitete Reglerentwurf werden anhand diverser Simulationen eines beispielhaften Umrichtersystems verdeutlicht und validiert.

Abstract

Due to the ever increasing number of renewable energy systems in the electrical power grid, the application of power electronic-based circuits, such as voltage-source converters, is gaining more and more importance. Although the used technologies enable turning away from fossil fuels and offer a variety of new possibilities, it has been known for a while that interactions of one or multiple converters with resonances in the grid can lead to poorly damped oscillations, and thus, may threaten the stability of parts of the power system.

Over the years, the passivity theory has proven to be particularly powerful in preventing such situations. Accordingly, the stability of the power grid can be guaranteed by design if all components act passive. This means that all active loads and energy feeding converters have an input admittance with a non-negative real part. Assuming a quasi-analog operation of the converters, as in most of the scientific research, a complete passivation of the input admittances is relatively easy to achieve by means of passive or active damping strategies. However, the digital implementation of the control algorithm as well as real effects, which arise from the sampling of high-frequency switching harmonics are generally neglected. But the correct representation is of central importance especially for the stability analysis of grids with a large number of power electronic-based circuits.

The aim of this dissertation is therefore to review the complete modeling and analysis of digitally current-controlled grid-connected converters and to extend the controller as well as filter design. After deriving two well-known single-input single-output models, the resulting input admittances are thoroughly analyzed regarding their passivity properties. On this basis, methods for the design of a passive damping or an

active feed-forward are proposed and it is discussed which aspects have to be considered when implementing the filters.

However, since the used single-input single-output models are only suitable for an initial analysis and not all alias effects can be reproduced, in the further part of the thesis a multiple-input multiple-output converter model is developed. Hereby, the modeling is focused on the sampling process as well as the pulsewidth modulation. It is shown that the mirroring of high-frequency signal components onto low-frequency components can in principle be described by a dynamic uncertainty that affects the behavior of the converters' baseband dynamics. With this new insight, a number of essential conclusions can be drawn about the design and integration of power plants with voltage-source converters in poorly damped grids. In particular, it becomes clear which criteria passive or active filters should fulfill in order to specifically counteract the often negative mirroring effects of digital control. Finally, it is demonstrated that a robust passivation of the converter input admittance can prevent the generation of critical oscillations, and thus, a destabilization of the power system by harmonics. The presented theory and the developed controller design are illustrated and verified by various simulations of an exemplary converter system.

1 Introduction

1.1 Motivation

As a consequence of greenhouse gas emissions and the finite amount of fossil energy reserves, renewable energy sources (RES) have become more and more important, displacing conventional power production facilities worldwide [18,69–71,79]. In Germany, for example, the installed capacity of wind power plants increased from around $12\,\mathrm{GW}$ in the year 2002 to more than $60\,\mathrm{GW}$ in 2020 [40]. This corresponds to an increase of approximately $400\,\%$. The trend becomes even more apparent in the expansion of solar systems, as the installed capacity rose from nearly $0.3\,\mathrm{GW}$ to over $51\,\mathrm{GW}$ in the same time period [40]. This corresponds to an increase of approximately $16900\,\%$. According to the Fraunhofer Institute for Solar Energy Systems ISE, RES set a new record in Germany and account for $55.8\,\%$ of the net electricity production for public electricity generation in the first half of 2020 [40].

Independent of the input power source, grid-connected voltage-source converters (VSCs) represent the most common grid interface of sustainable and distributed RES in low- and medium-voltage power grids [20]. Although their design and principle control structures are well known from electrical drive systems, stability issues have appeared over and over again in power grids with a high penetration of converter-based energy sources, see e.g., [26,36,37,66,80,95]. In this context, the EU-Horizon-2020 funded MIGRATE project conducted a survey among 21 European Transmission System Operators (TSO)s, which concluded that instability phenomena related to the interaction of multiple power converters or to the excitation of poorly damped (grid) resonances are ranked among the most challenging power system stability issues today [48]. As known from research, the underlying current control of the VSCs as well as the

time delay that is caused by the pulsewidth modulation (PWM) plus computation time can clearly be assigned to the reported problems, as they can introduce negative damping to the grid-converter system [55, 57].

Therefore, in order to prevent such harmonic stability issues [124], recent works have intensively concentrated on the converter modeling and revision of the associated VSC control structure. However, even though many approaches and solutions have been developed, simplifications such as the assumption of a quasi-analog operating system have often been made and controller and filter design guidelines that cover all low- and high-frequency effects are still missing. This motivates further research, particularly with regard to the implementation of digitally controlled converter systems.

1.2 Related Work

In contrast to the conventional theory on dynamical systems, where the term stability concerns the stability of the equilibrium points of a system, the (orbital) stability of the output trajectory or the structural stability of a system itself [32, 74], the stability of a power system is conventionally classified by the cause of instability. It can be distinguished between the rotor angle stability, the voltage stability, and the frequency stability [77, 78, 91]. While these classical stability terms are based on the operational principle of rotating synchronous generators, stability issues which are related to the amplification of harmonics (mainly caused by resonances of power lines in combination with converter input admittances [140]) are referred to as harmonic instability or resonance instability [124, 140]. Although such harmonic instability effects have been known since the sixties, see e.g., [7, 61, 101], the topic is again gaining importance with the constant expansion of converter-based RES [26, 36, 48, 66, 95, 112].

1.2.1 Small-Signal Modeling of Power Converters

In general, for the analysis it is crucial to model all relevant effects that emerge in the frequency range of interest. However, since switching

power converters represent nonlinear, time-discontinuous systems, the modeling becomes a complex task. Among others, linearized modeling techniques are well suited to describe the converters behavior with respect to small signal changes, see [122, 140, 165] for an overview and comparison of different methods.

Most commonly, the modeling approach from classical linear control theory [10, 119] is applied. Here, the switching behavior of the PWM is implicitly neglected and the VSC's output voltage is averaged over a switching period, resulting in a time-invariant single-input single-output (SISO) small-signal converter model. In the beginning, mainly time-continuous models in the Laplace-domain were deduced, while newer works also consider the effects of the digital control, see e.g., [41, 42, 53]. With help of the impulse modulation technique and the discrete (or starred) Laplace transform [39, 114], it becomes possible to mathematically describe the sampling process, and thus, to model the converter's dynamics more accurately. However, since averaged SISO models only focus on the dynamics of the fundamental signal components, the generation of PWM harmonics and the mirroring of above Nyquist frequency harmonics on low-frequency signal components (referred to as aliasing [39, 119]) cannot be covered precisely.

Hence, in order to incorporate such effects, there is a growing tendency in the literature to use the theory of linear time-periodic systems [95, 114, 151]. Here, the idea is to linearize the system around a time-periodic operating trajectory instead of a (constant) operating point. In doing so, multiple-input multiple-output (MIMO) small-signal converter models can be derived, which cover the frequency coupling of multiple time-periodic trajectories. Assuming an exponentially modulated periodic input signal [151], the Fourier series expansion of the system matrices yields a so called harmonic state-space model [81, 95, 140, 165]. Although the modeling accuracy is increased, two disadvantages of harmonic state-space models are that the model order is usually high and that the derivation of the input-output relationship through the Fourier coefficients of the input and output signals (also referred to as harmonic transfer function) requires a matrix inversion. This makes the resulting harmonic

transfer functions difficult to interpret and the assignment of specific system properties to individual system components is lost.

1.2.2 Harmonic Stability of Power Systems

Over the years it has been shown that small-signal models are often sufficiently accurate to predict stability issues and to avoid the application of nonlinear analyzing methods. In particular, in [140] it is pointed out that the phenomena of harmonic instability can be considered as a small-signal stability problem. Hence, depending on the adopted small-signal model, the harmonic stability of power systems can be analyzed by different methods [140]. As summarized in Fig. 1.1, it can mainly be distinguished between two approaches, namely 1) the eigenvalue and eigenvector analysis based on state-space models in the time-domain and 2) the impedance-based analysis based on Norton and Thevenin equivalent circuits in the frequency-domain.

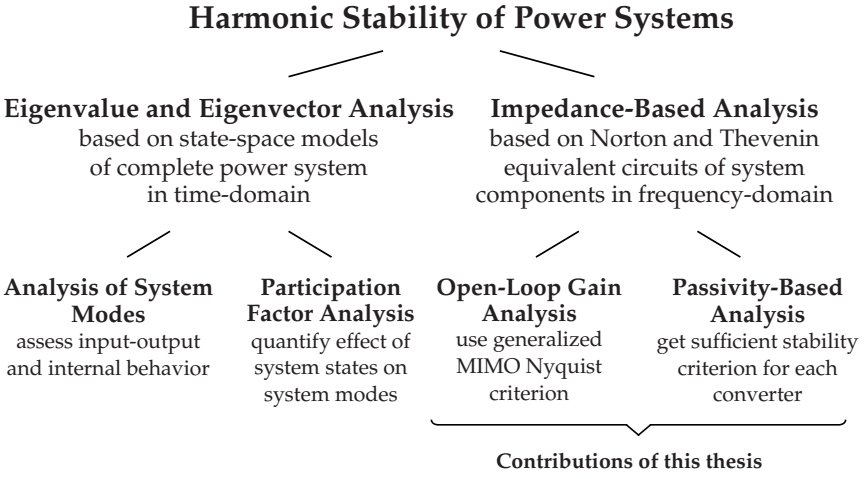

Fig. 1.1: Overview of methods for harmonic stability analysis of power systems.

Eigenvalue and Eigenvector Analysis

The advantage of the first method is that not only the system's input-output behavior can be studied, but also the internal behavior of the modes of a complex power system [65, 147]. Among others, especially the research of Pogaku, Kroutikova and Green et al. should be highlighted here, since they derived and analyzed detailed state-space converter models, that include current, voltage, as well as power control loops, see e.g., [76, 102]. Moreover, given an adequate small-signal state-space model, the application of a participation analysis allows to reveal the contribution of different components (or parameters) to the small-signal stability [102, 147]. However, the system order is significantly increased if time delays are incorporated. For instance, in [147], the authors adopted a third- and fifth-order Padé approximation to model the time delay of the PWM and the digital controller computation, but admitted that the Padé order can have a significant effect on the accuracy of the harmonic stability analysis and the deduced results. A further disadvantage of state-space models is that sampling effects of the digital control can only be taken into account with difficulty. Thus, the eigenvalue-based analysis methods are rather limited to the study of time-continuous systems and low-frequency harmonic oscillations, where time delay approximations are valid.

Impedance-Based Analysis

On the other hand, mainly Sun et al. established to interpret the small-signal dynamics of each actively controlled grid-connected converter as a non-ideal current (or voltage) source with associated input admittance [122, 123]. This allows a simple visualization and interconnection of multiple converters and network components, where theoretically derived models can be readily combined with identified or measured black-box impedance models [19, 112]. Depending on the underlying control structure or measurement principle, the impedance models can be obtained in the (d, q)-domain, the (α, β)-domain or some modified sequence domain, that aims to remove internal cross couplings or helps to assess the sys-

tem stability more easily, see e.g., [2, 12, 51, 115, 120, 122, 144, 148, 150]. In the end, the impedance-based modeling approach allows to apply well known tools from the electric circuit theory in the same way as classical frequency-domain methods from linear control theory.

Given an impedance-based system model, harmonic stability is most frequently analyzed by evaluating the interconnected system's open-loop gain and applying the Nyquist stability criterion [10, 89, 98, 119]. In the most simple case, the system only consists of a single VSC that is connected to a passive load or a power grid, which is represented by a voltage source with associated grid impedance [86, 89, 112, 123, 144, 146]. On this basis, many controller and filter design guidelines that aim to prevent harmonic instability have been developed, see e.g., [30, 51, 52, 125, 157, 158, 171]. In particular, the papers [49, 87, 153] give a good overview of passive and active damping methods for grid-connected VSCs with inductive-capacitive-inductive (LCL) output filters. In addition to the system with a single converter, the (MIMO) Nyquist stability criterion [121] can also be applied to analyze the harmonic stability of multiple, interconnected power converters [88, 135, 143, 150]. In this context, the authors of [163] proposed a stabilizing procedure, where stable grid components are structured by a passive component network, which is sequentially extended by adding single converters. Similar to the participation analysis of power grids in state-space representation, this method allows to assess the contribution of single converters to the overall system's stability. Nevertheless, since each VSC changes the effective grid impedance, and thus, contributes to the power system stability, every network has to be analyzed individually. Hence, from a system perspective, it is not possible to deduce detailed stability statements nor generally valid guidelines for the controller or filter design.

A special approach derived from the Nyquist stability criterion is the concept of passivity [14, 32, 74, 169]. According to this concept, a linear passive system is characterized by the fact that it is stable and that its Nyquist curve or eigenloci shows no negative real part (or equivalently, its phase response always lies within $-90°$ and $+90°$). This implies that, if two passive systems are interconnected in feedback, the total phase shift of

the open-loop system never crosses $-180°$, and thus, the Nyquist stability criterion is always fulfilled [10, 89, 98, 119]. Beyond that, it can be shown that the parallel or feedback-interconnection of two passive systems again results in a passive system. If this concept is applied to power systems by assuming that the power network only consists of passive components, the system stability is guaranteed by design, if all grid-connected converters are passive, i.e., the real part of each VSC input admittance is non-negative. Hence, with the help of passivity theory, sufficient criteria for the harmonic stability of power systems can be derived, which are independent of the specific configuration and the number of converters. But this approach requires the rigorous passivation of all grid-connected components. Due to the easy verifiability and the inherent high robustness properties [14, 73, 74, 92], passivity is already a requirement for components in railway applications. In particular, the railway standard EN 50388-2 [6] enforces active-front-ends to behave dissipative from the fifth harmonic (e.g., $250\,\mathrm{Hz}$ for $50\,\mathrm{Hz}$ grids) up to the Nyquist frequency, defined by the converter's sampling frequency [42, 110].

On the basis of passivity, especially Harnefors and Wang et al. investigated and advanced the frequency-domain controller and filter design as well as the stability assessment of (multiple) grid-connected VSCs, see e.g., [11, 52, 55–57, 60, 139, 141]. In their initial works in 2007 and 2008, Harnefors et al. assumed an ideal operation, neglecting any computation and PWM time delay, and showed that, in this case, it is easy to achieve a non-negative real part of the VSC's conductance for all frequencies [52, 60]. However, taking non-idealized, practical conditions into account, the authors admitted in their later studies that a passive input admittance for all frequencies is hard to obtain and additional damping has to be introduced. Over the years, other authors have also extended the findings and proposed different passivity-based damping strategies, either directly in the continuous Laplace-domain [4, 16, 33, 156, 157] or in the discrete z-domain [41, 110, 111]. At this point, especially our work from [4] should be mentioned, in which the concept of passivity indices is used to quantify the degree of a converter system's passivity, see also [14, 74, 94, 169] for a detailed (theoretical) description of the concept. The use of passivity

indices allows to interpret the interconnected grid-converter system as a system of passive and (partially) non-passive subsystems which can be passivated by components that show a sufficient excess of passivity. Due to various advantages, including the physical interpretation and the easy passivity assessment of multiple interconnected system components, the concept of passivity indices is revisited and deepened in this thesis.

1.3 Problem Statement and Contributions

While recent research is mostly focused on the analysis or passivation of the VSC input admittance up to the Nyquist frequency (which is in accordance with the EN 50388-2 [6]), the authors of [125] demonstrated that an above Nyquist frequency LCL filter resonance may yet destabilize a converter system. Among others, this initiated the research [42, 53, 116], where Harnefors, Freijedo, and San et al. again put more emphasis on the small-signal modeling of the PWM and the sampling process, aiming to derive more complete and accurate models of the converter conductance. But, even though the observations of Tang et al. in [125] motivated a reflection of the modeling and the passivity assessment concept of digitally controlled grid-connected VSCs, the last contributions were not yet able to clarify all the open questions. In particular, in [53], Harnefors et al. used the discrete Laplace transform [39, 119] to derive a SISO converter model in the s-domain, which was claimed to cover all aliasing effects. However, as in [42], the authors of [53] make it relatively easy for themselves by considering a converter that is equipped with a simple inductive output filter. Since an (in practice unrealistic) increase of the filter resistance is used for the converter passivation, possible aliasing effects resulting from the implementation of more efficient active damping strategies in combination with higher-order filters are overlooked. In addition, our studies on the small-signal representation of the PWM from [1] reveal that the adopted zero-order-hold (ZOH) PWM model represents an overoptimistic modulator approximation, which may lead to incorrect conclusions. In contrast, San et al. propose a multiple-frequency PWM model that represents a kind of worst case modulator approximation in [116].

Similar to the s-domain model from [53] or common z-domain models as those used in e.g., [41, 110, 111], the derived (multiple-frequency) converter model in [116] also allows to consider the aliased signal components of selected PWM sideband harmonics. But, although the presented converter modeling is reasonable, the underlying PWM model is based on a sum representation in the frequency-domain, which is first combined with the VSC output filter and controller dynamics, and then simplified by several Padé approximations to obtain an explicit frequency- and converter parameter-dependent PWM gain. This procedure again weakens the accuracy of the model and it can be assumed that the suggested simplification cannot readily be adapted to other filter structures or any kind of grid impedance. Lastly, even though the proposed MIMO frequency-domain converter model of Freijedo et al. in [42] is similar to the harmonic state-space representation [81, 140], and thus, basically allows to model the mirroring of above Nyquist frequency components, it also has a few drawbacks. In particular, the model also includes only a simple inductive output filter and does not consider any grid impedance. Moreover, the implicit structure of the VSC's input admittance matrix does not allow to assign the origin of frequency ranges with negative damping to specific system components or parameters. This in turn makes an analytical controller and filter design more difficult and rather limits the applicability of the converter model to simulation studies.

In the end, any present converter model that focuses on the effects of the digital control has its own weaknesses and none of the found works contains a detailed controller or filter design, but deals (more or less) only with the converter modeling itself. Furthermore, unlike the previous findings of e.g., [4, 55, 57, 60, 141, 156], the deduced passivity criterion of Harnefors et al. in [53] indicates that a passive total VSC input admittance seen from the grid only implies stability for a specific (passive) grid impedance. This raises the question whether this is really always the case or, in general, which influence the grid impedance and aliasing effects have on the stability of grid-converter systems. In this regard, it should also be analyzed to what extent existing filter design methods can

be adapted to digitally controlled converters and how above Nyquist frequency components should be taken into account during the design.

Since the identified issues have not yet been finally clarified, the aim of this thesis is to review and to extend the complete modeling, passivity assessment, and controller plus filter design process of digitally current-controlled grid-connected VSCs. The structure and the main contributions are summarized as follows:

Chapter 2: Background This chapter summarizes the key facts on the frequency-domain passivity theory of linear systems. Hereby, the focus is on the concept of passivity indices, which allow to quantify the degree of a system's passivity. Next, the passivation and the stabilization of interconnected systems is reviewed and it is explained why it is mostly still sufficient to concentrate the analysis on the frequency range up to the Nyquist frequency. Furthermore, the chapter gives a short overview of the basic operating principles of grid-connected converters and describes the impedance-based modeling idea and the concept of harmonic stability more in detail.

Chapter 3: System Modeling After introducing the converter system under study and presenting a set of example parameters, which are used during the thesis to illustrate the developed theory, this chapter thoroughly reviews the most important components of digitally current-controlled power converters. Besides the modeling and the design of the VSC's output filter, special emphasis is put on the small-signal behavior of the PWM. It is demonstrated that commonly used PWM models either represent an overoptimistic approximation of the modulator or yield too conservative results, which strengthens the use of our suggested SISO PWM model from [1]. Moreover, this chapter proposes a new, more accurate digital realization of a damped proportional-resonant (PR) controller with phase compensation that is based on two discretized integrators, allowing to implement several current limiting and resonator anti-windup schemes. Finally, using the resulting converter current dynamics, two frequently found SISO models of the VSC's input

admittance are derived and it is described why none of the models consider all aliasing effects.

Chapter 4: Current Controller Design This chapter summarizes the basic procedure and typical design recommendations for stationary-frame PR current controllers which implement multiple (high-frequency) resonators. The content is mainly based on our work [3], where the interaction between multifrequency resonators and the resulting difficulties in the selection of the integral gains are discussed. In this context, it is again shown how this problem can be overcome and that the application of the proposed PR controller design results in a stable converter reference dynamics, which in the next step enables a simple and (almost) independent passivation of the converter's disturbance dynamics.

Chapter 5: Passivity Assessment and Filter Design In order to prevent stability issues that might result when the VSC is connected to the power grid, the first part of this chapter performs a detailed, analytic passivity assessment of the converter admittance models from Ch. 3. Following the current controller design recommendations from the previous chapter, the passivity indices of the converter conductance models are derived and the limits of the non-passive regions are determined. This extends our analysis from [4], but also confirms some well known passivity properties of VSCs from a different perspective. Based on the findings, the second part of the chapter concentrates on the converter passivation by means of passive and active damping methods. While the first approach is only briefly addressed due to the rather limited damping effect which is present in different advanced LCL filter topologies, the remaining content deals with the passivation using an active feed-forward. In particular, as the feed-forward of the voltage at the VSC's terminals or, alternatively, the feed-forward of the current through the capacitive branch of an LCL filter has proven to be very powerful, these two methods are thoroughly reviewed. In this regard, a new simplified passivity criterion is proposed and it is discussed how the digital realization and the underlying current controller affect the

feed-forward filter design. Hereby, it also becomes clear that, even though all investigated damping approaches fulfill their purpose in a certain frequency range, a complete passivation of the input admittance of the digitally-controlled converter can only be achieved by a capacitor current feed-forward.

Chapter 6: PWM Harmonics and Aliasing Effects As the converter model used for the analysis and controller plus filter design does generally not consider all aliasing effects, this chapter revises the modeling of the PWM and the sampling process by taking baseband as well as high-frequency sideband components into account. By introducing a new representation of sampled signals and developing a piece-wise defined multiple-frequency PWM model in the Laplace-domain, a new MIMO converter model is proposed. The model allows to accurately reflect the generation of switching harmonics, but also the mirroring of above Nyquist frequency components that are aliases of the PWM's reference voltage. Considering that the LCL filter suppresses high-frequency signal components from the grid side, the model of the closed-loop grid-converter system can again be simplified to a SISO model. It shows that the effects of aliased signal components can basically be interpreted as a dynamic uncertainty, which perturbs the baseband dynamics of the converter. This also explains the challenges associated with LCL filters whose resonance frequency is above the Nyquist frequency and finally clarifies which influence the grid impedance has on the VSC input admittance. But, it is finally demonstrated that the grid impedance is mostly not a major issue for the system stability by aiming for a robust converter passivation.

Chapter 7: Simulation and Verification In this chapter, the theoretical findings are verified by computer simulations, where the identification of a realistic converter model with and without active feed-forward shows the reliability of the derived models. Furthermore, the discussion of several transient studies, where the converter is connected to a grid with one or multiple dominant below or above Nyquist frequency resonances, completes the thesis.

2 Background

At the beginning of this chapter, the preliminaries to frequency-domain passivity theory are summarized. Based on [14, 25, 74], passivity is defined for linear MIMO as well as linear SISO systems, the concept of passivity indices is explained, and some main passivity theorems are listed. Further, in the second part, a classification of grid-connected converter systems is given and a typical control structure is introduced. Finally, the concept of harmonic stability is discussed and related to the content of this thesis.

2.1 Frequency-Domain Passivity Theory

2.1.1 Passivity Definition of Linear Systems

A square, real rational transfer function matrix $\underline{\underline{G}}(s)$ is called passive, if 1) $\underline{\underline{G}}(s)$ is stable, i.e., $\mathrm{Re}\{s_\lambda\} \leq 0$, $\lambda = 1, \ldots, n$, were s_λ are the poles of all elements of $\underline{\underline{G}}(s)$ and 2) for all real $\omega \in \mathbb{R}$ for which $j\omega$ is not a pole of any element of $\underline{\underline{G}}(s)$, the matrix $\underline{\underline{G}}(j\omega) + \underline{\underline{G}}^H(j\omega)$, where $\underline{\underline{G}}^H(j\omega)$ denotes the Hermitian transposed $\underline{\underline{G}}^H(j\omega) = \underline{\underline{G}}^T(-j\omega)$, is positive semidefinite. If there exist poles s_λ on the imaginary axis, they have to be non-repeated and the residual matrix at the poles $\lim_{s \to s_\lambda} (s - s_\lambda)\underline{\underline{G}}(s)$ has to be Hermitian and positive semidefinite. Moreover, $\underline{\underline{G}}(s)$ is said to be strictly passive, if 1) $\underline{\underline{G}}(s)$ is asymptotically stable (or Hurwitz), i.e., $\mathrm{Re}\{s_\lambda\} < 0$, $\lambda = 1, \ldots, n$, 2) $\underline{\underline{G}}(j\omega) + \underline{\underline{G}}^H(j\omega)$ is positive definite for all $\omega \in \mathbb{R}$, and 3) $\underline{\underline{G}}(j\infty) + \underline{\underline{G}}^H(j\infty)$ is positive definite [14, 74, 75].

In the SISO case, the definition of a passive system can be simplified as follows. Given an asymptotically stable SISO system with rational transfer function $G(s)$, the real part of the frequency response must be non-negative, i.e., $\mathrm{Re}\{G(j\omega)\} \geq 0$, $\forall \omega \in \mathbb{R}$, for the system to be passive and

positive, i.e., $\mathrm{Re}\{G(j\omega)\} > 0, \forall\omega \in \mathbb{R}$, for the system to be strictly passive [14, 25, 74]. Graphically, this implies that the phase response of each stable SISO passive system lies always within $[-90°, 90°]$, or equivalently, the system's Nyquist curve is always in the closed complex right half plane. Similarly, if the SISO system is strictly passive, then the phase response of the system is always within $(-90°, 90°)$, or the system's Nyquist curve always lies in the open complex right half plane.

It should be noted that the given passivity definition is a frequency-domain test for the more general property of positive realness. Accordingly, a square transfer function matrix $\underline{\underline{G}}(s)$ is positive-real, if 1) $\underline{\underline{G}}(s)$ has only stable poles $\mathrm{Re}\{s_\lambda\} \leq 0, \lambda = 1, \ldots, n$, 2) $\underline{\underline{G}}(s)$ is real for all positive real s, and 3) $\underline{\underline{G}}(s) + \underline{\underline{G}}^H(s) \geq 0$ for all $\mathrm{Re}\{s\} > 0$. Moreover, $\underline{\underline{G}}(s)$ is strictly positive-real if there exists a $\kappa > 0$, such that $\underline{\underline{G}}(s - \kappa)$ is positive real [25, 75]. The term positive-real basically means that the considered function is positive (or non-negative) and real for real and positive s. A detailed discussion including different criteria for passivity and positive realness can, for example, be found in [25, 75]. At this point it should however be pointed out that in contrast to common passivity definitions, positive realness is not limited to systems with rational transfer function matrices and also covers systems with irrational functions. Those naturally arise when considering infinite-dimensional control systems [25]. But, as the authors of [46] recently showed, the (more intuitive) frequency-domain test for passivity can be generalized to a larger class of irrational transfer function matrices. In particular, focusing on asymptotically stable systems described by proper, meromorphic matrix functions[1], it can be verified that the above presented definition of passivity corresponds to the definition of positive realness, see also [106] for the SISO case equivalent. Among others, this especially allows to assess the passivity properties of linear time-delay systems [44, 98, 99, 137], whose transfer functions are defined by a quotient of (retarded) quasi-polynomials containing terms of the form $e^{-s\kappa T}$, $\kappa T \geq 0$.

[1] A complex-valued function $G(s)$, which depends on the complex variable $s = \sigma + j\omega$, is called meromorphic if it is analytic on the whole complex plane expect for a finite number of isolated singularities, representing the poles s_λ of $G(s)$, defined by $\lim_{s\to s_\lambda} G(s) = \pm\infty$ [103].

Although the control system theory often refers to (strictly) positive-real systems, the nomenclature of passivity has established in large parts of the power engineering community, dealing with the modeling and design of grid-connected power converters. In this regard, most authors rather understand passivity as the physical property of a system to provide positive damping or to dissipate energy, similar to a (positive) resistance. It is therefore often sufficient to focus on ensuring that the dynamics of the converter conductance are stable and do not show negative values in a certain frequency range, see e.g., [8,42,52,53,55,57,60,110,139,141,156].

2.1.2 Passivity Indices and Passivation

The idea of passivity can be extended so that not only passive and non-passive systems can be distinguished. By introducing passivity indices, the degree of a system's passivity (or property to provide positive damping) can be quantified in terms of a frequency-dependent excess or shortage of passivity [14, 25, 169].

In the following, the input feed-forward passivity (IFP) index for a stable linear system with transfer function matrix $\underline{\underline{G}}(s)$ at frequency ω is defined as

$$\text{IFP}\left\{\underline{\underline{G}}(j\omega)\right\} = \nu(\omega) = \frac{1}{2}\underline{\lambda}\left\{\underline{\underline{G}}(j\omega) + \underline{\underline{G}}^{H}(j\omega)\right\}, \tag{2.1}$$

where $\underline{\lambda}$ denotes the minimum eigenvalue. Similarly, the output feedback passivity (OFP) index for a system that has no zeros in the right half plane is defined by

$$\text{OFP}\left\{\underline{\underline{G}}(j\omega)\right\} = \rho(\omega) = \frac{1}{2}\underline{\lambda}\left\{\underline{\underline{G}}^{-1}(j\omega) + [\underline{\underline{G}}^{-H}(j\omega)]\right\}. \tag{2.2}$$

For linear SISO systems, the definition of (2.1) simplifies to $\text{IFP}\left\{G(j\omega)\right\} = \nu(\omega) = \text{Re}\left\{G(j\omega)\right\}$ and (2.2) becomes

$$\text{OFP}\left\{G(j\omega)\right\} = \rho(\omega) = \text{Re}\left\{G^{-1}(j\omega)\right\} = \frac{\nu(\omega)}{\left|G(j\omega)\right|^2} \tag{2.3}$$

which directly shows that a positive (or negative) IFP index inherently implies a positive (or negative) OFP index and vice versa. At this point it should be emphasized that, throughout this thesis, passivity indices are defined as frequency-dependent quantities, whereas definitions in the literature often refer to constant scalars, which are specified by IFP $\{\underline{\underline{G}}\} = \nu = \frac{1}{2}\min_{\omega\in\mathbb{R}}\lambda\{\underline{\underline{G}}(j\omega)+\underline{\underline{G}}^{H}(j\omega)\}$ and OFP $\{\underline{\underline{G}}\} = \rho = \frac{1}{2}\min_{\omega\in\mathbb{R}}\lambda\{\underline{\underline{G}}^{-1}(j\omega)+\underline{\underline{G}}^{-H}(j\omega)\}$ [155, 169]. In addition, it is important to note that the transfer functions of the considered systems do not necessarily have to be rational, see also [4, 154, 155, 169]. For the evaluation of the systems' IFP and OFP indices, the functions $\underline{\underline{G}}(s)$ or $G(s)$ may thus contain time delays, which, as will be seen, is crucial for the modeling of digitally controlled power converters. The discussed theory can be applied directly if the functions of the numerators and denominators are given by (meromorphic) quasi-polynomials of the generic form

$$m(s) = \sum_{k=0}^{n}\sum_{q=0}^{p} a_{kq}s^{k}e^{-s\kappa_{kq}T}, \qquad \kappa_{kq}T \geq 0 \tag{2.4}$$

where the respective denominators have a higher degree than the corresponding numerators and contain the term with the highest degree in s, which is additionally delay-free, i.e., $\kappa_{nq}T = 0, \forall q$ [46, 106]. But even if the time-delay systems under study can not be represented in this form, the passivity concept can be employed taking into account that any term of the form $e^{-s\kappa T}$ can be approximated with reasonable accuracy by a rational polynomial using a Padé approximation of a sufficiently high order. Hence, an asymptotically stable MIMO system with transfer function matrix $\underline{\underline{G}}(s)$ or SISO system with transfer function $G(s)$ can be regarded as passive, if $\nu(\omega) \geq 0$ (or $\rho(\omega) \geq 0$). On the other hand, if $\nu(\omega) < 0$, the system shows a shortage of passivity and can be rendered passive by employing a minimum positive feed-forward of $|\nu(\omega)|$, see Fig. 2.1A. Referring to Section 2.1.1, the system becomes strictly passive, if the used feed-forward gain is larger than $|\nu(\omega)|\ \forall\omega \in \mathbb{R}$. Similarly, if $\rho(\omega)$ is negative, the system also lacks passivity and can be ren-

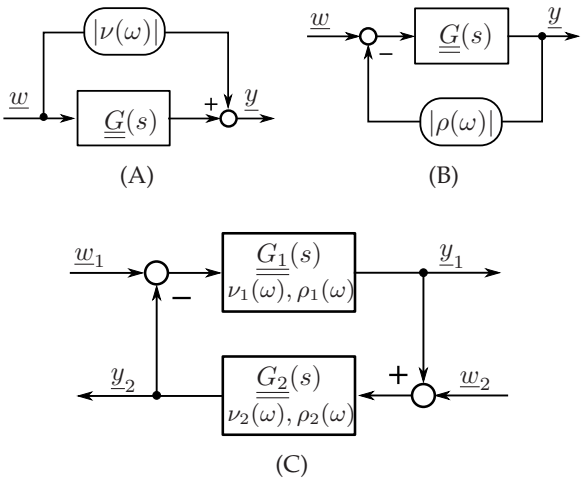

Fig. 2.1: Passivation of $\underline{\underline{G}}(s)$ (A) with IFP $\left\{\underline{\underline{G}}(j\omega)\right\} = \nu(\omega) < 0$ by input feed-forward and (B) with OFP $\left\{\underline{\underline{G}}(j\omega)\right\} = \rho(\omega) < 0$ by output feedback. (C) Feedback interconnection of two systems $\underline{\underline{G}}_1$ and $\underline{\underline{G}}_2$, showing the IFP and OFP indices $\nu_1(\omega), \rho_1(\omega)$ and $\nu_2(\omega), \rho_2(\omega)$, respectively.

dered passive by employing a minimum negative feedback of $|\rho(\omega)|$ as shown in Fig. 2.1B [74]. Focusing on SISO systems, the ideas of Fig. 2.1A and Fig. 2.1B can also graphically be examined, by noticing that the feed-forward action shifts the Nyquist plot of $G(j\omega)$ by $|\nu(\omega)|$ in the right direction, such that $\mathrm{Re}\{G(j\omega)\} \geq 0, \forall\omega \in \mathbb{R}$, while the feedback action transforms the Nyquist plot in a circle that crosses the real axis at $s = 0$ and $s = 1/|\rho(\omega)|$ [25,74].

Furthermore, if passive or (partially) non-passive systems are interconnected in a negative feedback-loop, as illustrated in Fig. 2.1C, passivity indices can also be utilized to quantify the passivity of the resulting closed-loop system [169]. In particular, given two asymptotically stable SISO systems $G_1(s)$ and $G_2(s)$ with the IFP and OFP indices $\nu_1(\omega), \rho_1(\omega)$ and $\nu_2(\omega), \rho_2(\omega)$, respectively, rather simple passivity criteria can be derived. If $G_1(s)$ has the form of the system in Fig. 2.1B and $G_2(s)$ has the form of the system in Fig. 2.1A, it can directly be seen that the OFP index of the interconnected system is given by $\rho(\omega) + \nu(\omega)$. Thus, the feedback-

loop is passive, if $\rho(\omega) + \nu(\omega) > 0, \forall\omega \in \mathbb{R}$. In addition, summarizing the results from Appendix A.1, the interconnected system is passive if $\rho_1(\omega) + \nu_2(\omega) \geq 0, \forall\omega \in \mathbb{R}$ or if $\nu_1(\omega) \geq 0, \forall\omega \in \mathbb{R}$ and simultaneously $\rho_2(\omega) \geq 0, \forall\omega \in \mathbb{R}$. In this context, the first condition shows one of the basic concepts of passivity-based control, namely that a shortage of OFP can be compensated for by an feedback-action that has an excess of IFP, i.e., $\nu_2(\omega) \geq |\rho_1(\omega)|$ [74, 94, 169].

2.1.3 Passivity Theorems

A direct implication from the passivity definitions from Sec. 2.1.1 is that every passive system is stable, i.e., $\mathrm{Re}\{s_\lambda\} \leq 0, \forall\lambda$. Further, each strictly passive system is asymptotically stable, i.e, $\mathrm{Re}\{s_\lambda\} < 0, \forall\lambda$. Regarding Fig. 2.1C, the closed-loop system thus always results in an asymptotically stable system, if the subsystem in the forward path is strictly passive and the subsystem in the feedback path is passive [25, 74]. In case of proper SISO systems, this can directly be seen by applying the Nyquist stability criterion [10, 89, 98, 119]. It follows that the total phase response of the open-loop system's Bode plot is bounded and never reaches $-180°$ or the open-loop system's Nyquist curve always remains in the third and fourth quadrant of the complex plane. This property is especially useful to maintain (robust) stability even if large variations in the system parameters occur or large (modeling) uncertainties are to be expected [14, 25, 73, 92]. Beyond that, passive systems feature the property that two passive subsystems which are either connected in parallel or in a feedback-loop both result in a passive system again [74, 169]. These are also the reasons why the concept of passivity represents a powerful approach for the assessment and stabilization of power systems, where all energy producers and loads are connected in parallel.

Finally it should be noted that, even though the formal passivity definition from Sec. 2.1.1 and the stated passivity theorems require an evaluation of the system characteristics for (almost) all frequencies from $-\infty$ to $+\infty$, practical applications often allow to weaken this strict demand. More specifically, regarding (symmetrical) digital control systems, it is

typically sufficient to restrict the passivity assessment to frequencies from $\omega = 0$ up to the Nyquist frequency ω_{N}, defined by the system's sampling time, see [39,75]. This can be explained by the fact that digital controllers misinterpret signal components above the Nyquist frequency as components below ω_{N}, which thus defines the active, controllable frequency limit of the system [39, 42, 110, 119]. In order to identify and prevent a critical excitation of above Nyquist frequency signal components, the less conservative small gain theorem [32,74] can be incorporated in the next step. Accordingly, the stability of an interconnected system can be guaranteed, if every system $1)$ is strictly passive in the frequency range $[0, \omega_{\mathrm{N}}]$ and $2)$ provides a gain less than one in the higher frequency range, i.e., $\overline{\sigma}\left\{\underline{\underline{G}}(j\omega)\right\} < 1, \forall\omega \in (\omega_{\mathrm{N}}, \infty)$, where $\overline{\sigma}$ denotes the maximum singular value [14]. With regard to the stringent requirements of today's grid standards, see e.g., [6, 15], and the resulting necessity to implement passive (damping) output filters, it can be assumed that the second condition is always fulfilled for the converter systems under study. For this reason, and in accordance with the majority of related works, the following analysis mainly focuses on the low frequency range up to the Nyquist frequency.

2.2 Grid-Connected VSCs

2.2.1 Classification and Operating Principles

Depending on the type and functionality in the power system, grid-connected VSCs can generally be classified into grid-feeding, grid-supporting, and grid-forming power converters [20, 108, 127]. While the latter realization is controlled to represent an (ideal) AC voltage source and aims to preset a voltage with amplitude $|V_{\mathrm{PCC,set}}|$ and frequency ω_{set} at the point of common coupling (PCC), the first converter type acts as a current source that delivers a desired active power P_{set} and reactive power Q_{set} to an energized power grid. In order to properly regulate the exchanged power, grid-feeding converters typically use phase-locked-loops (PLLs) to synchronize with the voltage at the PCC [2]. In this

regard, we proposed a simple model of a synchronous reference frame PLL in [5], where an overview of different (other) PLL realizations and synchronization techniques can be found in e.g., [47, 83, 127]. The last type of converter, the grid-supporting converter, is in between the other two types and can be implemented either as a current or a voltage source, with or without PLL, see e.g., [108] for more details. Depending on the realization, these converters utilize different outer control loops, including a droop or a reverse droop control [24, 102, 127], trying to maintain the grid voltage and grid frequency at their nominal values, or provide other ancillary services, such as balancing energy imbalances, working in island mode or restoring the grid by black starting. [71, 108].

At the moment, most RES are still operated as simple grid-feeding units, but the trend is more and more moving towards grid-supporting realizations or grid-forming converters [18, 132, 136]. Since there exists no uniform VSC control structure for the implementation of the desired converter functionality, it is difficult to present a general control block diagram. However, the systems are always operated in a similar way. Fig. 2.2 shows an exemplary three-phase circuit diagram of a grid-connected VSC with a selection of optional outer-loop controllers.

While the implementation of an outer control loop, like an AC voltage or power control structure mainly defines the type of converter, almost all grid-connected VSCs have a fast current control loop on the lowest layer of a cascaded control [108, 127]. The current control can either use the grid-side current $\boldsymbol{I}_{\mathrm{g}}^{t}$ or the converter-side current $\boldsymbol{I}^{t}$ as control variable. While the feedback of the grid-side current has the advantage that the injected current is directly regulated, the feedback of the converter-side current results in a simpler controller design, where the resonant part of the LCL filter can be considered as a part of the grid impedance Z_{g}.

In order to specifically regulate the injected active and reactive current components, and thus, to realize a desired converter functionality, most converters use the concept of voltage oriented control [127]. With this approach, the input $\boldsymbol{I}_{\mathrm{ref}}$ of the inner current control loop is specified in a rotating (d, q)-frame that is controlled to be aligned with the complex voltage space vector of $\boldsymbol{V}_{\mathrm{PCC}}^{t}$. Then, since the current setpoints represent DC

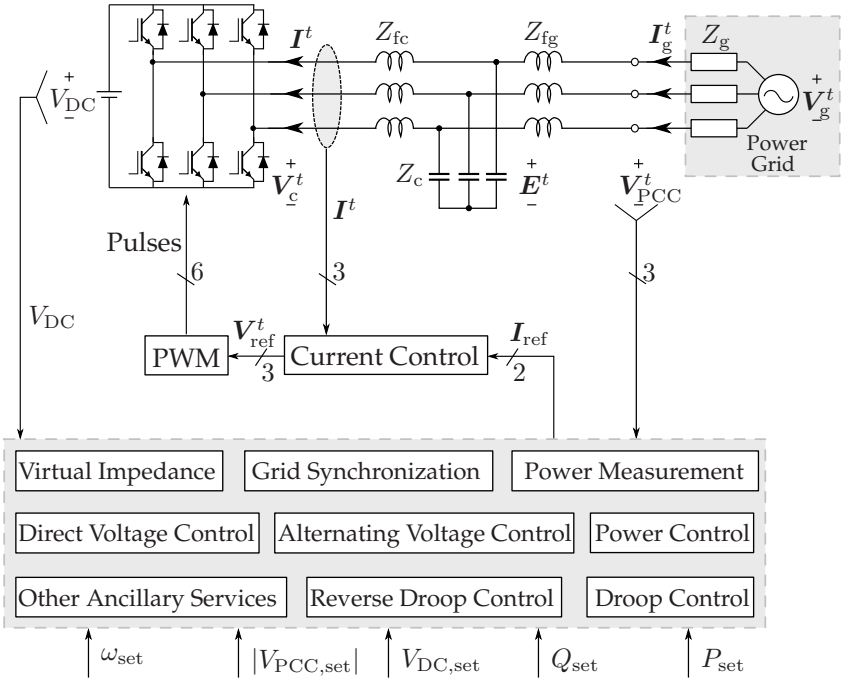

Fig. 2.2: Principle three-phase circuit diagram of a grid-connected VSC with optional outer-loop controllers.

quantities, two simple proportional-integral (PI) controllers can be implemented to achieve a zero steady-state error. However, such synchronous frame controllers have to cope with cross coupling effects, which are introduced by the transformation of the converter plus filter dynamics into a rotating (d, q)-frame [72]. To achieve a better performance, additional (decoupling) feed-forward actions must be designed [20, 118]. Besides that, the required transformations may cause an unwanted active or reactive current injection if the synchronous frame identification is inaccurate.

Alternatively, in order to avoid complex decoupling strategies and simultaneously reduce the computational effort of multiple nonlinear transformations, resonant current controllers in the stationary (α, β)-domain can be utilized. This control strategy has attended a lot of

interest in the past years, see e.g., [3, 22, 29, 56, 63, 82, 160, 161, 164, 170]. In addition to their simple implementation in the continuous Laplace-domain, proportional-resonant current controllers offer the opportunity to compensate for multiple harmonics without the need of multiple rotating reference frames. They inherently take both, the positive- as well as negative-sequence components into account [27, 126], but require a transformation of the DC reference current $\boldsymbol{I}_{\mathrm{ref}}$ into sinusoidal signals in the (α, β)-domain. The current controller output acts as three-phase voltage reference $\boldsymbol{V}_{\mathrm{ref}}^{t}$ for the PWM, which generates the firing pulses for the semiconductor switches of the VSC. For simplicity, it is often assumed that the DC voltage control, also referred to as direct voltage control (DVC), works perfectly and the DC-link voltage V_{DC} remains constant during the operation.

2.2.2 Impedance-Based Modeling and Harmonic Stability Concept

The concept of harmonic stability is based on the impedance-based modeling idea, where every active energy producer or consumer in the power grid can be interpreted as a voltage or current source with associated input impedance or admittance, respectively [123]. In case of grid-feeding and grid-supporting power converters without outer AC voltage control loop, the interconnected grid-converter system from Fig. 2.2 can also be represented by the simplified impedance-based equivalent circuit diagram shown in Fig. 2.3.

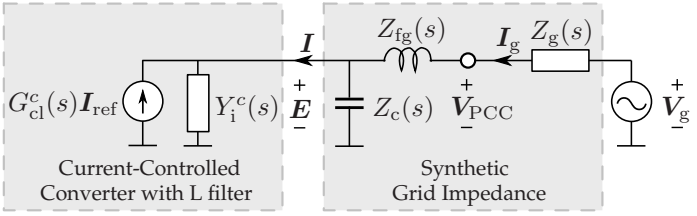

Fig. 2.3: Simplified impedance-based equivalent circuit diagram of a grid-connected VSC with LCL filter and converter-side current control.

Due to the underlying current control structure, the converter basically shows the behavior of a current source, which output current is specified by outer control loops. Ideally, the current source would inject the desired reference current $\boldsymbol{I}_{\mathrm{ref}}$ without any time delay and independent of the power grid condition. However, because of the finite controller bandwidth, the current source has a non-ideal behavior and shows the reference current dynamics $G_{\mathrm{cl}}^{c}(s) \neq 1$ and the parallel input admittance $Y_{\mathrm{i}}^{c}(s)$ [4, 11, 30, 57, 140, 143, 150].

Applying basic rules known from linear circuit theory, all remaining passive filter components on the right side of Fig. 2.3 can be combined to a synthetic grid impedance $\tilde{Z}_{\mathrm{g}}(s)$, i.e.,

$$\tilde{Z}_{\mathrm{g}}(s) = Z_{\mathrm{c}}(s) \,\|\, (Z_{\mathrm{fg}}(s)+Z_{\mathrm{g}}(s)) = \frac{Z_{\mathrm{c}}(s)(Z_{\mathrm{fg}}(s)+Z_{\mathrm{g}}(s))}{Z_{\mathrm{c}}(s)+Z_{\mathrm{fg}}(s)+Z_{\mathrm{g}}(s)} = \frac{Z_{\mathrm{c}}(s)}{1+Z_{\mathrm{c}}(s)\tilde{Y}_{\mathrm{fg}}(s)} \tag{2.5}$$

where $\tilde{Y}_{\mathrm{fg}}(s) = 1/(Z_{\mathrm{fg}}(s) + Z_{\mathrm{g}}(s))$ is the common admittance of the grid-side filter inductance $Z_{\mathrm{fg}}(s)$ in series with the grid impedance $Z_{\mathrm{g}}(s)$. Then, the synthetic PCC voltage $\boldsymbol{E}$ that is seen from the converter can be expressed as

$$\boldsymbol{E}(s) = \tilde{\boldsymbol{V}}_{\mathrm{g}}(s) - \tilde{Z}_{\mathrm{g}}(s)\boldsymbol{I}(s) = \tilde{Z}_{\mathrm{g}}(s)\tilde{Y}_{\mathrm{fg}}(s)\boldsymbol{V}_{\mathrm{g}}(s) - \tilde{Z}_{\mathrm{g}}(s)\boldsymbol{I}(s). \tag{2.6}$$

In combination with the converter dynamics

$$\boldsymbol{I}(s) = G_{\mathrm{cl}}^{c}(s)\boldsymbol{I}_{\mathrm{ref}} + Y_{\mathrm{i}}^{c}(s)\boldsymbol{E}(s), \tag{2.7}$$

the overall closed-loop system can be described by

$$\boldsymbol{I}(s) = \frac{G_{\mathrm{cl}}^{c}(s)}{1 + Y_{\mathrm{i}}^{c}(s)\tilde{Z}_{\mathrm{g}}(s)}\boldsymbol{I}_{\mathrm{ref}}(s) + \frac{Y_{\mathrm{i}}^{c}(s)}{1 + Y_{\mathrm{i}}^{c}(s)\tilde{Z}_{\mathrm{g}}(s)}\tilde{\boldsymbol{V}}_{\mathrm{g}}(s). \tag{2.8}$$

In the following, it is presupposed that the grid voltage $\boldsymbol{V}_{\mathrm{g}}$ is stable without the connected converter and that all passive filter components represent (asymptotically) stable minimum phase systems. Then, given (2.8), it can be seen that both, the reference current dynamics from $\boldsymbol{I}_{\mathrm{ref}}$ to $\boldsymbol{I}$

as well as the disturbance dynamics from $\tilde{\boldsymbol{V}}_\mathrm{g}$ to $\boldsymbol{I}$ are stable, if $G_\mathrm{cl}^c(s)$ is stable and the feedback-interconnection of the VSC's input admittance $Y_\mathrm{i}^c(s)$ with the synthetic grid impedance $\tilde{Z}_\mathrm{g}(s)$ satisfies the SISO Nyquist stability criterion [10, 89, 98, 119]. Consistent with common practice, it can always be assumed that the former condition is fulfilled, since only a stable reference current behavior $G_\mathrm{cl}^c(s)$ makes sense if grid-feeding or grid-supporting converters shall be connected to the grid. In this context, Ch. 4 reviews our current controller design from [3], which aims to result in an asymptotically stable reference current dynamics.

Then, the system's stability is determined by the interconnection of $Y_\mathrm{i}^c(s)$ and $\tilde{Z}_\mathrm{g}(s)$. The grid impedance results from the status of the power network, where besides the impedances of power cables or active and passive loads, also other grid-connected VSCs have to be considered [11, 88, 141, 143, 147]. Further, the grid-side filter components, i.e., in this case the capacitance Z_c and the inductance Z_fg are added to Z_g, which introduces a resonance to the synthetic grid impedance $\tilde{Z}_\mathrm{g}$. According to common design guidelines for low- as well as medium-voltage converters with switching frequencies between $5\,\mathrm{kHz}$ and $10\,\mathrm{kHz}$, this filter resonance typically lies between ten times the grid's fundamental frequency f_r and the converter's Nyquist frequency $f_\mathrm{N} = f_\mathrm{s}/2$, where f_s denotes the switching frequency [13, 17, 84]. In some applications, the resonance can also be located at higher frequencies [125]. As shown in this thesis, the active or passive damping of this filter resonance is one of the main challenges in the converter design, where the concept of harmonic stability can be used.

On the other hand, the VSC's input admittance $Y_\mathrm{i}^c(s)$ depends on the converter's output filter as well as the implemented controller structure and parameterization. In particular, $Y_\mathrm{i}^c(s)$ may have a positive, zero, or a negative real part in different frequency ranges, where mainly two ranges can be distinguished, i.e., 1) the low-frequency range near the grid's fundamental frequency f_r and 2) the high-frequency range from hundreds of Hertz up to a few Kilohertz above the converter's switching frequency f_s [55, 140]. The first frequency range is predominantly influenced by outer control loops as the power control, the DVC, and the alter-

nating voltage control (AVC) [2, 24, 52, 55]. Moreover, the PLL is known to introduce negative damping in the low-frequency q-axis dynamics, see e.g., [31,52,55,144,148,149], where the effects have more influence in weak grids, showing a low short-circuit-ratio [168]. On the other hand, the converter input admittance in the high-frequency range is mainly shaped by the VSC's output filter and the current control in combination with the PWM and the sampling process [11, 42, 53, 57]. In this context, especially the frequency region between approximately $f_\mathrm{s}/6$ up to the Nyquist frequency is crucial for stability, since converters with single-update PWMs and no active or passive damping usually show a conductance with negative real part there [4, 55, 111, 141, 156]. Additionally, it has recently been shown that the sampling process, or more precisely, the aliasing of above Nyquist frequency signal components, can negatively affect the VSC's input admittance in the high-frequency range [42, 53].

Following the concept of harmonic stability, the interconnection of the input admittance $Y_\mathrm{i}^c(s)$ and the synthetic grid impedance $\tilde{Z}_\mathrm{g}(s)$ may result in resonances, that are either over/under-damped, critically damped or exponentially amplifying [140]. If there is positive damping at each resonance frequency, decaying, and thus, stable harmonic oscillations will emerge. Contrary, if there is zero or negative damping at at least one resonance frequency, a critically damped or an (exponentially) increasing harmonic oscillation will be created. Under certain circumstances it is also possible that a growing harmonic oscillation causes the converter impedance to change and introduce additional damping. Then, the system may reach a critically stable point with zero damping [124]. Otherwise, the unstable oscillations continue to rise until protection units are triggered or physical damage is caused.

One possibility to prevent a power system destabilization is to demand passivity of all grid-connected components. Given the dynamics of the grid-converter system (2.8), this concept can simply be verified regarding the passivity theorems from Sec. 2.1.3. Assuming that the power network only consists of passive components, that is $\tilde{Z}_\mathrm{g}(s)$ from (2.5) is passive, (asymptotic) stability can be guaranteed by design, if the VSC input admittance $Y_\mathrm{i}^c(s)$ is also (strictly) passive. In this case, all emerging reso-

nances are necessarily positively damped, and thus, critical oscillations cannot arise. However, as there are still some open questions regarding the inclusion of effects from the digital control, which could not yet be clarified conclusively, the next chapters discuss the converter modeling, control and passivation in more detail.

3 System Modeling

In this chapter, the system modeling is demonstrated on the digitally current-controlled grid-connected VSC from Fig. 2.2. The content is mainly based on our work [4] and the research of Harnefors et al. with our proposed SISO small-signal PWM representation of [1]. After introducing the adopted notation and the system under study, Sec. 3.2 describes all converter components in detail. Based on the resulting converter current dynamics from Sec. 3.3, the last section deduces two typical SISO models for the VSC's input admittance [53], namely 1) the single-frequency and 2) multiple-frequency model, which, in this thesis, are referred to as quasi-analog and primary-frequency model, respectively.

3.1 Circuit Diagram and Basic Control Structure

Throughout this thesis, three-phase systems are considered, but the contributions can also be applied to single-phase systems in a similar way. In this context, supposing symmetric conditions, where $I_\mathrm{a}(t) + I_\mathrm{b}(t) + I_\mathrm{c}(t) = 0$, each three-phase quantity can equivalently be understood as a rotating space vector in the stationary (α, β)-domain. In the following, the transformation between the three-phase representation and the (α, β)-domain is performed by the power-invariant Clarke transformation [51, 64, 91, 118, 127], e.g.,

$$\boldsymbol{I}(t) = I_\alpha(t) + jI_\beta(t) = \sqrt{\frac{2}{3}}\left(I_\mathrm{a}(t) + I_\mathrm{b}(t)e^{j\frac{2}{3}\pi} + I_\mathrm{c}(t)e^{j\frac{4}{3}\pi}\right). \quad (3.1)$$

Here, $\boldsymbol{I}(t)$ represents a complex space vector, which is, for instance, given by $\boldsymbol{I}(t) = I\sqrt{3/2}\cdot e^{j\phi_i}e^{j\omega_i t}$ if $I_\mathrm{a}(t) = I\cos(\omega_i t + \phi_i)$, $I_\mathrm{b}(t) = I\cos(\omega_i t + \phi_i - 2\pi/3)$, $I_\mathrm{c}(t) = I\cos(\omega_i t + \phi_i - 4\pi/3)$ with I, ω_i, and ϕ_i as the currents (peak)

amplitude, frequency, and phase shift, respectively. For brevity, the signals' time-dependency or dependency on the complex Laplace variable $s = \sigma + j\omega$ is omitted where there is no risk of confusion from now on. Since digital converter systems are considered, the * denotes sampled data signals in the time-domain or the discrete Laplace-transformed of signals and systems in the s-domain [39, 114, 119].

Using the introduced notation, Fig. 3.1 shows the basic stationary (α, β)-frame control block diagram of the VSC under study.

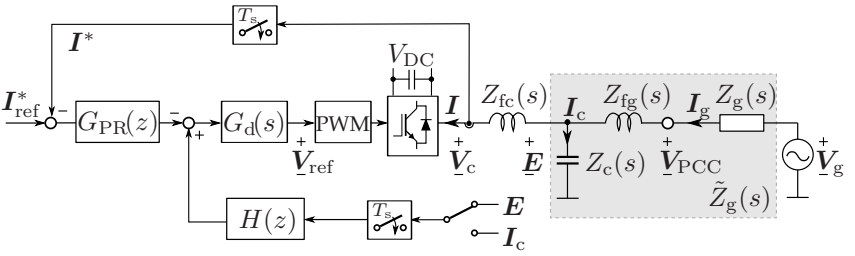

Fig. 3.1: Basic single-phase circuit and stationary (α, β)-frame control block diagram of a digitally current-controlled VSC that is connected to the grid over an LCL filter.

The grid is modeled by a voltage source $\boldsymbol{V}_{\mathrm{g}}$ with fundamental frequency f_{r}, e.g., $50\,\mathrm{Hz}$ or $60\,\mathrm{Hz}$, and an associated grid impedance Z_{g}. The converter implements a digital stationary-frame current controller $G_{\mathrm{PR}}(z)$, which uses the sampled converter-side current $\boldsymbol{I}^*$ as control variable and $\boldsymbol{I}^*_{\mathrm{ref}}$ as digital current reference. To be consistent with common literature, like [4, 41, 42, 53, 55, 57, 100, 110], the converter current $\boldsymbol{I}$ is defined to flow into the converter. For the purpose of active damping, the system implements a filter $H(z)$, which either utilizes the synthetic PCC voltage $\boldsymbol{E}$ or the LCL filter's capacitor current $\boldsymbol{I}_{\mathrm{c}}$ as a feed-forward quantity. In comparison to damping strategies that use the voltage $\boldsymbol{E}$, see e.g., [41, 42, 110, 111], the usage of $\boldsymbol{I}_{\mathrm{c}}$ allows to implement feed-forward filters with differentiation actions more easily [4, 57, 157]. In order to provide sufficient time for the analog-to-digital conversion and the digital computation, the controller plus feed-forward filter output is delayed by

the computation time T_c, which is modeled by $G_\mathrm{d}(s)$. The resulting converter reference voltage $\boldsymbol{V}_\mathrm{ref}$ acts as the input of the PWM. For simplicity, it is assumed that the DC-link voltage V_DC remains constant during the operation and that overmodulation does not occur, i.e., $|\boldsymbol{V}_\mathrm{ref}| \leq V_\mathrm{DC}/2$. To begin with, effects of the outer loop controllers are not considered, but should be investigated in future works.

Throughout this thesis, the exemplary VSC test-system parameters of Tab. 3.1 are used to demonstrate the proposed methods by example.

Table 3.1: Exemplary converter test-system parameters

Parameter	Symbol	Value	Units
Rated converter power	S_b	10.4	kVA
Nominal grid phase voltage	E_b	$400/\sqrt{3} \approx 230$	V (rms)
Nominal converter phase current	I_b	15	A (rms)
Converter base impedance	$Z_\mathrm{b} = E_\mathrm{b}/I_\mathrm{b}$	15.396	Ω
DC-link voltage	V_DC	700	V
Fundamental grid frequency	$\omega_\mathrm{r} = 2\pi f_\mathrm{r}$	$2\pi 50 \approx 314.16$	rad/s
Switching frequency	f_PWM	10	kHz
Sampling time	$T_\mathrm{s} = 1/f_\mathrm{PWM}$	0.1	ms
Computation time	$T_\mathrm{c} = T_\mathrm{s}$	0.1	ms

3.2 System Components

3.2.1 Normalized Converter Filter Dynamics

In order to meet harmonic current limits that are enforced by grid connection standards, like the IEEE 1547 [68] or the BDEW norm for generating plants connected to the medium-voltage network [15], grid-connected converters typically implement inductive passive output filters [17,49,84, 109, 138]. While filters with a single inductance are highly efficient, the high costs and the excessive voltage drop across the inductor limits their application to the small kilowatt range. Moreover, to overcome their poor high-frequency attenuation capability of $-20\,\mathrm{dB/dec}$, most of the modern low- and medium-voltage grid-connected VSCs implement LCL filters or

other high-order filters, see e.g., [16, 17, 49, 100, 109, 117, 138, 152] for an overview. As these filters provide two or three times more attenuation at high frequencies, the output filter size and the associated costs can be reduced significantly [17, 49]. One drawback in the use of LCL filters, however, is the introduction of an additional (output filter) resonance, which in turn might result in harmonic stability issues, if the filter's resonance falls in the frequency range, where the undamped converter shows a negative input admittance [88, 140, 144, 153, 156]. In order to facilitate a stable operation on the grid, it can often be beneficial to implement some kind of passive damping strategy. In this context, Fig. 3.2 shows three selected LCL filter topologies, which components are described in the following.

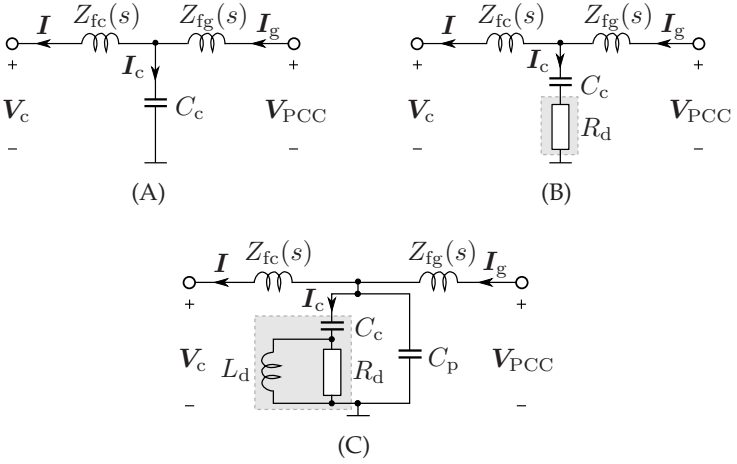

Fig. 3.2: Single-phase schematics of different LCL filter topologies, where (A) represents an ideal LCL filter, (B) uses a series resistor for passive damping, and (C) implements a split-capacitor with resistive-inductive passive damping.

Converter-Side Inductance

Given the topologies from Fig. 3.2 and assuming that the filter component on the converter-side, Z_{fc}, consists of an inductance L_{fc} and some (series)

resistance R_{fc}, the continuous-time dynamics of the converter current $\boldsymbol{I}$ in Fig. 3.1 are given by

$$L_{\mathrm{fc}} \frac{d\boldsymbol{I}(t)}{dt} = -R_{\mathrm{fc}} \boldsymbol{I}(t) + \boldsymbol{E}(t) - \boldsymbol{V}_{\mathrm{c}}(t) \tag{3.2}$$

where $\boldsymbol{V}_{\mathrm{c}}$ and $\boldsymbol{E}$ are the VSC output voltage and the synthetic PCC voltage, respectively. At this point it should be noticed that the modeled resistance R_{fc} has no filtering purpose, but introduces additional damping in the low- as well as high-frequency range. As shown in [4, 53, 110], this damping property can be used to render the converter system passive or at least makes active damping approaches more robust against modeling uncertainties. Mostly, R_{fc} does not have to be installed physically and the parasitic resistance of L_{fc} [38] may act sufficiently dissipative.

In order to become independent of the power class and specific converter parameters, (3.2) can be normalized by the converter's base values. Using the nominal rated PCC phase voltage $E_{\mathrm{b}} = |\boldsymbol{E}_{\mathrm{b}}| / \sqrt{3}$, the nominal rated converter phase current $I_{\mathrm{b}} = |\boldsymbol{I}_{\mathrm{b}}| / \sqrt{3}$, and the converter's nominal power $S_{\mathrm{b}} = |\boldsymbol{E}_{\mathrm{b}}| \, |\boldsymbol{I}_{\mathrm{b}}| = 3 E_{\mathrm{b}} I_{\mathrm{b}}$, a relation of (3.2) to E_{b} yields

$$\frac{L_{\mathrm{fc}}}{Z_{\mathrm{b}}} \frac{d\boldsymbol{I}(t)/I_{\mathrm{b}}}{dt} = -\frac{R_{\mathrm{fc}} I_{\mathrm{b}}^2}{S_{\mathrm{b}}} \frac{\boldsymbol{I}(t)}{I_{\mathrm{b}}} + \frac{\boldsymbol{E}(t)}{E_{\mathrm{b}}} - \frac{\boldsymbol{V}_{\mathrm{c}}(t)}{E_{\mathrm{b}}} \tag{3.3}$$

where $Z_{\mathrm{b}} = E_{\mathrm{b}}/I_{\mathrm{b}} = S_{\mathrm{b}}/(3 I_{\mathrm{b}}^2)$ defines the converter's base impedance. Then, introducing the normalized values

$$\frac{L_{\mathrm{fc}}}{Z_{\mathrm{b}}} = l_{\mathrm{fc}}, \quad \frac{3 R_{\mathrm{fc}} I_{\mathrm{b}}^2}{S_{\mathrm{b}}} = \frac{R_{\mathrm{fc}}}{Z_{\mathrm{b}}} = r_{\mathrm{fc}}, \quad \frac{\boldsymbol{I}}{I_{\mathrm{b}}} = \boldsymbol{i}, \quad \frac{\boldsymbol{E}}{E_{\mathrm{b}}} = \boldsymbol{e}, \quad \frac{\boldsymbol{V}_{\mathrm{c}}}{E_{\mathrm{b}}} = \boldsymbol{v}_{\mathrm{c}} \tag{3.4}$$

where l_{fc} has the unit seconds and all other quantities are dimensionless, the normalized converter-side filter dynamics in the Laplace-domain can be derived as

$$\boldsymbol{i}(s) = Y_{\mathrm{fc}}(s) \left(\boldsymbol{e}(s) - \boldsymbol{v}_{\mathrm{c}}(s) \right) = \frac{1}{l_{\mathrm{fc}} s + r_{\mathrm{fc}}} \left(\boldsymbol{e}(s) - \boldsymbol{v}_{\mathrm{c}}(s) \right). \tag{3.5}$$

Besides optimized filter design approaches as in [16, 17], the inductance L_{fc} is typically chosen depending on a desired maximum peak-to-peak

current ripple, defined by $\Delta I_{\max}$, and the converter's switching frequency f_{PWM}, i.e.,

$$L_{\mathrm{fc}} \geq \frac{1}{\kappa_{\mathrm{PWM}}} \frac{V_{\mathrm{DC}}}{f_{\mathrm{PWM}} \Delta I_{\max}}. \tag{3.6}$$

Here, κ_{PWM} depends on the converter type and the implemented PWM scheme, e.g., $\kappa_{\mathrm{PWM}} = 8$ for a classical single-phase PWM [49, 125, 138] or $\kappa_{\mathrm{PWM}} = 24$ for a three-phase space-vector modulation (SVM) [17, 109]. In general, the selection of the current ripple $\Delta I_{\max}$ represents a trade-off between switching and conduction losses, and inductor coil and core losses. Depending on the power rating, it is therefore often suggested to choose the maximum current ripple as $10\% - 40\%$ of the rated converter current [84, 109, 125, 138]. For instance, using a VSC with the parameters from Tab. 3.1 and requiring a current ripple of approximately 15%, i.e., a peak-to-peak ripple of $\Delta I_{\max} \approx 3.2\,\mathrm{A}$, the converter-side inductance can be selected as $L_{\mathrm{fc}} = 3\,\mathrm{mH}$, which, with the suggested normalization (3.4) becomes $l_{\mathrm{fc}} = L_{\mathrm{fc}}/Z_{\mathrm{b}} \approx 0.195\,\mathrm{ms}$. By evaluating the given filter parameters in the works [13, 17, 84, 104, 109, 117, 125] which specifically concentrate on the LCL filter design of low- and medium-voltage converters with power ratings between a few kilowatts and several megawatts, it shows that common values of the normalized inductance l_{fc} range from about $0.07\,\mathrm{ms}$ to $0.5\,\mathrm{ms}$, also verifying that the designed inductance complies with typical configurations.

Grid-Side Inductance

Following the same line of reasoning, similar to (3.5), the normalized dynamics of the grid-side current are given by

$$\boldsymbol{i}_{\mathrm{g}}(s) = \tilde{Y}_{\mathrm{fg}}(s)\,(\boldsymbol{v}_{\mathrm{g}}(s) - \boldsymbol{e}(s)) = \frac{1}{l_{\mathrm{fg}} s + r_{\mathrm{fg}} + Z_{\mathrm{g}}(s)}\,(\boldsymbol{v}_{\mathrm{g}}(s) - \boldsymbol{e}(s)) \tag{3.7}$$

where $\boldsymbol{v}_{\mathrm{g}} = \boldsymbol{V}_{\mathrm{g}}/E_{\mathrm{b}}$, $\boldsymbol{i}_{\mathrm{g}} = \boldsymbol{I}_{\mathrm{g}}/I_{\mathrm{b}}$, and $l_{\mathrm{fg}} = L_{\mathrm{fg}}/Z_{\mathrm{b}}$, $r_{\mathrm{fg}} = R_{\mathrm{fg}}/Z_{\mathrm{b}}$ are the normalized inductance and resistance of the grid-side filter Z_{fg}, respectively. Moreover, $Z_{\mathrm{g}}(s)$ represents the usually unknown (and con-

tinuously varying) normalized grid impedance, which normally shows a predominant resistive-inductive behavior in the low-frequency range [19]. Based on prior knowledge, it can thus often be modeled as $Z_{\mathrm{g}}(s) = L_{\mathrm{g}}/Z_{\mathrm{b}}s + R_{\mathrm{g}}/Z_{\mathrm{b}} = l_{\mathrm{g}}s + r_{\mathrm{g}}$ [30, 86] and be considered as a part of the effective grid-side impedance $Z_{\mathrm{fg}}(s)$ during the design. In other scenarios however, where, e.g., the VSC is connected to the grid over a long transmission line [166] or a large number of other neighboring converters are connected in parallel [11, 88, 141], the grid impedance model $Z_{\mathrm{g}}(s)$ might take a more complex form and must be adapted accordingly for each individual case. If, in addition, the converter is connected to the grid over a transformer, the transformer's inductance and resistance should also be taken into account as part of L_{fg} and R_{fg}, respectively. Keeping these aspects in mind, L_{fg} is typically chosen as $L_{\mathrm{fg}} = \kappa_{\mathrm{L}} L_{\mathrm{fc}}$, where large ratios of κ_{L} make the location of the LCL filter's resonance frequency, and thus, the high-frequency current attenuation more robust against changes of the grid impedance. Nevertheless, to keep the costs low, it is often suggested that the fundamental voltage drop over the total inductance $L_{\mathrm{t}} = L_{\mathrm{fc}} + L_{\mathrm{fg}}$ should not be higher than approximately 10% of the base voltage [17, 84], i.e.,

$$L_{\mathrm{t}} = L_{\mathrm{fc}} + L_{\mathrm{fg}} \leq 0.1 \frac{E_{\mathrm{b}}}{\omega_{\mathrm{r}} I_{\mathrm{b}}} = 0.1 \frac{Z_{\mathrm{b}}}{\omega_{\mathrm{r}}}. \tag{3.8}$$

Hence, again given the parameters of the converter under study and noticing that the total admittance L_{t} should be lower than $4.9\,\mathrm{mH}$, the grid-side inductance can be chosen as $L_{\mathrm{fg}} = L_{\mathrm{t}} - L_{\mathrm{fc}} \approx 1.5\,\mathrm{mH}$, corresponding to a normalized inductance of $l_{\mathrm{fg}} = L_{\mathrm{fg}}/Z_{\mathrm{b}} = 97.43\,\mu\mathrm{s}$.

Capacitive Branch with Series Resistance

As shown in Fig. 3.2, the capacitive branch of an ideal LCL filter only consists of a capacitor C_{c}, while the simplest, damped LCL filter also shows a resistor R_{d} in series. Thus, using the normalized capacitance $c_{\mathrm{c}} = C_{\mathrm{c}} Z_{\mathrm{b}}$ in seconds and the normalized damping resistance $r_{\mathrm{d}} = R_{\mathrm{d}}/Z_{\mathrm{b}}$, $r_{\mathrm{d}} \geq 0$,

the dynamics of the (effective) capacitive impedance $Z_{\mathrm{c}}(s)$ from Fig. 3.2A and Fig. 3.2B can generally be described by

$$\boldsymbol{e}(s) = Z_{\mathrm{c}}(s)\boldsymbol{i}_{\mathrm{c}}(s) = \left(\frac{1}{c_{\mathrm{c}}s} + r_{\mathrm{d}}\right)\boldsymbol{i}_{\mathrm{c}}(s) = \frac{1 + r_{\mathrm{d}}c_{\mathrm{c}}s}{c_{\mathrm{c}}s}\left(\boldsymbol{i}_{\mathrm{g}}(s) - \boldsymbol{i}(s)\right) \quad (3.9)$$

where $\boldsymbol{i}_{\mathrm{c}} = \boldsymbol{I}_{\mathrm{c}}/I_{\mathrm{b}}$. In order to fulfill the desired high-frequency attenuation requirements and simultaneously avoid an increase of the converter-side inductance L_{fc}, the capacitance C_{c} should not be chosen too small. On the other hand, a large capacitance results in a large reactive power demand, and thus, requires a higher current that can flow into the capacitor. Therefore, it is typically suggested to select the capacitance as

$$C_{\mathrm{c}} = \kappa_{\mathrm{C}}\frac{S_{\mathrm{b}}}{3\,\omega_{\mathrm{r}}E_{\mathrm{b}}^2} = \kappa_{\mathrm{C}}\frac{1}{\omega_{\mathrm{r}}Z_{\mathrm{b}}} \quad (3.10)$$

where κ_{C} is chosen with respect to the maximum tolerated absorption of reactive power at rated conditions, e.g., $2\% - 15\%$ for low- and medium power VSC's [17, 84, 138] and $20\% - 50\%$ for high-power VSCs [139]. In the low power range, it is also advisable to verify that the resonance frequency of the LCL filter, $\omega_{\mathrm{r,G_{LCL}}} \approx 1/\sqrt{(L_{\mathrm{fc}} \parallel L_{\mathrm{fg}})C_{\mathrm{c}}} = \sqrt{(L_{\mathrm{fc}}+L_{\mathrm{fg}})/(L_{\mathrm{fc}}L_{\mathrm{fg}}C_{\mathrm{c}})}$, is well separated from the fundamental grid-frequency ω_{r} and lies below the Nyquist frequency ω_{N}, for example is in the range of $10\,\omega_{\mathrm{r}} < \omega_{\mathrm{r,G_{LCL}}} < \omega_{\mathrm{N}}$ [13, 84]. This constraint can also be used for the design of the grid-side inductance L_{fg} or the capacitance C_{c}, where the limits may change in some specific applications [125].

With regard to the exemplary VSC test-system, the reactive power that is consumed by the capacitance shall be limited to 2.5% of the converter's rated power. This can be satisfied by selecting the capacitance of the LCL filter to be $C_{\mathrm{c}} = 4.7\,\mu\mathrm{F}$, yielding a normalized capacitance of $c_{\mathrm{c}} = C_{\mathrm{c}}Z_{\mathrm{b}} = 72.36\,\mu\mathrm{s}$. According to the recommended filter parameters from [13,17,84, 104, 109, 117, 125], this choice of c_{c} can again be verified as being within a usual range of about $20\,\mu\mathrm{s}$ to $0.45\,\mathrm{ms}$, where the LCL filter resonance frequency is located at $\omega_{\mathrm{r,G_{LCL}}} \approx 14586\,\frac{\mathrm{rad}}{\mathrm{s}}$, and thus, also complies with the constraint $10\,\omega_{\mathrm{r}} \approx 3141.6\,\frac{\mathrm{rad}}{\mathrm{s}} < \omega_{\mathrm{r,G_{LCL}}} < \omega_{\mathrm{N}} \approx 31416\,\frac{\mathrm{rad}}{\mathrm{s}}$.

In addition to the design of the filter capacitor, passive damping approaches also require to select a reasonable value for the series resistor R_d. This resistance is often designed empirically, where e.g., the authors of [84] recommend the selection $R_\mathrm{d} = 1/(3\,\omega_{\mathrm{r,G_{LCL}}} C_\mathrm{c})$. In general, R_d should be chosen sufficiently large to prevent critical oscillations, but not too large in order to avoid an unreasonable decrease in efficiency. Here, especially the works [13, 17, 100] should be highlighted, which analyze and compare the losses of different (advanced) passive damping methods. At this point, however, no precise design of R_d is carried out here and reference is made to Sec. 5.2.2, which discusses a passivity-based parameterization more in detail. In the following, R_d is assumed to be $0.4\,\Omega \ll 1/(3\,\omega_{\mathrm{r,G_{LCL}}} C_\mathrm{c}) \approx 4.86\,\Omega$, or $r_\mathrm{d} = R_\mathrm{d}/Z_\mathrm{b} = 0.026 \ll 0.316$.

Capacitive Branch with Split-Capacitor and Resistive-Inductive Damping

The main drawback of the capacitive branch with series resistance is that all current components flow through the damping resistor R_d. This generally results in high resistive losses [100]. The damping scheme from Fig. 3.2C mitigates this disadvantage by implementing two separated capacitor branches, where one contains a resistive-inductive damping circuit, which allows to bypass individual current components. More precisely, the low-frequency (fundamental) and the high-frequency (current ripple) components of the converter current $\boldsymbol{I}$ are largely bypassed by the inductance L_d and the parallel capacitance C_p, respectively, where only the current components near the resonance frequency flow through the damping resistor R_d [13]. In this context, reviewing the LCL filter topology from Fig. 3.2C and defining the current $\boldsymbol{I}_\mathrm{c}$ to flow through the shown damping circuit, the associated normalized damping impedance can be specified as

$$Z_\mathrm{d}(s) = \frac{\boldsymbol{e}(s)}{\boldsymbol{i}_\mathrm{c}(s)} = \frac{1}{c_\mathrm{c} s} + \frac{l_\mathrm{d} r_\mathrm{d} s}{l_\mathrm{d} s + r_\mathrm{d}} = \frac{c_\mathrm{c} l_\mathrm{d} r_\mathrm{d} s^2 + l_\mathrm{d} s + r_\mathrm{d}}{c_\mathrm{c} s (l_\mathrm{d} s + r_\mathrm{d})} \tag{3.11}$$

where $l_\mathrm{d} = L_\mathrm{d}/Z_\mathrm{b}$ denotes the normalized damper inductance. In combination with the normalized parallel capacitance $c_\mathrm{p} = C_\mathrm{p} Z_\mathrm{b}$, the dynamics between the total current through both capacitive branches and the normalized synthetic PCC voltage $\boldsymbol{e}$ can then be redefined by

$$\boldsymbol{e}(s) = Z_\mathrm{c}(s)\left(\boldsymbol{i}_\mathrm{g}(s) - \boldsymbol{i}(s)\right) = \frac{Z_\mathrm{d}(s)}{1 + Z_\mathrm{d}(s) c_\mathrm{p} s}\left(\boldsymbol{i}_\mathrm{g}(s) - \boldsymbol{i}(s)\right). \tag{3.12}$$

In order to obtain more or less the same resonance frequency $\omega_{\mathrm{r,G_{LCL}}}$ as in the ideal, undamped case, it is recommended to select the capacitances such that the sum $C_\mathrm{c} + C_\mathrm{p}$ approximately corresponds to the capacitance of an undamped (reference) filter. Here, the ratio between C_c and C_p represents a trade-off between the introduced damping at $\omega_{\mathrm{r,G_{LCL}}}$ (or the losses) and the attenuation capabilities of the filter. The larger the C_c in the damping branch, the less attenuation at the high-frequency range [138]. On the other hand, to provide sufficient damping at the LCL filter's resonance frequency, it is proposed to select the cut-off frequency of the damper circuit as $R_\mathrm{d}/L_\mathrm{d} < \omega_{\mathrm{r,G_{LCL}}}$, keeping the introduced inductor losses in mind. Applied to the converter under study, these considerations result in the exemplary parameters $C_\mathrm{c} = 3.3\,\mu\mathrm{F}$, $C_\mathrm{p} = 1\,\mu\mathrm{F}$, $R_\mathrm{d} = 1\,\Omega$, and $L_\mathrm{d} = 0.5\,\mathrm{mH}$, which yields a cut-off frequency of $R_\mathrm{d}/L_\mathrm{d} = 2000\,\frac{\mathrm{rad}}{\mathrm{s}} < \omega_{\mathrm{r,G_{LCL}}}/5$. In terms of normalized quantities, the respective components are given by $c_\mathrm{c} = C_\mathrm{c} Z_\mathrm{b} = 50.81\,\mu\mathrm{s}$, $c_\mathrm{p} = C_\mathrm{p} Z_\mathrm{b} = 15.4\,\mu\mathrm{s}$, $r_\mathrm{d} = R_\mathrm{d}/Z_\mathrm{b} = 0.065$, and $l_\mathrm{d} = L_\mathrm{d}/Z_\mathrm{b} = 32.48\,\mu\mathrm{s}$.

Resulting Filter Dynamics

Finally, combining (3.5), (3.7), and (3.9) or (3.12), respectively, and further using the normalized version of the synthetic grid impedance $\tilde{Z}_\mathrm{g}(s)$ from (2.5), i.e.,

$$\tilde{Z}_\mathrm{g}(s) = \left.\frac{\boldsymbol{e}(s)}{\boldsymbol{i}(s)}\right|_{\boldsymbol{v}_\mathrm{g}(s)=\boldsymbol{0}} = \frac{Z_\mathrm{c}(s)}{1 + Z_\mathrm{c}(s)\tilde{Y}_\mathrm{fg}(s)}, \tag{3.13}$$

the normalized transfer function of the LCL filter can derived to be

$$G_{\mathrm{LCL}}(s) = \left.\frac{\boldsymbol{i}_{\mathrm{g}}(s)}{\boldsymbol{v}_{\mathrm{c}}(s)}\right|_{\boldsymbol{v}_{\mathrm{g}}(s)=\boldsymbol{0}} = \frac{\tilde{Z}_{\mathrm{g}}(s)\tilde{Y}_{\mathrm{fg}}(s)Y_{\mathrm{fc}}(s)}{1+\tilde{Z}_{\mathrm{g}}(s)Y_{\mathrm{fc}}(s)}. \tag{3.14}$$

If the parameters from Tab. 3.2 are used and all parasitic effects are disregarded, Fig. 3.3 shows the Bode plots of the LCL filter dynamics $G_{\mathrm{LCL}}(s)$ and Fig. 3.4 depicts the Bode plots of the normalized synthetic grid impedance $\tilde{Z}_{\mathrm{g}}(s)$ for different LCL filter topologies and $Z_{\mathrm{g}}(s) = 0$.

Table 3.2: Summary of exemplary normalized parameters for different LCL filter topologies

Normalized parameter	Symbol	Value	Units
Ideal LCL filter parameters			
Converter-side inductor	l_{fc}	0.195	ms
Converter-side resistor	r_{fc}	0.013	-
Converter-side time constant	$l_{\mathrm{fc}}/r_{\mathrm{fc}}$	15	ms
Grid-side inductor	l_{fg}	97.43	μs
Grid-side resistor	r_{fg}	0.0065	-
LCL filter capacitor	c_{c}	72.36	μs
LCL filter resonance frequency	$\omega_{\mathrm{r,G_{LCL}}}$	14586	rad/s
Parameter for series damping resistor			
Damping resistor	r_{d}	0.026	-
Parameters for split-capacitor and resistive-inductive circuit			
Damper capacitor	c_{c}	50.81	μs
Damper inductor	l_{d}	32.48	μs
Damping resistor	r_{d}	0.065	-
Damper time constant	$l_{\mathrm{d}}/r_{\mathrm{d}}$	0.5	ms
Parallel capacitor	c_{p}	15.4	μs

As illustrated in Fig. 3.3, the filter's resonance frequency as well as the resonance peak value can be specified and shaped by the described rules of thumb. Here, the damping resistance r_{d} does not affect the LCL filter's frequency response in the low-frequency range, but introduces damping in the high-frequency range near and above the filter's resonance frequency $\omega_{\mathrm{r,G_{LCL}}}$. By increasing r_{d}, the magnitude of the resonance peak is lowered and, if the topology from Fig. 3.2B is used, the filter's high-frequency magnitude attenuation is decreased from $-60\,\mathrm{dB/dec}$ to $-40\,\mathrm{dB/dec}$. Contrarily, the advanced damping strategy from Fig. 3.2C

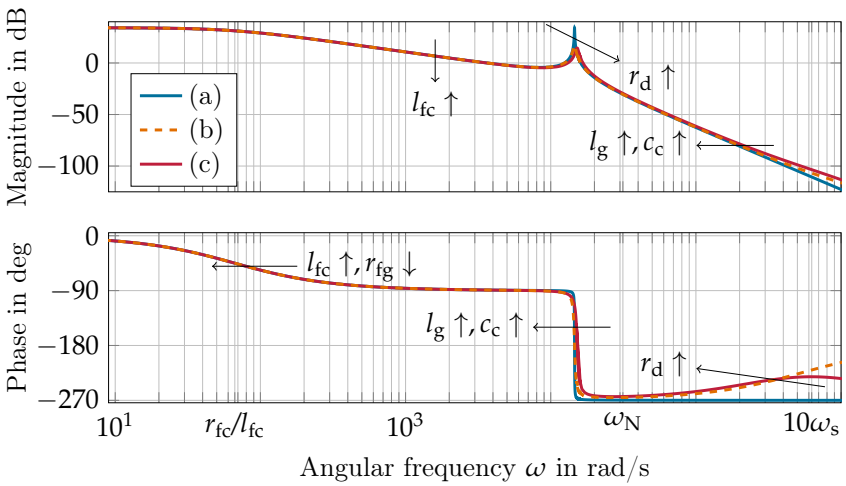

Fig. 3.3: Bode plots of $G_{\mathrm{LCL}}(s)$ with $Z_g(s) = 0$, where (a) represents the dynamics of an ideal LCL filter, (b) the dynamics of the filter with series damping resistance, and (c) the filter with split-capacitor and resistive-inductive damping circuit.

still shows an attenuation of $-60\,\mathrm{dB/dec}$ at high frequencies and only a local phase lead above $\omega_{\mathrm{r,G_{LCL}}}$ emerges. At very high frequencies it should however be regarded that more and more (unmodeled) parasitic effects [38] occur and that the model becomes increasingly less precise.

If the parasitic effects are neglected again, a similar resonant behavior can also be observed in Fig. 3.4. As can be seen, the synthetic grid impedance $\tilde{Z}_g(s)$ shows the characteristics of a low-pass (or band-pass) filter, where high-frequency components are attenuated by $-20\,\mathrm{dB/dec}$ if the LCL filter is undamped or the damping circuit from Fig. 3.2C is used. But, in comparison to a simple resistive-inductive grid impedance, $Z_g(s)$, the synthetic grid impedance $\tilde{Z}_g(s)$ also shows a resonance at $\omega_{\mathrm{r},\tilde{Z}_g} \approx 1/\sqrt{L_{fg}C_c} < \omega_{\mathrm{r,G_{LCL}}}$, which is in this case approximately located at $\omega_{\mathrm{r},\tilde{Z}_g} \approx 11910\,\frac{\mathrm{rad}}{\mathrm{s}}$. While the LCL filter's damping resistance r_d can also be used to reduce the corresponding resonance peak value, an increased grid inductance shifts the resonance frequency $\omega_{\mathrm{r},\tilde{Z}_g}$ to the left, providing an even higher attenuation of high-frequency compo-

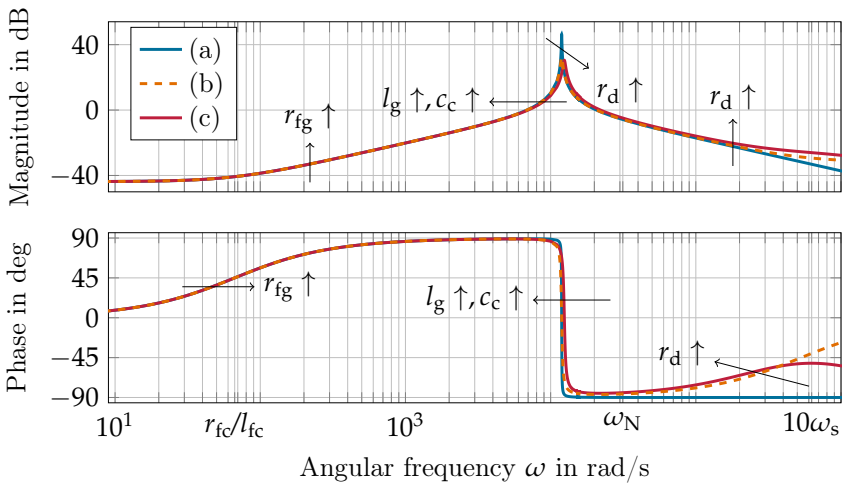

Fig. 3.4: Bode plots of $\tilde{Z}_g$ with $Z_g(s) = 0$, where (a) the LCL filter is ideal, (b) the LCL filter implements a series damping resistance, and (c) the LCL filter uses a split-capacitor and resistive-inductive damping circuit.

nents in practical applications. At this point it should be noticed that the resonance frequency of the synthetic grid impedance lies above the frequency $\omega_s/6 \approx 10471\,\frac{\text{rad}}{\text{s}}$, and thus, coincides with the region, where VSCs usually show a negative conductance. As will be shown later, the grid-converter system cannot be operated safely without any passive or active damping. This was intended to demonstrate the effectiveness, but also the sometimes overlooked risks, of different passivation methods.

3.2.2 SISO Small-Signal Behavior of the PWM

As can be observed from the converter's control block diagram of Fig. 3.1, the desired VSC output voltage $\boldsymbol{V}_c$ is typically generated by a pulsewidth modulator that drives the semiconductor switches. While analog implementations, like the naturally-sampled PWM, counted as the state of the art for many years, digital regularly-sampled pulsewidth modulators, as illustrated in Fig. 3.5 have become standard nowadays [34, 64, 105, 133].

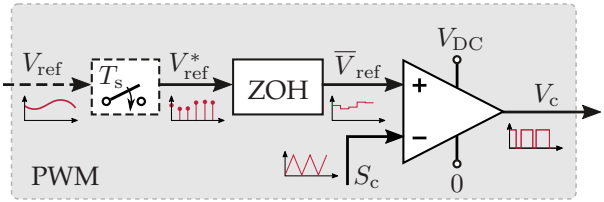

Fig. 3.5: Principle structure of a digital pulsewidth modulator [1].

Depending on the PWM module realization, the modulator input is either given by a continuous-time reference signal $V_{\mathrm{ref}}(t)$ or the sampled sequence $V^*_{\mathrm{ref}}(t)$. The latter can mathematically be described with the help of the impulse modulation technique [39, 119] and is given by a string of impulses of the form

$$V^*_{\mathrm{ref}}(t) = \sum_{k=-\infty}^{\infty} V_{\mathrm{ref}}(t)\delta(t - kT_{\mathrm{s}}) = \sum_{k=0}^{\infty} V_{\mathrm{ref}}(kT_{\mathrm{s}})\delta(t - kT_{\mathrm{s}}), \qquad (3.15)$$

presupposing that $V_{\mathrm{ref}}(t)$ is a smooth right-sided signal with $V_{\mathrm{ref}}(t) = 0, \forall t < 0$. In case of the regular-sampled PWM, the discrete-time impulse sequence is passed through a zero-order hold (ZOH) circuit, which holds the last sampled value until the next sampled value is available, i.e.,

$$\overline{V}_{\mathrm{ref}}(t + kT_{\mathrm{s}}) = V_{\mathrm{ref}}(kT_{\mathrm{s}}), \qquad \forall\, 0 \leq t < T_{\mathrm{s}}, \quad k = 0, 1, 2, \ldots. \qquad (3.16)$$

Then, if it is assumed that overmodulation does not occur, the PWM output $V_{\mathrm{c}}(t)$ is generated by comparing the time-continuous piecewise constant input signal $\overline{V}_{\mathrm{ref}}(t)$ with a carrier waveform $S_{\mathrm{c}}(t)$, as illustrated in Fig. 3.6.

The carrier waveform is typically a triangular or a sawtooth signal with amplitude V_{DC} and frequency $f_{\mathrm{PWM}} = 1/T_{\mathrm{PWM}}$, where T_{PWM} represents the converter switching period. To avoid unwanted DC offsets and other errors that might be caused by a poor selection of the sampling points, most applications synchronize the sampling frequency with the switching frequency. In particular, choosing $T_{\mathrm{PWM}} = T_{\mathrm{s}}$, yields the single-update (symmetrically sampled) PWM [55, 62, 105, 167]. As illustrated in Fig. 3.6,

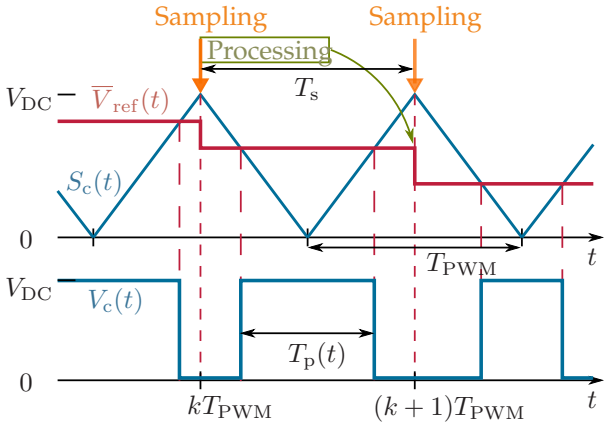

Fig. 3.6: Pulsewidth pattern for a single-update symmetric-on-time PWM with triangular carrier signal [1].

the samples are synchronized with the carrier and can either be taken at the beginning of each carrier period or in the middle of each carrier period [62, 118]. If the switch-off (zero-) states are placed symmetrically around the carrier's minima and maxima, this scheme allows to sample the AC converter current roughly in its mean value, which reduces the harmonics seen by the control system. Besides the single-update PWM, also double-update (asymmetrically sampled) modulators with $T_{\mathrm{PWM}} = 2\,T_{\mathrm{s}}$ are available, where the samples are typically taken at the positive and negative peaks of the carrier signal. In addition, multiple-sampling strategies are becoming more and more popular in high-power converter applications [167].

In order to provide sufficient time for the analog-to-digital conversion and processing time for the digital control algorithm, the PWM reference signal $V^*_{\mathrm{ref}}(t)$ is typically delayed by a computational time T_{c}. This additional computation delay can be modeled by a pure time delay model of the form $G_{\mathrm{d}}(s) = e^{-sT_{\mathrm{c}}}$. In case of a single-update PWM, T_{c} is often chosen to be one sampling period, i.e., $T_{\mathrm{c}} = T_{\mathrm{s}}$, see Fig. 3.6. Several works also propose to shift the sampling instant closer to the switching instant, which allows to reduce the computational delay to $T_{\mathrm{c}} = \kappa T_{\mathrm{s}}$, $\kappa = 0 \ldots 1$ [53, 55]. In doing so, the additional delay and its associated phase lag is

minimized, but in return, there will be larger (sampling) harmonics on the measured current that result from the sampling near the switching instants.

Concerning the toggling of the output signal $V_{\mathrm{c}}(t)$, a further division can be made: 1) symmetric-on-time and 2) symmetric-off-time switching. While the former switches from potential 0 to V_{DC} if the sampled-and-held reference signal $\overline{V}_{\mathrm{ref}}(t)$ is greater than the carrier signal $S_{\mathrm{c}}(t)$, the latter switching strategy does the reverse [64, 105, 133]. In this regard, it does not matter whether the modulator switches between the potentials 0 and V_{DC} or between the potentials $-V_{\mathrm{DC}}/2$ and $+V_{\mathrm{DC}}/2$, since the considered VSC has no clamped neutral point, and thus, only the differential voltages are relevant.

PWM Model in the Time-Domain

In this thesis, a converter system is considered that is equipped with the classical single-update PWM. It is assumed that the controller's output reference voltage is preliminarily mapped to the input voltage range of the modulator and that the signal does not exceed the maximum DC-link voltage. Moreover, it is supposed that the reference voltage $V_{\mathrm{ref}}(t)$ consists of a single sinusoidal with constant frequency, which allows to describe the PWM's input by an unique, periodical impulse sequence, $V_{\mathrm{ref}}(kT_{\mathrm{s}})$. Given the pulse-width pattern of Fig. 3.6, this implies that the switching instants of the k-th pulse between $t = kT_{\mathrm{PWM}}$ and $t = (k+1)T_{\mathrm{PWM}}$, $k = 0, 1, 2, \ldots$, can also be understood as a periodical impulse sequence, which depends on the PWM's reference signal and can be calculated by evaluating the normalized line equation

$$\frac{V_{\mathrm{ref}}(kT_{\mathrm{s}})}{E_{\mathrm{b}}} = v_{\mathrm{ref}}(kT_{\mathrm{s}}) = \frac{V_{\mathrm{DC}}}{E_{\mathrm{b}}} - \frac{V_{\mathrm{DC}}}{E_{\mathrm{b}}} \cdot \frac{T_0(kT_{\mathrm{s}})}{T_{\mathrm{PWM}}/2}, \tag{3.17}$$

yielding

$$T_0(kT_{\mathrm{s}}) = \left(\frac{1 - v_{\mathrm{ref}}(kT_{\mathrm{s}})/(V_{\mathrm{DC}}/E_{\mathrm{b}})}{2} \right) T_{\mathrm{PWM}}. \tag{3.18}$$

Then, using the impulse sequence $T_0(kT_\mathrm{s})$, $k = 0, 1, 2, \ldots$ to reproduce the switching instants of the PWM pulses and $\sigma(t)$ to denote the Heaviside step function, the normalized PWM output $v_\mathrm{c}(t) = V_\mathrm{c}(t)/E_\mathrm{b}$ can mathematically be described by the infinite sum [1]

$$v_\mathrm{c}(t) = \sum_{k=0}^{\infty} \frac{V_\mathrm{DC}}{E_\mathrm{b}} \left[\sigma(t - kT_\mathrm{PWM} - T_0(kT_\mathrm{s})) - \sigma(t - (k+1)T_\mathrm{PWM} + T_0(kT_\mathrm{s}))\right]. \tag{3.19}$$

In general, if the converter system reaches a steady-state operating point, or more precisely, a steady-state operating trajectory, the converter's PWM reference $V^*_\mathrm{ref}(t)$ represents a periodic sinusoidal impulse sequence. Hence, $V_\mathrm{c}(t)$ also represents a periodic signal and can thus be interpreted as an infinite Fourier-series. In this context, Appendix A.2 derives an analytic description of the digital single-update PWM for the special case where $V_\mathrm{ref}(t)$ (or $V^*_\mathrm{ref}(t)$ respectively) consists of a single sinusoidal with frequency $\omega_\mathrm{r} = 2\pi/T_\mathrm{r}$, where the cycle time T_r is an integer multiple of the sampling time T_s, i.e., $T_\mathrm{r} = \kappa_\mathrm{T} T_\mathrm{s}$, $\kappa_\mathrm{T} = 1, 2, 3, \ldots$. The resulting PWM pulse pattern can be represented in terms of a fundamental component, a constant DC offset as well as baseband, carrier and sideband harmonics, see also [64]. However, since the Fourier coefficients are implicitly given by infinite sums, where the summands involve the Bessel functions of the first kind, which nonlinearly depend on the reference signal's frequency and magnitude (see (A.18)), a tangible system description is difficult. In fact, the analytic description of the PWM behavior becomes even more complex, if $T_\mathrm{r} \neq \kappa_\mathrm{T} T_\mathrm{s}$, $\kappa_\mathrm{T} = 1, 2, 3, \ldots$ or the input signal $V_\mathrm{ref}(t)$ consists of multiple sinusoidal components, which is always the case in practice because of the feedback of harmonics. Moreover, research into the generation and modeling of interharmonics, i.e., signal components at frequencies that are not an integer multiple of ω_r, is still in its infancy [128]. But, in the meanwhile, there exist a few simplified PWM models that take certain nonlinear PWM effects into account, see e.g., [129, 159], and there are also some (linear) PWM modeling methods that allow to incorporate the injected harmonics at

$\omega_\mathrm{r} \pm k\omega_\mathrm{s}$, $k = 1, 2, \ldots$ [42, 116, 140, 165]. The latter idea of a multiple-frequency PWM model is revisited in Ch. 6 and is further developed in regard to the modeling and assessment of aliasing effects.

However, assuming that high-frequency harmonics above the converter's Nyquist frequency are sufficiently suppressed by the LCL filter, most researchers focus on the fundamental signal component and use averaged SISO small-signal models to describe the PWM's behavior. They mainly aim to reflect the voltage-time area of the generated pulses in one switching period and also have the purpose to accurately model the averaged phase lag. If any nonlinear effects are disregarded, the digital pulsewidth modulator is typically modeled by a simple first-order lag element, a pure time delay or a ZOH element in either the continuous- or discrete-time domain, see e.g., [4, 31, 53, 63, 88, 110, 141, 162, 167]. The first approximation was mainly used in initial studies, whereas it was verified that the latter approximations accurately model the phase response of the PWM and that the ZOH element only shows little magnitude deviations [90]. However, as we have demonstrated in [1], a dead time model generally represents a far too conservative small-signal PWM approximation and the ZOH PWM model always shows an overoptimistic magnitude response.

In contrast, following the idea of [1] and adapting the principle behavior of a ZOH element to a linear PWM model, which generates pulses with a constant duty cycle and a varying output amplitude, the modulator's small-signal behavior can be better reproduced. Linearizing (3.19) around a constant averaged duty cycle $D_0 \approx T_\mathrm{p}(kT_\mathrm{s})/T_\mathrm{PWM} = v_\mathrm{ref}(kT_\mathrm{s})/(V_\mathrm{DC}/E_\mathrm{b})$, where $T_\mathrm{p}(kT_\mathrm{s}) = T_\mathrm{PWM} - 2T_0(kT_\mathrm{s})$ is the on duration as defined in Fig. 3.6, the normalized PWM output $v_\mathrm{c}(t)$ can be approximated by

$$v_\mathrm{c}(t) \approx \sum_{k=0}^{\infty} \frac{v_\mathrm{ref}(kT_\mathrm{s})}{D_0} \left[\sigma\left(t - kT_\mathrm{PWM} - \left(\frac{1-D_0}{2}\right) T_\mathrm{PWM} \right) - \sigma\left(t - (k+1)T_\mathrm{PWM} + \left(\frac{1-D_0}{2}\right) T_\mathrm{PWM} \right) \right]. \quad (3.20)$$

Due to the adopted linearization, the output becomes independent of the actual DC-link voltage V_{DC}, but still maintains the (normalized) voltage-time area of each PWM pulse, i.e., $T_{\mathrm{p}}(kT_{\mathrm{s}})\cdot(V_{\mathrm{DC}}/E_{\mathrm{b}}) = v_{\mathrm{ref}}(kT_{\mathrm{s}})\cdot T_{\mathrm{PWM}}$.

PWM Model in the Continuous Laplace-Domain

Since (3.20) represents a linear relation between the PWM's normalized input signal $v_{\mathrm{ref}}(kT_{\mathrm{s}})$ and its normalized output $v_{\mathrm{c}}(t)$, (3.20) can be transformed to the continuous Laplace-domain, yielding [39,119]

$$v_{\mathrm{c}}(s) = \sum_{k=0}^{\infty} v_{\mathrm{ref}}(kT_{\mathrm{s}}) e^{-skT_{\mathrm{PWM}}} \cdot \frac{1 - e^{-sD_0T_{\mathrm{PWM}}}}{sD_0} e^{-s\left(\frac{1-D_0}{2}\right)T_{\mathrm{PWM}}}. \quad (3.21)$$

For the single-update PWM, where $T_{\mathrm{PWM}} = T_{\mathrm{s}}$, the term $v_{\mathrm{ref}}(kT_{\mathrm{s}})e^{-skT_{\mathrm{s}}}$ represents the Laplace transform of $v_{\mathrm{ref}}(kT_{\mathrm{s}})\delta(t - kT_{\mathrm{s}})$. Hence, the first part of (3.21) can also be written as

$$\sum_{k=0}^{\infty} v_{\mathrm{ref}}(kT_{\mathrm{s}}) e^{-skT_{\mathrm{s}}} = \mathcal{L}\left\{\sum_{k=0}^{\infty} v_{\mathrm{ref}}(kT_{\mathrm{s}})\delta(t - kT_{\mathrm{s}})\right\} = v^*_{\mathrm{ref}}(s), \quad (3.22)$$

which defines the discrete (or starred) Laplace transform of the (right-sided) normalized impulse-sampled reference signal $v^*_{\mathrm{ref}}(t)$ from (3.15) [39,114,119]. Finally, using (3.21), (3.22), and setting $T_{\mathrm{PWM}} = T_{\mathrm{s}}$, the SISO small-signal PWM model from [1] is derived as

$$G_{\mathrm{PWM}}(s) = \frac{v_{\mathrm{c}}(s)}{v^*_{\mathrm{ref}}(s)} = \frac{1 - e^{-sD_0T_{\mathrm{s}}}}{sD_0} e^{-s\left(\frac{1-D_0}{2}\right)T_{\mathrm{s}}} \quad (3.23)$$

where the corresponding frequency response is given by

$$G_{\mathrm{PWM}}(j\omega) = \frac{\sin(\omega D_0 T_{\mathrm{s}}/2)}{\omega D_0/2} e^{-j\omega T_{\mathrm{s}}/2}. \quad (3.24)$$

The model (3.23) with sampled input $v^*_{\mathrm{ref}}(s)$ and continuous output $v_{\mathrm{c}}(s)$ represents an interface between the discrete and the continuous-time domain. If a continuous signal $v_{\mathrm{ref}}(s)$ is used as the PWM input, (3.23) must be scaled by $1/T_{\mathrm{s}}$ to reproduce the output amplitude correctly [39,119].

As can be seen, the phase lag from (3.24) is identical to that of a pure time delay model $T_\mathrm{s} e^{-sT_\mathrm{s}/2}$, while the magnitude decreases from T_s at $\omega = 0$ to 0 at $\omega = \omega_\mathrm{s}/D_0$, following a weighted sinc-function. Compared to the classical ZOH element, i.e., $G_\mathrm{ZOH}(s) = (1 - e^{-sT_\mathrm{s}})/s$, the proposed model (3.23) provides an additional degree of freedom, namely the averaged duty cycle D_0, $0 \leq D_0 \leq 1$, which can be adapted such that $G_\mathrm{PWM}(s)$ represents different PWM schemes, see [1]. In this context, Fig. 3.7 shows the frequency responses of $G_\mathrm{ZOH}(s)/T_\mathrm{s}$ and the proposed model $G_\mathrm{PWM}(s)/T_\mathrm{s}$ in comparison to the normalized characteristics of a digital single-update PWM, which is triggered by a sinusoidal reference signal of the form $V_\mathrm{ref}(t) = V_\mathrm{DC}/2 + a_\mathrm{m} V_\mathrm{DC}/2 \sin(\omega_\mathrm{r} t)$, where $a_\mathrm{m} \in [0.05, 1]$ is an amplitude modulation index between (dark blue) 0.05 and (light blue) 1.

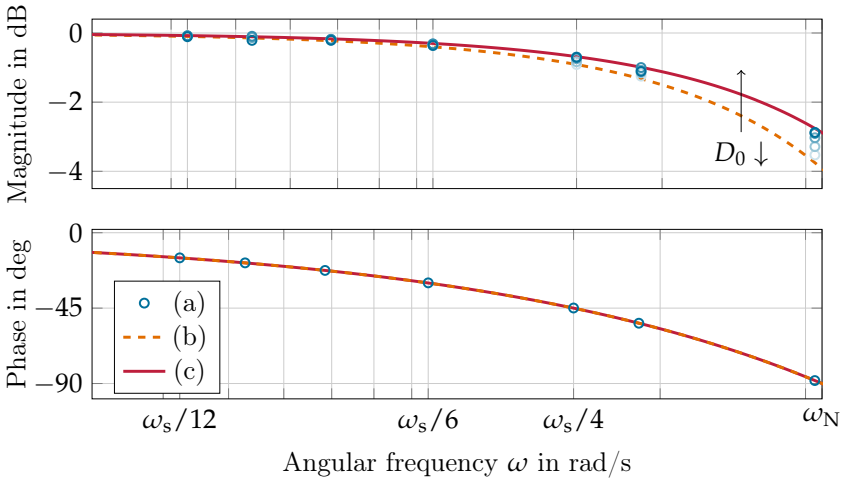

Fig. 3.7: Magnitude and phase characteristics of (a) the identified nonlinear single-update PWM for varying modulation indices, and Bode plots of (b) the ZOH PWM model $G_\mathrm{ZOH}(j\omega)/T_\mathrm{s}$, and (c) the proposed PWM model $G_\mathrm{PWM}(j\omega)/T_\mathrm{s}$ with $D_0 = 0.868$.

As expected, the modulator's output does not only depend on the input signal's frequency, but also on its amplitude. If the reference signal amplitude is decreased, the attenuation of the output's fundamental component decreases as well. Following our suggestion from [1], the aver-

aged duty cycle for a single-update PWM can be defined as $D_0 = 0.868$. This choice of D_0 results in a worst-case small-signal PWM model, which underestimates the nonlinear modulator's amplitude attenuation at low frequencies, but yields an upper magnitude bound for frequency components close to and above the critical frequency $\omega_\mathrm{s}/6$. This is particularly important for the system analysis of Ch. 5, which aims to derive sufficient small-signal stability criteria for the controller and filter design.

At this point it should be remarked that the proposed averaged model and the classical ZOH PWM model do not represent a small-signal model in the narrower sense. While a small amplitude of the reference signal results in small duty cycle changes, large amplitudes result in a duty cycle that may vary between 0 and 1. Therefore, some authors refer to those kind of averaging PWM models as large-signal, instead of small-signal models, see e.g. [62]. However, since the averaged voltage-time area in one switching period is identical to that of the nonlinear PWM and the identified (steady-state) frequency responses converge for decreasing input signal magnitudes, the applicability of the proposed worst-case small-signal PWM model is justified for linear stability analyses.

3.2.3 Plant Dynamics in the Discrete z-Domain

Adopting the considerations of Sec. 2.2.2 and treating the LCL filter's capacitive branch and the grid-side inductance as a part of the grid impedance, the analysis and controller design can be simplified for converters that implement a converter-side current control. Reviewing the schematic circuit from Fig. 3.1, it shows that the dynamics, which are seen from the digital controller are given by the converter-side admittance $Y_\mathrm{fc}(s)$ preceded by the small-signal model of the PWM plus computational delay. Therefore, it is reasonable to transform the resulting plant dynamics, $Y_\mathrm{fc}(s)G_\mathrm{PWM}(s)G_\mathrm{d}(s)$, into the discrete z-domain, i.e., obtain

$$(Y_\mathrm{fc}G_\mathrm{PWM}G_\mathrm{d})(z) = \mathcal{Z}\left\{\mathcal{L}^{-1}\left\{\frac{1/l_\mathrm{fc}}{s+r_\mathrm{fc}/l_\mathrm{fc}}\frac{1-e^{-sD_0T_\mathrm{s}}}{sD_0}e^{-s\left(\left(\frac{1-D_0}{2}\right)T_\mathrm{s}+T_\mathrm{c}\right)}\right\}\right\}. \tag{3.25}$$

Considering a symmetrically sampled single-update PWM with $T_\mathrm{c} = T_\mathrm{s}$ and following the derivations from the Appendix A.3, the plant's common z-transform $(Y_\mathrm{fc}G_\mathrm{PWM}G_\mathrm{d})(z)$ can be calculated to be

$$(Y_\mathrm{fc}G_\mathrm{PWM}G_\mathrm{d})(z) = \frac{1}{D_0 r_\mathrm{fc}} \frac{e^{-\frac{1-D_0}{2}\frac{r_\mathrm{fc}}{l_\mathrm{fc}}T_\mathrm{s}} - e^{-\frac{1+D_0}{2}\frac{r_\mathrm{fc}}{l_\mathrm{fc}}T_\mathrm{s}}}{z\left(z - e^{-\frac{r_\mathrm{fc}}{l_\mathrm{fc}}T_\mathrm{s}}\right)}. \tag{3.26}$$

If other converter filters or sampling strategies are to be considered, reference is made to [1], where two generic transformations for plants with n single poles and arbitrary delays are derived. Since $(Y_\mathrm{fc}G_\mathrm{PWM}G_\mathrm{d})(z)|_{z=e^{j\omega T_\mathrm{s}}}$ does not represent a rational function of ω, Bode's 'hand-plotting' techniques do not apply [39]. However, regarding the design recommendation for the converter-side filter from (3.6), it can be noticed that $r_\mathrm{fc}/l_\mathrm{fc}T_\mathrm{s} \sim r_\mathrm{fc}I_\mathrm{b}/V_\mathrm{DC}$, which can be supposed to approach zero for small normalized resistances. As suggested in [3], this allows to simplify (3.26) by

$$(Y_\mathrm{fc}G_\mathrm{PWM}G_\mathrm{d})(z) \approx \lim_{\frac{r_\mathrm{fc}}{l_\mathrm{fc}}T_\mathrm{s}\to 0} \left\{ \frac{T_\mathrm{s}}{D_0 l_\mathrm{fc}} \frac{e^{-\frac{1-D_0}{2}\frac{r_\mathrm{fc}}{l_\mathrm{fc}}T_\mathrm{s}} - e^{-\frac{1+D_0}{2}\frac{r_\mathrm{fc}}{l_\mathrm{fc}}T_\mathrm{s}}}{\frac{r_\mathrm{fc}}{l_\mathrm{fc}}T_\mathrm{s} \cdot z\left(z - e^{-\frac{r_\mathrm{fc}}{l_\mathrm{fc}}T_\mathrm{s}}\right)} \right\} = \frac{T_\mathrm{s}}{l_\mathrm{fc}} \frac{1}{z(z-1)} \tag{3.27}$$

where the associated frequency response can be expressed as

$$\begin{aligned}(Y_\mathrm{fc}G_\mathrm{PWM}G_\mathrm{d})(z)|_{z=e^{j\omega T_\mathrm{s}}} &\approx \left(\frac{T_\mathrm{s}}{l_\mathrm{fc}} \frac{1}{z(z-1)}\right)\Bigg|_{z=e^{j\omega T_\mathrm{s}}} \\ &= \frac{T_\mathrm{s}}{l_\mathrm{fc}} \frac{j\omega}{j\omega(1-e^{-j\omega T_\mathrm{s}})} e^{-j2\omega T_\mathrm{s}} = \frac{1}{j\omega l_\mathrm{fc}} \frac{\omega T_\mathrm{s}}{2\sin(\omega T_\mathrm{s}/2)} e^{-j\omega T_\mathrm{d}}\end{aligned} \tag{3.28}$$

with $T_\mathrm{d} = 0.5T_\mathrm{s} + T_\mathrm{c} = 1.5\,T_\mathrm{s}$ as the total time delay that is introduced through the PWM plus computational delay. As might be noticed, (3.27) is equivalent to the z-transform of $e^{-sT_\mathrm{s}}/(l_\mathrm{fc}s)$ that is preceded by a ZOH element. At this point it is worth to compare the frequency responses of the original discretized plant dynamics (3.26) and the simplified dynamics (3.27) with that of the continuous equivalent dynamics

$Y_{\mathrm{fc}}(s)G_{\mathrm{PWM}}(s)/T_{\mathrm{s}}G_{\mathrm{d}}(s)$. Fig. 3.8 shows the corresponding Bode plots of the exemplary converter system with the parameters from Tab. 3.1 and Tab. 3.2.

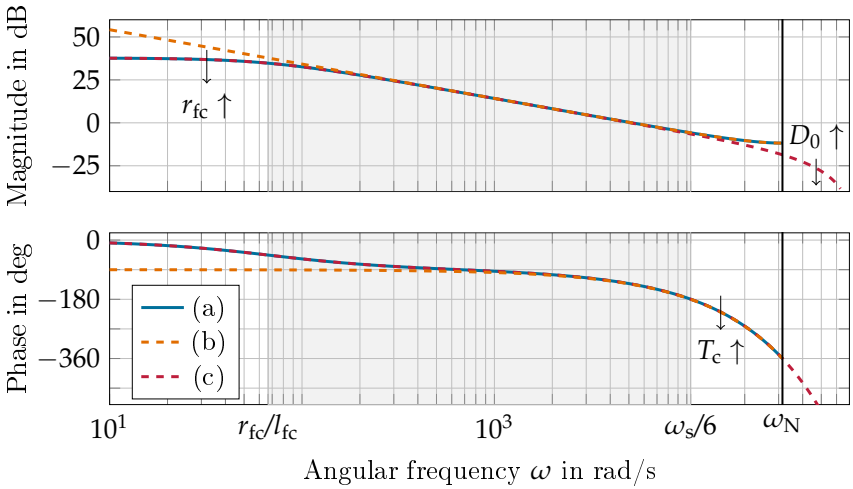

Fig. 3.8: Bode plots of the VSC's (a) discretized plant dynamics $(Y_{\mathrm{fc}}G_{\mathrm{PWM}}G_{\mathrm{d}})(z)$, (b) simplified discretized plant dynamics, where $r_{\mathrm{fc}}/l_{\mathrm{fc}}T_{\mathrm{s}} = 0$, and (c) continuous plant dynamics $Y_{\mathrm{fc}}(s)G_{\mathrm{PWM}}(s)/T_{\mathrm{s}}G_{\mathrm{d}}(s)$ with $D_0 = 0.868$, respectively [3].

As can be observed, the responses of the discretized plant dynamics (3.26) and (3.27) only differ in the low frequency range below and near the output filter's cut-off frequency $r_{\mathrm{fc}}/l_{\mathrm{fc}}$. In contrast, the Bode plots of $(Y_{\mathrm{fc}}G_{\mathrm{PWM}}G_{\mathrm{d}})(z)$ and $Y_{\mathrm{fc}}(s)G_{\mathrm{PWM}}(s)/T_{\mathrm{s}}G_{\mathrm{d}}(s)$ show a notable mismatch in their amplitudes in the high-frequency range above $\omega_{\mathrm{s}}/6 = 10472\,\frac{\mathrm{rad}}{\mathrm{s}}$. In fact, the PWM model (3.23) attenuates high frequency components, which has a damping effect on the continuous-time equivalent plant dynamics, whereas the PWM in (3.26) and (3.27) has an amplifying effect.

3.2.4 Digital Stationary-Frame PR Current Controller

As already described, the VSC's current control is typically realized by two PI controllers with feed-forward and cross-coupling compensation

actions in a rotating (d,q)-reference frame or by two PR controllers in stationary (α,β)-coordinates [20, 108, 127]. The main advantage of stationary-frame PR controllers is the reduction of coordinate transformations and the avoidance of decoupling strategies in the synchronous (d,q)-frame [72, 93, 126, 170]. Because of this and other beneficial properties, this thesis aims to further advancing research and focuses on the application of PR current controllers.

Per definition, resonant controllers show poles on or near the imaginary axis, which allow to regulate sinusoidal reference signals without any (significant) steady-state control error [164, 170]. Due to its behavior, the resonant part is thus also referred to as sinusoidal signal integrator (SSI) [22] or second-order generalized integrator (SOGI) [27, 127] and in its reduced form as reduced-order generalized integrator (ROGI) [27, 55]. While the SOGI implementation inherently provides a very high gain to the positive- as well as negative-sequence of a sinusoidal input signal, the ROGI realization can only deal with the positive- or negative-sequence component, but requires less processing load and fewer states in its implementation.

Since a key issue of grid-connected converters is not only to track a reference current but also to suppress selected harmonics, multiple resonant parts can be connected in parallel, where the resonator frequencies are typically selected as integer multiples of the fundamental grid frequency $\omega_\mathrm{r} = 2\pi f_\mathrm{r}$, i.e., $h_i\omega_\mathrm{r}$, $h_i \in h$. Here, the harmonics are typically selected as $h = \{1,3,5,7,\ldots\}$ for single-phase and $h = \{1,5,7,11,13,17,19,\ldots\}$ for (α,β)-frame control [29, 56]. If the multifrequency PR controller is to be used in a symmetrical three-phase system, the implementation effort can be reduced by operating (multiple) SOGI-based resonators in a synchronous-reference frame, rotating at the measured or estimated grid-frequency ω_r [93]. In doing so, the SOGI's high gains at the negative- and positive-sequence components can be utilized to compensate for two harmonics with only one resonator [3, 22, 82].

Multifrequency PR Controller in the Continuous Laplace-Domain

In general, PR controllers show great similarities to harmonic filters in the stationary reference frame, which aim to extract selected harmonics from a distorted sinusoidal signal by applying a frequency-modulation [93, 126, 170]. Basically, the measured signal is in turn multiplied by sine and cosine functions at the frequency of interest, where the specified signal component is transformed to a DC quantity in the synchronous (d, q)-frame, leaving all the other components as AC quantities. After low-pass filtering and processing by some filter $G^c_{\mathrm{DC}}(s)$, the signal is again transformed back to the stationary frame. Mathematically, this frequency-modulation process can be described in the (α, β)-frame by

$$G^c_{\mathrm{AC}}(s) = \frac{1}{2}\left(G^c_{\mathrm{DC}}(s - jh_i\omega_{\mathrm{r}}) + G^c_{\mathrm{DC}}(s + jh_i\omega_{\mathrm{r}})\right) \tag{3.29}$$

where $h_i\omega_{\mathrm{r}}$ is the selected (constant) angular frequency of the synchronous (d, q)-frame. If the filter is chosen as a simple integrator, i.e., $G^c_{\mathrm{DC}}(s) = 1/s$, the terms $G^c_{\mathrm{DC}}(s - jh_i\omega_{\mathrm{r}})$ and $G^c_{\mathrm{DC}}(s + jh_i\omega_{\mathrm{r}})$ represent ideal ROGIs, showing an infinite gain at $h_i\omega_{\mathrm{r}}$ and $-h_i\omega_{\mathrm{r}}$, respectively, while $G^c_{\mathrm{AC}}(s)$ represents an ideal SOGI [27]. More generally, using a low-pass filter of the form $G^c_{\mathrm{DC}}(s) = k_{\mathrm{I},h_i}/(s + \omega_{\mathrm{c},h_i})$, where ω_{c,h_i} is the filter's cut-off frequency and k_{I,h_i} is its gain, (3.29) becomes

$$G^c_{\mathrm{AC}}(s) = \frac{k_{\mathrm{I},h_i}(s + \omega_{\mathrm{c},h_i})}{s^2 + 2\omega_{\mathrm{c},h_i}s + \omega^2_{\mathrm{c},h_i} + (h_i\omega_{\mathrm{r}})^2} \approx \frac{k_{\mathrm{I},h_i}s}{s^2 + 2\omega_{\mathrm{c},h_i}s + (h_i\omega_{\mathrm{r}})^2}, \tag{3.30}$$

assuming that $\omega_{\mathrm{c},h_i} \ll h_i\omega_{\mathrm{r}}, \forall h_i \in h$, which allows to neglect the quadratic part in the denominator, $\omega^2_{\mathrm{c},h_i}$, and ω_{c,h_i} in the numerator. Further, it is common to introduce an additional degree of freedom for possible phase corrections by adopting a ϕ_{h_i} degree phase-sifted sine and cosine function for the transformation of the DC signals to the stationary frame [93]. In terms of linear operations, Fig. 3.9 shows the control block diagram of the resulting damped resonator.

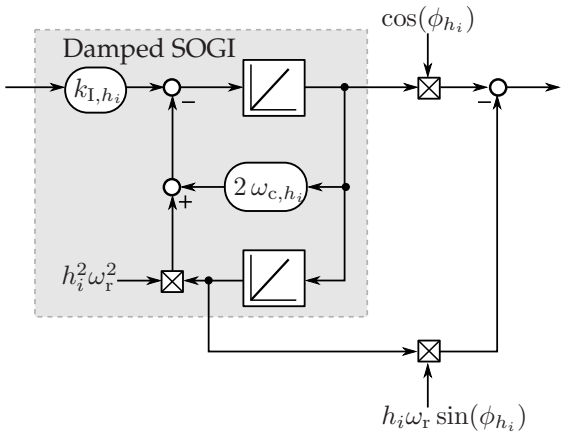

Fig. 3.9: Linear control block diagram of a single damped SOGI-based resonator with phase compensation.

Then, in combination with a proportional path, the normalized transfer function of a damped PR controller with multiple (α,β)-frame harmonic compensators can be derived as [3]

$$G_{\mathrm{PR}}^{c}(s) = k_{\mathrm{P}} + \sum_{i=1}^{m} k_{\mathrm{I},h_i}\frac{s\cos(\phi_{h_i}) - h_i\omega_{\mathrm{r}}\sin(\phi_{h_i})}{s^2 + 2\,\omega_{\mathrm{c},h_i}s + (h_i\omega_{\mathrm{r}})^2}. \tag{3.31}$$

Here, $k_{\mathrm{P}} = K_{\mathrm{P}}/Z_{\mathrm{b}}$ and $k_{\mathrm{I},h_i} = K_{\mathrm{I},h_i}/Z_{\mathrm{b}}$ in $\frac{\mathrm{rad}}{\mathrm{s}}$ are the normalized proportional and integral gains, respectively, m specifies the number of included resonators, ω_{c,h_i} denotes the h_i-th resonant cut-off frequency, and ϕ_{h_i} represents the h-th compensation angle. As an alternative to the (α,β)-frame realization (3.31), the high-frequency harmonic resonators can also be implemented in a synchronous reference-frame, rotating at ω_{r} [22, 82, 93]. In this case, an equivalent (α,β)-frame description of the PR controller can be derived by using the theory on complex transfer functions, see [3, 51, 131]. Then, all following considerations can be applied in a similar way, but are not to be discussed further. Fig. 3.10 shows the associated Bode diagram of a PR controller with $m = 1$ for varying parameters [3]. If, for some h_i, $k_{\mathrm{I},h_i} > 0$ and $\omega_{\mathrm{c},h_i} = 0$, the associated resonator provides an infinite gain at the resonance frequency $h_i\omega_{\mathrm{r}}$ and shows a relative phase change of $180°$ at frequencies infinitely close to $h_i\omega_{\mathrm{r}}$. Increas-

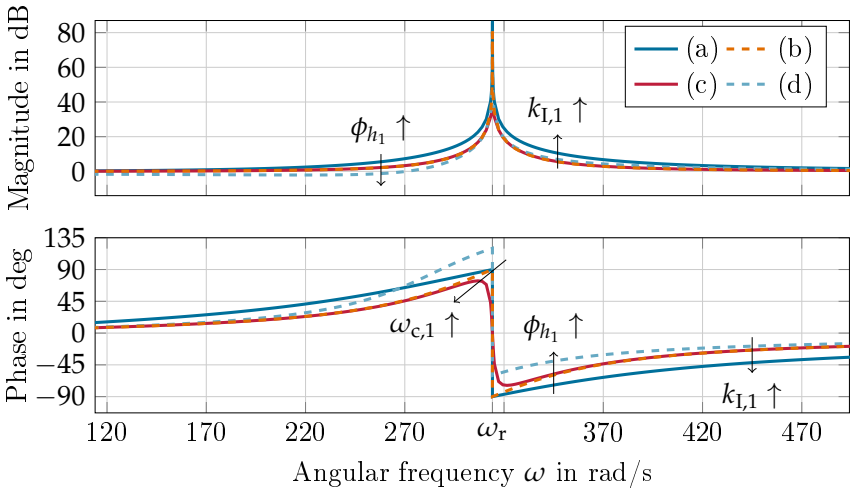

Fig. 3.10: Detailed Bode plots of the continuous PR controller dynamics $G^c_{\mathrm{PR}}(s)$ for different parameters with $k_\mathrm{P} = 1, \omega_\mathrm{r} = 2\pi 50\,\mathrm{rad/s}$ and (a) $k_{\mathrm{I},1} = 200\,\mathrm{rad/s}, \omega_{\mathrm{c},1} = 0, \phi_1 = 0°$, (b) $k_{\mathrm{I},1} = 100\,\mathrm{rad/s}, \omega_{\mathrm{c},1} = 0, \phi_1 = 0°$, (c) $k_{\mathrm{I},1} = 100\,\mathrm{rad/s}, \omega_{\mathrm{c},1} = 1\,\mathrm{rad/s}, \phi_1 = 0°$, and (d) $k_{\mathrm{I},1} = 100\,\mathrm{rad/s}, \omega_{\mathrm{c},1} = 0, \phi_1 = 30°$.

ing values of k_{I,h_i} result in an increased gain of $|G^c_{\mathrm{PR}}(j\omega)|$ close to the corresponding resonance frequency, and thus, make the controller less sensitive against variations of the frequencies to be tracked or compensated [3, 170]. On the other hand, by increasing the respective cut-off frequency $\omega_{\mathrm{c},h_i} > 0$, the gain at the resonance frequency is reduced to $|G^c_{\mathrm{PR}}(jh_i\omega_\mathrm{r})| \approx \left|k_\mathrm{P} + k_{\mathrm{I},h_i}/(2\omega_{\mathrm{c},h_i} \cdot e^{j\phi_{h_i}})\right|$ and the phase response close to $h_i\omega_\mathrm{r}$ is compressed, see Fig. 3.10. Hence, while the parameterization $\omega_{\mathrm{c},h_i} = 0$ yields an ideal resonator with two poles at $s_\lambda = \pm jh_i\omega_\mathrm{r}$, the resonator gets damped with $\omega_{\mathrm{c},h_i} > 0$, showing two poles at approximately $s_\lambda = -\omega_{\mathrm{c},h_i} \pm jh_i\omega_\mathrm{r}$ for $\omega_{\mathrm{c},h_i} \ll h_i\omega_\mathrm{r}$. This additional degree of freedom is particularly useful for the digital controller implementation, see e.g., [50, 126], and for the passivation of the converter system near the resonance frequencies [4]. Further, to counteract the phase lag of the PWM plus computational delay, the compensation angle ϕ_{h_i} can be used to in-

troduce an additional phase lead at $h_i\omega_\mathrm{r}$, but also leads to an additional gain attenuation below the resonance frequency.

Digital Controller Implementation

In the context of present-day systems, the current controller is mostly to be implemented on a digital control system, using either floating-point or fixed-point arithmetic [43,50,93,126]. Here, the discrete z-domain representation of the control law represents the basis for any implementation. While the floating-point algorithm can directly be derived from the associated difference equation, fixed-point implementations often utilize the delta-operator $\delta = (z-1)/\Delta$, $\Delta \leq 1$, in place of the shift operator to reduce round-off errors, caused by the finite word length [50,126].

Independent of the selected arithmetic, one possible discrete realization is to straightforwardly implement the proportional path and the described nonlinear frequency-modulation process with discretized filters $G_\mathrm{DC}(z)$ [93,127]. However, since this method is similar to the PI control in a synchronous (d,q)-reference frame, which needs an estimated phase angle of the rotating frame and further requires trigonometric functions to be calculated online or with the help of lookup tables, the implementation uses many resources and is thus rather impractical. On the contrary, the PR controller transfer function (3.31) can also be transformed to the z-domain by common approximations, allowing a direct discrete realization as digital filter [119]. Besides the classical for- and backward Euler approximations or the bilinear Tustin approximation with/without prewarping, also pole-zero matching or impulse-invariant transformations can be used, see [9,39,119]. Especially the research of Yepes et al. in [160,161] should be highlighted, where different discretization techniques for resonant controllers are investigated and compared to each other.

Accordingly, as grid-feeding or grid-supporting power converters work with well specified (more or less constant) harmonic frequencies, $h_i\omega_\mathrm{r}$, the prewarped Tustin method or the impulse-invariant discretization method represent the most suitable transformations for PR controllers with delay compensation [160]. Here, the prewarped Tustin approximation guar-

antees a perfectly aligned resonator response at $h_i\omega_\mathrm{r}$, and also leads to a better compliance in the high frequency range, where $h_i\omega_\mathrm{r} \ll \omega < \omega_\mathrm{s}/2$. Therefore, this approach is often favored in the literature, see e.g., [4, 53, 57, 67, 126, 162]. Given (3.31) and applying the prewarped Tustin method, i.e., $s = K_{\mathrm{pr},h_i}(z-1)/(z+1)$, $K_{\mathrm{pr},h_i} = h_i\omega_\mathrm{r}/(\tan(h_i\omega_\mathrm{r}T_\mathrm{s}/2))$, on each resonator yields a discretized PR current controller of the form

$$G_\mathrm{PR}^{tu}(z) = k_\mathrm{P} + \sum_{i=1}^{m} k_{\mathrm{I},h_i} \frac{\sin(h_i\omega_\mathrm{r}T_\mathrm{s})}{2h_i\omega_\mathrm{r}} \cdot \frac{(1-z^{-2})\cos(\phi_{h_i}) - (1+2z^{-1}+z^{-2})\sin(\phi_{h_i})h_i\omega_\mathrm{r}/K_{\mathrm{pr},h_i}}{1-2z^{-1}\cos(h_i\omega_\mathrm{r}T_\mathrm{s}) + z^{-2} + \omega_{\mathrm{c},h_i}/(h_i\omega_\mathrm{r})\sin(h_i\omega_\mathrm{r}T_\mathrm{s})(1-z^{-2})}. \tag{3.32}$$

If $\omega_{\mathrm{c},h_i} = 0$, it can be verified that the (undamped) resonator poles of the discretized controller $G_\mathrm{PR}^{tu}(z)$ exactly correspond to their continuous equivalent s_λ, since $z^2 - 2z\cos(h_i\omega_\mathrm{r}T_\mathrm{s}) + 1 = (z - e^{jh_i\omega_\mathrm{r}T_\mathrm{s}})(z - e^{-jh_i\omega_\mathrm{r}T_\mathrm{s}})$. In addition, the zeros can also accurately be reproduced, see [160], and the DC gains of the continuous and discretized controllers match, i.e., $G_\mathrm{PR}^{c}(s)|_{s=0} = G_\mathrm{PR}^{tu}(z)|_{z=1}$. Thus, (3.32) represents an effective and accurate digital implementation of the PR controller in form of a (linear) infinite impulse response (IIR) filter.

Alternatively, regarding converter applications with varying tracking frequencies, ω_r, it became popular to implement a resonator discretization, which is based on the principle control block diagram of a SOGI [161]. Given Fig. 3.9, the idea is to transform both integrators separately to the z-domain, preserving the original (physical) relationships of the states. Since the application of the (prewarped) Tustin method would yield an algebraic loop, the forward and backward Euler approximation are typically used for the discretization of the direct integrator and the integrator in the feedback path, respectively. This leads to the following pulse transfer function of a SOGI in the z-domain

$$G_\mathrm{AC}(z) = k_{\mathrm{I},h_i}T_\mathrm{s} \frac{z^{-1} - z^{-2}}{1 - 2z^{-1}(1 - h_i^2\omega_\mathrm{r}^2T_\mathrm{s}^2/2) + z^{-2} + 2\omega_{\mathrm{c},h_i}T_\mathrm{s}(z^{-1} - z^{-2})}. \tag{3.33}$$

The implementation of (3.33) allows a resonance frequency adaption without substantial computational burden, but causes a displacement of the resonant poles and, if the phase compensation from Fig. 3.9 is implemented, in an error of the desired phase lead [43,161]. To overcome this disadvantage, Yepes et al. proposed a correction, which basically aims to modify the resulting pulse transfer function, such that it is equivalent to that obtained by discretizing (3.31) with the impulse-invariant method [161]. However, as already described, the application of the prewarped Tustin approximation is known to produce an even more accurate resonator discretization than the impulse-invariant method. Therefore, it is proposed to use a similar approach as in [161] and adapt the discretized SOGI block diagram from Fig. 3.9 such that the resulting pulse transfer function (approximately) matches the discrete PR controller realization (3.32). In particular, Fig. 3.11 shows the resulting control block diagram, which yields the PR controller pulse transfer function

$$G_{\mathrm{PR}}(z) = k_{\mathrm{P}} + \sum_{i=1}^{m} \frac{k_{\mathrm{I},h_i} T_{\mathrm{s}}}{2} \cdot \frac{(1-z^{-2})K_{\mathrm{c},h_i} - (1+2z^{-1}+z^{-2})K_{\mathrm{s},h_i}}{1-2z^{-1}(1-K_{\mathrm{n},h_i}T_{\mathrm{s}}^2/2)+z^{-2}+2\omega_{\mathrm{c},h_i}T_{\mathrm{s}}(z^{-1}-z^{-2})} \tag{3.34}$$

where the factors K_{c,h_i}, K_{s,h_i}, and K_{n,h_i} depend on the harmonic frequency $h_i\omega_{\mathrm{r}}$ and are determined by

$$K_{\mathrm{c},h_i} = \frac{\sin(h_i\omega_{\mathrm{r}}T_{\mathrm{s}})}{h_i\omega_{\mathrm{r}}T_{\mathrm{s}}}\cos(\phi_{h_i}), \tag{3.35}$$

$$K_{\mathrm{s},h_i} = \frac{\sin(h_i\omega_{\mathrm{r}}T_{\mathrm{s}})}{K_{\mathrm{pr},h_i}T_{\mathrm{s}}}\sin(\phi_{h_i}) = \frac{1-\cos(h_i\omega_{\mathrm{r}}T_{\mathrm{s}})}{h_i\omega_{\mathrm{r}}T_{\mathrm{s}}}\sin(\phi_{h_i}), \tag{3.36}$$

$$K_{\mathrm{n},h_i} = \frac{2}{T_{\mathrm{s}}^2}(1-\cos(h_i\omega_{\mathrm{r}}T_{\mathrm{s}})). \tag{3.37}$$

Setting $\omega_{\mathrm{c},h_i} = 0$ and comparing the numerator and denominator of (3.32) with those of (3.34), it can be seen that both pulse transfer functions are identical. In the end, only the damping term differs, but this does not affect the principle behavior of the resonator for small values of ω_{c,h_i}. If an

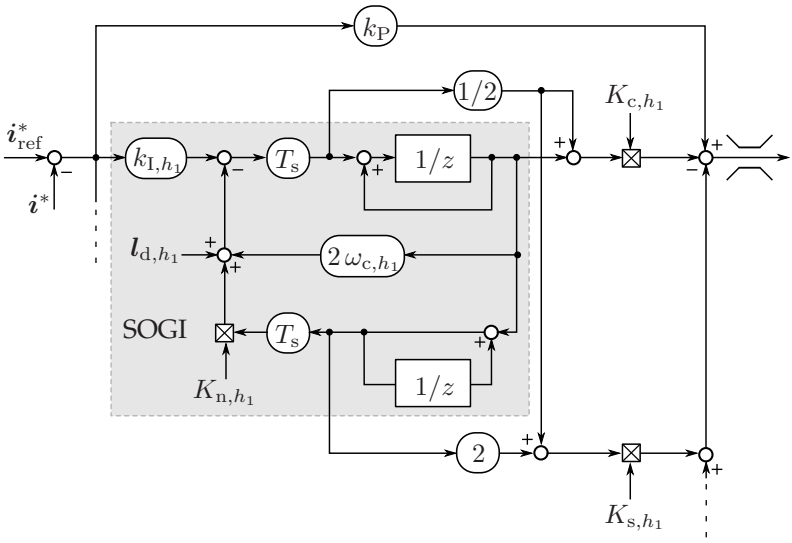

Fig. 3.11: z-Domain control block diagram of the proposed damped PR controller with phase compensation, where the integrator in the forward and feedback path are approximated by the forward and backward Euler method, respectively.

almost constant grid frequency is assumed, and thus, constant harmonic resonance frequencies $h_i\omega_\mathrm{r}, \forall h_i \in h$ are specified, the factors K_{c,h_i}, K_{s,h_i}, and K_{n,h_i} represent constant scalars. On the other hand, if the harmonic frequencies are to be adapted during the operation, e.g., using a PLL, and the online calculation of trigonometric functions should be avoided, it is suggested to approximate (3.35), (3.36), and (3.37) by Taylor series expansions around the nominal grid frequency [43,161]. Thus, the proposed PR controller $G_\mathrm{PR}(z)$ can either be implemented as a digital IIR filter or by means of discrete elements as shown in Fig. 3.11.

Current Limiting and Resonator Anti-Windup

From a practical point of view, the implementation of the control structure from Fig. 3.11 offers the opportunity to access and modify individual signals, like the in- and outputs of the discretized integrators or the input $\boldsymbol{l}_{\mathrm{d},h_i}$. Based on the physical interpretation of the signals, different

current limiting strategies and resonator anti-windup schemes can be realized. Particularly, in order to prevent a resonator windup, the authors of [23,59,107,130] adapt and extend the classical idea of back-calculation, known from the traditional PI control [10]. In this context, it is proposed to regulate the damping of each SOGI via $\boldsymbol{l}_{\mathrm{d},h_i}$, depending on the output of the respective resonator or the converter reference voltage $\boldsymbol{v}_{\mathrm{ref}}$. Further, to minimize the current distortion during a saturated operation, it is also advisable to recalculate the converter reference current $\boldsymbol{i}^*_{\mathrm{ref}}$ by considering the realizable references for multifrequency PR controllers, see [45,58].

The detailed digital implementation and the current limiting shall not be discussed further here and it is assumed that the converter always remains within its normal operation range and that no saturation occurs. Due to the described benefits, the proposed discretized PR controller transfer function (3.34) is used throughout the remaining thesis.

3.3 Converter Current Dynamics

The converter current dynamics can be derived by reviewing the VSC control block diagram from Fig. 3.1. Given the $\alpha\beta$-frame PR current controller $G_{\mathrm{PR}}(z)$ from Sec. 3.2.4 plus an additional active damping filter $H(z)$, which uses the synthetic PCC voltage as feed-forward quantity, the normalized converter output voltage is given by

$$\boldsymbol{v}_{\mathrm{c}}(s) = G_{\mathrm{PWM}}(s)G_{\mathrm{d}}(s)\left[-G_{\mathrm{PR}}(z)\left(\boldsymbol{i}^*_{\mathrm{ref}}(s) - \boldsymbol{i}^*(s)\right) + H(z)\boldsymbol{e}^*(s)\right] \quad (3.38)$$

where $\boldsymbol{i}^*_{\mathrm{ref}}(s) = \boldsymbol{I}^*_{\mathrm{ref}}(s)/I_{\mathrm{b}}$, $\boldsymbol{i}^*(s) = \boldsymbol{I}^*(s)/I_{\mathrm{b}}$, and $\boldsymbol{e}^*(s) = \boldsymbol{E}^*(s)/E_{\mathrm{b}}$ are the discrete Laplace transforms of the sampled normalized reference current, converter-side filter current, and synthetic PCC voltage, respectively. If the LCL filter's capacitor current is to be used for active filtering, $\boldsymbol{e}^*(s)$ in (3.38) can be replaced by $\boldsymbol{i}^*_{\mathrm{c}}(s) = \boldsymbol{I}^*_{\mathrm{c}}(s)/I_{\mathrm{b}}$. This applies to all following derivations, where, for the sake of brevity, exclusively $\boldsymbol{e}^*(s)$ is used as feed-forward quantity. Then, after substituting (3.38) into the VSC output filter dynamics (3.5), the continuous converter-side current becomes

$$\begin{aligned}\boldsymbol{i}(s) =& Y_{\mathrm{fc}}(s)\boldsymbol{e}(s) + Y_{\mathrm{fc}}(s)G_{\mathrm{PWM}}(s)G_{\mathrm{d}}(s)G_{\mathrm{PR}}(z)\left(\boldsymbol{i}^{*}_{\mathrm{ref}}(s) - \boldsymbol{i}^{*}(s)\right)\\ &- Y_{\mathrm{fc}}(s)G_{\mathrm{d}}(s)G_{\mathrm{PWM}}(s)H(z)\boldsymbol{e}^{*}(s).\end{aligned} \tag{3.39}$$

Current Dynamics in the Discrete Laplace-Domain

As noticed before, the converter system from Fig. 3.1 represents a hybrid sampled-data system, where the main challenge is to simultaneously cope with continuous and sampled signals. This also becomes visible by observing the associated dynamics (3.39). Nevertheless, the analysis can be carried out by considering that the ideal sampling operation can be represented by an impulse modulation [53]. This allows to perform the further system modeling in the continuous s-domain and to utilize the extensions of block-diagram analysis from standard literature on digital control systems, see e.g., [39]. An important property of this approach is that the Laplace-transformed of each impulse-sampled signal (or system's impulse response) is related to the discrete z-domain by $\boldsymbol{x}^{*}(s) = \boldsymbol{x}(z)|_{z=e^{sT_{\mathrm{s}}}}$. Given a continuous right-sided signal with $\boldsymbol{x}(t) = \boldsymbol{0}, \forall t < 0$, the discrete Laplace transform $\boldsymbol{x}^{*}(s)$ can also be expressed as[1]

$$\boldsymbol{x}^{*}(s) = \mathcal{L}\left\{\boldsymbol{x}^{*}(t)\right\} = \sum_{k=0}^{\infty}\boldsymbol{x}(kT_{\mathrm{s}})e^{-skT_{\mathrm{s}}} = \frac{1}{T_{\mathrm{s}}}\sum_{k=-\infty}^{\infty}\boldsymbol{x}(s+jk\omega_{\mathrm{s}}). \tag{3.40}$$

In this thesis, $\boldsymbol{x}(s)/T_{\mathrm{s}}$ and $\boldsymbol{x}(s+jk\omega_{\mathrm{s}})/T_{\mathrm{s}}$, $\forall k,\ k \neq 0$ are referred to as primary and complementary signal components, respectively [39]. As can be seen from (3.40), each impulse-sampled signal represents a summation of primary and complementary signal components, i.e., frequency-shifted versions of its Laplace-transformed that are weighted by $1/T_{\mathrm{s}}$. This im-

[1] It should be noted that the sum representation in (3.40) must be understood as a sum of the form $\lim_{N\to\infty}\sum_{k=-N}^{N}\boldsymbol{x}(s+jk\omega_{\mathrm{s}})$, known from classical theory on Fourier series [28]. Further, as shown in [114] using the Fourier series expansion of the so-called displaced pulse frequency response $\sum_{k=-\infty}^{\infty}\boldsymbol{x}(t+kT_{\mathrm{s}})e^{-s(t+kT_{\mathrm{s}})}$, it is important to emphasize that the given relationship (3.40) is only valid, if the original function $\boldsymbol{x}(t)$ is continuous with respect to t and the associated pulse frequency response is a function of bounded variation. Unless otherwise noted, it is assumed that these conditions are satisfied. In other cases, e.g., when the right-sided function $\boldsymbol{x}(t)$ has a discontinuity at $t = 0$, with $\boldsymbol{x}(t) = \boldsymbol{0}$, $\forall t < 0$, (3.40) must be replaced by $\boldsymbol{x}^{*}(s) = 1/T_{\mathrm{s}}\sum_{k=-\infty}^{\infty}\boldsymbol{x}(s+jk\omega_{\mathrm{s}}) + \boldsymbol{x}(0^{+})/2$, which can also be extended to functions with more discontinuities, see [114].

plies that the frequency spectrum is reproduced an infinite number of times, resulting in an infinite number of sidebands. Thus, $\boldsymbol{x}^*(s)$ represents a continuous signal with the period ω_s, where a shifting by an integer number of periods leaves the signal unchanged, i.e., $\boldsymbol{x}^*(s + jk\omega_\mathrm{s}) = \boldsymbol{x}^*(s)$, $k = 0, \pm1, \pm2, \ldots$, see [39] for a detailed derivation.

Now, applying the discrete Laplace transform (3.40) on (3.39), the sampled converter-side current that is seen from the converter is given by

$$\begin{aligned}\boldsymbol{i}^*(s) = &[Y_\mathrm{fc}(s)\boldsymbol{e}(s)]^* + [Y_\mathrm{fc}(s)G_\mathrm{PWM}(s)G_\mathrm{d}(s)G_\mathrm{PR}(z)\,(\boldsymbol{i}^*_\mathrm{ref}(s) - \boldsymbol{i}^*(s))]^* \\ &- [Y_\mathrm{fc}(s)G_\mathrm{PWM}(s)G_\mathrm{d}(s)H(z)\boldsymbol{e}^*(s)]^* \,. \end{aligned} \tag{3.41}$$

Considering the described periodicity of impulse-sampled signals and systems, and noticing that the periodic parts in (3.41) can be factorized, after rearranging, the sampled current dynamics become

$$\begin{aligned}\boldsymbol{i}^*(s) = &\frac{1}{1 + (Y_\mathrm{fc}G_\mathrm{PWM}G_\mathrm{d})^*(s)G^*_\mathrm{PR}(s)}\boldsymbol{i}^*_\mathrm{l}(s) \\ &+ \frac{(Y_\mathrm{fc}G_\mathrm{PWM}G_\mathrm{d})^*(s)G^*_\mathrm{PR}(s)}{1 + (Y_\mathrm{fc}G_\mathrm{PWM}G_\mathrm{d})^*(s)G^*_\mathrm{PR}(s)}\boldsymbol{i}^*_\mathrm{ref}(s) \\ &- \frac{(Y_\mathrm{fc}G_\mathrm{PWM}G_\mathrm{d})^*(s)H^*(s)}{1 + (Y_\mathrm{fc}G_\mathrm{PWM}G_\mathrm{d})^*(s)G^*_\mathrm{PR}(s)}\boldsymbol{e}^*(s) \end{aligned} \tag{3.42}$$

where $\boldsymbol{i}_\mathrm{l}(s) = Y_\mathrm{fc}(s)\boldsymbol{e}(s)$ specifies the current component that results from the voltage drop, $\boldsymbol{e}$, over the VSC's output filter inductance. The term $(Y_\mathrm{fc}G_\mathrm{PWM}G_\mathrm{d})^*(s) = (Y_\mathrm{fc}G_\mathrm{PWM}G_\mathrm{d})(z)|_{z=e^{sT_\mathrm{s}}}$ corresponds to the common z-transform of the plant dynamics (3.26). At this point it should be emphasized that, unlike some simplifications in the literature, see e.g., [41, 110,111], it is formally not possible to deduce two single (discrete) closed-loop transfer functions with the inputs $\boldsymbol{e}^*(s)$, $\boldsymbol{i}^*_\mathrm{ref}(s)$ and the output $\boldsymbol{i}^*(s)$ from (3.42). As highlighted in [39, 119], it must be taken into account that generally $\boldsymbol{i}^*_\mathrm{l}(s) = (Y_\mathrm{fc}\boldsymbol{e})^*(s) \neq Y^*_\mathrm{fc}(s)\boldsymbol{e}^*(s)$, since the filter's transfer function $Y_\mathrm{fc}(s)$ has no periodic properties. Nevertheless, as $\boldsymbol{i}^*_\mathrm{l}(s)$ and $\boldsymbol{e}^*(s)$ are periodic, the impulse-sampled current and synthetic PCC voltage show primary-frequency components as well as an infinite number of mirrored (complementary) components. This is exemplarily illustrated

by the resulting linear-scaled amplitude spectra of $\boldsymbol{i}_1(j\omega) = Y_{\mathrm{fc}}(j\omega)\boldsymbol{e}(j\omega)$ and $T_\mathrm{s}\boldsymbol{i}_1^*(j\omega) = T_\mathrm{s}\,(Y_{\mathrm{fc}}\boldsymbol{e})^*(j\omega)$ in Fig. 3.12, where the (real) voltage $\boldsymbol{e}(t) = \cos(\omega_1 t)+\cos(\omega_2 t) = (e^{j\omega_1 t}+e^{-j\omega_1 t})/2+(e^{j\omega_2 t}+e^{-j\omega_2 t})/2$ consists of two purely sinusoidal components, with ω_1 lying in the low-frequency range and ω_2 lying above the Nyquist frequency.

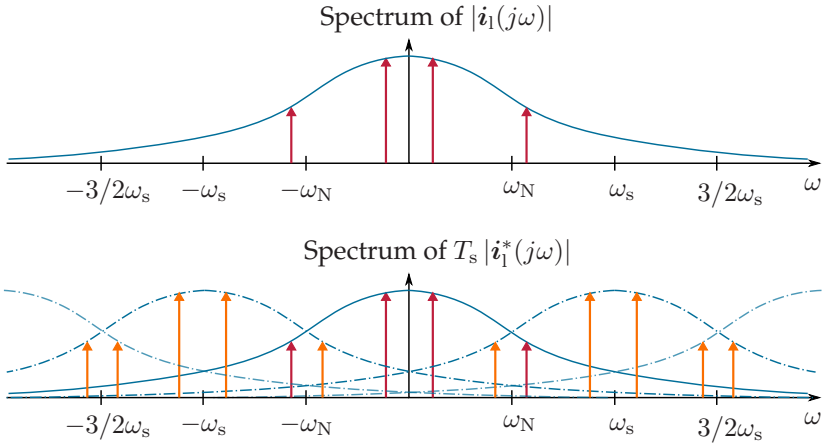

Fig. 3.12: Amplitude spectra of the current component $\boldsymbol{i}_1(j\omega) = Y_{\mathrm{fc}}(j\omega)\boldsymbol{e}(j\omega)$ and the sampled current component $T_\mathrm{s}\cdot\boldsymbol{i}_1^*(j\omega) = T_\mathrm{s}\,(Y_{\mathrm{fc}}\boldsymbol{e})^*(j\omega)$, where the red arrows mark the primary-frequency components and the orange arrows show the aliased signal components that are introduced by the sampling process.

In general, the digital controller cannot distinguish between the low-frequency components that physically exist in the signal and those that are aliased sidebands of high-frequency components above the Nyquist frequency ω_N. From this observation it also becomes clear that apart from the dynamics in the low-frequency range, also the effects of above Nyquist frequency components must (somehow) be taken into account. Therefore, to begin with, the following considerations focus on the converter's low-frequency behavior, while Ch. 6 extends the findings and describes how high-frequency signal components influence the discussed analysis and the converter passivation.

Current Dynamics in the Continuous Laplace-Domain

For the further analysis, the sampled current dynamics (3.42) are transformed (back) to the continuous Laplace-domain as suggested in [53]. This can be done by substituting (3.42) into the hybrid equation (3.39) and solving for the converter-side current $\boldsymbol{i}(s)$. If it is considered that $\boldsymbol{x}^*(s) = \boldsymbol{x}(z)|_{z=e^{sT_\mathrm{s}}}$, the resulting system dynamics can be completely described by linear transfer functions in the s-domain. Hence, defining the closed-loop reference transfer function $G_\mathrm{cl}(s)$ and the active damping transfer function $G_\mathrm{H}(s)$ as

$$G_\mathrm{cl}(s) = \left.\frac{\boldsymbol{i}(s)}{\boldsymbol{i}^*_\mathrm{ref}(s)}\right|_{\boldsymbol{e}(s)=\boldsymbol{0}} = \frac{Y_\mathrm{fc}(s)G_\mathrm{PWM}(s)G_\mathrm{d}(s)G^*_\mathrm{PR}(s)}{1+(Y_\mathrm{fc}G_\mathrm{PWM}G_\mathrm{d})^*(s)G^*_\mathrm{PR}(s)}, \tag{3.43}$$

$$G_\mathrm{H}(s) = G_\mathrm{cl}(s)\frac{H^*(s)}{G^*_\mathrm{PR}(s)} = \frac{Y_\mathrm{fc}(s)G_\mathrm{PWM}(s)G_\mathrm{d}(s)H^*(s)}{1+(Y_\mathrm{fc}G_\mathrm{PWM}G_\mathrm{d})^*(s)G^*_\mathrm{PR}(s)}, \tag{3.44}$$

the resulting converter current dynamics can be expressed as

$$\boldsymbol{i}(s) = \underbrace{G_\mathrm{cl}(s)\boldsymbol{i}^*_\mathrm{ref}(s)}_{\text{reference dynamics}} + \underbrace{\boldsymbol{i}_\mathrm{l}(s) - G_\mathrm{cl}\boldsymbol{i}^*_\mathrm{l}(s) - G_\mathrm{H}(s)\boldsymbol{e}^*(s)}_{\text{disturbance dynamics}}. \tag{3.45}$$

Regarding the definition of the discrete Laplace transform (3.40), the inputs of the disturbance dynamics $\boldsymbol{e}^*(s)$ and $\boldsymbol{i}^*_\mathrm{l}(s)$ should be understood as infinite sums of the form

$$\boldsymbol{e}^*(s) = \frac{1}{T_\mathrm{s}}\sum_{k=-\infty}^{\infty}\boldsymbol{e}(s+jk\omega_\mathrm{s}), \tag{3.46}$$

$$\boldsymbol{i}^*_\mathrm{l}(s) = (Y_\mathrm{fc}\boldsymbol{e})^*(s) = \frac{1}{T_\mathrm{s}}\sum_{k=-\infty}^{\infty}Y_\mathrm{fc}(s+jk\omega_\mathrm{s})\boldsymbol{e}(s+jk\omega_\mathrm{s}). \tag{3.47}$$

Similarly, if the LCL filter's capacitor current is to be used as the feedforward quantity, $\boldsymbol{e}^*(s)$ in (3.45) can be replaced by $\boldsymbol{i}^*_\mathrm{c}(s)$. In case of the topology from Fig. 3.2A or Fig. 3.2B, the impulse-sampled current is accordingly defined by $\boldsymbol{i}^*_\mathrm{c}(s) = (\boldsymbol{e}/Z_\mathrm{c})^*(s) = (Y_\mathrm{c}\boldsymbol{e})^*(s)$, where $Y_\mathrm{c}(s) = c_\mathrm{c}s/(c_\mathrm{c}s + r_\mathrm{d})$, see (3.9). On the other hand, if the filter topology with the advanced damping circuit from Fig. 3.2C is used, $\boldsymbol{i}^*_\mathrm{c}(s) = (Y_\mathrm{c}\boldsymbol{e})^*(s)$ must

be replaced by $\boldsymbol{i}_{\mathrm{c}}^{*}(s) = (Y_{\mathrm{d}}\boldsymbol{e})^{*}(s)$, where $Y_{\mathrm{d}}(s) = c_{\mathrm{c}}s(l_{\mathrm{d}}s + r_{\mathrm{d}})/(c_{\mathrm{c}}l_{\mathrm{d}}r_{\mathrm{d}}s^2 + l_{\mathrm{d}}s + r_{\mathrm{d}})$, see (3.11).

Then, following the considerations of Sec. 2.2.2 and reviewing that $\boldsymbol{e}(s) = \tilde{\boldsymbol{v}}_{\mathrm{g}}(s) - \tilde{Z}_{\mathrm{g}}(s)\boldsymbol{i}(s)$, where $\tilde{Z}_{\mathrm{g}}$ is defined by (3.13) and $\tilde{\boldsymbol{v}}_{\mathrm{g}}(s) = (\tilde{Z}_{\mathrm{g}}(s)\tilde{Y}_{\mathrm{fg}}(s))\boldsymbol{V}_{\mathrm{g}}(s)/E_{\mathrm{b}}$, Fig. 3.13 shows the corresponding normalized control block diagram of the digitally current-controlled grid-connected converter.

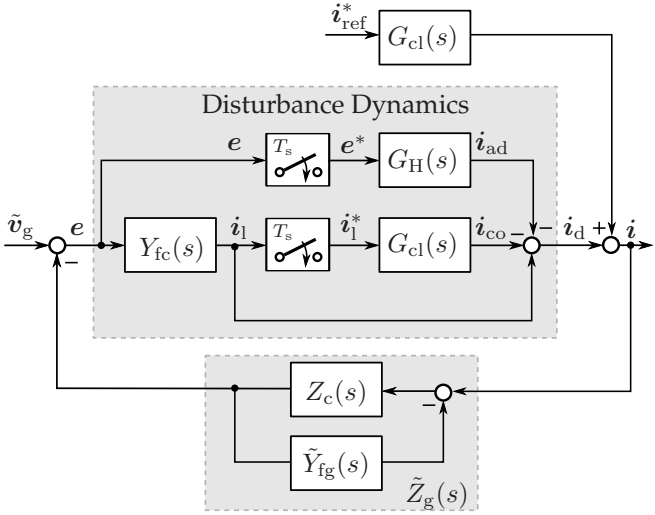

Fig. 3.13: Normalized control block diagram of a digitally current-controlled grid-connected VSC with active PCC voltage feed-forward.

As before, the dynamics (3.45) cannot be described by two single transfer functions, where one represents the reference current dynamics from $\boldsymbol{i}_{\mathrm{ref}}^{*}(s)$ to $\boldsymbol{i}(s)$ and the other one the disturbance dynamics from $\boldsymbol{e}(s)$ to $\boldsymbol{i}(s)$, respectively. As illustrated in Fig. 3.13, the disturbance dynamics are instead composed of the passive current component through the VSC output filter admittance, i.e., $\boldsymbol{i}_{\mathrm{l}}(s) = Y_{\mathrm{fc}}(s)\boldsymbol{e}(s)$, and two active voltage-dependent current components $\boldsymbol{i}_{\mathrm{co}}(s) = -G_{\mathrm{cl}}(s)\,(Y_{\mathrm{fc}}\boldsymbol{e})^{*}(s)$ and $\boldsymbol{i}_{\mathrm{ad}}(s) = -G_{\mathrm{H}}(s)\boldsymbol{e}^{*}(s)$. If $G_{\mathrm{cl}}(s)$ is designed to be stable and further a stable PR controller and feed-forward filter transfer function is assumed, it can be seen that the disturbance dynamics basically consist of a parallel (and se-

ries) connection of stable systems, and thus, generally represent a stable system as well.

3.4 Impedance-Based Equivalent Circuit

With respect to the impedance-based modeling idea [123], the discussed grid-converter system can also be interpreted as an electric circuit. Disregarding the active filter path, i.e., $H(z) = 0$, Fig. 3.14 shows the associated equivalent circuit diagram.

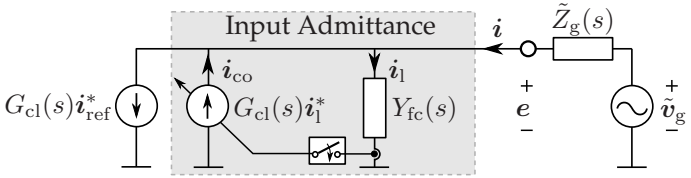

Fig. 3.14: Normalized impedance-based equivalent circuit diagram of a digitally current-controlled grid-connected converter without active damping.

Compared to the (simplified) circuit diagrams that can be found in the literature, see e.g., [11, 30, 57, 140, 143, 150], or that from the background section, see Fig. 2.3, Fig. 3.14 refines the VSC's input admittance model by taking sampling effects into account. As with the simple models, the current source injects the desired current component $\boldsymbol{i}^*_{\mathrm{ref}}$ according to its reference dynamics $G_{\mathrm{cl}}(s)$. Since the voltage drop $\boldsymbol{e}$ over the output filter admittance $Y_{\mathrm{fc}}(s)$ yields an unwanted current component $\boldsymbol{i}_{\mathrm{l}}$, the VSC reacts with a superimposed current component $\boldsymbol{i}_{\mathrm{co}}$, that aims to compensate for $\boldsymbol{i}_{\mathrm{l}}$. In case of infinite computing, sampling, and switching rates, both current components would cancel each other at any time and the current-controlled VSC would represent an ideal current source. However, in real applications, the bandwidth of the system is limited and the VSC shows the behavior of a non-ideal current source with an active, voltage-dependent input admittance. From a control engineering point of view, the converter's input admittance is equivalent to the converter's distur-

bance dynamics from Fig. 3.13 and can thus be reshaped by implementing an active feed-forward path.

3.4.1 Quasi-Analog Model

In most of the recent literature on the impedance-based modeling of grid-connected converters, the VSC's control is assumed to work quasi-analog, see e.g., [4, 31, 49, 55, 57, 144, 145, 148, 156, 158]. In this context, neglecting sampling effects and disregarding all the effects of the digital control, the converter current dynamics (3.45) simplify to the normalized current dynamics (2.7) from Sec. 2.2.2, which are given by [4]

$$\boldsymbol{i}(s) = G_{\mathrm{cl}}^{c}(s)\boldsymbol{i}_{\mathrm{ref}} + Y_{\mathrm{i}}^{c}(s)\boldsymbol{e}(s). \tag{3.48}$$

In this simplified case, $G_{\mathrm{cl}}^{c}(s)$ represents the continuous-time equivalent to the closed-loop reference transfer function (3.43), i.e.,

$$G_{\mathrm{cl}}^{c}(s) = \left.\frac{\boldsymbol{i}(s)}{\boldsymbol{i}_{\mathrm{ref}}(s)}\right|_{\boldsymbol{e}(s)=\boldsymbol{0}} = \frac{Y_{\mathrm{fc}}(s)G_{\mathrm{PWM}}(s)/T_{\mathrm{s}}G_{\mathrm{d}}(s)G_{\mathrm{PR}}^{c}(s)}{1 + Y_{\mathrm{fc}}(s)G_{\mathrm{PWM}}(s)/T_{\mathrm{s}}G_{\mathrm{d}}(s)G_{\mathrm{PR}}^{c}(s)} \tag{3.49}$$

and $Y_{\mathrm{i}}^{c}(s)$ denotes the associated continuous-time equivalent of the VSC input admittance, which is given by

$$\begin{aligned} Y_{\mathrm{i}}^{c}(s) &= \left.\frac{\boldsymbol{i}(s)}{\boldsymbol{e}(s)}\right|_{\boldsymbol{i}_{\mathrm{ref}}(s)=\boldsymbol{0}} = Y_{\mathrm{fc}}(s) - G_{\mathrm{cl}}^{c}(s)Y_{\mathrm{fc}}(s) - G_{\mathrm{cl}}^{c}(s)\frac{H^{c}(s)}{G_{\mathrm{PR}}^{c}(s)} \\ &= \frac{Y_{\mathrm{fc}}(s)\left[1 - G_{\mathrm{d}}(s)G_{\mathrm{PWM}}(s)/T_{\mathrm{s}}H^{c}(s)\right]}{1 + Y_{\mathrm{fc}}(s)G_{\mathrm{PWM}}(s)/T_{\mathrm{s}}G_{\mathrm{d}}(s)G_{\mathrm{PR}}^{c}(s)}. \end{aligned} \tag{3.50}$$

The transfer function $H^{c}(s)$ specifies the continuous-time equivalent of the feed-forward filter $H(z)$, which becomes $H^{c}(s)Y_{\mathrm{d}}(s)$, if $\boldsymbol{i}_{\mathrm{c}}$ is used for active damping. Since $Y_{\mathrm{i}}^{c}(s)$ only consists of non-periodic transfer functions, it is also referred to as single-frequency input admittance in [53].

3.4.2 Primary-Frequency Model

Next, the quasi-analog converter model (3.48) is extended by also taking the digital controller implementation and parts of the mirrored current

components into account. Given the control block diagram from Fig. 3.13 and recalling the principle low-pass characteristic of the synthetic grid impedance for signal components above the Nyquist frequency, it can be supposed that high-frequency current ripple components in $\boldsymbol{i}(s)$ as well as high-frequency grid voltage components in $\boldsymbol{v}_\mathrm{g}(s)$ are largely suppressed by $\tilde{Z}_\mathrm{g}(s)$ and $\tilde{Z}_\mathrm{g}(s)\tilde{Y}_\mathrm{fg}(s)$, respectively. As a result, the voltage $\boldsymbol{e}$ mainly consists of signal components below the Nyquist frequency ω_N in most applications. If, in addition, it is again considered that the synchronous sampling effectively acts as a kind of anti-aliasing filter, the low-frequency content of the sampled signals $\boldsymbol{e}^*$, $\boldsymbol{i}_\mathrm{l}^*$ (or $\boldsymbol{i}_\mathrm{c}^*$) can roughly be approximated by their primary signal components, i.e., $\boldsymbol{e}_\mathrm{p}(s) = \boldsymbol{e}(s)/T_\mathrm{s}$, $\boldsymbol{i}_\mathrm{l,p}(s) = Y_\mathrm{fc}(s)/T_\mathrm{s}\,\boldsymbol{e}(s)$ (or $\boldsymbol{i}_\mathrm{c,p}(s) = Y_\mathrm{c}(s)/T_\mathrm{s}\,\boldsymbol{e}(s)$ or $\boldsymbol{i}_\mathrm{c,p}(s) = Y_\mathrm{d}(s)/T_\mathrm{s}\,\boldsymbol{e}(s)$), respectively. This allows to combine the transfer functions of the disturbance dynamics in (3.45) and the behavior of the primary-frequency components of the converter-side current, $\boldsymbol{i}_\mathrm{p}(s) = \boldsymbol{i}(s)/T_\mathrm{s}$, can be expressed by

$$\begin{aligned}\boldsymbol{i}_\mathrm{p}(s) &= \frac{G_\mathrm{cl}(s)}{T_\mathrm{s}}\boldsymbol{i}_\mathrm{ref,p}(s) + \boldsymbol{i}_\mathrm{l,p}(s) - \frac{G_\mathrm{cl}(s)}{T_\mathrm{s}}\boldsymbol{i}_\mathrm{l,p}(s) - \frac{G_\mathrm{H}(s)}{T_\mathrm{s}}\boldsymbol{e}_\mathrm{p}(s)\\ &= \frac{G_\mathrm{cl}(s)}{T_\mathrm{s}}\boldsymbol{i}_\mathrm{ref,p}(s) + Y_\mathrm{i,p}(s)\boldsymbol{e}_\mathrm{p}(s). \end{aligned} \tag{3.51}$$

While the reference current dynamics $G_\mathrm{cl}(s)$ are still given by (3.43), the associated VSC's primary-frequency input admittance $Y_\mathrm{i,p}(s)$ is defined as

$$\begin{aligned}Y_\mathrm{i,p}(s) &= \left.\frac{\boldsymbol{i}_\mathrm{p}(s)}{\boldsymbol{e}_\mathrm{p}(s)}\right|_{\boldsymbol{i}_\mathrm{ref,p}(s)=\boldsymbol{0}} = Y_\mathrm{fc}(s) - \frac{G_\mathrm{cl}(s)}{T_\mathrm{s}}Y_\mathrm{fc}(s) - \frac{G_\mathrm{cl}(s)}{T_\mathrm{s}}\frac{H^*(s)}{G_\mathrm{PR}^*(s)}\\ &= Y_\mathrm{fc}(s) - \underbrace{\left(1 + \frac{1}{Y_\mathrm{fc}(s)}\frac{H^*(s)}{G_\mathrm{PR}^*(s)}\right)}_{\Gamma(s)}\underbrace{\frac{G_\mathrm{cl}(s)}{T_\mathrm{s}}Y_\mathrm{fc}(s)}_{Y_\mathrm{cl,p}(s)}. \end{aligned} \tag{3.52}$$

If the LCL filter's sampled capacitor current $\boldsymbol{i}_\mathrm{c}^*$ is to be used as the feed-forward quantity, $\Gamma(s)$ in (3.52) can be redefined to be $\Gamma(s) = 1 + Y_\mathrm{c}(s)H^*(s)/(Y_\mathrm{fc}(s)G_\mathrm{PR}^*(s))$ or $\Gamma(s) = 1 + Y_\mathrm{d}(s)H^*(s)/(Y_\mathrm{fc}(s)G_\mathrm{PR}^*(s))$, respectively.

At this point it should be emphasized that, although $G_{\mathrm{cl}}(s)$ and $G_{\mathrm{H}}(s)$ consider aliases of the sampled converter current, $\boldsymbol{i}^*$, the input admittance model (3.52) does not allow to take aliased images of the sampled current, $\boldsymbol{i}_{\mathrm{l}}^*$, nor images of the sampled synthetic PCC voltage, $\boldsymbol{e}^*$, (or the sampled capacitor current, $\boldsymbol{i}_{\mathrm{c}}^*$) at the terminals of the converter into account. However, these should not be neglected readily, especially when thinking of active damping schemes that use $\boldsymbol{e}^*$ or $\boldsymbol{i}_{\mathrm{c}}^*$ as a feed-forward quantity. In fact, high-frequency switching harmonics of the PWM may interact with poorly damped grid resonances and appear significantly at the input of the converter. As it will be shown, the mirroring of these high-frequency harmonics onto low-frequency primary signal components can result in a critical positive feedback when connecting the converter to the grid, as shown in Fig. 3.13. Referring to the findings of e.g., [42,116,140,159,165], the resulting phenomena cannot be analyzed by the classical SISO converter models. This also illustrates that the disregarded aliased components cannot simply be considered as disturbances. Hence, even though Harnefors et al. propose more or less the same converter model in [53] and referred to it as multiple-frequency model, (3.51) should be called primary-frequency model throughout this thesis to prevent a misleading interpretation. Nevertheless, as experimentally elaborated in [53] and also confirmed by a variety of simulations in this work, it can be assumed that the primary-frequency input admittance $Y_{\mathrm{i,p}}(s)$ accurately reflects the VSC's disturbance behavior at most frequencies, and thus, can be used for an initial analysis plus controller and damping filter design.

4 Current Controller Design

Over the years, many PI and PR controller design methods for converter systems have been developed with the aim to optimally regulate a sinusoidal current through a resistive-inductive load. In the electrical drive systems literature, the PWM plus computation delay is typically approximated as a first-order lag element, which allows to apply the amplitude optimum method [118, 119]. Although the amplitude or symmetrical optimum method are used from time to time with regard to grid-feeding converters, see e.g., [16, 84], the design approach is often different in the power systems engineering literature.

Here, besides trial-and-error methods, the current controller design is most commonly performed with respect to the converter's (actual) open-loop current dynamics in the continuous frequency-domain. In order to be able to regulate reference signals without any significant (steady-state) control error and effectively suppress voltage harmonics, the designs typically aim to maximize the controller gain with respect to a desired stability margin [54, 56, 60, 63, 162]. Following this idea and adapting the well established and elaborated parameterization guidelines of Holmes et al. [63] and Harnefors et al. [60], we proposed an extended design procedure for multifrequency PR controllers in [3]. In the following, Sec. 4.1 and Sec. 4.2 summarize the main aspects of the suggested procedure for stationary-frame multifrequency controllers of the form (3.31), where similar parameterization guidelines for the synchronous-frame implementation can be found in [3]. Afterwards, Sec. 4.3 applies the design to the current controller of the VSC under study and examines some important properties of the resulting open-loop and closed-loop system as well as the converter's input admittance.

4.1 System Analysis and Preliminary Considerations

In the next sections, it is assumed that the controller $G_{\mathrm{PR}}^{c}(s)$ can be implemented (quasi) perfectly in its discrete form $G_{\mathrm{PR}}(z)$, see Sec. 3.2.4. Then, given the discretized plant's frequency response from (3.28) and the frequency response of the continuous PR controller from (3.31), the current controller design can be performed with respect to the quasi-continuous VSC open-loop dynamics

$$G_{\mathrm{o}}^{qc}(j\omega) = G_{\mathrm{PR}}^{c}(j\omega) \cdot (Y_{\mathrm{fc}} G_{\mathrm{PWM}} G_{\mathrm{d}})(z)|_{z=e^{j\omega T_{\mathrm{s}}}}. \tag{4.1}$$

After parameterization, $G_{\mathrm{PR}}^{c}(s)$ is transformed to the discrete z-domain by (3.34), which can be implemented on a digital control system. As argued in the control engineering literature [39,119], this approach will only lead to satisfactorily accurate results, if the sampling rate is much faster than the system's bandwidth. This however can be assumed in most of the present-day converter systems and is presupposed here.

If $\omega_{\mathrm{c},h_i} > 0, \forall i$, (4.1) always represents a stable system showing no, or with $r = 0$ at worst one pole in the origin. According to the Nyquist stability criterion for discrete systems, the closed-loop system will thus also be asymptotically stable, if the Nyquist curve of $G_{o}^{qc}(j\omega)$ does not cross or encircle the critical point $(-1 + j0)$ for $0 \leq \omega \leq \omega_{\mathrm{N}}$ [39, 98]. Due to the abrupt phase lag and the rapid increase in gain, however, every high-frequency resonator poses a potential risk for an encirclement. In fact, the system's open-loop gain often crosses $0\,\mathrm{dB}$ multiple times, which makes the stability assessment more difficult [3]. As a possible solution, the authors of [162] suggest to find and evaluate the inverse of the minimum distance between the open-loop system's Nyquist curve and the critical point $(-1 + j0)$, i.e., assess the system's sensitivity peak, see also [10]. But, if the phase response of $G_{\mathrm{o}}^{qc}(j\omega)$ is designed to cross $-180°$ only once and the PR controller does not implement any (high-frequency) resonators close to or above the associated crossover frequency, it can be assumed that the minimum distance between the open-loop system's Nyquist curve and the critical point $(-1 + j0)$ lies on the negative real

axis of the complex plane. Hence, instead of evaluating the rather complex sensitivity function of the system, the gain margin of $G_{\mathrm{o}}^{qc}(j\omega)$ can equivalently be used as reliable stability measure, allowing to quantify how much the open-loop gain can increase before instability occurs [3].

In this context, given the simplification (3.28), the crossover frequency ω_π at which $\arg\{G_{\mathrm{o}}^{qc}(j\omega)\}$ crosses -180° can approximately be obtained from

$$-\pi = \arg\{G_{\mathrm{o}}^{qc}(j\omega_\pi)\} \approx \arg\{G_{\mathrm{PR}}^{c}(j\omega_\pi)\} - \frac{\pi}{2} - \omega_\pi T_{\mathrm{d}}, \tag{4.2}$$

where the gain margin g_{m} is defined as the reciprocal of $|G_{\mathrm{o}}^{qc}(j\omega_\pi)|$, or in terms of decibels as $-20\log(|G_{\mathrm{o}}^{qc}(j\omega_\pi)|)$ [10]. If no harmonic resonator is to be implemented at or close to ω_π, it can be seen that the maximum phase crossover frequency is limited by

$$\omega_\pi \approx \frac{\arg\{G_{\mathrm{PR}}^{c}(j\omega_\pi)\} + \pi/2}{T_{\mathrm{d}}} \leq \frac{\pi}{2T_{\mathrm{d}}} = \frac{\omega_{\mathrm{s}}}{6}. \tag{4.3}$$

Therefore, in order to use the system's gain margin as design specification, it is recommended that the resonance frequency of the highest compensator $h_m\omega_{\mathrm{r}}$ should lie well below $\omega_\pi \leq \omega_{\mathrm{s}}/6$. This also confirms the suggestions of [56,58] and basically enforces the point $G_{\mathrm{o}}^{qc}(jh_m\omega_{\mathrm{r}})$ to have a sufficiently large distance to the point where the Nyquist curve crosses the negative real axis. Considering the exemplary introduced VSC system with $f_{\mathrm{s}} = 10\,\mathrm{kHz}$ and $f_{\mathrm{r}} = 50\,\mathrm{Hz}$, this guideline still allows to reliably compensate for harmonics up to the order $h_m < f_{\mathrm{s}}/(6f_{\mathrm{r}}) = 33$.

On the other hand, presupposing that the plant's cut-off frequency $r_{\mathrm{fc}}/l_{\mathrm{fc}}$ is much smaller than the desired current control loop bandwidth, the open-loop system's phase margin Φ_{m} can be approximated by

$$\Phi_{\mathrm{m}} \approx \pi + \arg\{G_{\mathrm{PR}}^{c}(j\alpha_{\mathrm{c}})\} - \frac{\pi}{2} - \alpha_{\mathrm{c}} T_{\mathrm{d}}, \tag{4.4}$$

where α_{c} denotes the frequency at which the open-loop gain first crosses unity. If the influence of the controller's resonators at the gain crossover

frequency α_c is neglected, and thus, $\arg\{G^c_\mathrm{PR}(j\alpha_\mathrm{c})\} \approx 0°$, (4.4) can be rearranged and α_c can be bounded from above by [55, 63, 97]

$$\alpha_\mathrm{c} \approx \frac{\arg\{G^c_\mathrm{PR}(j\alpha_\mathrm{c})\} + \pi/2 - \Phi_\mathrm{m}}{T_\mathrm{d}} \leq \frac{\pi/2 - \Phi_\mathrm{m}}{T_\mathrm{d}} = \left(\frac{\pi}{2} - \Phi_\mathrm{m}\right)\frac{\omega_\mathrm{s}}{3\pi}. \quad (4.5)$$

To ensure a sufficiently small gain at ω_π, a commonly found recommendation for the choice of α_c can be deduced by setting $\Phi_\mathrm{m} = \pi/5 = 36°$ [54,55], which results in $\alpha_\mathrm{c} \leq \omega_\mathrm{s}/10 < \omega_\pi$. Hence, since the gain crossover frequency specifies the system's gain margin and is directly related to the system's closed-loop bandwidth, α_c and g_m are used as design parameters in the following [3].

4.2 Controller Parameterization

4.2.1 Selection of the Proportional Gain

Since the gain crossover frequency α_c corresponds to the frequency where the open-loop gain is unity, the PR controller's proportional gain k_P can be obtained by evaluating the constraint [3, 4, 63]

$$|G^{qc}_\mathrm{o}(j\alpha_\mathrm{c})| \approx \left| G^c_\mathrm{PR}(j\alpha_\mathrm{c}) \frac{1}{j\alpha_\mathrm{c} l_\mathrm{fc}} \frac{\alpha_\mathrm{c} T_\mathrm{s}}{2\sin(\alpha_\mathrm{c} T_\mathrm{s}/2)} e^{-j\alpha_\mathrm{c} T_\mathrm{d}} \right| = 1. \quad (4.6)$$

Taking into account that the PR controller basically acts like a pure proportional controller, which only shows high gains at some specified (narrow) frequency ranges, the resonators can be neglected at this point and $|G^c_\mathrm{PR}(j\alpha_\mathrm{c})| \approx k_\mathrm{P}$. Further considering the findings of the previous section and noticing that $|\alpha_\mathrm{c} T_\mathrm{s}/(2\sin(\alpha_\mathrm{c} T_\mathrm{s}/2))| \approx 1$ for $r_\mathrm{fc}/l_\mathrm{fc} \ll \alpha_\mathrm{c} \leq \omega_\mathrm{s}/10$, see Fig. 3.8, from (4.6) it follows that

$$k_\mathrm{P} \approx \alpha_\mathrm{c} l_\mathrm{fc}. \quad (4.7)$$

It is important to notice that the guideline (4.7) allows for a simple selection of k_P, where the resulting system becomes (more or less) independent of the converter filter inductance, l_fc, as well as the sampling

frequency, as l_{fc} is typically chosen anti-proportionally to ω_{s}, see the filter selection rule (3.6) [52]. Referring to the filter design recommendations of [13, 17, 84, 104, 109, 117, 125], this can be assumed to apply to both low- and medium voltage converters with power ratings between a few kilowatts and several megawatts. Thus, following the considerations of the previous section and requiring a crossover frequency of $\alpha_{\mathrm{c}} = \omega_{\mathrm{s}}/10 \approx 6283.2\,\frac{\mathrm{rad}}{\mathrm{s}}$, the normalized proportional gain of the converter under study is determined by $k_{\mathrm{P}} \approx 1.22$.

4.2.2 Selection of the Compensation Angles and the Cut-off Frequencies

With respect to the Nyquist stability criterion, stability issues only occur if the phase response of the stable open-loop system crosses $-180°$ and the system's gain is greater than unity [10, 39, 98, 119]. Reviewing the principle low-pass characteristic of the plant $(Y_{\mathrm{fc}}G_{\mathrm{PWM}}G_{\mathrm{d}})(z)|_{z=e^{j\omega T_{\mathrm{s}}}}$ from Fig. 3.8, where the associated phase lag in the high-frequency range can be approximated by $-\pi/2 - \omega T_{\mathrm{d}}$, it would thus be desirable that the controller's phase response does not drop below $-\pi/2 + \omega T_{\mathrm{d}}$ for the widest possible frequency range. Hence, since the PR controller's compensation angles ϕ_{h_i} can be used to introduce a phase lead at every $h_i\omega_{\mathrm{r}}$, it is reasonable to counteract the PWM and computation phase lag, by selecting

$$\phi_{h_i} = -\arg\left\{\frac{h_i\omega_{\mathrm{r}}T_{\mathrm{s}}}{2\sin(h_i\omega_{\mathrm{r}}T_{\mathrm{s}}/2)}e^{-jh_i\omega_{\mathrm{r}}T_{\mathrm{d}}}\right\} = h_i\omega_{\mathrm{r}}T_{\mathrm{d}}, \qquad \forall h_i \in h. \tag{4.8}$$

This is in accordance to typical recommendations in the literature, see e.g., [4, 55, 57, 67, 162]. With regard to the converter's passivity properties, the authors of [56] suggest an alternative, more complex selection of ϕ_{h_i}, which incorporates not only the behavior of the PWM plus PR controller, but also of an additional feed-forward filter. This approach is not to be pursued further here, since similar results can be achieved by implementing a sufficiently large, but still small cut-off frequency $0 < \omega_{\mathrm{c},h_i} \ll k_{\mathrm{I},h_i}, \forall i$ [4]. A drawback in this case, however, is that it must

be balanced between the robustness against uncertainties and the reference tracking capabilities of the converter system, taking into account that $|G^c_{\mathrm{PR}}(jh_i\omega_\mathrm{r})| \approx \left|k_\mathrm{P} + k_{\mathrm{I},h_i}/(2\omega_{\mathrm{c},h_i} \cdot e^{j\phi_{h_i}})\right|$. For the VSC test-system, the cut-off frequencies are set to $\omega_{\mathrm{c},h_i} = 0.1\,\frac{\mathrm{rad}}{\mathrm{s}}$, $\forall i$.

4.2.3 Selection of the Integral Gains

In general, high resonator integral gains are beneficial to accurately track (or compensate for) sinusoidal currents and simultaneously achieve a low controller sensitivity to variations of the grid frequency [29, 170]. But, as shown in [3], the integral gains should not be increased arbitrarily, due to the interaction between neighboring resonators. More precisely, low-order resonators introduce an unwanted phase lag to the higher resonators, where the effects get worse with increasing integral gains, see also Fig. 3.10. As a consequence, the phase lag above the m-th resonator is more and more lowered, such that the open-loop system's phase response $\arg\{G^{qc}_\mathrm{o}(j\omega)\}$ reaches $-180°$ at lower frequencies. If this interaction is not taken into account, the required stability margin might not be achieved or the system could even be destabilized. In order to avoid such critical situations, the integral gain of the highest resonator, k_{I,h_m}, is selected first, followed by a recursive gain adjustment according to [3].

Design of the m-th Integral Gain k_{I,h_m}

Applying the design guidelines (4.7) and (4.8), the system stability is determined by its high-frequency behavior, where the system's gain margin g_m can be used as stability measure. Given the open-loop dynamics (4.1) and neglecting the influence of all low-frequency resonators, g_m can be approximated by

$$g_\mathrm{m} = \frac{1}{|G_\mathrm{o}(j\omega_\pi)|} \approx \left| \frac{j\omega_\pi l_\mathrm{fc}}{G^c_{\mathrm{PR}}(j\omega_\pi)} \, \frac{2\sin(\omega_\pi T_\mathrm{s}/2)}{\omega_\pi T_\mathrm{s}} \, e^{j\omega_\pi T_\mathrm{d}} \right| \approx \frac{\omega_\pi l_\mathrm{fc}}{k_\mathrm{p}} = \frac{\omega_\pi}{\alpha_\mathrm{c}}. \quad (4.9)$$

Here, similar to the simplifications in (4.7), it is taken into account that $|G^c_{\mathrm{PR}}(j\omega_\pi)| \approx k_\mathrm{P}$ for $h_m\omega_\mathrm{r} \ll \omega_\pi$ and further that $|2\sin(\omega_\pi T_\mathrm{s}/2)/(\omega_\pi T_\mathrm{s})| \approx$

1 for $\omega_\pi \leq \omega_\mathrm{s}/6$, where the mismatch at $\omega = \omega_\mathrm{s}/6$ is still quite small, showing a relative error of about 4.5%. Then, taking into account that

$$\begin{aligned}\arg\left\{G_{\mathrm{PR}}^{c}(j\omega)\right\} &\approx \arg\left\{k_\mathrm{P} + k_{\mathrm{I},h_m}\frac{j\omega\cos(\phi_{h_m}) - h_m\omega_\mathrm{r}\sin(\phi_{h_m})}{((h_m\omega_\mathrm{r})^2-\omega^2) + j\omega_{\mathrm{c},h_m}\omega}\right\}\\ &\approx \tan^{-1}\left(\frac{k_{\mathrm{I},h_m}\omega\cos(\phi_{h_m})}{((h_m\omega_\mathrm{r})^2-\omega^2)\,k_\mathrm{P} - k_{\mathrm{I},h_m}h_m\omega_\mathrm{r}\sin(\phi_{h_m})}\right)\\ &\approx -\frac{k_{\mathrm{I},h_m}}{(1-(h_m\omega_\mathrm{r})^2/\omega^2)\,\omega k_\mathrm{P}}, \qquad \omega \gg h_m\omega_\mathrm{r} \end{aligned} \tag{4.10}$$

where it is considered that usually $0^\circ \leq \phi_{h_m} < 90^\circ$ and $\omega_{\mathrm{c},h_m} \approx 0$, the m-th integral gain can be calculated using (4.2), (4.9), and (4.10) with $\omega = \omega_\pi \gg h_m\omega_\mathrm{r}$. In particular, displacing $\arg\{G_{\mathrm{PR}}^{c}(j\omega_\pi)\}$ in (4.2) by its corresponding small argument approximate from (4.10), (4.9) can be substituted into (4.2) and solved for k_{I,h_m}, yielding

$$k_{\mathrm{I},h_m} \approx \underbrace{\left(\frac{\pi}{2} - g_\mathrm{m}\alpha_\mathrm{c}T_\mathrm{d}\right)\cdot\left(1-\left(\frac{h_m\omega_\mathrm{r}}{g_\mathrm{m}\alpha_\mathrm{c}}\right)^2\right)g_\mathrm{m}\alpha_\mathrm{c}}_{\alpha_{\mathrm{I},h_m}}\cdot k_\mathrm{P} = \alpha_{\mathrm{I},h_m}\alpha_\mathrm{c}\,l_\mathrm{fc}. \tag{4.11}$$

Similarly, a typical design guideline that can be found in the literature is to choose $k_{\mathrm{I},h_m} \ll \alpha_\mathrm{c}k_\mathrm{P}$ [63] or $\alpha_{\mathrm{I},h_m} \ll \alpha_\mathrm{c}$, see e.g., [57, 58, 60]. However, if (4.11) results in an $\alpha_{\mathrm{I},h_m} \approx 0$ or $\alpha_{\mathrm{I},h_m} \leq 0$, the desired design specifications cannot be fulfilled (or only with great difficulty) and the requirements on g_m or α_c must be relaxed. In this context, since $\alpha_\mathrm{c} \leq \omega_\mathrm{s}/10$ and $\omega_\pi \leq \omega_\mathrm{s}/6$, from (4.9) it follows that $g_\mathrm{m} \leq 5/3 = 1/0.6$, where the maximum achievable gain margin decreases the closer $h_m\omega_\mathrm{r}$ is to ω_π.

Recursive Gain Adjustment

As motivated at the beginning of this section, the parameterization (4.11) should not directly be applied to the resonators. In contrast, to maintain the desired gain margin g_m and counteract the unwanted phase lag that is introduced by each additional low-frequency resonator, all integral gains should be adjusted by the recursive procedure from [3]. Accordingly, the previously designed resonator with resonance frequency $h_m\omega_\mathrm{r}$ and gain

$k_{\mathrm{I},h_m} = \alpha_{\mathrm{I},h_m} k_{\mathrm{P}}$ is utilized as a reference resonator, which defines the desired controller behavior in the high-frequency range for $\omega > h_m \omega_{\mathrm{r}}$. Since it can be assumed that each resonator is most negatively influenced by its next lower resonator, the idea is to adapt the gains of two neighbored resonators, such that their superimposed frequency response approaches the previously specified reference behavior. Considering that the cut-off frequencies and the compensation angles reshape the controller's frequency response only in a well-limited frequency range, their influences as well as the influences of the other resonators can be neglected in the following.

Following this idea and setting the frequency response of the two highest resonators, $jk_{\mathrm{I},h_{m-1}}\omega/((h_{m-1}\omega_{\mathrm{r}})^2-\omega^2) + jk_{\mathrm{I},h_m}\omega/((h_m\omega_{\mathrm{r}})^2-\omega^2)$, equal to the response of the reference resonator, $j\tilde{k}_{\mathrm{I},h_m}\omega/((h_m\omega_{\mathrm{r}})^2-\omega^2)$, where $\tilde{k}_{\mathrm{I},h_m}$ denotes the integral gain of the reference resonator, which is calculated by (4.11), an evaluation at $\omega = (h_m+\beta)\omega_{\mathrm{r}}$, $\beta > 0$, yields [3]

$$k_{\mathrm{I},h_{m-1}} = \frac{(h_m+\beta)^2 - h_{m-1}^2}{(h_m+\beta)^2 - h_m^2} \left(\tilde{k}_{\mathrm{I},h_m} - k_{\mathrm{I},h_m}\right). \tag{4.12}$$

For a given resonator with gain k_{I,h_m}, the design guideline (4.12) thus describes how the integral gain of the lower resonator has to be chosen, such that their superimposed frequency response at $\omega = (h_m+\beta)\omega_{\mathrm{r}}$ corresponds to that of the single reference resonator. Hence, regarding a multifrequency PR controller of the form (3.31), (4.12) can successively be applied to the remaining resonator pairs at $h_{m-1}\omega_{\mathrm{r}}$ and $h_{m-2}\omega_{\mathrm{r}}$, $h_{m-2}\omega_{\mathrm{r}}$ and $h_{m-3}\omega_{\mathrm{r}}$, and so forth, by using the previously calculated integral gain as new reference gain. This results in a recursive gain adjustment of the form

$$k_{\mathrm{I},h_i} = \frac{(h_{i+1}+\beta)^2 - h_i^2}{(h_{i+1}+\beta)^2 - h_{i+1}^2} \left[\ldots \frac{(h_m+\beta)^2 - h_{m-1}^2}{(h_m+\beta)^2 - h_m^2} \left(\tilde{k}_{\mathrm{I},h_m} - k_{\mathrm{I},h_m}\right) - \ldots - k_{\mathrm{I},h_{i+1}} \right], \tag{4.13}$$

for all $i = 1, \ldots, m-1$. As can be seen, the integral gain k_{I,h_i} can now be calculated depending on $\tilde{k}_{\mathrm{I},h_m}$, the other still to be specified gains

$k_{\mathrm{I},h_{i+1}}, \ldots, k_{\mathrm{I},h_m}$, and the factor β. Here, β allows to specify how fast the controller's phase lag $\arg\{G^c_{\mathrm{PR}}(j\omega)\}$ recovers to zero for frequencies above $h_m\omega_\mathrm{r}$, and is thus also referred to as recovery factor [3]. Increasing values generally result in decreasing integral gains, but in return, in a better compliance to the desired reference behavior at high frequencies. Based on several simulative test studies, we suggest to choose $\beta \approx g_\mathrm{m}\alpha_\mathrm{c}/\omega_\mathrm{r} - h_m$, which achieves a good compromise between the implemented controller gain and the resulting gain margin of the open-loop system, see [3]. However, with regard to a passivity-based feed-forward filter design, it might be beneficial to increase β in some applications, allowing to approximate the PR controller's high frequency behavior more accurately by its proportional path plus the characteristics of the reference resonator.

In addition, the design can further be simplified by introducing individual weightings γ_{h_i} for every harmonic $h_i \in h$ that is to be compensated for. In doing so, the undefined integral gains in (4.13) can be expressed in terms of one (common) integral gain k_I, i.e., $k_{\mathrm{I},h_i} = \gamma_{h_i} k_\mathrm{I}$, $\forall i$. Then, from the recursive gain calculation (4.13) with $\tilde{k}_{\mathrm{I},h_m} = \alpha_{\mathrm{I},h_m} k_\mathrm{P}$, it finally follows that the PR controller's integral gains can be calculated by

$$k_{\mathrm{I},h_i} = \gamma_{h_i} k_\mathrm{I}, \qquad i = 1, ..., m \tag{4.14}$$

where

$$k_\mathrm{I} = \underbrace{\frac{\alpha_{\mathrm{I},h_m}}{\gamma_{h_m} + \sum_{q=1}^{m-1} \gamma_{h_q} \prod_{\nu=q}^{m-1} \frac{(h_{\nu+1}+\beta)^2 - h_\nu^2}{(h_{\nu+1}+\beta)^2 - h_\nu^2}}}_{\alpha_\mathrm{I}} k_\mathrm{P}. \tag{4.15}$$

It is suggested to specify weightings that range between zero and one, where a larger γ_{h_i} also implies a higher gain. With respect to the requirements of grid connection standards, see e.g., [15, 17, 68, 68, 134], it is mostly advisable to prioritize the fundamental component and some selected low-frequency harmonics or to choose a decreasing prioritization, where $\gamma_{h_1} \geq \ldots \geq \gamma_{h_m}$ [67, 82]. As can be verified, a gradation of some (not so important) harmonics automatically leads to a boost of the

common integral gain k_{I}, and thus, to a further increase of k_{I,h_i} of the higher weighted harmonics h_i [3].

4.3 Application to the Exemplary Converter System

Using the VSC test-system parameters from Tab. 3.1 and Tab. 3.2, Tab. 4.1 summarizes an exemplary current controller parameterization, which results from the design guidelines (4.7), (4.8), (4.14), and (4.15), where the gain of the reference resonator $\tilde{k}_{\mathrm{I},h_m} = \alpha_{\mathrm{I},h_m} k_{\mathrm{P}}$ is calculated by (4.11). For simplicity, all resonator cut-off frequencies are set to $\omega_{\mathrm{c},h_i} = 0.1\,\frac{\mathrm{rad}}{\mathrm{s}}$. Then, Fig. 4.1, Fig. 4.2, and Fig. 4.3 illustrate the corresponding Bode plots of the converter's open-loop system, closed-loop system, and input admittance, respectively. In addition to (analytically) calculated Bode plots, the results of a system identification are also shown, whereby the converter simulation model used is described in more detail in Sec. 7.1 and the measurements are here only intended to confirm the theoretical findings of this section.

Table 4.1: Control specifications and normalized current controller parameters

Parameter	Parameterization
Current control specifications	
Gain crossover frequency	$\alpha_{\mathrm{c}} = \omega_{\mathrm{s}}/10 = 6283.2\,\mathrm{rad/s}$
Gain margin	$g_{\mathrm{m}} = 1/0.62 \approx 1.61$
Resonator orders	$h = \{1, 5, 7, 11, 13, 17, 19\}$
Harmonic weightings	$\gamma_1 = 1, \gamma_5 = \gamma_7 = 0.6, \gamma_{11} = \gamma_{13} = 0.4,$ $\gamma_{17} = \gamma_{19} = 0.1$
Alignment factor	$\beta = 40$
Reference resonator gain	$\tilde{k}_{\mathrm{I},h_m} = 410.59\,\mathrm{rad/s}$
Controller parameters	
Proportional gain	$k_{\mathrm{P}} = 1.22$
Compensation angles	$\phi_1 = 2.7^\circ, \phi_5 = 13.5^\circ, \phi_7 = 18.9^\circ,$ $\phi_{11} = 29.7^\circ, \phi_{13} = 35.1^\circ, \phi_{17} = 45.9^\circ,$ $\phi_{19} = 51.3^\circ$
Common integral gain	$k_{\mathrm{I}} = 142.14\,\mathrm{rad/s},$
Cut-off frequencies	$\omega_{\mathrm{c},h_i} = 0.1\,\mathrm{rad/s},\ \forall i$

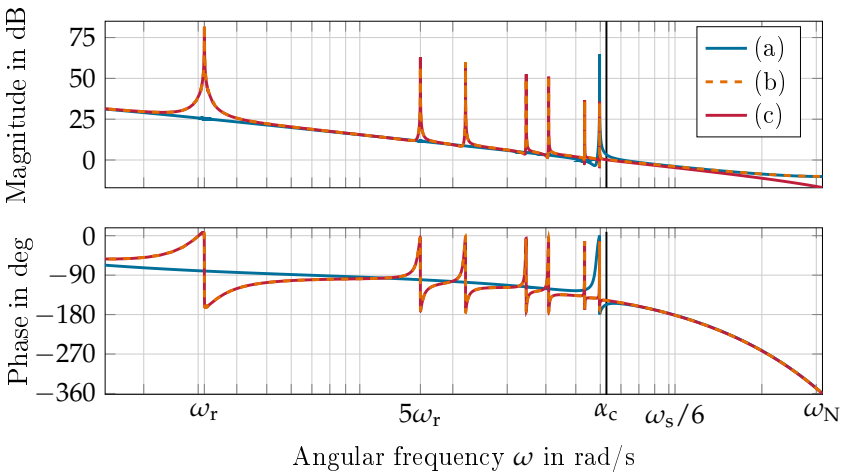

Fig. 4.1: Bode plots of the converter's (a), (b) discretized open-loop system $G_{\mathrm{PR}}(z)(Y_{\mathrm{fc}}G_{\mathrm{PWM}}G_{\mathrm{d}})(z)$ and (c) its continuous equivalent $G^{\mathrm{c}}_{\mathrm{PR}}(s)Y_{\mathrm{fc}}(s)G_{\mathrm{PWM}}(s)/T_{\mathrm{s}}G_{\mathrm{d}}(s)$, where the PR controller implements (a) one reference resonator at $19\,\omega_\mathrm{r}$, and (b), (c) stationary-frame resonators of order $1, 5, 7, 11, 13, 17, 19$.

As can be observed in Fig. 4.1, the frequency responses approach the desired high-frequency (reference) behavior for $\omega \gg 19\,\omega_\mathrm{r}$. Moreover, similar to the findings of Sec. 3.2.3, the responses of the VSC's discrete and continuous equivalent systems show an almost identical behavior in the low-frequency range, where there is an increasing mismatch in the high-frequency range. This important fact is discussed in more detail later, but should be kept in mind by now. Taking a closer look at Fig. 4.1, it becomes clear that the adopted design approximately satisfies the required design specifications and results in an asymptotically stable closed-loop system with adequate stability measures [10,98,119]. The phase response of the open-loop system $G_{\mathrm{PR}}(z)(Y_{\mathrm{fc}}G_{\mathrm{PWM}}G_{\mathrm{d}})(z)$ crosses $-180°$ only once at $\omega_\pi \approx 10293\,\frac{\mathrm{rad}}{\mathrm{s}}$, yielding a gain margin of $g_\mathrm{m} \approx 1/0.64$. In addition, the system's open-loop amplitude response illustrates the applied harmonic prioritization.

In this context, Fig. 4.2 and Fig. 4.3 verify that signal components at the selected harmonic frequencies can be regulated (or compensated) with-

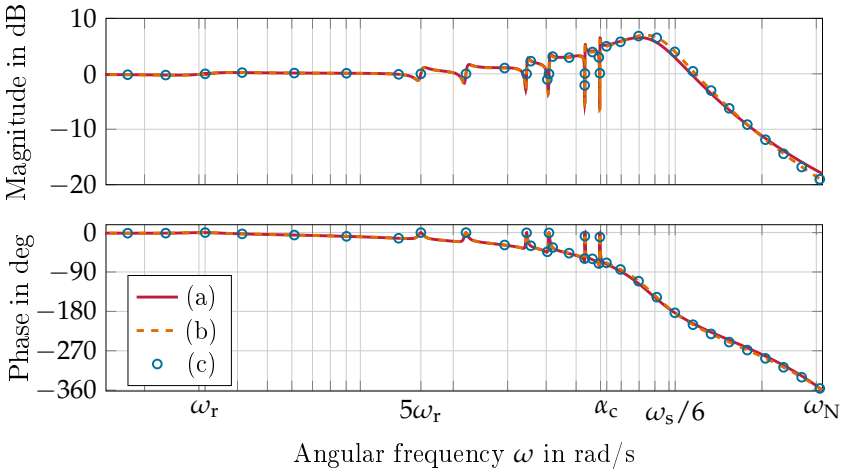

Fig. 4.2: Bode plots of the converter's (a) reference current dynamics $G_\mathrm{cl}(s)/T_\mathrm{s}$, (b) its continuous equivalent $G_\mathrm{cl}^c(s)$, and (c) the corresponding identified magnitude and phase characteristics of a simulation model with (nonlinear) single-update PWM.

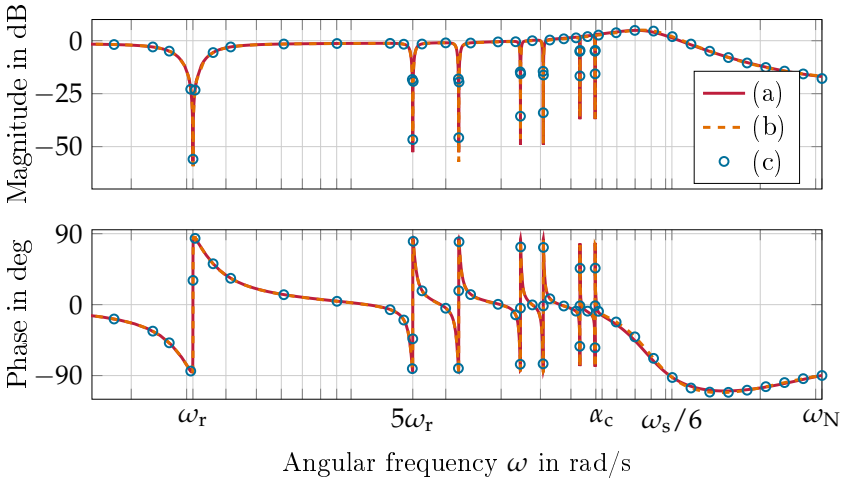

Fig. 4.3: Bode plots of the converter's inherent (a) primary-frequency input admittance model $Y_\mathrm{i,p}(s)$, (b) quasi-analog input admittance model $Y_\mathrm{i}^c(s)$, and (c) the corresponding identified magnitude and phase characteristics of a simulation model without additional passive or active damping method.

out any significant steady-state control error, where the harmonics with higher weightings γ_{h_i} show a lower sensitivity to grid frequency variations [3]. However, at this point it should be noted that the implementation of high-frequency resonators introduces resonances to the system's closed-loop amplitude response $|G_{\mathrm{cl}}(s)/T_{\mathrm{s}}|$, see also [3]. These closed-loop resonances, which are also referred to as anomalous peaks in [162], can lead to an unwanted amplification of current components near the associated resonance frequencies $h_i\omega_{\mathrm{r}}$ as well as signal components that lie between $h_m\omega_{\mathrm{r}}$ and $\omega_{\mathrm{s}}/6$. The same applies to PCC voltage components that fall into the high-frequency resonance peak of the converter's input admittance from Fig. 4.3. These observations can also be verified by the shown results of a converter system identification, using a test signal injection which angular frequency is swept over the frequency range of interest, see also the measurement procedures described in [8,53,110]. At this point, it should however be noticed that even though the measured characteristics accurately match the theoretical models from Sec. 3.4 for most frequency samples, the nonlinear converter shows an ever decreasing attenuation capability at the specified high-frequency resonators. But more importantly, $Y_{\mathrm{i,p}}(s)$ exactly models the VSC's input admittance for frequencies above $h_m\omega_{\mathrm{r}}$ again. In this context, reviewing the passivity definition from Sec. 2.1.1, it can directly be concluded that the VSC's conductance is not inherently passive, since its phase response shows values below $-90°$ for frequencies between $\omega_{\mathrm{crit}} \approx \omega_{\mathrm{s}}/6 = 10472\,\frac{\mathrm{rad}}{\mathrm{s}}$ and $\omega_{\mathrm{N}} = 31415.9\,\frac{\mathrm{rad}}{\mathrm{s}}$.

Stability of the Closed-Loop Grid-Converter System

Due to the converter's identified negative input admittance in the high-frequency range, there is a great possibility that the grid-connected converter interacts with poorly damped grid resonances, which in turn might cause a power system destabilization [4, 11,53,57,110,141]. Depending on the LCL filter's resonance frequency, stability issues may even arise if the converter is connected to a stiff grid with a grid impedance of $Z_{\mathrm{g}}(s) = 0$. This risk can exemplarily be demonstrated by the converter system un-

der study, whose LCL filter is specifically designed to have its resonance within the critical frequency range between $\omega_{\mathrm{crit}} \approx \omega_{\mathrm{s}}/6$ and ω_{N}, see Fig. 3.3. If the converter test-system implements an ideal (undamped) LCL filter with parameters as in Tab. 3.2, Fig. 4.4 shows the Nyquist plots of the open-loop grid-converter system $Y_{\mathrm{i,p}}(s)\tilde{Z}_{\mathrm{g}}(s)$ and $Y_{\mathrm{i}}^{\mathrm{c}}(s)\tilde{Z}_{\mathrm{g}}(s)$, corresponding to the series connection of the VSC's input admittance models from Fig. 4.3 with the synthetic grid impedance (3.13) from Fig. 3.4.

All the shown Nyquist curves start for $\omega = 0$ close to the origin of the complex plane and approach the origin again from the second quadrant for $\omega \to \omega_{\mathrm{N}}$. Hereby, the systems' low-frequency dynamics up to the gain crossover frequency α_{c} are mainly reflected by the circle-like parts of the Nyquist curves with low amplitudes, whereas the resonance in $\tilde{Z}_{\mathrm{g}}(s)$ in combination with the high-frequency behavior of the VSC input admittances cause the circle-like parts of the Nyquist curves with relatively high gain, visible in Fig. 4.4A and Fig. 4.4C. In this context, an increase of the effective grid inductance, l_{g}, basically leads to a further expansion of the Nyquist curves, but does not change the principle shape of the curves much. Hence, since the converter conductance is stable, but all shown Nyquist curves of the open-loop models encircle the point $(-1 + j0)$ for $\omega \in [0, \omega_{\mathrm{N}}]$, it can be concluded that the interconnection of the digitally current-controlled converter with a power network mostly results in an unstable closed-loop system [39, 89, 98]. If the connected grid does not provide sufficient positive damping, it is likely that critically damped or exponentially growing harmonic oscillations will occur.

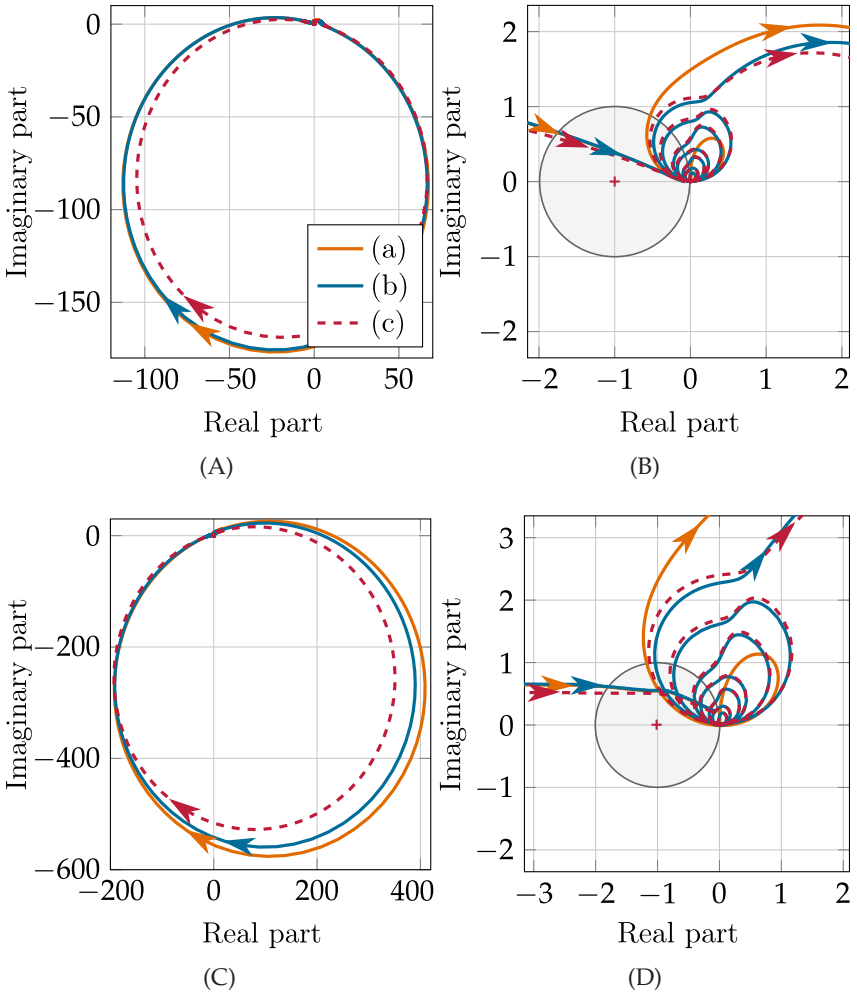

Fig. 4.4: Nyquist plots of the open-loop grid-converter system without damping method, using (a), (b) the primary-frequency input admittance model $Y_{\mathrm{i,p}}(s)$ and (c) the quasi-analog input admittance model $Y_{\mathrm{i}}^{c}(s)$, where the PR controller implements (a) one reference resonator at $19\,\omega_{\mathrm{r}}$, and (b), (c) stationary-frame resonators of order $1, 5, 7, 11, 13, 17, 19$. Subfigures (A), (C) and subfigures (B), (D) show the complete and detailed plots for $\omega \in [0, \omega_{\mathrm{N}}]$, respectively, where the VSC is connected (A), (B) to a stiff grid with $Z_{\mathrm{g}}(s) = 0$, and (C), (D) to an inductive grid with $Z_{\mathrm{g}}(s) = l_{\mathrm{g}} s$, $l_{\mathrm{g}} = 64.95\,\mu\mathrm{s}$.

5 Passivity Assessment and Filter Design

In order to prevent stability issues, which are likely to arise from the found inherent non-passive region of the converter's input admittance, this chapter further discusses the stabilization of the grid-converter system from Fig. 3.13. As motivated in Sec. 2.2.2, the system stability can be guaranteed for every passive (synthetic) grid impedance, if the reference current dynamics $G_{\mathrm{cl}}(s)$ are stable and the converter's disturbance dynamics are passive. Throughout the remaining thesis, it is assumed that the first condition is always fulfilled, e.g., using the presented current controller design of the previous chapter. In addition, it is presupposed that the preceding current controller design also yields an asymptotically stable converter conductance. Hence, the remaining goal is to render the VSC input admittance (strictly) passive by means of passive or active damping filters.

For this purpose, Sec. 5.1 first quantifies the inherent passivity properties of the converter's primary-frequency input admittance $Y_{\mathrm{i,p}}(s)$ more in detail. Similar to the findings of our work [4], the calculation of the system's passivity indices allows to deduce generalized and necessary criteria, which can later on be used for a passivation up to the Nyquist frequency, defining the active, controllable frequency range of the converter. This time, however, the effects of the digital controller implementation are also assessed, where in this chapter it should still be assumed that no aliasing occurs. Afterwards, Sec. 5.2 and Sec. 5.3 review and examine two commonly used passive and active filter methods, respectively. Hereby, special emphasis is put on the passivation by active feed-forward filters, where along with the principal idea, a new filter design is proposed and associated implementation aspects are discussed. In particular, our conclusion from [4] is confirmed and it is shown that the converter passivation must not be limited to the high frequency range, but it is also ad-

visable to examine each frequency region near the specified resonance frequencies separately.

5.1 Passivity of the VSC's Disturbance Dynamics

5.1.1 IFP Index of the Primary-Frequency Input Admittance

As can be seen from the definition of the primary-frequency input admittance (3.52), $Y_{\mathrm{i,p}}(s)$ consists of a parallel connection of $Y_{\mathrm{fc}}(s)$ and $-\Gamma(s)Y_{\mathrm{cl,p}}(s)$. Since the output filter dynamics $Y_{\mathrm{fc}}(s)$ always represent a passive system, the active part, $-\Gamma(s)Y_{\mathrm{cl,p}}(s)$, must be responsible for the non-passive region which was identified in the Bode plot from Fig. 4.3. In this context, the VSC disturbance dynamics can be understood as an interconnection of a passive subsystem with a partially passive and partially non-passive subsystem. Hence, considering the concept of (frequency-depending) passivity indices to quantify the degree of a system's passivity at some frequency ω, the IFP index of $Y_{\mathrm{i,p}}(s)$ is given by

$$\mathrm{IFP}\left\{Y_{\mathrm{i,p}}(j\omega)\right\} = \mathrm{IFP}\left\{Y_{\mathrm{fc}}(j\omega)\right\} - \mathrm{IFP}\left\{\Gamma(j\omega)Y_{\mathrm{cl,p}}(j\omega)\right\}. \tag{5.1}$$

Reviewing the definition of the admittance $Y_{\mathrm{cl,p}}(s) = G_{\mathrm{cl}}(s)/T_{\mathrm{s}}Y_{\mathrm{fc}}(s)$ and considering that $\arg\left\{Y_{\mathrm{fc}}(j\omega)\right\} \approx -\pi/2$ for all $\omega \gg r_{\mathrm{fc}}/l_{\mathrm{fc}}$, it shows that the latter term in (5.1) has a shortage of passivity in the high-frequency range, if

$$\begin{aligned} &-\mathrm{IFP}\left\{\Gamma(j\omega)Y_{\mathrm{cl,p}}(j\omega)\right\} = \\ &\quad -\left|\Gamma(j\omega)Y_{\mathrm{cl,p}}(j\omega)\right| \cdot \cos\left(\arg\left\{\Gamma(j\omega)\right\} + \arg\left\{G_{\mathrm{cl}}(jw)/T_{\mathrm{s}}\right\} - \frac{\pi}{2}\right) < 0, \end{aligned} \tag{5.2}$$

and thus, when $\arg\left\{\Gamma(j\omega)\right\} + \arg\left\{G_{\mathrm{cl}}(jw)/T_{\mathrm{s}}\right\}$ lies not within the range $(-180°, 0°)$. According to Sec. 2.1.2, this shortage of passivity can either be compensated for by a sufficiently large excess of passivity from $Y_{\mathrm{fc}}(s)$ or by a filter $\Gamma(s)$ that introduces a phase lead to $G_{\mathrm{cl}}(s)/T_{\mathrm{s}}$ in the high-

frequency range. These two possibilities for the passivation of the VSC input admittance are further discussed in Sec. 5.2.1 and Sec. 5.3, respectively, where (5.1) is to be analyzed more in detail first.

Using the basic concept of a loop transformation [119], the active subsystem $\Gamma(s)Y_{\mathrm{cl,p}}(s)$ can be interpreted as a (standard) feedback-interconnection of the form

$$\Gamma(s)Y_{\mathrm{cl,p}}(s)=\frac{\Gamma(s)Y_{\mathrm{fc}}^2(s)G_{\mathrm{PWM}}(s)/T_{\mathrm{s}}G_{\mathrm{d}}(s)G_{\mathrm{PR}}^*(s)}{1+(Y_{\mathrm{fc}}G_{\mathrm{PWM}}G_{\mathrm{d}})^*(s)G_{\mathrm{PR}}^*(s)}=\frac{G_{\mathrm{ff}}(s)}{1+G_{\mathrm{ff}}(s)G_{\mathrm{fb}}(s)} \tag{5.3}$$

where

$$G_{\mathrm{ff}}(s)=\Gamma(s)Y_{\mathrm{fc}}^2(s)G_{\mathrm{PWM}}(s)/T_{\mathrm{s}}G_{\mathrm{d}}(s)G_{\mathrm{PR}}^*(s), \tag{5.4}$$

$$G_{\mathrm{fb}}(s)=\frac{(Y_{\mathrm{fc}}G_{\mathrm{PWM}}G_{\mathrm{d}})^*(s)}{\Gamma(s)Y_{\mathrm{fc}}^2(s)G_{\mathrm{PWM}}(s)/T_{\mathrm{s}}G_{\mathrm{d}}(s)}. \tag{5.5}$$

This allows to apply the findings from Appendix A.1 and the IFP index of the feedback system (5.3) can simply be calculated by (A.2). Hence, (5.1) can also be expressed as

$$\begin{aligned}\mathrm{IFP}\left\{Y_{\mathrm{i,p}}(j\omega)\right\}=\mathrm{IFP}\left\{Y_{\mathrm{fc}}(j\omega)\right\}-\mathrm{OFP}\left\{G_{\mathrm{ff}}(j\omega)\right\}\left|Y_{\mathrm{cl,p}}(j\omega)\right|^2\\-\mathrm{IFP}\left\{G_{\mathrm{fb}}(j\omega)\right\}\left|Y_{\mathrm{cl,p}}(j\omega)\right|^2.\end{aligned} \tag{5.6}$$

IFP Index of the Inherent Input Admittance without Active Filter

On the basis of (5.6), the passivity properties of the converter's (inherent) input admittance without active feed-forward filter can be investigated. Therefore, $H(z)=0$ (or $\Gamma(s)=1$) in the following. Even though each term in (5.6) contributes to the system's IFP index, the analysis can further be simplified by supposing that the converter output filter shows a negligible normalized filter resistance r_{fc}. In this case, the IFP index of $Y_{\mathrm{fc}}(s)=1/(l_{\mathrm{fc}}s)$ in (5.6) vanishes. Moreover, noticing that the common z-transform of $Y_{\mathrm{fc}}(s)G_{\mathrm{PWM}}(s)G_{\mathrm{d}}(s)$ from (3.26) simplifies to (3.27) for $r_{\mathrm{fc}}\to 0$, the system (5.5) becomes

$$G_{\mathrm{fb}}(s)=\frac{(Y_{\mathrm{fc}}G_{\mathrm{PWM}}G_{\mathrm{d}})(z)|_{z=e^{sT_{\mathrm{s}}}}}{Y_{\mathrm{fc}}^2(s)G_{\mathrm{PWM}}(s)/T_{\mathrm{s}}G_{\mathrm{d}}(s)}\approx\frac{l_{\mathrm{fc}}T_{\mathrm{s}}^2s^3D_0}{(e^{sT_{\mathrm{s}}}-1)(1-e^{-D_0T_{\mathrm{s}}s})e^{-(\frac{1-D_0}{2})T_{\mathrm{s}}s}}. \tag{5.7}$$

Then, taking the frequency responses of $G_{\mathrm{PWM}}(s)$ and $G_{\mathrm{ZOH}}(s)$ into account, see e.g., [1], the frequency response of (5.7) can be derived to be

$$G_{\mathrm{fb}}(j\omega)=-j\frac{l_{\mathrm{fc}}T_{\mathrm{s}}^2\omega^3D_0}{4\sin(\omega T_{\mathrm{s}}/2)\sin(\omega D_0T_{\mathrm{s}}/2)}. \tag{5.8}$$

Since the simplified frequency response of $G_{\mathrm{fb}}(s)$ only consists of a complex part, where the real part is equal to zero, IFP $\{G_{\mathrm{fb}}(j\omega)\}$ in (5.6) vanishes. Hence, setting $H(z)=0$ and assuming that $r_{\mathrm{fc}}\approx 0$, the IFP index of the converter's inherent input admittance can be approximated by

$$\begin{aligned}\mathrm{IFP}\,\{Y_{\mathrm{i,p}}(j\omega)\}&\approx-\mathrm{IFP}\,\{Y_{\mathrm{cl,p}}(j\omega)\}\approx-\mathrm{OFP}\,\{G_{\mathrm{ff}}(j\omega)\}\,|Y_{\mathrm{cl,p}}(j\omega)|^2\\&\approx\left|\frac{l_{\mathrm{fc}}^2T_{\mathrm{s}}\omega^3D_0}{2\sin(\omega D_0T_{\mathrm{s}}/2)}\right|\frac{|Y_{\mathrm{cl,p}}(j\omega)|^2}{|G_{\mathrm{PR}}^*(j\omega)|}\cos(\omega T_{\mathrm{d}}-\arg\{G_{\mathrm{PR}}^*(j\omega)\}).\end{aligned} \tag{5.9}$$

At this point it should be emphasized that, even though $r_{\mathrm{fc}}=0$ is a rather theoretical assumption, (5.9) also represents an adequate high-frequency approximation of (5.6) for $0<r_{\mathrm{fc}}\ll 1$. This mainly results from the fact that $Y_{\mathrm{fc}}(s)$ increasingly acts as a pure inductance for frequencies above $r_{\mathrm{fc}}/l_{\mathrm{fc}}$, see Fig. 3.8, and thus, $r_{\mathrm{fc}}\approx 0$ is a valid assumption in the high-frequency range. In particular, using the system under study, Fig. 5.1 illustrates the contributions of the individual components of IFP $\{Y_{\mathrm{i,p}}(j\omega)\}$ from (5.6) for increasing converter-side filter resistances. In general, considering small filter resistances, $r_{\mathrm{fc}}\ll 1$, the term IFP $\{Y_{\mathrm{fc}}(j\omega)\}-\mathrm{IFP}\,\{G_{\mathrm{fb}}(j\omega)\}\,|Y_{\mathrm{cl,p}}(j\omega)|^2$ mainly influences the VSC's low-frequency IFP index, but does only marginally contribute to IFP $\{Y_{\mathrm{i,p}}(j\omega)\}$ in the high-frequency range, especially at frequencies above $\omega_{\mathrm{s}}/6$. On the contrary, $-\mathrm{OFP}\,\{G_{\mathrm{ff}}(j\omega)\}\,|Y_{\mathrm{cl,p}}(j\omega)|^2$ contributes to the complete frequency range and significantly determines the IFP index of the VSC's inherent input admittance for all frequencies $\omega\gg\omega_{\mathrm{r}}$. At this

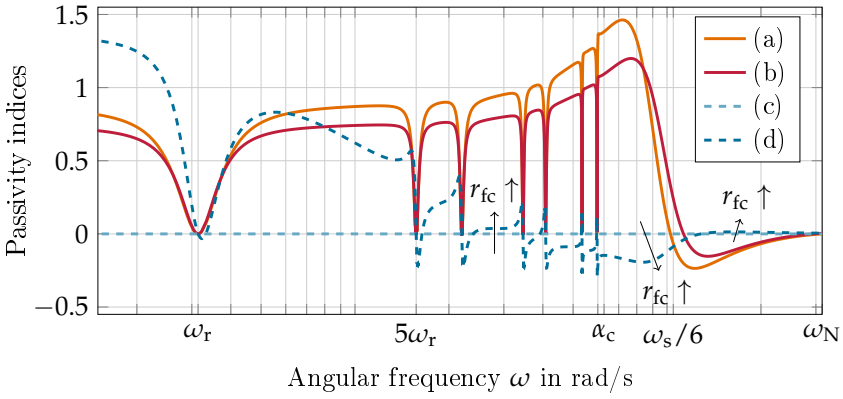

(A)

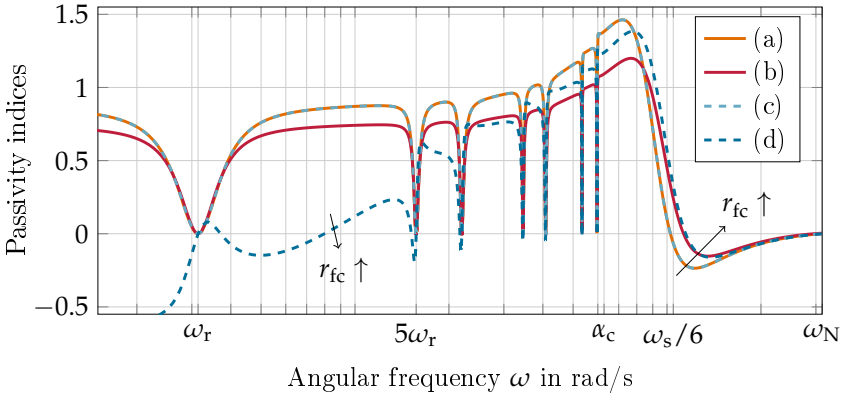

(B)

Fig. 5.1: IFP index of the VSC's inherent primary-frequency input admittance model for (a) $r_{\mathrm{fc}} = 0$ and (b) $r_{\mathrm{fc}} = 0.2$, where (c) and (d) in subfigure (A) show the corresponding contribution of IFP $\{Y_{\mathrm{fc}}(j\omega)\}$ − IFP $\{G_{\mathrm{fb}}(j\omega)\}\,|Y_{\mathrm{cl,p}}(j\omega)|^2$ and (c) and (d) in subfigure (B) show the corresponding contribution of $-$OFP $\{G_{\mathrm{ff}}(j\omega)\}\,|Y_{\mathrm{cl,p}}(j\omega)|^2$, respectively.

point it should further be noticed that an increase of r_{fc} also leads to an increase of the frequency ω_{crit} at which the converter's input admittance becomes non-passive. This confirms the preceding consideration, where Fig. 5.1A additionally shows that an increased converter-side filter resistance reduces the system's degree of passivity at frequencies between $h_m\omega_{\mathrm{r}}$ and ω_{crit}, but yields an increase of the IFP index in the frequency range $[\omega_{\mathrm{crit}}, \omega_{\mathrm{N}}]$.

5.1.2 OFP Index of the Primary-Frequency Input Admittance

Even though the IFP index of the VSC's primary-frequency input admittance completely describes the converter's passivity properties, it is often beneficial to know the system's OFP index as well. Hence, reviewing the definition of the OFP index (2.3) for a linear SISO system from the background chapter, OFP $\{Y_{\mathrm{i,p}}(j\omega)\}$ can be expressed depending on IFP $\{Y_{\mathrm{i,p}}(j\omega)\}$ and is given by

$$\mathrm{OFP}\left\{Y_{\mathrm{i,p}}(j\omega)\right\} = \frac{\mathrm{IFP}\left\{Y_{\mathrm{i,p}}(j\omega)\right\}}{\left|Y_{\mathrm{i,p}}(j\omega)\right|^2} = \frac{\cos(\arg\left\{Y_{\mathrm{i,p}}(j\omega)\right\})}{\left|Y_{\mathrm{i,p}}(j\omega)\right|}. \tag{5.10}$$

As expected, the system's IFP index and OFP index yield the same non-passive region and only differ in their amplitudes. At this point it can already be noticed, that the converter's primary-frequency input admittance shows a large excess of OFP at the selected resonance frequencies $h_i\omega_{\mathrm{r}}$, where $|Y_{\mathrm{i,p}}(j\omega)|$ is almost zero, see Fig. 4.3.

Alternatively, the OFP index of the converter's input admittance can be specified more precisely by performing a loop transformation on $Y_{\mathrm{i,p}}(s)$ which aims to decompose the system into a chain of standard feedback-loops. In particular, taking the system decomposition from (5.3) into account, the converter's primary-frequency input admittance (3.52) can also be written as

$$Y_{\mathrm{i,p}}(s) = \frac{Y_{\mathrm{fc}}(s)}{1 + Y_{\mathrm{fc}}(s)\underbrace{\dfrac{\dfrac{G_{\mathrm{ff}}(s)}{Y_{\mathrm{fc}}^2(s)}}{1 + \dfrac{G_{\mathrm{ff}}(s)}{Y_{\mathrm{fc}}^2(s)}\left[G_{\mathrm{fb}}(s) Y_{\mathrm{fc}}^2(s) - Y_{\mathrm{fc}}(s)\right]}}_{G_{\mathrm{fb2}}(s)}}. \tag{5.11}$$

Then, if the passivity theory on interconnected systems from Sec. 2.1.2 is considered, i.e., that the OFP index of a feedback-loop is determined by the OFP index of the subsystem in the forward path plus the IFP index of the subsystem in the feedback path, the OFP index of (5.11) can be expressed as

$$\begin{aligned}\mathrm{OFP}\left\{Y_{\mathrm{i,p}}(j\omega)\right\} &= \mathrm{OFP}\left\{Y_{\mathrm{fc}}(j\omega)\right\} + \mathrm{IFP}\left\{G_{\mathrm{fb2}}(j\omega)\right\} \\ &= \mathrm{OFP}\left\{Y_{\mathrm{fc}}(j\omega)\right\} + \mathrm{OFP}\left\{G_{\mathrm{ff}}(j\omega)/Y_{\mathrm{fc}}^2(j\omega)\right\}\left|G_{\mathrm{fb2}}(j\omega)\right|^2 \\ &\quad + \left[\mathrm{IFP}\left\{G_{\mathrm{fb}}(j\omega)Y_{\mathrm{fc}}^2(j\omega)\right\} - \mathrm{IFP}\left\{Y_{\mathrm{fc}}(j\omega)\right\}\right]\left|G_{\mathrm{fb2}}(j\omega)\right|^2 .\end{aligned} \tag{5.12}$$

OFP Index of the Inherent Quasi-Analog Input Admittance without Active Filter

Unlike the simplified analysis of $\mathrm{IFP}\left\{Y_{\mathrm{i,p}}(j\omega)\right\}$, where it is supposed that $r_{\mathrm{fc}} \approx 0$, the system's inherent OFP index can accurately be assessed by neglecting all effects of the digital control. Using the continuous-time equivalent systems of (5.4) and (5.5), i.e., $G_{\mathrm{ff}}^c(s) = \Gamma^c(s)Y_{\mathrm{fc}}^2(s)G_{\mathrm{PWM}}(s)/T_{\mathrm{s}}G_{\mathrm{d}}(s)G_{\mathrm{PR}}^c(s)$ and $G_{\mathrm{fb}}^c(s) = 1/(\Gamma^c(s)Y_{\mathrm{fc}}(s))$, and setting $H^c(s) = 0$ (or $\Gamma^c(s) = 1$), (5.12) yields the OFP index of the inherent quasi-analog input admittance $Y_{\mathrm{i}}^c(s)$, which is given by

$$\mathrm{OFP}\left\{Y_{\mathrm{i}}^c(j\omega)\right\} = \mathrm{OFP}\left\{Y_{\mathrm{fc}}(j\omega)\right\} + \mathrm{IFP}\left\{G_{\mathrm{PWM}}(j\omega)/T_{\mathrm{s}}G_{\mathrm{d}}(j\omega)G_{\mathrm{PR}}^c(j\omega)\right\}. \tag{5.13}$$

The resulting OFP index (5.13) is identical to that of our research from [4], where we directly interpreted the converter's quasi-analog input admittance (3.50) as a (standard) feedback interconnection with the subsystems $Y_{\mathrm{fc}}(s)$ and $G_{\mathrm{PWM}}(s)/T_{\mathrm{s}}G_{\mathrm{d}}(s)G_{\mathrm{PR}}^c(s)$ in the forward- and feedback path, respectively. With the definitions of the introduced system components from Sec. 3.2, (5.13) becomes

$$\mathrm{OFP}\left\{Y_{\mathrm{i}}^c(j\omega)\right\} = r_{\mathrm{fc}} + \left|\frac{2\sin(\omega T_{\mathrm{s}}D_0/2)}{\omega T_{\mathrm{s}}D_0}\right|\left|G_{\mathrm{PR}}^c(j\omega)\right|\cos(\omega T_{\mathrm{d}} - \arg\left\{G_{\mathrm{PR}}^c(j\omega)\right\}). \tag{5.14}$$

Focusing on frequencies well above the critical frequency ω_{crit}, it can usually be assumed that the dynamics of the PR controller can accurately be approximated by its proportional path, i.e., $|G_{\mathrm{PR}}^{c}(j\omega)| \approx k_{\mathrm{P}}, \arg\{G_{\mathrm{PR}}^{c}(j\omega)\} \approx 0, \forall\omega \gg \omega_{\mathrm{crit}}$. As in [4], this allows to estimate the minimum value of the system's simplified OFP index (5.14) in a generalized manner, by numerically evaluating the constraint

$$\left.\frac{\partial\,\mathrm{OFP}\left\{Y_{\mathrm{i}}^{c}(j\omega)\right\}}{\partial\,\omega T_{\mathrm{s}}}\right|_{\omega=\omega_{\min}} = 0. \tag{5.15}$$

Particularly, using a single-update PWM with $D_0 = 0.868$ and $T_{\mathrm{c}} = T_{\mathrm{s}}$, (5.15) shows a root at $\omega_{\min} \approx 2.0346/T_{\mathrm{s}}$, where the associated minimal OFP index is given by

$$\mathrm{OFP}\left\{Y_{\mathrm{i}}^{c}(j\omega_{\min})\right\} = \min_{\omega\in[0,\omega_{\mathrm{N}}]} \mathrm{OFP}\left\{Y_{\mathrm{i}}^{c}(j\omega)\right\} \approx r_{\mathrm{fc}} - 0.8715\,k_{\mathrm{P}} = r_{\mathrm{fc}} - 0.8715\,\alpha_{\mathrm{c}} l_{\mathrm{fc}}. \tag{5.16}$$

At this point it should be highlighted that the obtained frequency $\omega_{\min}$ does practically not depend on the converter-side filter parameters l_{fc} and r_{fc} nor on the selected current control specifications and the resulting PR controller parameters, as long as $k_{\mathrm{I},h_m} \ll \alpha_{\mathrm{c}} k_{\mathrm{P}}$. On the other hand, the identified local minimum of $\mathrm{OFP}\left\{Y_{\mathrm{i}}^{c}(j\omega)\right\}$ is exclusively specified by the VSC output filter's resistance r_{fc}, the desired crossover frequency α_{c}, and the filter inductance l_{fc}, which is usually fixed in advance by the maximum tolerable current ripple, see (3.6).

Difference to the OFP Index of the Inherent Primary-Frequency Input Admittance

With the parameters from Tab. 3.1, Tab. 3.2 and Tab. 4.1, Fig. 5.2 exemplarily illustrates the OFP indices of the test-system's primary-frequency input admittance $Y_{\mathrm{i,p}}(s)$ and quasi-analog input admittance $Y_{\mathrm{i}}^{c}(s)$.

As expected, both OFP indices provide a large excess at the specified resonance frequencies, but become negative in the high-frequency range above $\omega_{\mathrm{s}}/6$. Independent of the implemented filter resistance, the lo-

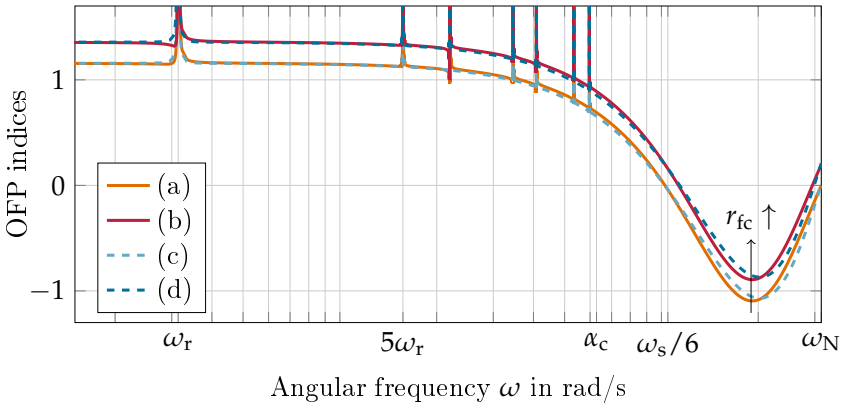

Fig. 5.2: OFP indices of the VSC's primary-frequency input admittance model for (a) $r_{\mathrm{fc}} = 0$ and (b) $r_{\mathrm{fc}} = 0.2$ and (c) and (d) the corresponding OFP indices of the quasi-analog input admittance model, respectively.

cal minima of OFP $\{Y_{\mathrm{i,p}}(j\omega)\}$ arise at lower frequencies than the minima of OFP $\{Y_{\mathrm{i}}^{c}(j\omega)\}$ and, in addition, show (marginally) deeper minimum values. This property also applies to the system's IFP index and was also observed by Harnefors et al. in [53], where the conductance of an experimental converter setup is compared to the theoretical VSC input admittance models from Sec. 3.4. However, since the OFP indices of $Y_{\mathrm{i,p}}(s)$ and $Y_{\mathrm{i}}^{c}(s)$ generally show a very similar behavior, (5.14) can also be used to approximate the OFP index of the converter's inherent primary-frequency input admittance. As can be verified, the differences between the passivity indices of the two models become even less, if the desired crossover frequency α_{c} is reduced, but change more significantly, if the converter-side filter inductance l_{fc} is increased.

5.1.3 Frequency Limits of the Inherent Non-Passive Region

Based on the results of the last sections, the critical frequency range in which the converter's inherent input admittance is non-passive can be made more specific. Observing Fig. 5.2, it can be seen that the OFP indices of $Y_{\mathrm{i,p}}(s)$ and $Y_{\mathrm{i}}^{c}(s)$ cross zero at almost the identical frequencies.

Therefore, given (5.14) and first assuming that $r_{\mathrm{fc}} = 0$ and that the phase lag of the PR controller is negligible for frequencies $\omega \gg h_m\omega_{\mathrm{r}}$, the critical frequency range where OFP $\{Y_{\mathrm{i,p}}(j\omega)\} \leq 0$ can be restricted to $[\omega_{\mathrm{s}}/6, \omega_{\mathrm{N}}]$, as $\cos(\omega T_{\mathrm{d}}) \leq 0$ for $\omega_{\mathrm{s}}/6 \leq \omega \leq \omega_{\mathrm{N}}$. This is also in accordance with the findings and observations from the literature, where the quasi-analog model's passivity is assessed, see [4, 52, 57, 141, 156], or the passivity properties of the primary-frequency model (3.52) are experimentally investigated [53].

However, while e.g., the authors of [110] additionally include the converter-side filter resistance to result in a better estimate, also the current controller's phase lag, $\arg\{G^{*}_{\mathrm{PR}}(j\omega)\} \approx \arg\{G^{c}_{\mathrm{PR}}(j\omega)\}$, might not always be negligible. This is especially the case in applications with multifrequency PR controllers. In particular, if the proposed integral gain adjustment from Sec. 4.2.3 is used for the design, the high-frequency dynamics of $G^{c}_{\mathrm{PR}}(s)$ can roughly be approximated by the controller's proportional path plus the behavior of the specified reference resonator at $h_m\omega_{\mathrm{r}}$. Hence, reviewing the associated simplification from (4.10), it is suggested to approximate the PR controller's phase lag by $\arg\{G^{c}_{\mathrm{PR}}(j\omega)\} \approx -k_{\mathrm{I},h_m}/(\omega k_{\mathrm{P}}), \omega \gg h_m\omega_{\mathrm{r}}$. Then, further considering that $|G^{c}_{\mathrm{PR}}(j\omega)| \approx k_{\mathrm{P}}$ and $|G_{\mathrm{PWM}}(j\omega)| \approx 1$ for frequencies close to $\omega_{\mathrm{s}}/6$, the critical frequency ω_{crit} at which the VSC's inherent input admittance becomes non-passive can approximately be obtained by evaluating the constraint

$$\mathrm{OFP}\left\{Y_{\mathrm{i}}^{c}(j\omega_{\mathrm{crit}})\right\} \approx r_{\mathrm{fc}} + k_{\mathrm{P}}\cos\left(\omega_{\mathrm{crit}}T_{\mathrm{d}} + \frac{k_{\mathrm{I},h_m}}{\omega_{\mathrm{crit}}k_{\mathrm{P}}}\right) = 0. \tag{5.17}$$

After rearranging (5.17) and solving the resulting quadratic equation for ω_{crit}, a more accurate estimate for the critical frequency is given by

$$\begin{aligned}\omega_{\mathrm{crit}} &\approx \frac{\arccos(-r_{\mathrm{fc}}/k_{\mathrm{P}})}{2T_{\mathrm{d}}} + \sqrt{\left(\frac{\arccos(-r_{\mathrm{fc}}/k_{\mathrm{P}})}{2T_{\mathrm{d}}}\right)^{2} - \frac{k_{\mathrm{I},h_m}}{k_{\mathrm{P}}T_{\mathrm{d}}}} \\ &\approx \frac{\omega_{\mathrm{s}}}{12} + \frac{1}{6\pi}\frac{r_{\mathrm{fc}}}{l_{\mathrm{fc}}}\frac{\omega_{\mathrm{s}}}{\alpha_{\mathrm{c}}} + \sqrt{\left(\frac{\omega_{\mathrm{s}}}{12} + \frac{1}{6\pi}\frac{r_{\mathrm{fc}}}{l_{\mathrm{fc}}}\frac{\omega_{\mathrm{s}}}{\alpha_{\mathrm{c}}}\right)^{2} - \frac{\omega_{\mathrm{s}}\,\alpha_{\mathrm{I},h_m}}{3\pi}}\end{aligned} \tag{5.18}$$

where the parameterization guidelines from (4.7) and (4.11) are considered and it is assumed that $\arccos(x) \approx \pi/2 - x$ for small values of $x = -r_{\mathrm{fc}}/k_{\mathrm{P}}$. Following the same line of reasoning, where $|G_{\mathrm{PWM}}(j\omega)| \approx 0.718$ for frequencies close to ω_{N}, the frequency $\omega_{\mathrm{crit},2}$ at which the converter's inherent input admittance becomes passive again can be approximated by

$$\omega_{\mathrm{crit},2} \approx \frac{\omega_{\mathrm{s}}}{4} - \frac{1}{4.308\pi}\frac{r_{\mathrm{fc}}}{l_{\mathrm{fc}}}\frac{\omega_{\mathrm{s}}}{\alpha_{\mathrm{c}}} + \sqrt{\left(\frac{\omega_{\mathrm{s}}}{4} - \frac{1}{4.308\pi}\frac{r_{\mathrm{fc}}}{l_{\mathrm{fc}}}\frac{\omega_{\mathrm{s}}}{\alpha_{\mathrm{c}}}\right)^2 - \frac{\omega_{\mathrm{s}}\,\alpha_{\mathrm{I},h_m}}{3\pi}}. \quad (5.19)$$

With the proposed current controller design and the definition of α_{I,h_m} from (4.11), the critical frequency range between ω_{crit} and $\omega_{\mathrm{crit},2}$ depends (more or less) only on the chosen gain crossover frequency α_{c}, the desired gain margin g_{m}, and the converter-side filter parameters r_{fc} and l_{fc}. The latter parameters, r_{fc} and l_{fc}, often have a rather negligible effect in (5.18) and (5.19), since usually $r_{\mathrm{fc}}/l_{\mathrm{fc}} \ll \alpha_{\mathrm{c}}$. On the other hand, the choice of α_{c} and g_{m} determines the non-passive region more importantly. By increasing α_{c} or g_{m}, the value of α_{I,h_m} is reduced and the zero crossings ω_{crit} and $\omega_{\mathrm{crit},2}$ approach the well known limits $\omega_{\mathrm{s}}/6$ and ω_{N}, respectively. At this point it should however be emphasized that in case of $r_{\mathrm{fc}} = 0$, the critical frequency ω_{crit} is always less (or equal) to $\omega_{\mathrm{s}}/6$. In fact, it can be noticed that the calculation of ω_{crit} is identical to the calculation of the phase crossover frequency $\omega_{\pi} \leq \omega_{\mathrm{s}}/6$ at which the phase response of the quasi-continuous open-loop system $G_{\mathrm{o}}^{qc}(s)$ crosses $-180°$, see (4.3).

For the converter test-system with the parameters from Tab. 3.1, Tab. 3.2 and Tab. 4.1, where $\alpha_{\mathrm{I},19} = 335.36\,\frac{\mathrm{rad}}{\mathrm{s}}$, Tab. 5.1 on the next page compares the emerging non-passive regions of OFP $\{Y_{\mathrm{i,p}}(j\omega)\}$ for increasing filter resistances. As can be verified, the estimates from (5.18) and (5.19) represent a good approximation of the exact frequencies at which OFP $\{Y_{\mathrm{i,p}}(j\omega)\} = 0$, as long as $r_{\mathrm{fc}} \ll 1$ (or $r_{\mathrm{fc}}/l_{\mathrm{fc}} \ll \alpha_{\mathrm{c}}$). But, if r_{fc} increases, the absolute error tends to increase as well. While $G_{\mathrm{PR}}^{c}(j\omega) \approx k_{\mathrm{P}}e^{-jk_{\mathrm{I},h_m}/(\omega k_{\mathrm{P}})}$ generally represents an accurate approximation of the PR controller's dynamics in the high-frequency range above $h_m\omega_{\mathrm{r}}$, the increasing errors can mainly be justified by the fact that the zero cross-

Table 5.1: Frequency limits of the inherent non-passive regions of the exemplary converter's primary-frequency input admittance for different converter-side filter resistances

Resistance	Exact frequency	Estimate	Absolute error
$r_{\mathrm{fc}} = 0$	$\omega_{\mathrm{crit}} \approx 10256\,\mathrm{rad/s}$	$\omega_{\mathrm{crit}} \approx 10254\,\mathrm{rad/s}$	$2\,\mathrm{rad/s}$
	$\omega_{\mathrm{crit},2} \approx 31415\,\mathrm{rad/s}$	$\omega_{\mathrm{crit},2} \approx 31345\,\mathrm{rad/s}$	$70\,\mathrm{rad/s}$
$r_{\mathrm{fc}} = 0.013$	$\omega_{\mathrm{crit}} \approx 10324\,\mathrm{rad/s}$	$\omega_{\mathrm{crit}} \approx 10326\,\mathrm{rad/s}$	$2\,\mathrm{rad/s}$
	$\omega_{\mathrm{crit},2} \approx 31283\,\mathrm{rad/s}$	$\omega_{\mathrm{crit},2} \approx 31246\,\mathrm{rad/s}$	$37\,\mathrm{rad/s}$
$r_{\mathrm{fc}} = 0.2$	$\omega_{\mathrm{crit}} \approx 11296\,\mathrm{rad/s}$	$\omega_{\mathrm{crit}} \approx 11364\,\mathrm{rad/s}$	$-68\,\mathrm{rad/s}$
	$\omega_{\mathrm{crit},2} \approx 29476\,\mathrm{rad/s}$	$\omega_{\mathrm{crit},2} \approx 29824\,\mathrm{rad/s}$	$-348\,\mathrm{rad/s}$

ings are shifted so far that the adopted approximations of $|G_{\mathrm{PWM}}(j\omega)|$ at $\omega_{\mathrm{s}}/6$ and ω_{N} are no longer valid, see also Fig. 3.7.

5.2 Passivation by Passive Damping Methods

Similar to the shaping of the quasi-analog input admittance $Y_{\mathrm{i}}^{\mathrm{c}}(s)$, the problem of rendering the primary-frequency input admittance $Y_{\mathrm{i,p}}(s)$ passive can be understood as a problem of introducing sufficiently large damping to the converter system [4, 110, 139]. In the simplest case, this can be achieved by adding enough dissipative components, such as passive resistors to the VSC output filter circuit [53]. But, although many passive damping methods have been developed and thoroughly investigated over the years, see [17, 49, 153] for an overview, the passivity-based analysis differs from most of the approaches followed in the literature. In contrast to conventional passive damper designs, which often apply the Nyquist stability criterion and concentrate only on the shaping of the VSC output filter resonance, see e.g., [13, 85, 87, 100, 109, 138, 152], the usage of passivity theory allows to deduce more general statements on the damping properties of different methods, even if the grid impedance is not exactly known. After analyzing the more theoretical example of a passivation, using an increased converter-side filter resistance, Sec. 5.2.2 reviews the damping effects of the advanced LCL filter topologies from Fig. 3.2B and Fig. 3.2C.

5.2.1 Adaption of the Converter-Side Filter Resistance

As was seen in the previous section, increasing values of the converter-side filter resistance r_{fc} lead to a reduction of the converter's non-passive region, and thus, can be used to render $Y_{\mathrm{i,p}}(s)$ passive. In this context, we derived a necessary passivation criterion for the VSC's quasi-analog model in [4], where the authors of [53] used this straightforward damping method to demonstrate the passivation of a digitally current-controlled converter as well. Hence, taking the findings from Sec. 5.1.2 into account, it can be assumed that (existing) passivation guidelines for the converter's quasi-analog model $Y_{\mathrm{i}}^{c}(s)$ can also be used for the passivation of the converter's primary-frequency input admittance and only marginally more damping is required to compensate for the deeper local minimum of OFP $\{Y_{\mathrm{i,p}}(j\omega)\}$. In particular, given (5.16) it directly follows that OFP $\{Y_{\mathrm{i}}^{c}(j\omega)\} \geq 0, \forall\omega > \omega_{\mathrm{crit}}$, and thus, also IFP $\{Y_{\mathrm{i}}^{c}(j\omega)\} \geq 0, \forall\omega > \omega_{\mathrm{crit}}$ if

$$r_{\mathrm{fc}} \geq 0.8715\,\alpha_{\mathrm{c}} l_{\mathrm{fc}} \qquad \text{or} \qquad r_{\mathrm{fc}}/l_{\mathrm{fc}} \geq 0.8715\,\alpha_{\mathrm{c}}. \tag{5.20}$$

As can exemplarily be verified by the application on the introduced test-system with parameters from Tab. 3.2 and Tab. 4.1, the choice of $\alpha_{\mathrm{c}} = \omega_{\mathrm{s}}/10 = 6283.2\,\frac{\mathrm{rad}}{\mathrm{s}}$ and $l_{\mathrm{fc}} = 0.195\,\mathrm{ms}$ (theoretically) requires a normalized filter resistance of at least 1.067 to remove the quasi-analog model's shortage of passivity in the high-frequency range. From Fig. 5.3 it can be seen that a further increase of r_{fc} by about 2% also renders the primary-frequency input admittance $Y_{\mathrm{i,p}}(s)$ passive for all frequencies between ω_{crit} and ω_{N}. But, since the output filter's bandwidth, $r_{\mathrm{fc}}/l_{\mathrm{fc}} \approx 0.89\,\alpha_{\mathrm{c}} \approx 5593.9\,\frac{\mathrm{rad}}{\mathrm{s}}$, is no longer well separated from α_{c}, such a dimensioning also requires to increase the PR controller's cut-off frequencies ω_{c,h_i} and to introduce additional damping at the specified resonance frequencies $h_i\omega_{\mathrm{r}}$, see the detailed section in Fig. 5.3B.

However, reviewing the definition of the normalized converter-side filter resistance from (3.4), i.e., $r_{\mathrm{fc}} = 3R_{\mathrm{fc}}I_{\mathrm{b}}^2/S_{\mathrm{b}}$, it can be noticed that this damping approach would result in massive power losses. In the above example, (over) 100% of the rated converter power would be lost at nom-

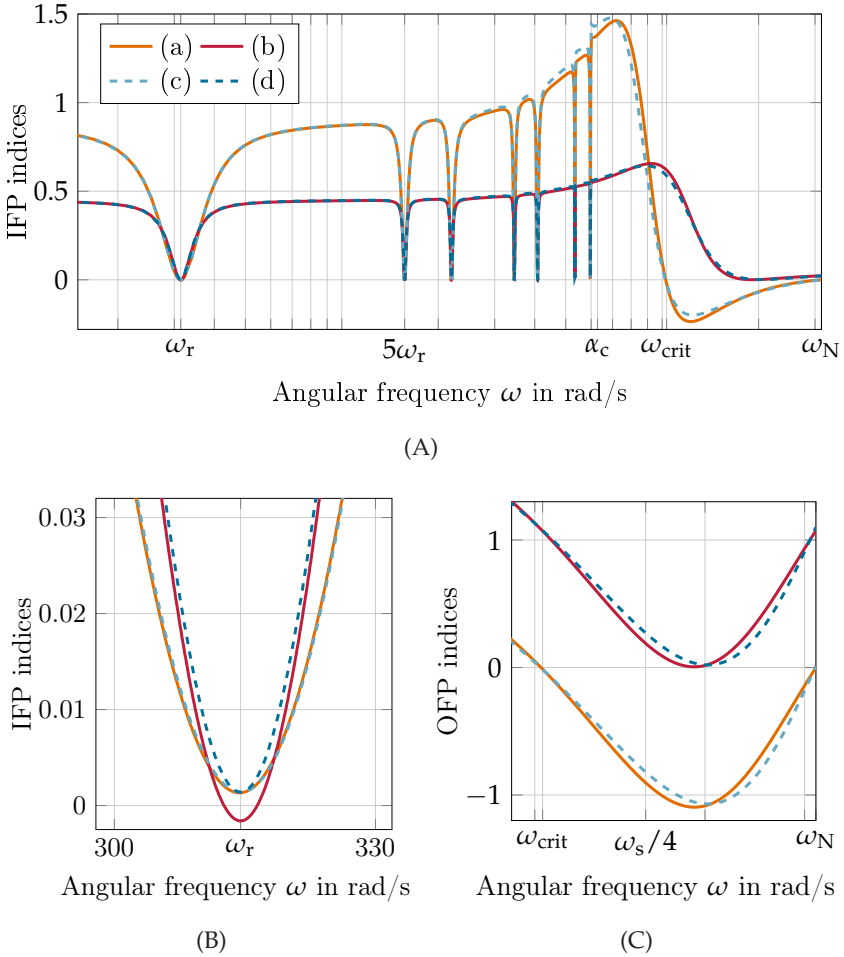

Fig. 5.3: Passivity indices of the VSC's (a), (b) primary-frequency input admittance and (c), (d) quasi-analog input admittance with (a), (c) $r_{fc} = 0$ and (b), (d) $r_{fc} = 1.09$. Subfigure (A) shows the IFP index of the converter's admittance in the complete frequency range of interest, (B) shows a detailed section of the system's IFP index near ω_r, and (C) illustrates the system's OFP index in the high-frequency range.

inal operation. Therefore, as also argued in [4, 49, 53], this solution is certainly not reasonable and would mostly not be applicable in practice even for lower inductances l_{fc} or gain crossover frequencies α_{c}.

5.2.2 Damping by Advanced LCL Filter Topologies

As already motivated in Sec. 3.2.1, there exist more efficient methods to introduce damping to the converter system only in frequency ranges, where it is needed, e.g., by implementing an LCL filter with a series resistance or a resistive-inductive circuit in the capacitive branch [13, 17, 100, 138]. If such a filter structure is to be used, the passivity theory on interconnected systems can also be applied to the converter's closed-loop system. Given the control block diagram of a digitally current-controlled grid-connected VSC from Fig. 3.13, with $G_{\mathrm{H}}(s) = 0$, it can be seen that the grid-converter system is passive, if

$$\mathrm{OFP}\left\{\frac{Y_{\mathrm{i,p}}(j\omega)}{1+Y_{\mathrm{i,p}}(j\omega)\tilde{Z}_{\mathrm{g}}(j\omega)}\right\} = \mathrm{OFP}\left\{Y_{\mathrm{i,p}}(j\omega)\right\} + \mathrm{IFP}\left\{\tilde{Z}_{\mathrm{g}}(j\omega)\right\} \geq 0, \forall\omega. \tag{5.21}$$

This implies that the identified VSC's shortage of OFP can be compensated by an excess of IFP from the synthetic grid impedance $\tilde{Z}_{\mathrm{g}}(s) = Z_{\mathrm{c}}(s)/(1 + Z_{\mathrm{c}}(s)\tilde{Y}_{\mathrm{fg}}(s))$. If the worst-case scenario is considered, where the grid-side inductance $Y_{\mathrm{fg}}(s)$ as well as the grid impedance $Z_{\mathrm{g}}(s)$ are passive, but do not have any dissipative components, it follows that $\mathrm{OFP}\left\{\tilde{Y}_{\mathrm{fg}}(j\omega)\right\} = \mathrm{IFP}\left\{\tilde{Y}_{\mathrm{fg}}(j\omega)\right\} = 0, \forall\omega$. Then, using (A.4) from the Appendix, the IFP index of $\tilde{Z}_{\mathrm{g}}(s)$ can be derived to be

$$\mathrm{IFP}\left\{\tilde{Z}_{\mathrm{g}}(j\omega)\right\} \geq \frac{\mathrm{IFP}\left\{Z_{\mathrm{c}}(j\omega)\right\}\mathrm{Im}^2\left\{\tilde{Y}_{\mathrm{fg}}^{-1}(j\omega)\right\}}{\mathrm{IFP}^2\left\{Z_{\mathrm{c}}(j\omega)\right\} + \left[\mathrm{Im}\left\{Z_{\mathrm{c}}(j\omega)\right\} + \mathrm{Im}\left\{\tilde{Y}_{\mathrm{fg}}^{-1}(j\omega)\right\}\right]^2}. \tag{5.22}$$

With the help of prior knowledge about the power grid, (5.22) allows to assess the damping properties of different LCL filter topologies. For in-

stance, considering the topology from Fig. 3.2B and implementing a series resistance for damping in the capacitive branch, (5.22) becomes

$$\mathrm{IFP}\left\{\tilde{Z}_\mathrm{g}(j\omega)\right\} \geq \frac{r_\mathrm{d}\left(\omega l_\mathrm{fg} + \mathrm{Im}\left\{Z_\mathrm{g}(j\omega)\right\}\right)^2}{r_\mathrm{d}^2 + \left(\omega l_\mathrm{fg} - \frac{1}{\omega c_\mathrm{c}} + \mathrm{Im}\left\{Z_\mathrm{g}(j\omega)\right\}\right)^2}. \tag{5.23}$$

Equivalently to $\tilde{Z}_\mathrm{g}(s)$, (5.23) shows a resonance at $\omega_{\mathrm{r},\tilde{\mathrm{Z}}_\mathrm{g}} \approx 1/\sqrt{l_\mathrm{fg} c_\mathrm{c}}$ for $Z_\mathrm{g}(s) = 0$, whereas $\mathrm{IFP}\left\{\tilde{Z}_\mathrm{g}(j\omega)\right\}$ approaches zero for $\omega \to 0$ and r_d for $\omega \to \infty$. Fig. 5.4 shows the corresponding IFP indices of the exemplarily designed LCL filter from Sec. 3.2.1 for varying parameters.

As can be seen, the damping effect of the damping method from Fig. 3.2B is limited to a rather narrow frequency range around the resulting resonance frequency $\omega_{\mathrm{r},\tilde{\mathrm{Z}}_\mathrm{g}}$. This coincides with the observations of the passivity-based damper design from [139] and cannot be changed significantly by a variation of the associated LCL filter parameters or by the usage of other (advanced) filter topologies like that from Fig. 3.2C, see Fig. 5.5. On the contrary, the effective damping is even more concentrated on the frequency range around $\omega_{\mathrm{r},\tilde{\mathrm{Z}}_\mathrm{g}} \approx 1/\sqrt{l_\mathrm{fg}(c_\mathrm{d} + c_\mathrm{p})}$ if a resistive-inductive damper circuit is implemented. As can be verified, the corresponding IFP index of $\tilde{Z}_\mathrm{g}(s)$ approaches zero for $\omega \to 0$ as well as for $\omega \to \infty$, which in turn saves power losses.

Hence, if a passive damping strategy is to be implemented, it can be concluded that it is advantageous to aim for a selection of C_c (or C_p plus C_d) and L_fg (plus L_g), which satisfies $10\,\omega_\mathrm{r} < \omega_\mathrm{crit} \leq \omega_{\mathrm{r},\tilde{\mathrm{Z}}_\mathrm{g}} < \omega_\mathrm{N}$ during the LCL filter design process. In doing so, the excess of $\mathrm{IFP}\left\{\tilde{Z}_\mathrm{g}(j\omega)\right\}$ can be used most effectively to compensate for the shortage of $\mathrm{OFP}\left\{Y_{\mathrm{i,p}}(j\omega)\right\}$ in the high-frequency range. This (general) design recommendation for the resonance frequency of the synthetic grid impedance $\tilde{Z}_\mathrm{g}(s)$ can be understood as a concretization of the well known and established guidelines for the selection of the LCL filter's resonance frequency $\omega_{\mathrm{r,LCL}}$ summarized in Sec. 3.2.1 [13, 16, 84]. Nevertheless it should be highlighted that the effective damping also depends strongly on the choice of the dissipative

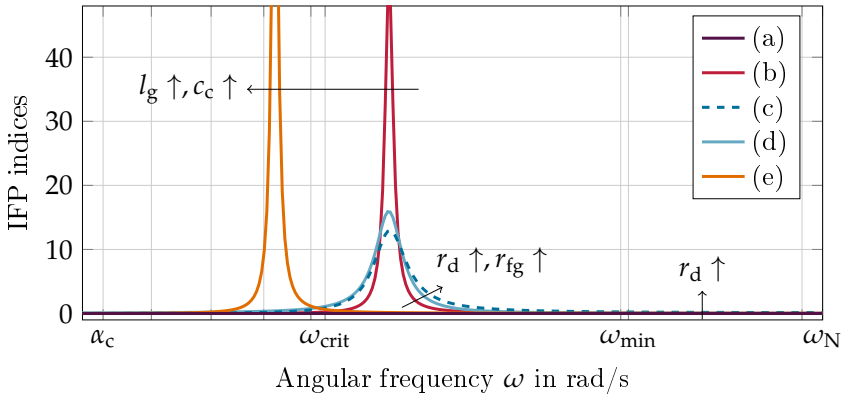

Fig. 5.4: Detailed IFP indices of the synthetic grid impedance $\tilde{Z}_g(s)$, where (a), (b), (c), (d) $Z_g(s) = 0$, and (e) $Z_g(s) = l_g s$, $l_g = 64.95\,\mu$s. The implemented LCL filter uses (a) no damper, (b), (d), (e) a series damping resistance of $r_d = 0.026$, (c) a four times higher damping resistance of $r_d = 0.104$, and (d) an increased grid-side resistance of $r_{fg} = 0.056$, respectively.

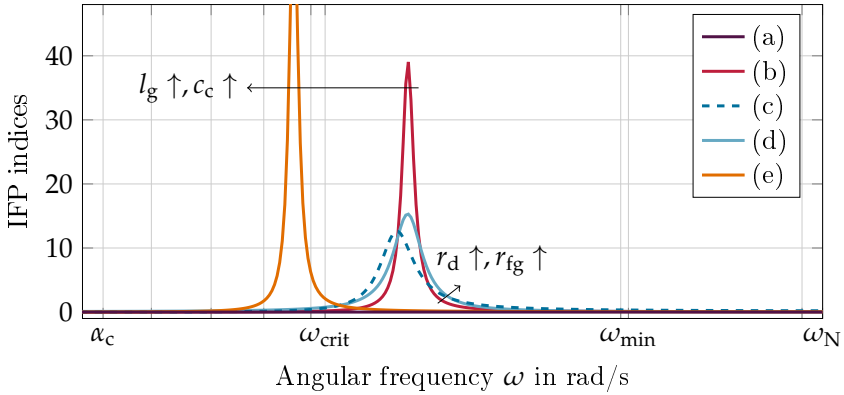

Fig. 5.5: Detailed IFP indices of the synthetic grid impedance $\tilde{Z}_g(s)$, where (a), (b), (c), (d) $Z_g(s) = 0$, and (e) $Z_g(s) = l_g s$, $l_g = 64.95\,\mu$s. The implemented LCL filter uses (a) no damper (b), (d), (e) the resistive-inductive damping circuit from Fig. 3.2C with $r_d = 0.065$, (c) an increased damping resistance of $r_d = 0.26$, and (d) an increased grid-side resistance of $r_{fg} = 0.056$, respectively.

filter components, which typically still requires an empirical parameterization that involves many time-consuming tests.

Passivity and Stability of the Closed-Loop Grid-Converter System

As already discussed in Sec. 4.3, the interconnection of the studied (digitally) current-controlled VSC with the power network inherently results in an unstable closed-loop system, if no active or passive damping strategy is applied. However, as shown by (5.21), the passivity properties of the synthetic grid impedance $\tilde{Z}_{\mathrm{g}}(s)$ can be used to render the converter's input admittance passive, and thus, prevent a power system destabilization. For instance, setting $Z_{\mathrm{g}}(s) = 0$ and considering the introduced (advanced) LCL filter topologies with the parameters of Tab. 3.2, Fig. 5.6 shows the passivity indices of the resulting closed-loop grid-converter systems. Given the synthetic grid impedance (3.13), it can be verified that $\tilde{Z}_{\mathrm{g}}(s)$ always adds damping to the converter system near the resonance frequency $\omega_{\mathrm{r},\tilde{\mathrm{Z}}_{\mathrm{g}}}$, as long as $Z_{\mathrm{c}}(s)$, $Z_{\mathrm{fg}}(s)$, or $Z_{\mathrm{g}}(s)$ have some dissipative component. But, as argued above and exemplarily shown in Fig. 5.6, the introduced damping is often not sufficient to render the interconnected system passive (or to stabilize the closed-loop system). This becomes particularly clear when using the advanced LCL filter topology from Fig. 3.2C. On the contrary, it can be seen that a sufficiently large series resistance in the capacitive branch of the LCL filter allows for a passivation of the VSC's primary-frequency input admittance model. In addition, following the observations from the previous section and shifting the resonance frequency $\omega_{\mathrm{r},\tilde{\mathrm{Z}}_{\mathrm{g}}}$ to higher frequencies by reducing the filter's capacitance from originally $C_{\mathrm{c}} = 4.7\,\mu\mathrm{F}$ to $C_{\mathrm{c}} = 2.7\,\mu\mathrm{F}$, the shortage of OFP $\{Y_{\mathrm{i,p}}(j\omega)\}$ can already be compensated by half of the damping resistance, where, as a drawback, a reduction of the attenuation capabilities of $G_{\mathrm{LCL}}(s)$ in the high-frequency range must be tolerated.

Besides the inherent power losses, the main disadvantage of a converter passivation (or stabilization) by means of damped LCL filters is its sensitivity to specific grid parameters. In particular, as illustrated in Fig. 5.4 and Fig. 5.5, the damping effect of $\tilde{Z}_{\mathrm{g}}(s)$ in the critical frequency range be-

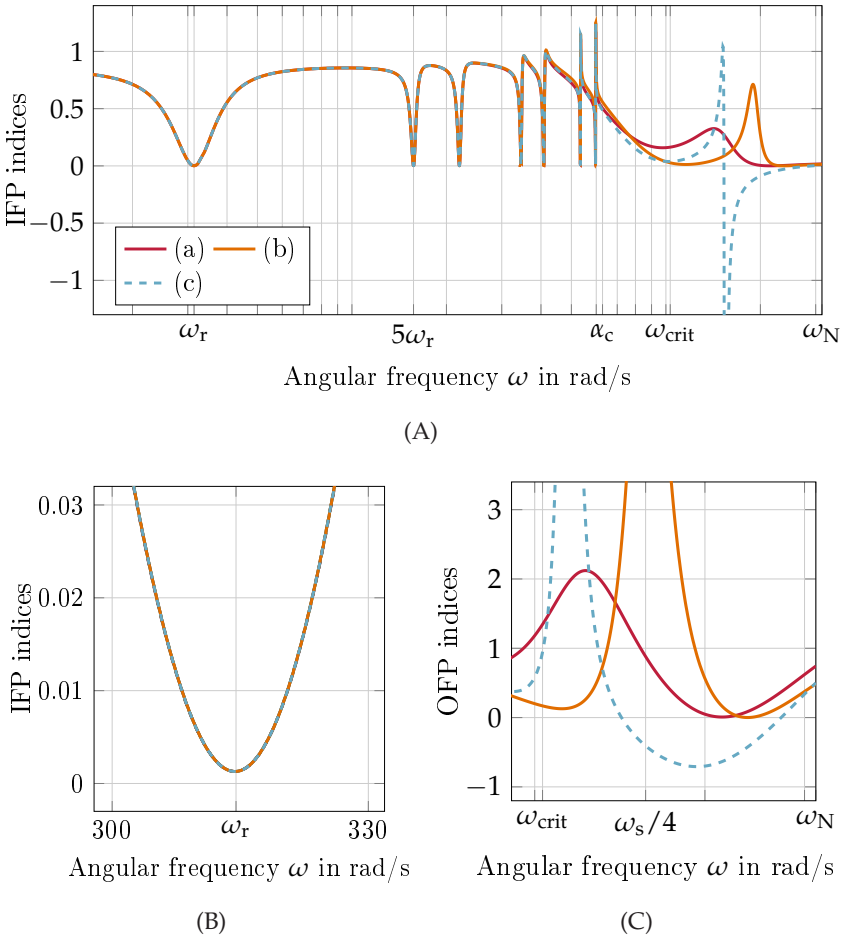

Fig. 5.6: Passivity indices of the closed-loop grid-converter system with $Z_g(s) = 0$, where the VSC is equipped with (a) an LCL filter which uses a huge series damping resistance of $r_d = 0.56$, (b) an optimized LCL filter with $c_c = 41.57\,\mu s$ and series damping resistance $r_d = 0.27$, and (c) an LCL filter which implements the resistive-inductive circuit from Fig. 3.2C with $r_d = 0.26$. Subfigure (A) shows the IFP index of the grid-converter system in the complete frequency range of interest, (B) shows a detailed section of the system's IFP index near ω_r, and (C) illustrates the system's OFP index in the high-frequency range.

tween ω_{crit} and ω_{N} highly depends on the effective (low-frequency) grid inductance l_{g}, which, in practice, continuously varies due to permanent grid changes. Therefore, it is generally not possible to ensure that the converter's input admittance always remains passive with a pre-optimized LCL filter. This also has a direct impact on the stability, see the exemplary Nyquist plots of the open-loop system $Y_{\mathrm{i,p}}(s)\tilde{Z}_{\mathrm{g}}(s)$ in Fig. 5.7. As can be verified, a simple increase of l_{g} already leads to a significant decrease of the stability measure, e.g., specified by the system's phase margin or the inverse of the minimum distance between the Nyquist curve and the point $(-1 + j0)$ [10, 119]. As a result, the converter can either not be operated safely on the grid from the beginning or there is room for unmodeled effects or other disturbances to destabilize the closed-loop system. Accordingly, the situation becomes more critical if the grid shows additional resonances, see Fig. 5.7D. Hence, since a stable operation of the grid-connected converter can only hardly be guaranteed by design, a complete passivation by means of passive damping methods is generally not recommended and should at most be used to support some active damping method, see also the conclusion of [53].

5.3 Passivation by Active Damping Methods

In order to avoid high power losses and simultaneously become (more) independent of certain power grid parameters, active filters can be implemented to damp resonances as well. Regarding the damping of the LCL filter's resonance peak, additional active filters in the forward path of the current control loop, i.e., filters in series or parallel to the PR current controller, represent a suitable solution. Here, lead-lag filters [141], notch filters [35, 86, 111], low-pass filters [35], or all-pass filters [113] are used particularly often in the current research. But, even though these methods have the advantage that no additional sensors must be installed, their robustness against parameter variations or uncertainties is subjected to the exact knowledge of all filter (and grid) components [49, 111]. Moreover, similar to related passive damping methods, active filters in the forward path of the current control loop generally focus only on the damping of

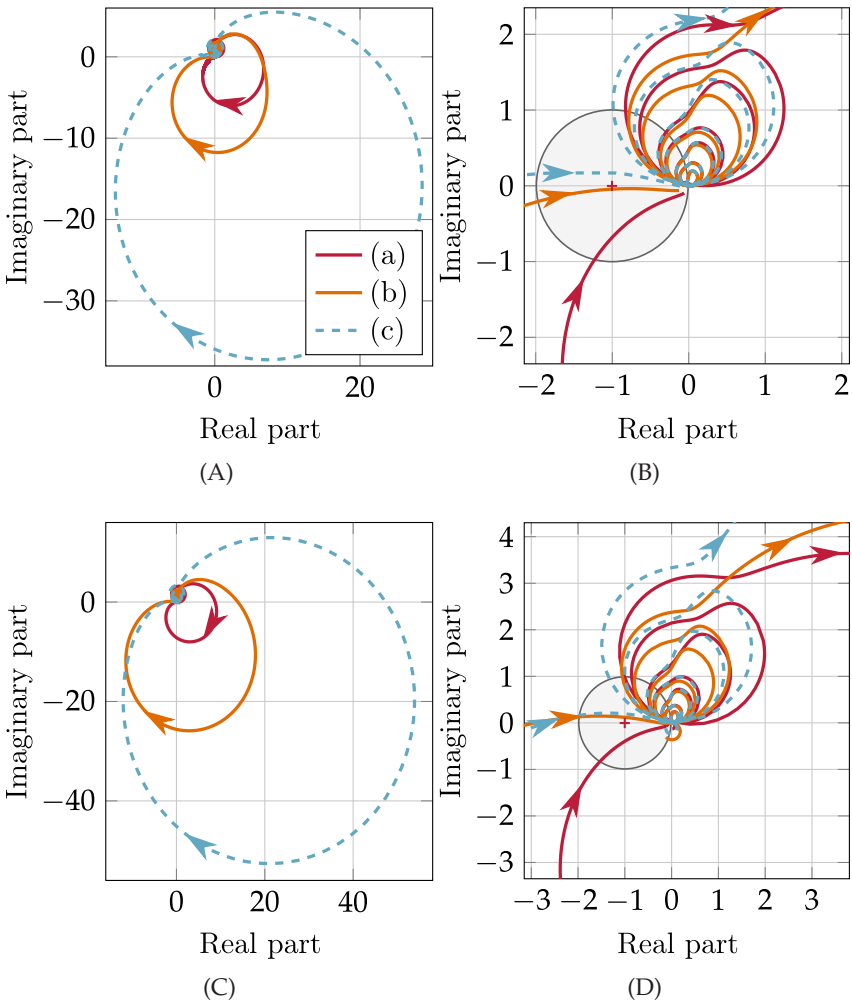

Fig. 5.7: Nyquist plots of the open-loop grid-converter system, where the converter under study is equipped with (a) an LCL filter which uses a series damping resistance of $r_\mathrm{d} = 0.56$, (b) an optimized LCL filter with $c_\mathrm{c} = 41.57\,\mu\mathrm{s}$ and series damping resistance $r_\mathrm{d} = 0.27$, and (c) an LCL filter which implements the resistive-inductive circuit from Fig. 3.2C with $r_\mathrm{d} = 0.26$. Subfigures (A), (C) and subfigures (B), (D) show the complete and detailed plots for $\omega \in [0, \omega_\mathrm{N}]$, respectively, where the VSC is connected (A), (B) to an inductive grid with $Z_\mathrm{g}(s) = l_\mathrm{g} s$, $l_\mathrm{g} = 64.95\,\mu\mathrm{s}$, and (C), (D) to a resistive-inductive grid, where $\tilde{Z}_\mathrm{g}(s)$ has a below Nyquist frequency resonance at $\omega_{\mathrm{r},\tilde{Z}_\mathrm{g},2} \approx 29128\,\frac{\mathrm{rad}}{\mathrm{s}} > \omega_\mathrm{crit}$.

the VSC's output filter resonance and overlook the need to damp other possibly emerging grid resonances.

On the contrary, the feed-forward of the synthetic PCC voltage [21, 30, 41, 42, 56, 60, 85, 110, 111, 156, 157] or the LCL filter's capacitor current [4, 8, 57, 87, 96, 97, 142, 156] can also be utilized to increase the damping of the grid-converter system over a wider range of frequencies and provide more robustness. Fig. 3.1 shows the corresponding control structure with the optional feed-forward of $\boldsymbol{E}^*$ or $\boldsymbol{I}_c^*$, respectively. Since the control effectively emulates a virtual impedance in parallel to the LCL filter's capacitive branch, those damping methods are also sometimes referred to as virtual impedance-based control or damping methods in the literature [87, 142, 145]. Particularly Harnefors et al. have recognized the beneficial properties of both feed-forward alternatives and continuously advanced the use of active filters for the passivation of the converter's quasi-analog input admittance, see e.g., [52, 56, 57, 60]. In recent years, other authors followed this idea and published related passivity-based design approaches as well [4, 8, 156], where meanwhile also some initial works for the passivation of VSC admittance models in the z-domain exist [41, 42, 110, 111]. Due to the high popularity and the clear advantages compared to other damping strategies, see [49, 153], the active feed-forward of either the synthetic PCC voltage or the capacitor current are also favored in this thesis and are discussed in more detail next.

5.3.1 Simplified Filter Design Criterion

As shown in our previous work [4], the OFP index of the converter's quasi-analog model can readily be used for the design of active filters that render the associated VSC input admittance passive. Given the general description of OFP $\{Y_{\mathrm{i,p}}(j\omega)\}$ from (5.12), the suggested approach may also be applied to the converter's primary-frequency input admittance in a similar form. A disadvantage in this case, however, is that the design must be performed in the complex plane, which is not very common and requires some experience. Alternatively, a different method is proposed in this thesis.

As already explained in Sec. 5.1.1 and determined by condition (5.2), the primary-frequency input admittance $Y_{\mathrm{i,p}}(s)$ can be rendered passive by either implementing a large dissipative component in $Y_{\mathrm{fc}}(s)$, or by modifying the phase response of the admittance's active part, $-\Gamma(s)Y_{\mathrm{cl,p}}(s)$. If for now it is assumed that the converter-side filter admittance $Y_{\mathrm{fc}}(s)$ shows a negligible resistance, $r_{\mathrm{fc}} \approx 0$, condition (5.2) requires that

$$-180^\circ \leq \arg\{\Gamma(j\omega)\} + \arg\{G_{\mathrm{cl}}(j\omega)/T_{\mathrm{s}}\} \leq 0^\circ, \quad \forall\omega \in [0, \omega_{\mathrm{N}}]. \tag{5.24}$$

As can mathematically be verified and is also visible in Fig. 4.2, the phase response of the converter's closed-loop system $G_{\mathrm{cl}}(s)/T_{\mathrm{s}}$ is monotonically falling for frequencies above the highest resonance frequency $h_m\omega_{\mathrm{r}}$, where $\arg\{G_{\mathrm{cl}}(j\omega_{\mathrm{crit}})/T_{\mathrm{s}}\} = -180^\circ$ and $\arg\{G_{\mathrm{cl}}(j\omega_{\mathrm{N}})/T_{\mathrm{s}}\} \approx -360^\circ$, as $G^*_{\mathrm{PR}}(j\omega_{\mathrm{N}}) \approx k_{\mathrm{P}}$. Therefore, in order to satisfy (5.24), it can be concluded that $\Gamma(s)$ must introduce a sufficiently large phase lead between the critical frequency ω_{crit} from (5.18) and the Nyquist frequency ω_{N}, at which $\arg\{\Gamma(j\omega_{\mathrm{N}})\}$ should show a phase lead of at least 180°. Moreover, since the PR controller's high integral gains enforce that $\arg\{G_{\mathrm{cl}}(jh_i\omega_{\mathrm{r}})/T_{\mathrm{s}}\} \approx 0^\circ$, $\forall h_i \in h$, it must also be ensured that $\Gamma(s)$ does not increase the phase response of $G_{\mathrm{cl}}(s)/T_{\mathrm{s}}$ at frequencies close to each $h_i\omega_{\mathrm{r}}$ too much. Keeping those conditions on $\Gamma(s)$ in mind, the active feed-forward filter design can be carried out in a simplified manner, using classical frequency response methods as described in e.g., [10, 119].

5.3.2 Synthetic PCC Voltage Feed-Forward

If the (sampled) synthetic PCC voltage $\boldsymbol{e}^*$ is to be used as the feed-forward quantity, $\Gamma(s)$ is defined by (3.52), that is

$$\Gamma(s) = 1 + \frac{1}{Y_{\mathrm{fc}}(s)} \frac{H^*(s)}{G^*_{\mathrm{PR}}(s)}. \tag{5.25}$$

Given (5.25) and the passivity condition (5.24), a general structure of the active feed-forward filter $H(z)$ can be deduced by requiring that $\Gamma(s)$ shows the behavior of some reasonable reference (model) filter, $F(s)$, that fulfills the found requirements. Since (5.25) consists of both, continuous-

time and impulse-sampled (discrete-time) systems, it is proposed to first neglect all periodic parts of $G^{*}_{\mathrm{PR}}(s)$ and $H^{*}(s)$ and consider the design problem to be quasi-continuous. As commonly practiced in control engineering, this approach allows to construct a digital filter indirectly from a continuous filter design, which is followed by a z-domain transformation by means of typical approximations [9,39,119].

Design of the Continuous-Time Equivalent Filter $H^{c}(s)$

If it is assumed that the VSC's control operates quasi-analog, the continuous equivalent filter $H^{c}(s)$ can be calculated by setting $F(s) \stackrel{!}{=} \Gamma^{c}(s) = 1 + H^{c}(s)/(Y_{\mathrm{fc}}(s)G^{c}_{\mathrm{PR}}(s))$, which results in the selection guideline

$$H^{c}(s) = Y_{\mathrm{fc}}(s)G^{c}_{\mathrm{PR}}(s)(F(s)-1) \approx k_{\mathrm{P}}\,\frac{F(s)-1}{l_{\mathrm{fc}}s}. \tag{5.26}$$

Taking the considerations from the previous section into account and requiring that $\Gamma^{c}(s)$ shows a (sudden) phase change from 0° to 180° at the frequency ω_{crit} at which the VSC's inherent input admittance becomes non-passive, the reference model $F(s)$ can, for example, be specified as the inverse of a standard second-order lag element [10,119], i.e.,

$$F(s) = \frac{s^2 + 2\delta\omega_{\mathrm{crit}}s + \omega^2_{\mathrm{crit}}}{\omega^2_{\mathrm{crit}}} = \frac{1}{\omega^2_{\mathrm{crit}}}s^2 + \frac{2\delta}{\omega_{\mathrm{crit}}}s + 1. \tag{5.27}$$

Here, ω_{crit} can be understood as the natural frequency and $0 \leq \delta \ll 1$ represents an adjustable damping ratio. With this choice, (5.26) yields a synthetic PCC voltage feed-forward filter of the form

$$H^{c}(s) = \frac{k_{\mathrm{P}}}{l_{\mathrm{fc}}\omega^2_{\mathrm{crit}}}\,(s + 2\delta\omega_{\mathrm{crit}}) = \frac{\alpha_{\mathrm{c}}}{\omega^2_{\mathrm{crit}}}\,(s + 2\delta\omega_{\mathrm{crit}}) \tag{5.28}$$

where $\Gamma^{c}(s)$ becomes

$$\Gamma^{c}(s) = \frac{k_{\mathrm{P}}}{G^{c}_{\mathrm{PR}}(s)}\left(\frac{1}{\omega^2_{\mathrm{crit}}}s^2 + \left(\frac{2\delta}{\omega_{\mathrm{crit}}} + \frac{r_{\mathrm{fc}}}{l_{\mathrm{fc}}\omega^2_{\mathrm{crit}}}\right)s + \frac{2\delta r_{\mathrm{fc}}}{l_{\mathrm{fc}}\omega_{\mathrm{c}}}\right) + 1. \tag{5.29}$$

The proportional-derivative structure of the suggested filter (5.28) is in accordance with the findings of many studies in the literature which come to the conclusion that it is advisable (or necessary) to implement a PCC voltage feed-forward filter with differentiating character, see e.g., [4, 41, 57, 110, 111, 157]. Among others, Harnefors et al. proposed to use a very similar active damping filter in [57], namely $H^c(s) = 4\alpha_c T_d^2 s/\pi^2 = k_P s/(l_{fc}(\omega_s/6)^2) = 36\alpha_c s/\omega_s^2$, which was also confirmed as a reasonable choice by the results of our previous work [4]. In fact, (5.28) differs from the high-pass filters from [4, 57] only in the estimate of the frequency at which the VSC's inherent input admittance becomes non-passive, see (5.18), and in the inclusion of an (optional) damping term.

Given $\Gamma^c(s)$ from (5.29) and reviewing the calculation of the converter's IFP index from Sec. 5.1.1, the basic principle of the proposed differentiating filters can be illustrated graphically by setting $\delta = 0$ and assuming that $r_{fc} \approx 0$ and $G^c_{PR}(s) \approx k_P, \forall\omega \gg h_m\omega_r$. In this specific case, (5.29) mainly represents a frequency-dependent real value in the high-frequency range and can be approximated by $\Gamma^c(j\omega) \approx 1 - \omega^2/\omega^2_{crit}, \forall\omega \gg h_m\omega_r$. This allows $\Gamma^c(j\omega)$ to be excluded from the continuous equivalent of (5.6), whereby the IFP index of the VSC's quasi-analog input admittance becomes $\text{IFP}\{Y_i^c(j\omega)\} \approx -\Gamma^c(j\omega) \cdot \text{OFP}\{G^c_{ff}(j\omega)/\Gamma^c(j\omega)\}\,|Y^c_{cl}(j\omega)|^2 \sim \Gamma^c(j\omega)\cos(\omega T_d - \arg\{G^c_{PR}(j\omega)\})$. Since the function $\Gamma^c(j\omega) \approx 1 - \omega^2/\omega^2_{crit}$ changes its sign from plus to minus at the frequency $\omega_{crit} \approx \omega_s/6$ at which $\cos(\omega T_d - \arg\{G^c_{PR}(j\omega)\})$ becomes negative, the recommended filters achieve that $\text{IFP}\{Y_i^c(j\omega)\}$ remains positive, and thus, passive for a wide frequency range, provided that the zero crossing at ω_{crit} is exactly known.

However, the presented passivation idea as well as most existing derivations in the literature presuppose a negligible filter resistance on the converter-side and that the PR controller shows a purely proportional behavior in the high-frequency range, see e.g., [8, 57, 110, 141, 157]. Even though the former assumption applies to most of today's grid-connected converter systems, there exist scenarios where r_{fc} is non-negligible. As can be observed in Tab. 5.1, this seems to cause problems for a purely differentiating filter since an increased resistance shifts the critical frequency

ω_{crit} to higher frequencies, which makes the approximation $\omega_{\mathrm{crit}} \approx \omega_{\mathrm{s}}/6$ or the estimation (5.18) less reliable. But, it should be kept in mind that a larger converter-side filter resistance generally adds further damping to the system [4], and according to Sec. 5.2.1, always has a beneficial effect on the VSC's passivity properties. In particular, regarding the passivity criterion (5.24) with the associated phase response of $G_{\mathrm{cl}}(j\omega)/T_{\mathrm{s}}$ from Fig. 4.2, it can be seen that $\arg\{\Gamma(j\omega)\}$ not necessarily needs to provide a sudden phase change from $0°$ to $180°$ at ω_{crit}, but instead a more moderate phase lead is also sufficient for the passivation. In this context, an $r_{\mathrm{fc}} > 0$ even helps to compensate errors in the estimation of the frequency at which the VSC's inherent input admittance becomes non-passive by enlarging the phase lead of $\Gamma^c(s)$ near ω_{crit}. But as a drawback, a non-zero filter resistance also yields a decrease of $\arg\{\Gamma(j\omega)\}$ in the high-frequency range near the Nyquist frequency.

At this point it is also important to notice that, depending on the filter and controller parameters, (5.29) might show a conjugate complex pair of zeros in the positive right half plane of s. This turns the required phase lead of $\Gamma^c(s)$ into a phase lag, which typically yields an undesired shortage of passivity at frequencies near ω_{crit}. Most likely, this is also the source of the identified non-passive region of $Y_{\mathrm{i}}^c(s)$ near $\omega_{\mathrm{s}}/6$ in [57], where the authors see themselves forced to implement a biquad filter in series to a purely differentiating filter to get an adjustable real part of $H^c(j\omega_{\mathrm{s}}/6)$. A more straightforward method to overcome this problem would be to incorporate the complete PR controller dynamics in $H^c(s)$ instead of approximating $G_{\mathrm{PR}}^c(s)$ by its proportional gain k_{P} only. In doing so, $k_{\mathrm{P}}/G_{\mathrm{PR}}^c(s)$ in (5.29) vanishes, which makes $\Gamma^c(s)$ a second-order transfer function with positive coefficients that always has two zeros with negative real part. However, as can be verified, this modification of the feed-forward filter (5.28) would lead to a noticeable change of the converter's input admittance $Y_{\mathrm{i}}^c(s)$ at the specified resonance frequencies and, in the end, result in a worse suppression of the voltage harmonics at every $h_i\omega_{\mathrm{r}}$, $\forall h_i \in h$. But, even more simple, it has been found that a potential non-minimal-phase behavior of $\Gamma^c(s)$, and thus, an unwanted non-passive region of $Y_{\mathrm{i}}^c(s)$ near ω_{crit} can be avoided if the (damping) terms

$2\delta/\omega_{\mathrm{crit}}$ or $r_{\mathrm{fc}}/(l_{\mathrm{fc}}\omega_{\mathrm{crit}}^2)$ in (5.29) show a sufficiently large value. Hence, since a raise of the introduced damping ratio δ has a similar effect as an increase of r_{fc}, but does not produce additional power losses, it is recommended to implement a proportional-derivative filter of the form (5.28) with a $\delta > 0$, see also the similarities to the suggested filters from [4]. After some simplifications of (5.29), an evaluation of the Hurwitz determinants of the numerator suggest that δ should be selected substantially larger than $k_{\mathrm{I}}/(2k_{\mathrm{p}}\omega_{\mathrm{crit}}) = \alpha_{\mathrm{I}}/(2\omega_{\mathrm{crit}}) \approx 3\alpha_{\mathrm{I}}/\omega_{\mathrm{s}}$, e.g., $10-20$ times larger, but not too large in order to avoid an unnecessary large amplification of the feed-forward. In the case of the converter system under study, an exemplary damping ratio of $\delta = 18 \cdot 3\alpha_{\mathrm{I}}/\omega_{\mathrm{s}} \approx 0.1$ should be considered in the following.

Digital Filter Implementation

Following the suggestion of (5.28), the high-pass filter $H^c(s)$ consists of a differentiating filter part and an (optional) proportional part. While the latter can simply be implemented on a digital control system, the exact transformation of the differentiating filter part, $\alpha_{\mathrm{c}}s/\omega_{\mathrm{crit}}^2$, to the discrete z-domain is challenging, because the required ideal derivative is non-causal, and thus, generally not realizable in practice. In order to avoid generating a pole at $z = -1$, which would cause an unacceptable noise amplification and an undamped oscillation by applying the Tustin method, see [57, 119, 157], most literature on digital control systems uses the first difference, i.e., the backward Euler method for the approximation of a differentiation [39, 119]. This method was also used in other related works, e.g., [41, 110, 111, 157], and should be applied here as well. The transformation of (5.28) with the backward Euler method results in a digital filter realization of the form

$$H(z) = \frac{\alpha_{\mathrm{c}}}{\omega_{\mathrm{crit}}^2}\frac{1-z^{-1}}{T_{\mathrm{s}}} + \frac{2\delta\alpha_{\mathrm{c}}}{\omega_{\mathrm{crit}}}. \tag{5.30}$$

However, in contrast to the (ideal) continuous filter (5.28), which shows a phase lead of $90°$ in the high-frequency range, the associated dig-

ital filter (5.30) has a pole at $z = 0$ and therefore always introduces an unavoidable phase lag. More specifically, it can be seen that the phase response of (5.30) approaches $0°$ at the Nyquist frequency, as $e^{j\omega_N T_s} = e^{-j\pi} = -1$, which implies that $H(z)|_{z=e^{j\omega_N T_s}}$ represents a real value, and thus, $\arg\left\{H(e^{j\omega_N T_s})\right\} = \tan^{-1}(0) = 0$. This is basically because of the necessity to wait for one cycle to compute the first difference $[\boldsymbol{e}(kT_s) - \boldsymbol{e}((k-1)T_s)]/T_s$ at $k = 1$ [39].

Equipping the converter test-system with the proposed PCC voltage feed-forward, Fig. 5.8 shows the resulting frequency responses of $\Gamma(s)$ and $\Gamma^c(s)$ for two different parameterizations and a constant high-pass filter cut-off frequency of $\omega_{crit} = 10326\,\frac{rad}{s}$.

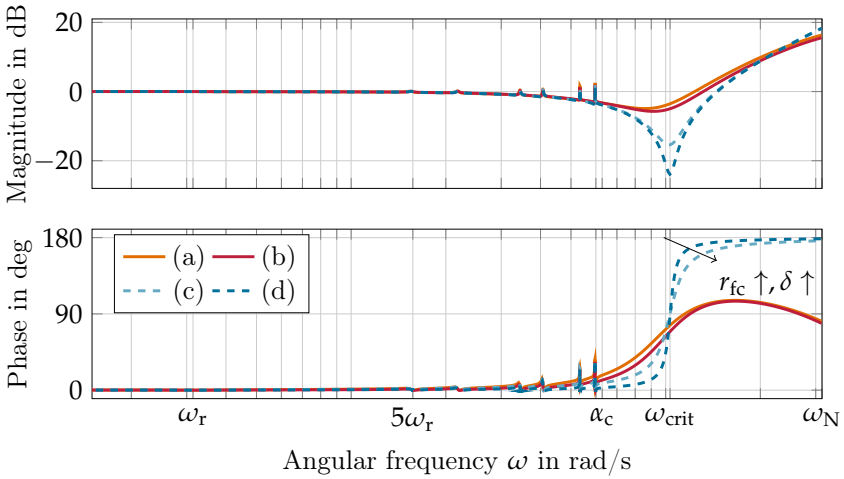

Fig. 5.8: Bode plots of (a), (b) $\Gamma(s)$ and (c), (d) its continuous-time equivalent $\Gamma^c(s)$ for an active synthetic PCC voltage feed-forward, where in (a), (c) $r_{fc} = 0.013$, $\delta = 0.1$ and in (b), (d) $r_{fc} = 0.2$, $\delta = 0$.

As required by the reference model (5.27), the resulting $\Gamma(s)$ and $\Gamma^c(s)$ are minimal-phase and show a phase lead, which is largely marginal in the low-frequency range and (suddenly) increases in the high-frequency range near and above the critical frequency ω_{crit}. But, since the proposed selection guideline (5.26) simplifies the PR controller's characteristics in

the low frequency range by neglecting any influence of the controller's resonators, the functions $\Gamma(s)$ and $\Gamma^c(s)$ show a resonant behavior near the frequencies $h_i\omega_\mathrm{r}$. Moreover, while $\arg\{\Gamma^c(j\omega_\mathrm{N})\}$ reaches a value of $176.4°$ and $178.6°$ for $r_\mathrm{fc} = 0.013$, $\delta = 0.1$ and $r_\mathrm{fc} = 0.2$, $\delta = 0$, respectively, the phase lead of $\Gamma(s)$ only approaches a value of $81.14°$ in the former case and $79.44°$ in the latter case. These unwanted decreases in the phase responses of $\Gamma(s)$ (as well as $\Gamma^c(s)$) have already been suspected and verify the preceding theoretical considerations.

Passivity of the Converter's Input Admittance

Fig. 5.9 illustrates the effects of the suggested PCC voltage feed-forward on the VSC's primary-frequency input admittance $Y_{\mathrm{i,p}}(s)$ and quasi-analog input admittance $Y_\mathrm{i}^c(s)$. As can be observed by the resulting passivity indices of $Y_\mathrm{i}^c(s)$, the active feed-forward renders the quasi-analog input admittances passive for a wide range of frequencies. Similar to a passivation by means of an increased converter-side filter resistance, see Fig. 5.3, a raise of r_fc or δ can effectively be used to increase IFP $\{Y_\mathrm{i}^c(j\omega)\}$ near the critical frequency ω_crit. Nevertheless, some non-passive regions emerge close to the resonance frequencies at $7\omega_\mathrm{r}, 11\omega_\mathrm{r}$, as well as $13\omega_\mathrm{r}$, and the test system with $r_\mathrm{fc} = 0.013$, $\delta = 0.1$ additionally shows a small shortage of passivity near the Nyquist frequency. The latter non-passive region may often emerge if r_fc is close to zero, see also [4], but is mostly overlooked in the present literature on the passivation of grid-connected converters, see e.g., [8, 55, 57, 60, 141, 156]. Analogously to the VSC's quasi-analog input admittance, the primary-frequency input admittances $Y_{\mathrm{i,p}}(s)$ also show non-passive regions near some resonance frequencies, but a much larger shortage of passivity in the high-frequency range.

As we highlighted in the conclusion of [4] and as the previous example has again demonstrated, the passivity assessment and the feed-forward filter design must not be limited to high-frequency components, but also has to focus on signal components below the critical frequency ω_crit. Facing similar problems near the specified resonance frequencies, the authors of [56] suggest to adapt the PR current controller's compensation

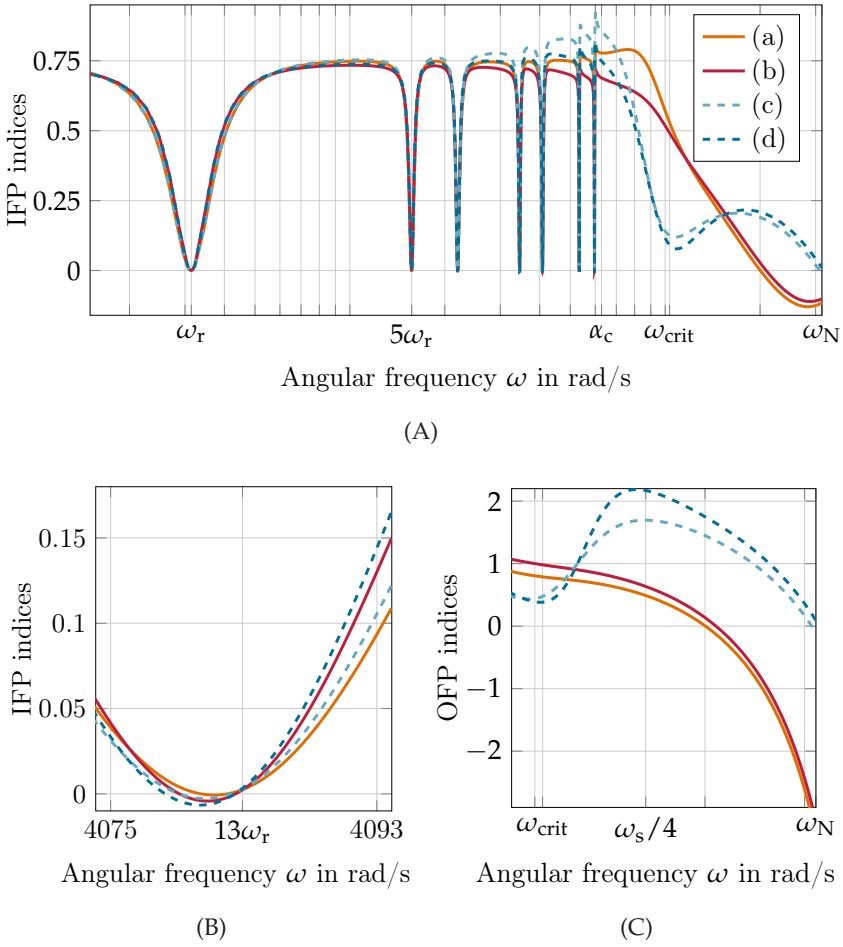

Fig. 5.9: Passivity indices of the VSC's (a), (b) primary-frequency input admittance model and (c), (d) quasi-analog input admittance model with active synthetic PCC voltage feed-forward with $\omega_{crit} = 10326\,\frac{rad}{s}$ and (a), (c) $r_{fc} = 0.013$, $\delta = 0.1$, and (b), (d) $r_{fc} = 0.2$, $\delta = 0$. Subfigure (A) shows the IFP index of the converter's admittance in the complete frequency range of interest, (B) shows a detailed section of the system's IFP index near $13\omega_r$, and (C) illustrates the system's OFP index in the high-frequency range.

angles ϕ_{h_i} to ensure the system's passivity at every $h_i\omega_\mathrm{r}$ by making IFP $\{Y_\mathrm{i}^c(jh_i\omega_\mathrm{r})\}$, $h_i \in h$ a local minimum. This method has however been found to be impractical, since the proposed adaption is rather complex and depends on the structure of $H(z)$, which makes an independent and successive current controller and active feed-forward filter design impossible. On the other hand, recalling the passivity criterion (5.24) and considering that the phase response of the reference current dynamics $\arg\{G_\mathrm{cl}(j\omega)/T_\mathrm{s}\}$ never exceeds zero degrees by utilizing the suggested parameterization from Ch. 4, it becomes clear that it is not necessarily required to adapt the current control loop. As an alternative, it is thus also possible to modify the feed-forward filter $H(z)$ such that $\Gamma(s)$ does not introduce too much phase lead near the resonance frequencies.

In particular, a closer look at (5.29) shows that the uncompensated PR controller generates resonances in $\Gamma^c(s)$, which lead to an undesired increase of $\arg\{\Gamma^c(j\omega)\}$ directly before each $h_i\omega_\mathrm{r}$. While this effect is rather minor in the very low-frequency range, it becomes more and more significant at harmonics of a higher order, see Fig. 5.8. Depending on the chosen damping ratio δ and the selection of the PR controller's integral gains k_{I,h_i}, this phase lead is the cause of the non-passive regions near some resonance frequencies when implementing a PCC voltage feed-forward. Hence, in order to reshape the emerging resonances in $\Gamma^c(s)$ and simultaneously maintain the rest of the converter's disturbance dynamics as unchanged as possible, it is proposed to cancel $G_\mathrm{PR}^c(s)$ in (5.29) and replace it by a filter $G_\mathrm{PRH}^c(s)$, which has the same form as (3.31), but with (slightly) different parameters. Following this idea and using (3.34) as digital filter realization of $G_\mathrm{PRH}^c(s)$, the feed-forward filter (5.30) can be extended to

$$H(z) = \frac{G_\mathrm{PR}(z)}{G_\mathrm{PRH}(z)} \left(\frac{\alpha_\mathrm{c}}{\omega_\mathrm{crit}^2} \frac{1 - z^{-1}}{T_\mathrm{s}} + \frac{2\delta\alpha_\mathrm{c}}{\omega_\mathrm{crit}} \right). \tag{5.31}$$

Here, it is suggested that $G_\mathrm{PRH}(z)$ implements the same parameters k_P and ω_{c,h_i}, $\forall i$ as the PR controller $G_\mathrm{PR}(z)$, but uses modified integral gains $k_{\mathrm{I,PRH},h_i}$ and compensation angles ϕ_{PRH,h_i} for all $h_i \in h$. This is comparable to the suggested method of [56], but avoids a direct adaption of

the already designed PR controller in the forward path of the current control loop. If the i-th integral gain, $k_{\mathrm{I,PRH},h_i}$, is greater than k_{I,h_i}, the added pulse transfer function $G_{\mathrm{PR}}(z)/G_{\mathrm{PRH}}(z)$ allows to implement a band-stop at $h_i\omega_{\mathrm{r}}$, whereas a $k_{\mathrm{I,PRH},h_i} < k_{\mathrm{I},h_i}$ yields a band-pass. The choice of the compensation angles $0° \leq \phi_{\mathrm{PRH},h_i} \leq \phi_{h_i}, \forall i$ can be considered as an additional degree of freedom. Since $G_{\mathrm{PR}}(z)$ as well as $G_{\mathrm{PRH}}(z)$ always represent two stable, non-minimal phase systems, (5.31) can directly be implemented by means of a digital IIR filter. Alternatively, the PR controller in the forward path of the current control loop can be used as a part of the feed-forward filter by implementing $G_{\mathrm{PRH}}^{-1}(z)$ in series to (5.30) and shifting the output of the feed-forward action in Fig. 3.1 from the output to the input of the current controller. This realization does not save any resources, but makes the current limiting and the anti-windup of the controller and filter resonators much easier.

Fig. 5.10 demonstrates the effects of the filter modification (5.31) on the corresponding frequency responses of $\Gamma(s)$ and the characteristics of IFP $\{Y_{\mathrm{i,p}}(j\omega)\}$ near the 13th harmonic for different parameters. As can be observed, the exemplarily shown resonance of $\Gamma(s)$ can effectively be reshaped by varying the filter's integral gain $k_{\mathrm{I,PRH},13}$ and compensation angle $\phi_{\mathrm{PRH},13}$. If the gain is increased, the local maximum of $\arg\{\Gamma(j\omega)\}$ is shifted to lower frequencies, which automatically yields a more moderate phase lead at frequencies very close to $13\omega_{\mathrm{r}}$. This modification of the filter's integral gains can generally be used to remove the possibly emerging non-passive regions of the VSC's input admittance near the resonance frequencies. In most applications, a minor increase of each gain $k_{\mathrm{I,PRH},h_i}, \forall i$ compared to k_{I,h_i} should be sufficient for a passivation. For example, considering the introduced converter test-system with the parameters from Tab. 3.1, Tab. 3.2, and Tab. 4.1 with $\delta = 0.1$, all non-passive regions in the low-frequency range can already be eliminated by implementing a $G_{\mathrm{PRH}}(z)$ with $k_{\mathrm{I,PRH},h_i} = 1.2k_{\mathrm{I},h_i}$, $\phi_{\mathrm{PRH},h_i} = \phi_{h_i}$, $\forall h_i \in h$. More moderate PR controller integral gains, k_{I,h_i}, even allow to further reduce the integral gains of $G_{\mathrm{PRH}}(z)$ or to set $k_{\mathrm{I,PRH},h_i} = k_{\mathrm{I},h_i}$ and $\phi_{\mathrm{PRH},h_i} = \phi_{h_i}$ for all $h_i \in h$, i.e., again implement the simpler feed-forward filter $H(z)$ from (5.30). On the other hand, higher PR controller

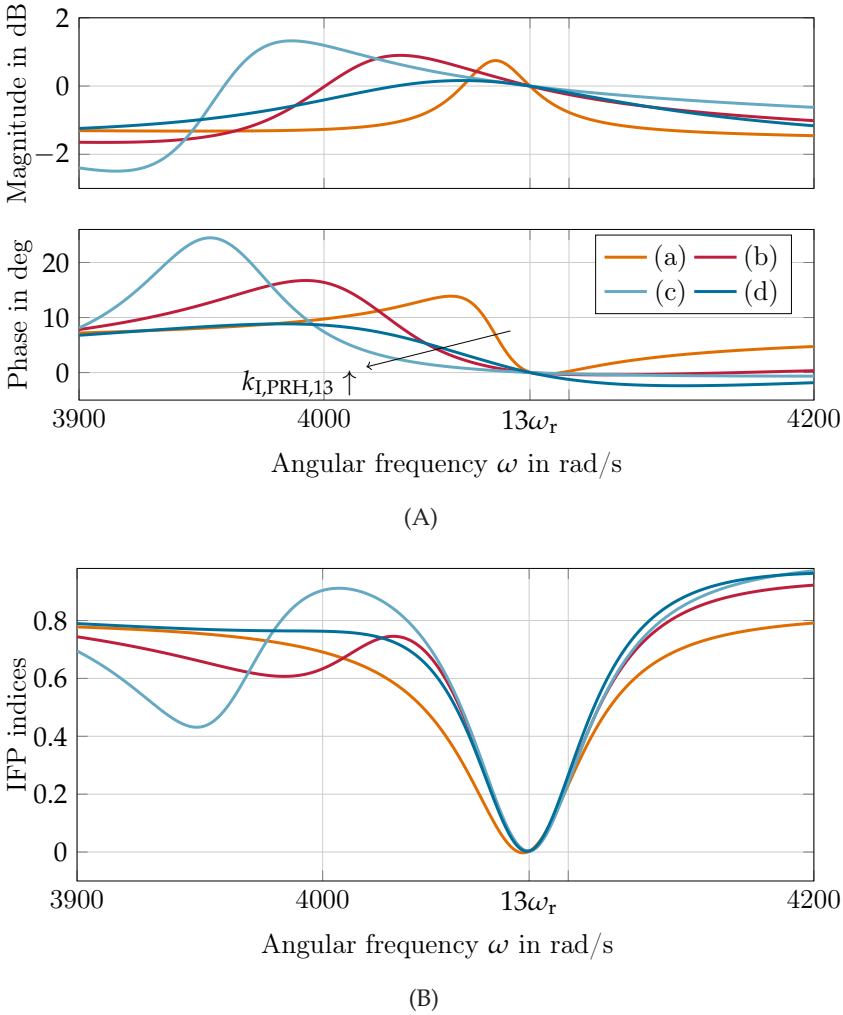

Fig. 5.10: Subfigure (A) shows the Bode plots of the modified $\Gamma(s)$ with $\omega_{\mathrm{crit}} = 10326\,\frac{\mathrm{rad}}{\mathrm{s}}$, $r_{\mathrm{fc}} = 0.013$, and $\delta = 0.1$ and subfigure (B) illustrates the resulting IFP indices of the VSC input admittance near $13\omega_{\mathrm{r}}$, where the filter $G^{\mathrm{c}}_{\mathrm{PRH}}(s)$ implements the parameters (a) $k_{\mathrm{I,PRH,13}} = k_{\mathrm{I,13}}$, $\phi_{\mathrm{PRH,13}} = \phi_{13}$, (b) $k_{\mathrm{I,PRH,13}} = 4k_{\mathrm{I,13}}$, $\phi_{\mathrm{PRH,13}} = \phi_{13}$, (c) $k_{\mathrm{I,PRH,13}} = 8k_{\mathrm{I,13}}$, $\phi_{\mathrm{PRH,13}} = \phi_{13}$, and (d) $k_{\mathrm{I,PRH,13}} = 4k_{\mathrm{I,13}}$, $\phi_{\mathrm{PRH,13}} = 0°$.

integral gains or the implementation of more harmonic resonators often require the use of higher filter integral gains $k_{\mathrm{I,PRH},h_i}$. But, as shown in Fig. 5.10, care should be taken not to increase the integral gains too much in order to avoid generating new critical minima in IFP $\{Y_{\mathrm{i,p}}(j\omega)\}$. In the end, each harmonic frequency should be examined individually and a trade-off between the amounts of the emerging minima in IFP $\{Y_{\mathrm{i,p}}(j\omega)\}$ and a shift of the resonances in $Y_{\mathrm{i,p}}(s)$ has to be found. Although this need not apply in general, various test studies showed that it is recommended to choose each $k_{\mathrm{I,PRH},h_i}$ at least twice as high as the corresponding k_{I,h_i} and, if required, reduce each compensation angle ϕ_{PRH,h_i}, which smooths the IFP index of $Y_{\mathrm{i,p}}(s)$ near the corresponding resonance frequency, but increases $|Y_{\mathrm{i,p}}(jh_i\omega_{\mathrm{r}})|$.

However, even though the proposed PCC voltage feed-forward filter (5.31) allows to render the VSC's primary-frequency input admittance passive for a wide range of frequencies, there typically emerges a large non-passive region in the high-frequency range. This problem also remains with other (either less or more complex) digital filters or different discretization methods, see also [41, 57, 110, 111, 156, 157]. Moreover, as can exemplarily be verified by the converter's OFP index from Fig. 5.9C, the lack of passivity can practically not be compensated or only with great difficulty and (very) high energy losses by the implementation of passive damping methods. For this reason, an active feed-forward of the synthetic PCC voltage might be used for the damping of the VSC's low-frequency conductance and the LCL filter's resonance, but is generally not suitable for the full passivation of digitally current-controlled converters.

Stability of the Closed-Loop Grid-Converter System

The potential risks that arise when the actively damped VSC is connected to the grid can be predicted from the Nyquist plots of the exemplary open-loop grid-converter systems shown in Fig. 5.11. In accordance with the passivity theorems from Sec. 2.1.3, the illustrated Nyquist curves of the quasi-analog system, $Y_{\mathrm{i}}^{c}(s)\tilde{Z}_{\mathrm{g}}(s)$, always approach the origin of the

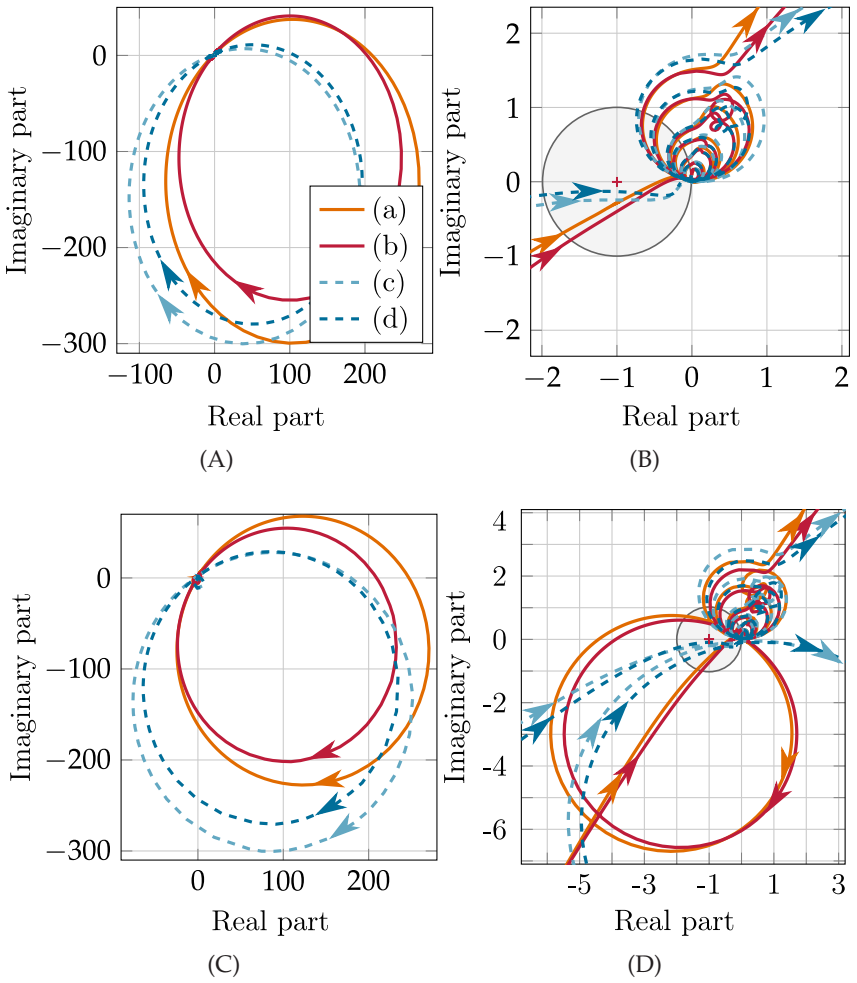

Fig. 5.11: Nyquist plots of the open-loop grid-converter system using (a), (b) the primary-frequency input admittance model and (c), (d) the quasi-analog input admittance model, where the VSC is equipped with an undamed LCL filter and implements the proposed active synthetic PCC voltage feed-forward with (a), (c) $r_{\mathrm{fc}} = 0.013$, $\delta = 0.1$, and (b), (d) $r_{\mathrm{fc}} = 0.2$, $\delta = 0$. Subfigures (A), (C) and subfigures (B), (D) show the complete and detailed plots for $\omega \in [0, \omega_{\mathrm{N}}]$, respectively, where the VSC is connected (A), (B) to an inductive grid with $Z_{\mathrm{g}}(s) = l_{\mathrm{g}} s$, $l_{\mathrm{g}} = 64.95\,\mu$s, and (C), (D) to a resistive-inductive grid, where $\tilde{Z}_{\mathrm{g}}(s)$ has a below Nyquist frequency resonance at $\omega_{\mathrm{r},\tilde{Z}_{\mathrm{g}},2} \approx 29128\,\frac{\mathrm{rad}}{\mathrm{s}} > \omega_{\mathrm{crit}}$.

complex plane from the third quadrant, implying that the systems' total phase responses always stay below $-180°$. Since the VSC's quasi-analog input admittance with active damping is designed to be passive and the synthetic grid impedance represents a passive system for any passive $Z_{\mathrm{g}}(s)$, an increase of the effective (low-frequency) grid inductance or an emerging below Nyquist frequency resonance do not change this behavior. Therefore, as the corresponding Nyquist curves can never encircle the point $(-1+j0)$ for all $\omega \in [0, \omega_{\mathrm{N}}]$ by design, it can be concluded that the closed-loop grid-converter systems are always asymptotically stable as long as $Z_{\mathrm{g}}(s)$ is passive. But, on the other hand, given the converter's (more accurate) primary-frequency model (3.52) that implements the digital feed-forward filter (5.31), an interconnection with an inductive grid typically results in a Nyquist curve which leaves the fourth and third quadrants and enters the second quadrant of the complex plane in the high-frequency range again, see Fig. 5.11B. Even though the corresponding frequency range might be narrow, the entry of the Nyquist curve of $Y_{\mathrm{i,p}}(s)\tilde{Z}_{\mathrm{g}}(s)$ into the second quadrant introduces a risk. A more complex grid impedance, which e.g., shows resonances due the dynamics of (long) transmission lines [141,166] or the dynamics of other grid-connected converters [11, 88, 141] may lead to an expansion of the Nyquist curve and, in the end, to an encirclement of the point $(-1+j0)$. This is also the case in the illustrated scenario in Fig. 5.11C and Fig. 5.11D. As indicated by the huge negative values of the OFP indices in Fig. 5.9C, it can be assumed that neither an increase of the introduced damping term δ nor a raise of the converter-side filter resistance r_{fc} or the implementation of an advanced passive damping strategy can change this disadvantageous property easily.

Hence, although the resonance of the converter's LCL filter can be well damped by an active synthetic PCC voltage feed-forward and the resulting closed-loop system can be expected to be stable for a simple (resistive-inductive) grid, an unfavorable grid resonance near the Nyquist frequency may still destabilize the grid-converter system.

5.3.3 Capacitor Current Feed-Forward

As motivated at the beginning of Sec. 5.3, another active damping method that can frequently be found in the literature utilizes the (sampled) LCL filter's capacitor current $\boldsymbol{i}_{\mathrm{c}}^{*}$ as a feed-forward quantity [4, 8, 57, 87, 96, 97, 142, 156]. With regard to the results of the previous section, the feed-forward of the capacitor current instead of the synthetic PCC voltage offers the useful property that the required differentiation in $H^{c}(s)$ or $H(z)$ can be avoided, since it is implicitly implemented by the hardware [4, 57, 157]. More specifically, given the introduced primary-frequency model from Sec. 3.4.1, where a capacitor current feed-forward is to be used this time, $\Gamma(s)$ can be redefined as

$$\Gamma(s) = 1 + \frac{Y_{\mathrm{c}}(s)}{Y_{\mathrm{fc}}(s)} \frac{H^{*}(s)}{G_{\mathrm{PR}}^{*}(s)} \quad \text{or} \quad \Gamma(s) = 1 + \frac{Y_{\mathrm{d}}(s)}{Y_{\mathrm{fc}}(s)} \frac{H^{*}(s)}{G_{\mathrm{PR}}^{*}(s)}, \tag{5.32}$$

if either an LCL filter topology from Fig. 3.2A or Fig. 3.2B is implemented or the more advanced topology from Fig. 3.2C, respectively. In contrast to (5.25), the calculation of $\Gamma(s)$ in (5.32) also includes the inverse dynamics of the effective capacitance from (3.9) or (3.11). Proceeding as before and requiring that the continuous-time equivalent $\Gamma^{c}(s)$ shows the behavior of some adequate reference model filter $F(s)$, (5.32) can be used to derive the filter design guideline

$$H^{c}(s) \approx \frac{Y_{\mathrm{fc}}(s)}{c_{\mathrm{c}} s} G_{\mathrm{PR}}^{c}(s)(F(s) - 1) \approx k_{\mathrm{P}} \frac{F(s) - 1}{l_{\mathrm{fc}} c_{\mathrm{c}} s^{2}}, \tag{5.33}$$

provided that $Z_{\mathrm{c}}(s) \approx 1/(c_{\mathrm{c}} s)$ (or $Z_{\mathrm{d}}(s) \approx 1/(c_{\mathrm{c}} s)$) for frequency components up to the Nyquist frequency. Hence, since the double integrator in (5.33) cancels any second-order derivative action in $F(s) - 1$, a differentiation in $H^{c}(s)$ can be avoided for any reasonable second-order high-pass reference model filter.

Design of the Continuous-Time Equivalent Filter $\boldsymbol{H^{c}(s)}$

A particularly simple feed-forward can be obtained by requiring $F(s)$ to be a high-pass filter of the form (5.27) with $\delta = 0$. In this specific case,

the capacitor current feed-forward filter represents a purely proportional gain and is given by

$$H^c(s) = H(z) = k_\mathrm{P} \frac{1}{l_\mathrm{fc} c_\mathrm{c} \omega_\mathrm{crit}^2} = \frac{\alpha_\mathrm{c}}{c_\mathrm{c} \omega_\mathrm{crit}^2} \tag{5.34}$$

where

$$\Gamma^c(s) \approx \frac{k_\mathrm{P}}{G_\mathrm{PR}^c(s)} \left(\frac{1}{\omega_\mathrm{crit}^2} s^2 + \frac{r_\mathrm{fc}}{l_\mathrm{fc} \omega_\mathrm{crit}^2} s \right) + 1. \tag{5.35}$$

As in the case of the PCC voltage feed-forward filter (5.28), the resulting filter (5.34) is almost identical to the suggested filter $H^c(s) = 36\alpha_\mathrm{c}/(c_\mathrm{c}\omega_\mathrm{s}^2) = k_\mathrm{P}/(l_\mathrm{fc} c_\mathrm{c} (\omega_\mathrm{s}/6)^2)$ from our work [4] or the filters from [57, 156]. Compared to (5.28), the filter (5.34) does not contain a differentiation, but yields approximately the same $\Gamma^c(s)$ as in (5.29) if the damping components in the LCL filter's capacitive branch are low and $\delta = 0$. Due to this similarity, all related considerations from the previous section on the positive influence of an increased converter-side filter resistance r_fc or the effects of the non-ideal compensation of $G_\mathrm{PR}^c(s)$ in $\Gamma^c(s)$ also apply here in a similar way.

Therefore, in order to become more robust against modeling uncertainties and simultaneously avoid that $\Gamma^c(s)$ becomes non-minimal-phase and leads to a non-passive region of $Y_\mathrm{i}^c(s)$ near ω_crit, it is again recommended that (5.35) does not introduce a sudden phase shift at ω_crit, but shows a more moderate phase lead. As before, one possibility is to increase the resistance r_fc, which would however also increase the power losses. Alternatively, the reference model filter can be specified to represent a damped high-pass filter, e.g., use $F(s)$ from (5.27) with a damping ratio greater than zero. In doing so, the resulting feed-forward filter would have the desired damping effect on $\Gamma^c(s)$, but $H^c(s)$ takes the form of a PI element, producing an extremely large feed-forward of the capacitor current in the low-frequency range. However, considering that the VSC's inherent input admittance is already passive for frequencies up to ω_crit, it can be seen that $H^c(s)$ (or $\Gamma^c(s)$) must not necessarily reshape the behavior of $Y_\mathrm{i}^c(s)$

in the low-frequency range. For this reason, it is proposed to choose a reference model filter of the form

$$F(s) = \frac{1}{\omega_{\mathrm{crit}}^2} s^2 + \frac{2\delta}{\omega_{\mathrm{crit}}} \frac{s^2}{s+\omega_\delta} + 1 \tag{5.36}$$

where ω_δ defines a cut-off frequency which allows to restrict the influence of the introduced damping term $2\delta s/\omega_{\mathrm{crit}}$, with $\alpha_{\mathrm{I}}/(2\omega_{\mathrm{crit}}) \ll \delta \ll 1$. While the additionally added filter $s/(s+\omega_\delta)$ acts like a pure derivative and attenuates the damping term at frequencies $\omega \ll \omega_\delta$, it shows the behavior of an unity gain at frequencies $\omega \gg \omega_\delta$. Hence, requiring that the damping of (5.36) is effective at frequencies close to and above ω_{crit}, it is suggested to select $\omega_{\mathrm{crit}}/10 \leq \omega_\delta \leq \omega_{\mathrm{crit}}/2$, where smaller values of ω_δ principally lead to a better damping effect, but an increased feed-forward of signal components in the low-frequency range. Then, again following the introduced design procedure and substituting the new reference model filter (5.36) into (5.33), the modified continuous equivalent feed-forward filter $H^c(s)$ becomes

$$H^c(s) = \frac{\alpha_{\mathrm{c}}}{c_{\mathrm{c}}\omega_{\mathrm{crit}}^2} \left(1 + \frac{2\delta\omega_{\mathrm{crit}}}{s+\omega_\delta}\right) = \frac{\alpha_{\mathrm{c}}}{c_{\mathrm{c}}\omega_{\mathrm{crit}}^2} \frac{s+\omega_\delta+2\delta\omega_{\mathrm{crit}}}{s+\omega_\delta}. \tag{5.37}$$

The resulting lead-lag filter aims to introduce a small phase lag around the frequency ω_{crit}, and thus, has a similar effect as the suggested biquad filters from [8, 57], but offers less degrees of freedom. However, while Akhavan et al. propose a time-consuming optimization of the adopted biquad filter in [8] and Harnefors et al. use many simplifications in [57], the filter (5.37) is derived from a more detailed system analysis and therefore allows a more intuitive and straight forward parameter selection. In this context it should also be noticed that the suggested filters from the literature [8, 57] principally lead to a higher damping of $\Gamma^c(s)$. This can however not be approved with regard to the use of multifrequency PR controllers, since an increased phase lead of $\Gamma^c(s)$ in the low frequency range increases the risk for deeper (negative) local minima of IFP $\{Y_{\mathrm{i}}^c(j\omega)\}$ near the specified resonance frequencies.

Digital Filter Implementation

This time, the feed-forward filter $H^c(s)$ from (5.37) does not contain a differentiation and can simply be transformed to the z-domain by using standard approximation methods, see e.g., [9,39,119]. Due to its simplicity as well as its high accuracy in the low- and high-frequency range, the Tustin approximation without prewarping, i.e., $s = 2/T_\mathrm{s}(z-1)/(z+1)$, is used in the following. In combination with the (optional) filter extension from (5.31), the digital realization of the capacitor current feed-forward filter is given by

$$H(z) = \frac{G_\mathrm{PR}(z)}{G_\mathrm{PRH}(z)} \frac{\alpha_\mathrm{c}}{c_\mathrm{c}\omega_\mathrm{crit}^2} \frac{\frac{T_\mathrm{s}(\omega_\delta+2\delta\omega_\mathrm{crit})+2}{T_\mathrm{s}\omega_\delta+2} + \frac{T_\mathrm{s}(\omega_\delta+2\delta\omega_\mathrm{crit})-2}{T_\mathrm{s}\omega_\delta+2} z^{-1}}{1 + \frac{T_\mathrm{s}\omega_\delta-2}{T_\mathrm{s}\omega_\delta+2} z^{-1}}. \quad (5.38)$$

With regard to the small sampling times of today's converter systems, it can be suspected that $H^c(s)$ and $H(z)$ accurately match at a wide range of frequencies up to the Nyquist frequency. But, the digital filter (5.38) even has an advantage over it's continuous-equivalent. If it is considered that the extension $G_\mathrm{PR}^c(s)/G_\mathrm{PRH}^c(s)$ acts like a pure proportional gain at frequencies $\omega \gg h_m\omega_\mathrm{r}$, the filter $H^c(s)$ represents a lead-lag element, which not only produces the desired phase shift at ω_crit, but also introduces an unavoidable phase lag in the high-frequency range. Even though the resulting decrease in phase is rather minor for small damping ratios δ, it has a negative effect on the passivation properties of the feed-forward. On the other hand, since $e^{j\omega_\mathrm{N}T_\mathrm{s}} = e^{-j\pi} = -1$, the phase response of the digital filter (5.38) is always enforced to approach the desired phase shift of $0°$ at the Nyquist frequency ω_N. This can also be verified in Fig. 5.12, which compares the frequency responses of possible (digital) capacitor current feed-forward filters using the exemplary parameters from Tab. 4.1 and Tab. 5.2 with $c_\mathrm{c} = 72.36\,\mu\mathrm{s}$.

If the recommended filter (5.38) is applied to the converter test-system, Fig. 5.13 illustrates the resulting frequency responses of $\Gamma(s)$ for different LCL filter topologies. As demanded by the reference model filter (5.36), all phase responses show a sudden, but moderate phase lead in the high-frequency range, where $\arg\{\Gamma(j\omega_\mathrm{N})\}$ approaches a value of $179.9°$,

Table 5.2: Normalized capacitor current feed-forward filter parameters

Parameter	Parameterization
Gain crossover frequency	$\alpha_\mathrm{c} = \omega_\mathrm{s}/10 = 6283.2\,\mathrm{rad/s}$
Damper capacitor	$c_\mathrm{c} = 72.36\,\mu\mathrm{s}$ and $c_\mathrm{c} = 50.81\,\mu\mathrm{s}$
Estimated critical frequency	$\omega_\mathrm{crit} = 10326\,\mathrm{rad/s}$
Sampling time	$T_\mathrm{s} = 0.1\,\mathrm{ms}$
Damping ratio	$\delta = 0.1$
Damping cut-off frequency	$\omega_\delta = \omega_\mathrm{crit}/5 \approx 2065.2\,\mathrm{rad/s}$
Proportional gain	$k_\mathrm{P,PRH} = k_\mathrm{P} = 1.22$
Compensation angles	$\phi_{\mathrm{PRH},h_i} = \phi_{h_i}, \forall i$
Integral gains	$k_{\mathrm{I,PRH,h_i}} = 3k_{\mathrm{I,h_i}}, \forall i$
Cut-off frequencies	$\omega_{\mathrm{c,PRH},h_i} = \omega_{\mathrm{c},h_i} = 0.1\,\mathrm{rad/s}, \forall i$

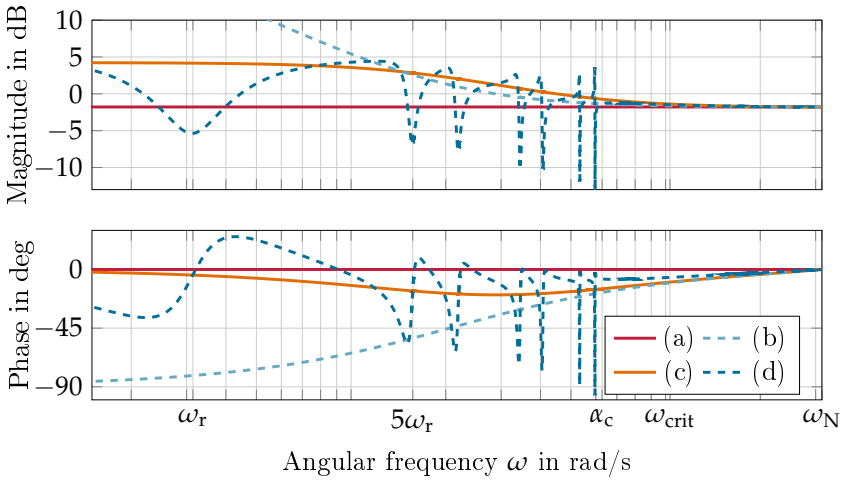

Fig. 5.12: Exemplary Bode plots of different capacitor current feed-forward filters, where (a) shows the purely proportional filter (5.34), (b) a filter that has the form of a (discretized) PI element, (c) the digital realization of the lead-lag filter (5.37), and (d) the extended filter (5.38).

176.1°, and 173.2° if the VSC implements an undamped LCL filter, an LCL filter with series damping resistance, and an LCL filter with resistive-inductive damping circuit, respectively. Comparing the Bode plots of $\Gamma(s)$ from Fig. 5.13 with the plots of $\Gamma^\mathrm{c}(s)$ from Fig. 5.8, the discussed similari-

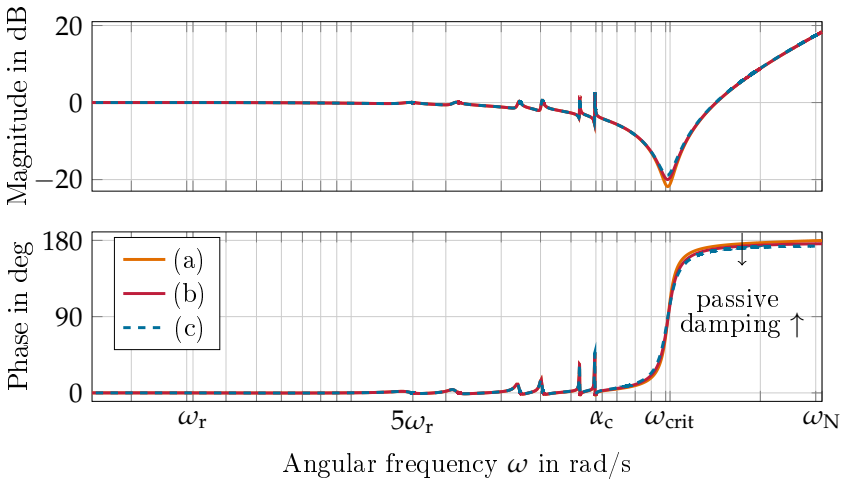

Fig. 5.13: Bode plots of $\Gamma(s)$ for the proposed capacitor current feed-forward filter (5.38), where the converter under study implements (a) an undamped LCL filter, (b) an LCL filter with series damping resistance, and (c) an LCL filter with resistive-inductive damping circuit according to Fig. 3.2C.

ties between an (ideal) PCC voltage feed-forward and a capacitor current feed-forward can clearly be seen. Here, it can also be noticed that an increase of the LCL filter's passive damping has a similar effect on $\Gamma(s)$ as an increase of the converter-side filter resistance r_fc. However, in contrast to a voltage feed-forward with the digital filter realization (5.31), the proposed digital capacitor current feed-forward does not negatively affect the phase lead of the corresponding $\Gamma(s)$ in the high-frequency range, which, in turn, is beneficial for the converter passivation.

Passivity of the Converter's Input Admittance

Fig. 5.14 shows the passivity indices of the converter's primary-frequency input admittance model $Y_\mathrm{i,p}(s)$ with the LCL filter topologies from Fig. 3.2. As initially intended, the proposed active feed-forward largely removes the VSC's non-passive regions. As can be verified, the added filter component $G_\mathrm{PR}(z)/G_\mathrm{PRH}(z)$ ensures the passivity at every speci-

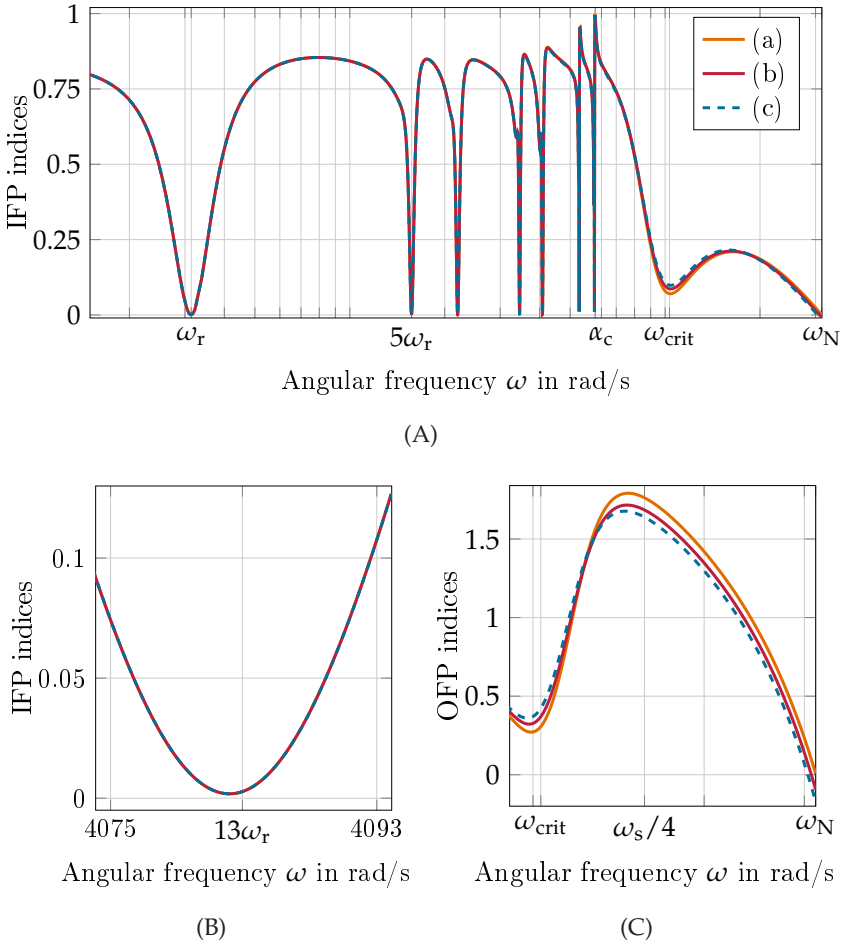

Fig. 5.14: Passivity indices of the VSC's primary-frequency input admittance model with active capacitor current feed-forward, where the converter under study implements (a) an undamped LCL filter, (b) an LCL filter with series damping resistance, and (c) an LCL filter with resistive-inductive damping circuit. Subfigure (A) shows the IFP index of the converter's admittance in the complete frequency range of interest, (B) shows a detailed section of the system's IFP index near $13\,\omega_r$, and (C) illustrates the system's OFP index in the high-frequency range.

fied resonance frequency $h_i\omega_\mathrm{r}$, $\forall h_i \in h$, where the introduced damping ratio δ effectively allows to raise the admittance's IFP index near the frequency ω_crit, without lowering IFP $\{Y_\mathrm{i,p}(j\omega)\}$ near and at the Nyquist frequency. In fact, if the converter is equipped with an ideal LCL filter, the VSC's input admittance is rendered strictly passive in the complete frequency range of interest, i.e., IFP $\{Y_\mathrm{i,p}(j\omega)\} > 0$, $\forall\omega \in [0, \omega_\mathrm{N}]$. On the other hand, while the implementation of a damped LCL filter further improves the converter's passivity properties near ω_crit by enforcing higher values of IFP $\{Y_\mathrm{i,p}(j\omega_\mathrm{crit})\}$, the damping circuit causes a phase lag in $\Gamma(s)$, which might lead to a shortage of passivity in the high-frequency range, see Fig. 5.14C. Due to the usually existing (unmodelled) parasitic resistance in the capacitive branch of the LCL filter [35, 38, 110], this applies to almost all converter systems, but is mostly overlooked in the present research on the passivation of the VSC's input admittance, see e.g., [4, 8, 11, 53, 57, 141, 156]. If the dissipative component is increased, the non-passive region even becomes more significant and can only be counteracted by an additional increase of the converter-side filter resistance r_fc.

Hence, although the exemplarily studied damping circuits from Fig. 3.2 act beneficial on the IFP index of the synthetic grid impedance $\tilde{Z}_\mathrm{g}(s)$, see Fig. 5.4 or Fig. 5.5, they have generally a negative effect on the passivity properties of the converter's primary-frequency input admittance in the high-frequency range when using an active capacitor current feedforward. From this point of view it is preferable to keep the dissipative component of the LCL filter's capacitive branch low or to aim for the implementation of an ideal (undamped) LCL filter. In doing so, a complete (strictly) passive converter input admittance can be guaranteed and a critical interaction of the converter with poorly damped grid resonances can be prevented by design.

Stability of the Closed-Loop Grid-Converter System

With regard to the converter's advantageous passivity properties when using the proposed active filter (5.38), Fig. 5.15 exemplarily illustrates dif-

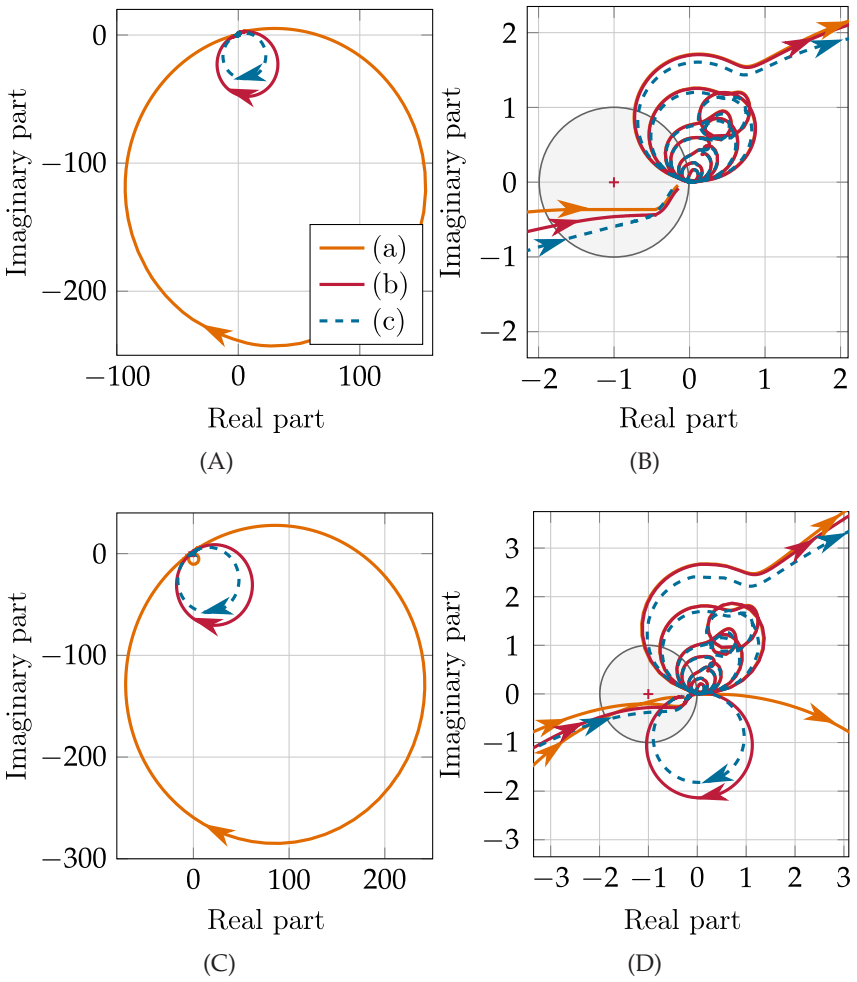

Fig. 5.15: Nyquist plots of the open-loop grid-converter system using the VSC's primary-frequency input admittance model with active capacitor current feed-forward, where the converter under study is equipped with (a) an undamped LCL filter, (b) an LCL filter with series damping resistance, and (c) an LCL filter with resistive-inductive damping circuit. Subfigures (A), (C) and subfigures (B), (D) show the complete and detailed plots for $\omega \in [0, \omega_{\mathrm{N}}]$, respectively, where the VSC is connected (A), (B) to an inductive grid with $Z_{\mathrm{g}}(s) = l_{\mathrm{g}} s$, $l_{\mathrm{g}} = 64.95\,\mu\mathrm{s}$, and (C), (D) to a resistive-inductive grid, where $\tilde{Z}_{\mathrm{g}}(s)$ has a below Nyquist frequency resonance at $\omega_{\mathrm{r},\tilde{\mathrm{Z}}_{\mathrm{g}},2} \approx 29128\,\frac{\mathrm{rad}}{\mathrm{s}} > \omega_{\mathrm{crit}}$.

ferent Nyquist plots of the open-loop system $Y_{\mathrm{i,p}}(s)\tilde{Z}_{\mathrm{g}}(s)$ for the VSC under study. Similar to the Nyquist curves of the quasi-analog open-loop models in Fig. 5.11, the Nyquist curves in Fig. 5.15 always approach the origin of the complex plane from the third quadrant. A closer look shows that none of the curves cross the negative real axis. For $\omega = \omega_{\mathrm{N}}$, the associated points always lie in the third quadrant, where a further increase of the effective grid inductance l_{g} only cause the Nyquist curves to approach the origin more and more. In accordance with the passivity theorems of Sec. 2.1.3, it can thus be verified that the designed converter yields an asymptotically stable closed-loop system when connected to a passive grid impedance, even if the grid shows one or multiple below Nyquist frequency resonances.

Since the identified possibly emerging non-passive regions in the IFP index of $Y_{\mathrm{i,p}}(s)$ near ω_{N} are relatively minor and are likely to be compensated by the (natural) damping effect of the synthetic grid impedance $\tilde{Z}_{\mathrm{g}}(s)$, this can also be assumed to be the case if the LCL filter implements an additional passive damping scheme or shows non-negligible parasitic resistances. In fact, dissipative components even act beneficial on the stability properties of the resulting closed-loop system, which is indicated by the larger stability measures in Fig. 5.15B and Fig. 5.15D. In the end, and in agreement with the results of present research [4, 57, 60, 156, 157], it can be concluded that a destabilization of the closed-loop grid-converter system by poorly damped (below Nyquist frequency) grid resonances is rather unlikely to occur if the VSC is equipped with the proposed active capacitor current feed-forward.

6 PWM Harmonics and Aliasing Effects

As emphasized in Sec. 3.4, the derived primary-frequency input admittance model (3.52) does not take all effects of the digital control into account by neglecting the mirrored components in $\boldsymbol{i}_1^*$, $\boldsymbol{e}^*$, or $\boldsymbol{i}_c^*$. This is also in accordance with most of the related converter models in the literature, see e.g., the equivalent model of Harnefors et al. in [53] or the z-domain models of [41, 110], but might not be reasonable in practical applications. In fact, aliasing effects reshape the converter's input admittance, where the mirroring of above Nyquist frequency signal components on low-frequency (primary) signal components could result in a positive feedback, and thus, even cause a system destabilization [140]. While it can still be assumed that the LCL filter in combination with the grid impedance effectively suppresses high-frequency voltage components that come from the power grid, the aliasing of switching harmonics that are injected by the PWM may have an influence on the current control.

Similar to the frequency-domain models that result from the harmonic state space modeling approach [81, 95, 140, 165], Freijedo et al. [42] and San et al. [116] each propose a linear converter model which includes switching harmonics that are aliases of the PWM's reference input voltage. Even though nonlinear sideband harmonics [64,129,159] or interharmonics [128] are still not regarded, the suggested converter representations in the frequency-domain allow to assess the (steady-state) effects of PWM harmonics that are mirrored onto low-frequency signal components in the baseband of the converter. However, while the authors of [42] mainly focus on the frequency-domain modeling of the analog-to-digital conversion of a sinusoidal signal, the authors of [116] derive a MIMO PWM model, but do not consider the effects of the digital controller implementation. Moreover, [116] proposes a multiple-frequency model which depends on the frequency ω of a sinusoidal input signal as

well as the Laplace variable s. From a control engineering point of view, this is rather inconvenient and not properly defined. Although the latest converter models containing sideband harmonics have been developed in the time- or frequency-domain, a model in the continuous Laplace-domain would still be desirable.

Hence, using the concept of complex transfer functions [51, 131], this section aims to derive a similar multiple-frequency grid-converter model in the continuous Laplace-domain, allowing to apply all the well known controller design and analysis methods from the classical linear control theory. After introducing the basic modeling idea and reviewing the principle of the impulse-sampling process and the small-signal representation of the PWM in Sec. 6.1, Sec. 6.2 derives the converter's multiple-frequency current dynamics. Based on the proposed model, Sec. 6.3 deduces a more accurate SISO converter model, which allows to reflect the mirrored high-frequency components that are aliases of the PWM's reference input voltage. Finally, Sec. 6.4 discusses the effects of aliasing on the converter's input admittance and assesses the passivity and stability properties of the resulting closed-loop grid-converter system.

6.1 Revision of the Small-Signal Converter Dynamics

In order to incorporate aliasing effects that are caused by the injection of PWM harmonics, it is proposed to extend the converter model from Sec. 3.51 and not only take the VSC's primary-frequency signal components, $\boldsymbol{x}_{\mathrm{p}}(s)$, into account, but also model the dynamics of multiple sidebands, $\boldsymbol{x}(s + jk\omega_{\mathrm{s}})$, $k = \pm 1, \pm 2, \ldots$. The suggested modeling approach first yields a MIMO input admittance model, which again simplifies to a SISO model if the closed-loop grid-converter system is considered.

6.1.1 Basic Modeling Idea

To begin with, it is assumed that the VSC's LCL filter effectively suppresses above Nyquist frequency components from the grid side, so that

the system's input voltage $\tilde{\boldsymbol{v}}_{\mathrm{g}}(s) = (\tilde{Z}_{\mathrm{g}}(s)\tilde{Y}_{\mathrm{fg}}(s))\boldsymbol{v}_{\mathrm{g}}(s)$ only shows signal components in the low-frequency range, i.e., $|\tilde{\boldsymbol{v}}_{\mathrm{g}}(j\omega)| \approx 0, \forall\, |\omega| > \omega_{\mathrm{N}}$. Then, reviewing the control block diagram of the digitally current-controlled grid-converter system from Fig. 3.13, Fig. 6.1 illustrates a corresponding principle signal flow model.

Here, the blue path represents the flow of low-frequency signal components that lie in the baseband of the converter, i.e., within the frequency range $[-\omega_{\mathrm{N}}, \omega_{\mathrm{N}}]$. For the sake of clarity, these signals are indexed with a 0. The red path exemplarily illustrates the flow of signal components that lie in the k-th sideband, which is defined by the frequency range $[(2k-1)\omega_{\mathrm{N}}, (2k+1)\omega_{\mathrm{N}}]$, $k = \pm 1, \pm 2, \ldots$. This could, for instance, be a pure sinusoidal of the form $\cos(\frac{2}{3}\omega_{\mathrm{s}}t) = (e^{j\frac{2}{3}\omega_{\mathrm{s}}t} + e^{-j\frac{2}{3}\omega_{\mathrm{s}}t})/2$, consisting of two components, one within the frequency range $[\omega_{\mathrm{N}}, 3\omega_{\mathrm{N}}]$ and one within the range $[-3\omega_{\mathrm{N}}, -\omega_{\mathrm{N}}]$. Since the digital control system misinterprets signal components above the converter's Nyquist frequency as components below ω_{N}, the sampler blocks can be understood as elements, which map all input signals to the converter's baseband [39, 119]. This is illustrated by the arrows in the sampler blocks. Deviating from the introduced notation of Sec. 3.2, the resulting low-frequency signal components seen by the digital converter control are denoted with a $'$, e.g., $\boldsymbol{i}_{\mathrm{l}}'$ specifying the primary and complementary baseband components of the sampled current caused through the voltage drop over the converter-side impedance $Y_{\mathrm{fc}}(s)$. After the signal processing by the digital PR controller and the feed-forward filter, the calculated reference voltage $\boldsymbol{v}_{\mathrm{ref}}'$ is transferred to the PWM, which generates a pulse pattern to trigger the semiconductor switches. As described in the Appendix A.2, the VSC output voltage contains a DC component, fundamental components as well as sideband and carrier harmonics. Taking this multiple-frequency behavior into account, the PWM's output $\boldsymbol{v}_{\mathrm{c},0}$ models the fundamental components in the baseband, where the most crucial sideband harmonics that represent aliases of the PWM's reference voltage are reflected by the modulator outputs $\boldsymbol{v}_{\mathrm{c},q}, \forall q > 0$. If the converter implements a single-update PWM, where the current sampling is synchronized to the PWM carrier signal, the in-

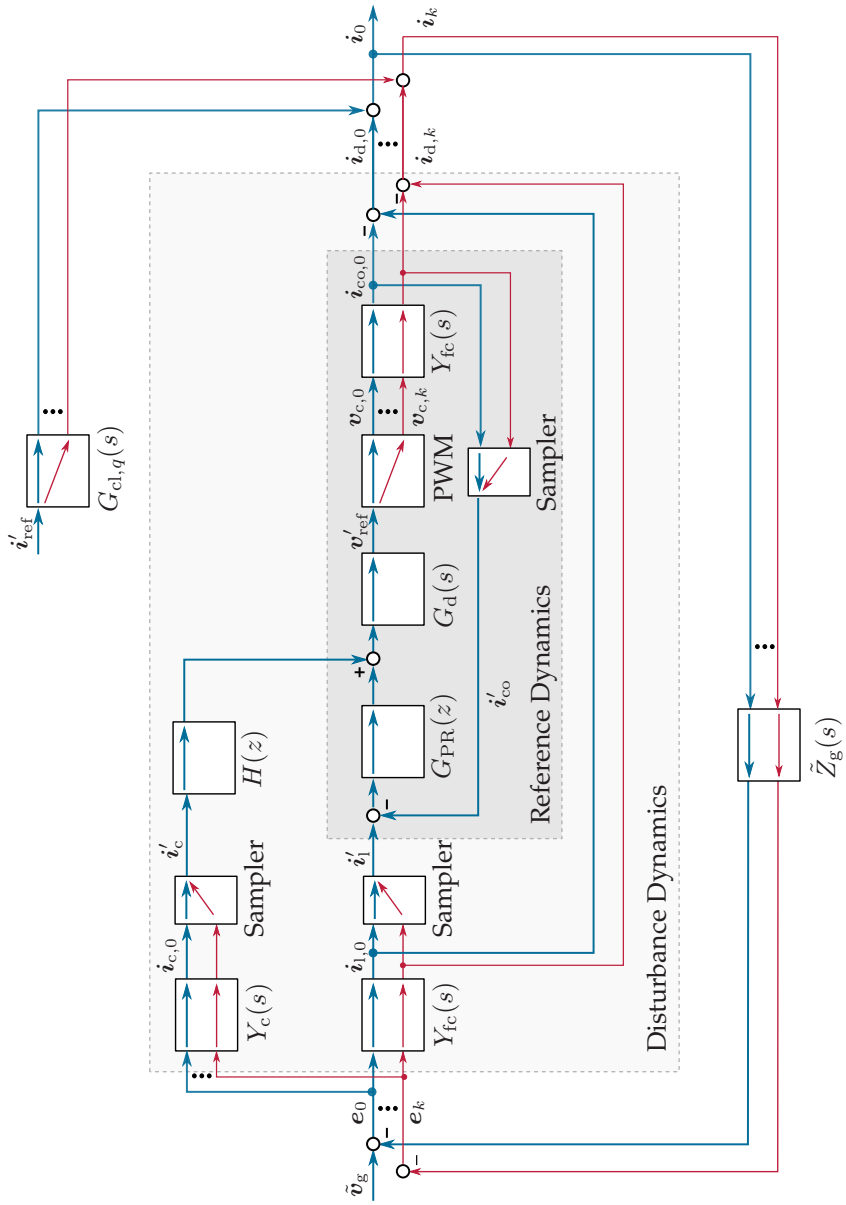

Fig. 6.1: Principle signal flow model of a digitally current-controlled grid-connected VSC with single-update PWM and capacitor current feed-forward, where the baseband and one exemplary above Nyquist frequency signal components are represented by the blue and red signal path, respectively.

tegers $q = k = \pm 1, \pm 2, \ldots$ exactly coincide, allowing to close all existing loops and to deduce a closed-form model of the grid-converter system.

Similar to the harmonic state space modeling concept, see e.g., [81, 140, 165], the presented modeling approach allows to describe each shown path in Fig. 6.1 by an individual transfer function. In particular, focusing on the highlighted dark gray block, the dynamics between the baseband components of the sampled current $\boldsymbol{i}'_1(s)$ and the output current component $\boldsymbol{i}_{\mathrm{co},q}(s)$ in the q-th sideband specify the converter's reference current dynamics, denoted as $G_{\mathrm{cl},q}(s)$. While each $G_{\mathrm{cl},q}(s), \forall q$ defines a (complex) SISO transfer function, the light gray block illustrates the new VSC disturbance dynamics, which can, in contrast to Sec. 3.4, be represented by a complex MIMO transfer function matrix with inputs $\boldsymbol{e}_k(s)$, $k = 0, \pm 1, \pm 2, \ldots$ and outputs $\boldsymbol{i}_{\mathrm{d},k}(s)$, $k = 0, \pm 1, \pm 2, \ldots$. As can be observed, the interconnection of the VSC's MIMO input admittance model with the synthetic grid impedance $\tilde{Z}_{\mathrm{g}}(s)$ results in multiple feedback-loops. At this point it can be imagined that, besides the feedback of baseband components, $\boldsymbol{i}_0$, an amplification of high-frequency current harmonics, $\boldsymbol{i}_k, k = \pm 1, \pm 2, \ldots$, by poorly damped grid resonances might also lead to stability problems [125, 140]. Therefore, in some applications, it could be risky to demand only the passivity of the converter's primary-frequency input admittance $Y_{\mathrm{i,p}}(s) = Y_{\mathrm{i},00}(s)$, defining the behavior between $\boldsymbol{e}_0(s)$ and $\boldsymbol{i}_{\mathrm{d},0}(s)$ and to neglect all mirrored input voltage components from the sidebands. On the other hand, since aliases of possibly emerging high-frequency components in the (stiff) grid voltage $\tilde{\boldsymbol{v}}_{\mathrm{g}} = \tilde{\boldsymbol{v}}_{\mathrm{g},0}$ can be considered as (independent) disturbances, those components do principally not change the stability properties of the linear closed-loop system, but they may worsen the quality of the injected current.

6.1.2 Multiple-Frequency Modeling of the System Components

Based on the reviewed functional principle and the associated system components of the grid-converter system from Fig. 6.1, this section aims

to derive the Laplace-domain models of the illustrated samplers and the discussed multiple-frequency behavior of the PWM.

Alternative Sampler Model

Besides the mathematical concept of describing the sampling process by the impulse-modulation technique (3.15) in the time-domain, a sampler can also be understood as a component in the frequency-domain that maps all signal components of its input into the baseband and generates a 'new' output, which can be processed by the digital control system. Instead of defining $\boldsymbol{x}(t)$ as the input of the sampler, which is modulated by a train of unit impulses [39, 119], from now on the sampler input should be given by an infinite number of right-sided, Laplace-transformable signals, $\boldsymbol{x}_k(t)$, $k = 0, \pm1, \pm2, \ldots$, with $\boldsymbol{x}_k(t) = \boldsymbol{0}\,\forall t < 0$, see Fig. 6.1. It is assumed that each (fictitious) signal $\boldsymbol{x}_k(t)$ sufficiently approximates the positive- or negative sequence components of the original input signal $\boldsymbol{x}(t)$, lying in the frequency range $[(2k-1)\omega_\mathrm{N}, (2k+1)\omega_\mathrm{N}]$, but also has components outside the limits. Then, it is proposed to redefine the sampling process of a continuous signal in the Laplace-domain as [1]

$$\begin{aligned}\boldsymbol{x}'(s) &= \mathcal{L}\left\{\frac{1}{T_\mathrm{s}}\sum_{k=-\infty}^{\infty}\boldsymbol{x}_k(t)\cdot e^{-jk\omega_\mathrm{s}t}\right\} = \frac{1}{T_\mathrm{s}}\sum_{k=-\infty}^{\infty}\boldsymbol{x}_k(s+jk\omega_\mathrm{s}) \\ &= \frac{1}{T_\mathrm{s}}\left[\ldots+\boldsymbol{x}_{-1}(s-j\omega_\mathrm{s})+\boldsymbol{x}_0(s)+\boldsymbol{x}_1(s+j\omega_\mathrm{s})+\ldots\right]. \qquad (6.1)\end{aligned}$$

Here, the individual summands, $\boldsymbol{x}_k(t)\cdot e^{-jk\omega_\mathrm{s}t}$, can be interpreted as (α,β)-frame space vector components that are transformed into a synchronous reference-frame, rotating with an integer multiple of the converter's sampling frequency, $k\omega_\mathrm{s}$, respectively [51]. By performing this

[1] Similar to the (exact) representation of the discrete Laplace transform $\boldsymbol{x}^*(s)$ via Laplace transforms, see [114], the introduced transformation (6.1) can be assumed to yield a reasonable sampler model only if certain conditions are met, compare also to the footnote on page 59. In the following it should be presupposed that the fictitious, right-sided signals or systems $\boldsymbol{x}_k(t)$ have a sufficiently high low-pass characteristic, such that the first sum in (6.1) converges and the element-wise application of the Laplace transform is justified. Further, it is assumed that, even though $\boldsymbol{x}_{-k}(t)$ and $\boldsymbol{x}_k(t)$ might be two different, complex functions, their sum, $\boldsymbol{x}_{-k}(t)+\boldsymbol{x}_k(t)$, always results in a purely real function with symmetric frequency response.

(coordinate) transformation, each signal component of the k-th sideband of $\boldsymbol{x}_k(t)$ is shifted to the baseband of the converter, while components outside the range $[(2k-1)\omega_\mathrm{N}, (2k+1)\omega_\mathrm{N}]$ are shifted to the neighboring sidebands. The associated idea is exemplarily illustrated by the resulting linear-scaled amplitude spectra of the current $\boldsymbol{i}_\mathrm{l}(j\omega) = Y_\mathrm{fc}(j\omega)\boldsymbol{e}(j\omega)$ and $T_\mathrm{s}\boldsymbol{i}_\mathrm{l}'(j\omega) = T_\mathrm{s}\left(Y_\mathrm{fc}\boldsymbol{e}\right)'(j\omega)$ in Fig. 6.2, where, as in Sec. 3.3, the (real) voltage $\boldsymbol{e}(t)$ consists of two purely sinusoidal components, one in the low-frequency range and one above the Nyquist frequency.

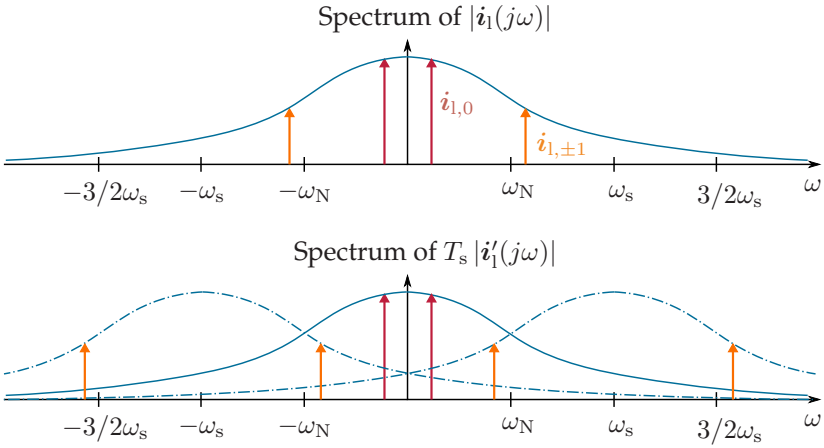

Fig. 6.2: Amplitude spectra of the current component $\boldsymbol{i}_\mathrm{l}(j\omega) = Y_\mathrm{fc}(j\omega)\boldsymbol{e}(j\omega)$ and the transformed component $T_\mathrm{s}\cdot\boldsymbol{i}_\mathrm{l}'(j\omega) = T_\mathrm{s}\left(Y_\mathrm{fc}\boldsymbol{e}\right)'(j\omega)$, where the red arrows mark signal components in the baseband of $\boldsymbol{i}_\mathrm{l}(j\omega)$ and the orange arrows indicate signal components lying within the 1-th and -1-th sideband of $\boldsymbol{i}_\mathrm{l}(j\omega)$.

At this point, it should be highlighted that (6.1) does not describe the discrete Laplace transform of $\boldsymbol{x}^*(t)$ (nor the z-transform of $\boldsymbol{x}(kT_\mathrm{s})$) and that the spectrum of $\boldsymbol{x}'(s)$ is not periodic in general, compare Fig. 6.2 to Fig. 3.12. However, if (6.1) converges, $\boldsymbol{x}'(s)$ represents the Laplace-transformed of a signal (or impulse response of a system), which baseband signal components are approximately equivalent to those of $\boldsymbol{i}^*(s) = \mathcal{L}\{\boldsymbol{x}^*(t)\}$ from (3.40). Since the remaining signal components of $\boldsymbol{x}'(s)$ outside the converter's baseband have no proper physical meaning, the Nyquist frequency thus simultaneously defines the range of validity of

the suggested alternative sampler model. This range is also in accordance with e.g., the EN 50388-2 [6], which requires to verify the passivity of active-font-ends from the fifth harmonic, $5\omega_\mathrm{r}$, up to ω_N, defined by the controller's sampling frequency.

If hypothetically it is assumed that all Laplace transforms, $\boldsymbol{x}_k(s)$, are ideally band-limited and all signal components lie in the respective frequency range $[(2k-1)\omega_\mathrm{N}, (2k+1)\omega_\mathrm{N}]$, the resulting $\boldsymbol{x}'(s)$ only contains signal components in the range $[-\omega_\mathrm{N}, \omega_\mathrm{N}]$ and does not have any high-frequency components in the sidebands, i.e., $|\boldsymbol{x}'(j\omega)| = 0, \forall\, |\omega| > \omega_\mathrm{N}$. This property should also be reflected by the shown signal flow model and sampler blocks in Fig. 6.1, where a noncompliance with the assumption of ideally band-limited signals (which do practically not exist due to the causality condition [39, 114]) does not affect the model and should therefore be considered for illustrative purposes only. Finally, it should be noticed that, if each continuous input signal $\boldsymbol{x}_k(t)$ is specified to be the same, (6.1) is identical to the discrete Laplace transform (3.40), and thus, $\boldsymbol{x}^*(s) = \boldsymbol{x}(z)|_{z=e^{sT_\mathrm{s}}} = \boldsymbol{x}'(s)$ if $\boldsymbol{x}_k(t) = \boldsymbol{x}(t), \forall k$.

Piece-Wise Defined Multiple-Frequency PWM Model

The main challenge in modeling the PWM is to maintain the identified small-signal behavior from Sec. 3.2.2 and not to neglect the generation of all the high-frequency switching harmonics at the same time. If aliasing effects are to be analyzed, it is reasonable to take those PWM voltage harmonics into account that coincide with the complementary components of the impulse-sampled currents [42, 81, 116, 140]. Using the introduced notation and considering a single-update PWM, where the sampling instants are synchronized to the switching instants, these voltage components are specified by $\boldsymbol{v}_{\mathrm{c},q}(s + jq\omega_\mathrm{s})$, $q = \pm 1, \pm 2, \ldots$. Similar to the identified small-signal PWM behavior in Fig. 3.7, Fig. 6.3 shows the normalized magnitude and phase characteristics of a digital single-update PWM with computational delay, using a single sinusoidal reference input voltage $V_\mathrm{ref}(t) = V_\mathrm{DC}/2 + a_\mathrm{m} V_\mathrm{DC}/2 \sin(\omega_\mathrm{r} t)$ with varying amplitude modulation indices, $a_\mathrm{m} \in [0.05, 1]$, and frequencies, $\omega_\mathrm{r} \in [\omega_\mathrm{s}/20, \omega_\mathrm{N}]$. This time,

not only the modulator's (steady-state) behavior of the fundamental components in the baseband is shown, but also the identified characteristics of several positive-sequence harmonics, representing an integer multiple of the reference signal's frequency, $\omega_\mathrm{r} + q\omega_\mathrm{s}, q = 1, 2, 3$.

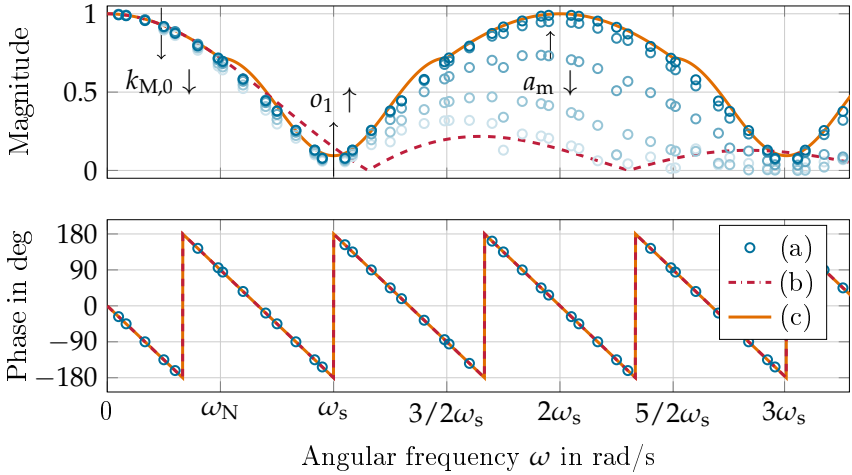

Fig. 6.3: Magnitude and phase characteristics of (a) the identified nonlinear single-update PWM with computational delay for decreasing modulation indices (from light blue to dark blue), and the Bode plots of (b) the (baseband) PWM model $G_\mathrm{PWM}(s)/T_\mathrm{s}G_\mathrm{d}(s)$ with $D_0 = 0.868$, and (c) the weighted concatenation of the proposed piece-wise defined multiple-frequency PWM model for ideally band-limited input signals.

As can be observed, the nonlinear modulator produces a significant number of high-frequency harmonics, which are most frequently neglected in classical small-signal converter modeling approaches [140, 165]. While a decreasing amplitude modulation index, a_m, leads to a rather moderate decrease in the attenuation of voltage components below the switching frequency ω_s, higher frequency components react much more sensitive to variations of the reference voltage's magnitude. Assuming ω_s to be an integer multiple of ω_r, this (nonlinear) behavior can also be verified by evaluating the fundamental and sideband components of the analytic PWM description (A.18) from the Appendix A.2, as exemplarily shown

in Fig. A.5. Hence, even though the derived PWM model $G_{\mathrm{PWM}}(s)/T_{\mathrm{s}}$ from (3.23) yields a worst-case approximation for the modulator's small-signal behavior in the low-frequency range up to the Nyquist frequency ω_{N}, see also Fig. 3.7, the PWM model attenuates higher switching harmonics far too much. For this reason, it is not recommended to use (3.23) for representing the converter's high-frequency behavior. As becomes clear, this is also the case for the more simple (classical) ZOH PWM model, $G_{\mathrm{ZOH}}(s)/T_{\mathrm{s}}$, which is nevertheless utilized in research that claims to model and assess the VSC's input admittance properties above the Nyquist frequency, see e.g., [41, 42, 53].

In order to model the crucial high-frequency sideband harmonics more accurately, it is proposed to use a piece-wise defined multiple-frequency PWM plus computational delay model of the form

$$\boldsymbol{v}_{\mathrm{c},q}(s+jq\omega_{\mathrm{s}}) = G_{\mathrm{PWM},q}(s)G_{\mathrm{d,q}}(s)\boldsymbol{v}'_{\mathrm{ref}}(s), \qquad q=0,\pm1,\pm2,\ldots. \tag{6.2}$$

Hereby, the transfer functions $G_{\mathrm{PWM},q}(s)G_{\mathrm{d,q}}(s)$, $q = 0,\pm1,\pm2,\ldots$ specify individual small-signal PWM models for every frequency band $[(2q-1)\omega_{\mathrm{N}},(2q+1)\omega_{\mathrm{N}}]$ and the transformation $s \mapsto s+jq\omega_{\mathrm{s}}$ in the argument of $\boldsymbol{v}_{\mathrm{c},q}(s)$ ensures that the baseband components of $G_{\mathrm{PWM},q}(s)G_{\mathrm{d,q}}(s)\boldsymbol{v}'_{\mathrm{ref}}(s)$ are transformed to the q-th sideband [51, 131]. This is in contrast to classical small-signal SISO PWM models, where the associated transfer function $G_{\mathrm{PWM}}(s)$ in combination with the periodic input, $\boldsymbol{v}^{*}_{\mathrm{ref}}(s)$, inherently define all high-frequency output voltage harmonics that are aliases of the input [39]. On the other hand, the adopted approach is somehow similar to the suggested frequency-domain PWM modeling idea from [116], but can completely be carried out in the continuous Laplace-domain and additionally provides more degrees of freedom in the definition of each $G_{\mathrm{PWM},q}(s)G_{\mathrm{d,q}}(s)$. In general, the PWM model (6.2) is constructed so that, if the (sampled) input $\boldsymbol{v}'_{\mathrm{ref}}(s)$ represents an ideally band-limited signal, which only has primary-signal components in the frequency range $[-\omega_{\mathrm{N}},\omega_{\mathrm{N}}]$, the outputs $\boldsymbol{v}_{\mathrm{c,q}}(s)$ each contain only signal components within the q-th sideband, i.e., $[(2q-1)\omega_{\mathrm{N}},(2q+1)\omega_{\mathrm{N}}]$. In combination with the proposed alternative sampler model (6.1), this

enables to describe the resulting (sampled-data) converter system more accurately by a complex MIMO transfer function matrix in the s-domain, instead of a SISO system in the z-domain.

After a thorough investigation of the identified PWM characteristic from Fig 6.3, it is suggested to choose the transfer functions $G_{\mathrm{PWM},q}(s)G_{\mathrm{d,q}}(s)$ for a single-update PWM with $T_{\mathrm{c}} = T_{\mathrm{s}}$ as

$$G_{\mathrm{PWM},q}(s)G_{\mathrm{d,q}}(s) = k_{\mathrm{M},q}\frac{1-e^{-sD_{0,q}T_{\mathrm{s}}}}{sD_{0,q}}e^{-s\left(T_{\mathrm{d}}-\frac{D_{0,q}}{2}T_{\mathrm{s}}\right)} \tag{6.3}$$

if q is even and

$$G_{\mathrm{PWM},q}(s)G_{\mathrm{d,q}}(s) = k_{\mathrm{M},q}\frac{1-e^{-sD_{0,q}T_{\mathrm{s}}}}{sD_{0,q}}e^{-s\left(\frac{1-D_{0,q}}{2}\right)T_{\mathrm{s}}}\cdot \left(\frac{\left(1-e^{-sD_{0,q}T_{\mathrm{s}}}\right)^2}{4}e^{-s(1-D_{0,q})T_{\mathrm{s}}} - o_q e^{-sT_{\mathrm{s}}}\right) \tag{6.4}$$

if q is odd. The parameters $k_{\mathrm{M},q}$, $D_{0,q}$, and o_q are individual PWM gains, averaged duty cycles, and offset terms for the q-th frequency band, respectively, allowing to adapt the model on different PWM schemes and averaged (a priori known) amplitude modulation indices. While the proposed PWM plus computational delay dynamics (6.3) for baseband and even sideband components are basically identical to the introduced model from Sec. 3.2.2, where, this time, the magnitude decreases from $T_{\mathrm{s}}k_{\mathrm{M},q}$ at $\omega = 0$ to 0 at $\omega = \omega_{\mathrm{s}}/D_{0,q}$, the model (6.4) shows (more or less) the opposite behavior for odd sidebands. More precisely, the frequency response of (6.4) for $q = \pm 1, \pm 3, \ldots$ can be calculated to be

$$G_{\mathrm{PWM},q}(j\omega)G_{\mathrm{d,q}}(j\omega) = -k_{\mathrm{M},q}\frac{\sin(\omega D_{0,q}T_{\mathrm{s}}/2)}{\omega D_{0,q}/2}\left(\sin^2(\omega D_{0,q}T_{\mathrm{s}}/2)+o_q\right)e^{-j\omega T_{\mathrm{d}}}. \tag{6.5}$$

As can be observed when neglecting the term $\sin(\omega D_{0,q}T_{\mathrm{s}}/2)/(\omega D_{0,q}/2)$, scaled by $1/T_{\mathrm{s}}$, the weighted and shifted (squared) sine function yields a magnitude that increases from $T_{\mathrm{s}}k_{\mathrm{M},q}o_q$ at $\omega = 0\,\mathrm{rad/s}$ to $T_{\mathrm{s}}k_{\mathrm{M},q}(1+o_q)$ at $\omega = \omega_{\mathrm{s}}/(2D_{0,q})$. In combination with the preceding sinc-function, this

behavior remains rather unchanged for small frequencies, $\omega \ll \omega_\mathrm{s}/6$, whereas the magnitude is more and more reduced for higher frequencies and approaches 0 for $\omega \to \infty$. This is similar to the frequency response of (6.3) and shows that both models act like a low-pass filter for high frequency components, ensuring that each $\boldsymbol{v}_{\mathrm{c},q}(s), \forall q$ predominantly has signal components in the q-th frequency band. The phase lag of (6.5) is principally the same as for even sidebands, but, due to the negative sign, shifted by $+\pi$, which guarantees a continuous reduction of the phase response when concatenating the piece-wise defined PWM transfer functions (6.3) and (6.4).

It is generally reasonable that the amplitude responses of neighbored frequency bands smoothly pass in each other, such that the concatenated response does not show any (jump) discontinuity, i.e., it should be ensured that $|G_{\mathrm{PWM},q}(jq\omega_\mathrm{s}/2)| = |G_{\mathrm{PWM},q-1}(jq\omega_\mathrm{s}/2)|, \forall q \geq 1$. Further, it is advisable to set $G_{\mathrm{PWM},-q}(s)G_{\mathrm{d,-q}}(s) = G_{\mathrm{PWM},q}(s)G_{\mathrm{d,q}}(s)$, $\forall q \geq 1$ to get a symmetrical concatenated PWM frequency response for positive- and negative input sequence components, which should not be overlooked when working with complex transfer functions [51,131]. Taking these two basic guidelines into account, less or more complex parameterizations for (6.3) and (6.4) can be deduced. For instance, regarding the findings from our work [1] and choosing $D_{0,q} = 0.868$ and $k_{\mathrm{M},q} = 1, q = 0, \pm 2, \pm 4, \ldots$, the provided degrees of freedom reduce to the choice of $k_{\mathrm{M},q}$, $D_{0,q}$, and o_q for all odd sidebands. If all o_q are set to e.g., 0.1, which seems to be an appropriate selection to result in an upper magnitude bound of the identified PWM characteristic if $k_{\mathrm{M},q} \approx 1$, see Fig. 6.3, the magnitude of (6.5) always shows a local maximum at $\omega D_{0,q} T_\mathrm{s}/2 \approx 1.304$. Requiring that the found maximum emerges exactly at $\omega_\mathrm{s}/2$, the averaged duty cycles for all odd PWM transfer functions can be set to $D_{0,q} = 1.304 \cdot 4/(T_\mathrm{s}\,\omega_\mathrm{s}) \approx 0.8302, q = \pm 1, \pm 3, \ldots$. And finally, evaluating the constraint $|G_{\mathrm{PWM},q}(jq\omega_\mathrm{s}/2)| = |G_{\mathrm{PWM},q-1}(jq\omega_\mathrm{s}/2)|, \forall q \geq 1$ with the given parameters, the gains $k_{\mathrm{M},q}$ can be selected as $k_{\mathrm{M},q} \approx 0.9415, q = \pm 1, \pm 3, \ldots$. Tab. 6.1 summarizes the suggested PWM model parameterization, which is characterized by only two parameter sets for the infinite number of

transfer functions, $G_{\mathrm{PWM},q}(s)G_{\mathrm{d,q}}(s)$, namely one for the even and one for the odd sideband components.

Table 6.1: Piece-wise defined transfer function parameters of the proposed multiple-frequency PWM model

Parameter	Parameterization
Even PWM gains	$k_{\mathrm{M},q} = 1, q = 0, \pm 2, \pm 4, \ldots$
Even duty cycles	$D_{0,q} = 0.868, q = 0, \pm 2, \pm 4, \ldots$
Odd PWM gains	$k_{\mathrm{M},q} = 0.9415, q = \pm 1, \pm 3, \ldots$
Odd duty cycles	$D_{0,q} = 0.8302, q = \pm 1, \pm 3, \ldots$
Odd offset terms	$o_q = 0.1, q = \pm 1, \pm 3, \ldots$

Applying the exemplary parameters from Tab. 6.1 to the transfer functions (6.3) and (6.4), Fig. 6.3 illustrates the resulting (concatenated) frequency response of the proposed multiple-frequency PWM model (6.2), weighted by $1/T_{\mathrm{s}}$. With this choice, each $G_{\mathrm{PWM},q}(s)G_{\mathrm{d,q}}(s)$ yields an upper bound for the attenuation of the identified samples in the associated frequency band, $[(2q-1)\omega_{\mathrm{N}}, (2q+1)\omega_{\mathrm{N}}]$. On the other hand, it can be seen that the phase responses exactly match the identified characteristic of the nonlinear modulator. It should be remarked that this does not necessarily apply to other components outside the respective q-th frequency band. The unavoidable mismatch does however not need to be considered further, as each individual transfer function, $G_{\mathrm{PWM},q}(s)G_{\mathrm{d,q}}(s)$, is only designed to be valid on the interval $[(2q-1)\omega_{\mathrm{N}}, (2q+1)\omega_{\mathrm{N}}]$. If necessary, the individual offset terms, o_q, can be increased or decreased to result in a more or less conservative model for odd harmonics near the frequencies $\pm\omega_{\mathrm{s}}, \pm 3\,\omega_{\mathrm{s}}, \ldots$. In addition, since it can be expected that the emerging switching harmonics become less and less significant for very high frequencies [64], the PWM gains, $k_{\mathrm{M},q}$, might be reduced progressively for an increasing q, but is not done here for simplicity.

Therefore, although the proposed piece-wise defined multiple-frequency PWM model does not describe the nonlinear generation of all switching harmonics, e.g., sideband harmonics that result from the combination of multiple signal components in the baseband, it can be assumed that the

proposed modeling approach mostly yields a rather conservative steady-state PWM approximation in each frequency band. But, the model still gives much less conservative results than utilizing a purely time delay PWM model of the form $T_\mathrm{s}e^{-sT_\mathrm{d}}$ and can be considered to be more accurate than other existing small-signal PWM models. In practice, the generated (steady-state) harmonics will most likely not appear as concentrated as modeled and the converter's output voltage spectrum will be spread over more frequencies, see e.g., [64, 159]. In this regard, the suggested model in Fig. 6.1 complies with the railway standard EN 50388-2 [6], which allows to focus on the linear steady-state behavior and neglect nonlinear (high-frequency) effects when calculating the converter input admittance of active-front-ends [42, 110].

6.2 Converter Current Dynamics

Similar to the procedure from Sec. 3.3, the multiple-frequency converter current dynamics can be derived from the VSC's principle signal flow model of Fig. 6.1. Given the modified sampler and PWM model from the previous section, the q-th current component, $\boldsymbol{i}_{\mathrm{co},q}$, at the output of the highlighted block of the reference current dynamics is described by

$$\begin{aligned}\boldsymbol{i}_{\mathrm{co},q}(s+jq\omega_\mathrm{s}) =& Y_\mathrm{fc}(s+jq\omega_\mathrm{s})G_{\mathrm{PWM},q}(s)G_{\mathrm{d,q}}(s)\cdot \\ & \left[G_\mathrm{PR}(z)\left(\boldsymbol{i}'_\mathrm{l}(s)-\boldsymbol{i}'_\mathrm{co}(s)\right)+H(z)\boldsymbol{i}'_\mathrm{c}(s)\right] \end{aligned} \tag{6.6}$$

where, due to the discussed advantages from Sec. 5.3, only a capacitor current feed-forward is considered from now on. Taking the extension with the associated initial value, $\boldsymbol{x}(0^+)$, into account, the PR controller's pulse transfer function (3.34) can also be expressed as $G_\mathrm{PR}(z)|_{z=e^{sT_\mathrm{s}}} = G^*_\mathrm{PR}(s) = G'_\mathrm{PR}(s)$ and similarly, $H(z)|_{z=e^{sT_\mathrm{s}}} = H^*(s) = H'(s)$. Then, in the special case of a single-update PWM, where the sampling instants are synchronized to the modulator's carrier signal, and thus, $k = q = 0, \pm1, \pm2, \ldots$, an application of the introduced transformation (6.1) on (6.6) yields the (baseband) components of the sampled current seen by the converter, i.e.,

$$\boldsymbol{i}'_{\mathrm{co}}(s) = \frac{1}{T_{\mathrm{s}}} \sum_{q=-\infty}^{\infty} Y_{\mathrm{fc}}(s + jq\omega_{\mathrm{s}}) G_{\mathrm{PWM},q}(s) G_{\mathrm{d,q}}(s) \cdot \left[G'_{\mathrm{PR}}(s) \left(\boldsymbol{i}'_{\mathrm{l}}(s) - \boldsymbol{i}'_{\mathrm{co}}(s) \right) + H'(s) \boldsymbol{i}'_{\mathrm{c}}(s) \right]. \tag{6.7}$$

Discretized Plant Dynamics

Observing that the reference voltage at the input of the PWM model (6.2) is the same for the baseband as well as all sideband components, it can be noticed that $\boldsymbol{v}'_{\mathrm{ref}}(s) = [G'_{\mathrm{PR}}(s) \left(\boldsymbol{i}'_{\mathrm{l}}(s) - \boldsymbol{i}'_{\mathrm{co}}(s) \right) + H'(s) \boldsymbol{i}'_{\mathrm{c}}(s)]$ in (6.7) can be factorized, where, according to (6.1), the remaining part on the right hand side is defined as

$$(Y_{\mathrm{fc}} G_{\mathrm{PWM}} G_{\mathrm{d}})'(s) = \frac{1}{T_{\mathrm{s}}} \sum_{q=-\infty}^{\infty} Y_{\mathrm{fc}}(s + jq\omega_{\mathrm{s}}) G_{\mathrm{PWM,q}}(s) G_{\mathrm{d,q}}(s). \tag{6.8}$$

If it is assumed that the converter-side filter admittance plus PWM model has a sufficiently large low-pass characteristic and consequently (6.8) converges, $(Y_{\mathrm{fc}} G_{\mathrm{PWM}} G_{\mathrm{d}})'(s)$ represents an equivalent to the plant's common z-transform $(Y_{\mathrm{fc}} G_{\mathrm{PWM}} G_{\mathrm{d}})(z)|_{z=e^{sT_{\mathrm{s}}}} = (Y_{\mathrm{fc}} G_{\mathrm{PWM}} G_{\mathrm{d}})^*(s)$ obtained by the impulse modulation technique [39, 119]. At this point, it should however be noticed that $(Y_{\mathrm{fc}} G_{\mathrm{PWM}} G_{\mathrm{d}})'(s)$ is only identical to $(Y_{\mathrm{fc}} G_{\mathrm{PWM}} G_{\mathrm{d}})^*(s)$ in the special case where $G_{\mathrm{PWM,q}}(s) G_{\mathrm{d,q}}(s)$ is specified to be $G_{\mathrm{PWM}}(s + jq\omega_{\mathrm{s}}) G_{\mathrm{d}}(s + jq\omega_{\mathrm{s}}), q = 0, \pm 1, \pm 2, \ldots$. Hence, in contrast to the plant's common z-transform (3.26), which assumes that the PWM's generated harmonics follow a sinc-function of the form (3.24), the transform (6.8) allows to model the modulator's (less optimistic) small-signal low- and high-frequency behavior more accurately. In this context, the introduced transformation can be understood as a more general method to describe the baseband dynamics of discretized plants that are preceded by digital single-update PWM units.

For instance, following the suggested parameterization from Tab. 6.1 and implementing the multiple-frequency PWM model shown in Fig. 6.3, Fig. 6.4 compares the (discretized) plant dynamics which are used by the quasi-analog, the primary-frequency, and the multiple-frequency model of the VSC under study. As can be noticed, there mainly exist

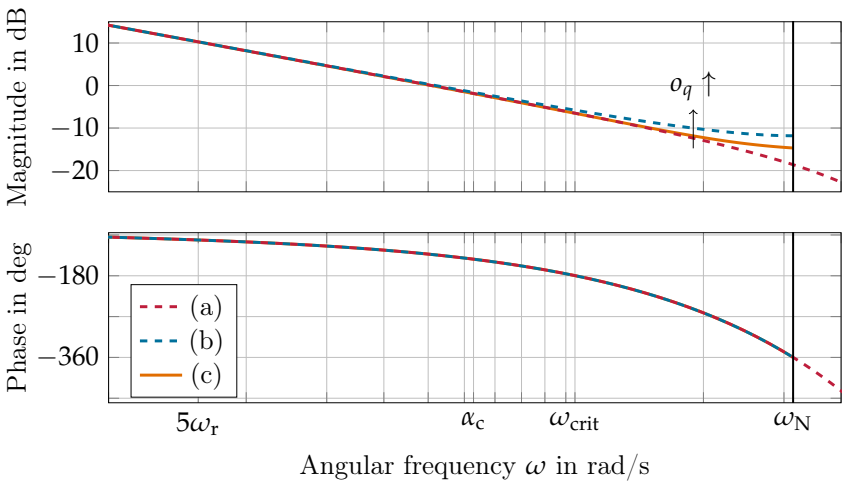

Fig. 6.4: Bode plots of (a) the continuous plant plus PWM dynamics $Y_\mathrm{fc}(s)G_\mathrm{PWM}(s)/T_\mathrm{s}G_\mathrm{d}(s)$, (b) the discretized dynamics $(Y_\mathrm{fc}G_\mathrm{PWM}G_\mathrm{d})^*(s)$ from (3.26), and (c) the dynamics $(Y_\mathrm{fc}G_\mathrm{PWM}G_\mathrm{d})'(s)$ from (6.8), which uses the transform (6.1) and the proposed multiple-frequency PWM model.

differences in the amplitude responses in the high-frequency range, where $\left|(Y_\mathrm{fc}G_\mathrm{PWM}G_\mathrm{d})'(s)\right|$ differs more or less from the other responses by varying the offset terms, o_q. On the other hand, the phase responses of all three models match well as long as the total effective time delay, T_d, keeps unchained. But, even though only little deviations emerge, it can be expected that the resulting (new) VSC reference and disturbance dynamics differ from the established primary-frequency model from Sec. 3.4.2. This might especially be considered when assessing the properties of the VSC input admittance in the most critical frequency range, near the Nyquist frequency.

By a first observation, the calculation of (6.8) may seem much more complex than the calculation of the plant's common z-transform $\left(Y_\mathrm{fc}G_\mathrm{PWM}G_\mathrm{d}\right)(z)|_{z=e^{sT_\mathrm{s}}}$ from (3.26), since the involved transfer functions of the piece-wise defined PWM model may be different in each frequency range. From a practical point of view, however, the low-pass

characteristic of $Y_{\mathrm{fc}}(s)$ from (3.5) as well as the PWM's attenuation effect for signal components in the very high frequency range should be taken into account. In this regard, the exact dynamics of (6.8) can usually be approximated with reasonable accuracy by restricting the calculation to the baseband components and a small number of positive- and negative-sequence components, instead of evaluating the full range of q up to $\pm\infty$. Some PWM transfer functions, $G_{\mathrm{PWM},q}(s)G_{\mathrm{d,q}}(s)$, even allow a more simple calculation of $(Y_{\mathrm{fc}}G_{\mathrm{PWM}}G_{\mathrm{d}})'(s)$ by exploiting the similarity of the introduced transformation (6.1) to the definition of the discrete Laplace transform (3.40) and its calculation via Laplace transforms from [114]. In particular, regarding the special case where all even and odd piece-wise defined PWM models are specified by $G_{\mathrm{PWM},0}(s)G_{\mathrm{d},0}(s)$ and $G_{\mathrm{PWM},1}(s)G_{\mathrm{d},1}(s)$, respectively, (6.8) can be decomposed into

$$\begin{aligned}(Y_{\mathrm{fc}}G_{\mathrm{PWM}}G_{\mathrm{d}})'(s) = {} & G_{\mathrm{PWM},0}(s)G_{\mathrm{d},0}(s)\frac{1}{T_{\mathrm{s}}}\sum_{\substack{q=-\infty\\ q\text{ even}}}^{\infty} Y_{\mathrm{fc}}(s+jq\omega_{\mathrm{s}}) \\ & + G_{\mathrm{PWM},1}(s)G_{\mathrm{d},1}(s)\frac{1}{T_{\mathrm{s}}}\sum_{\substack{q=-\infty\\ q\text{ odd}}}^{\infty} Y_{\mathrm{fc}}(s+jq\omega_{\mathrm{s}}).\end{aligned} \tag{6.9}$$

After some calculation, which is given in detail in the Appendix A.4, the infinite sums in (6.9) can be reformulated into two explicit transfer functions and (6.9) can finally also be expressed as

$$\begin{aligned}(Y_{\mathrm{fc}}G_{\mathrm{PWM}}G_{\mathrm{d}})'(s) = {} & \frac{G_{\mathrm{PWM},0}(s)G_{\mathrm{d},0}(s)}{4\,l_{\mathrm{fc}}}\frac{1+e^{-(s+\frac{r_{\mathrm{fc}}}{l_{\mathrm{fc}}})\frac{T_{\mathrm{s}}}{2}}}{1-e^{-(s+\frac{r_{\mathrm{fc}}}{l_{\mathrm{fc}}})\frac{T_{\mathrm{s}}}{2}}} \\ & + \frac{G_{\mathrm{PWM},1}(s)G_{\mathrm{d},1}(s)}{4\,l_{\mathrm{fc}}}\frac{1-e^{-(s+\frac{r_{\mathrm{fc}}}{l_{\mathrm{fc}}})\frac{T_{\mathrm{s}}}{2}}}{1+e^{-(s+\frac{r_{\mathrm{fc}}}{l_{\mathrm{fc}}})\frac{T_{\mathrm{s}}}{2}}}.\end{aligned} \tag{6.10}$$

Hence, due to the resulting simplification of (6.8) for identical even and odd piece-wise defined transfer functions, $G_{\mathrm{PWM},q}(s)G_{\mathrm{d,q}}(s)$, it is often not necessary to evaluate an infinite sum or make a restrictive approximation for modeling the converter current dynamics. This is in contrast

to the modeling approaches of e.g., Harnefors et al. in [53] or San et al. in [116], where both authors use a rather impractical sum representation in their suggested multiple-frequency converter models. Instead, given the proposed multiple-frequency PWM model (6.2) with the transfer functions (6.3), (6.4) and following the presented parameterization guidelines, (6.10) gives a simple closed-form equation of the (discretized) plant dynamics seen by the converter. Fig. 6.4 illustrates the resulting frequency response, where it was simulatively verified that the sum from (6.8) converges to the corresponding solution (6.10) when simultaneously increasing the number of positive and negative sidebands for the calculation.

Depending on the representative even and odd PWM transfer functions, $G_{\mathrm{PWM},0}(s)G_{\mathrm{d},0}(s)$ and $G_{\mathrm{PWM},1}(s)G_{\mathrm{d},1}(s)$, (6.10) can also be further simplified. Specifically, still focusing on a single-update PWM and defining $G_{\mathrm{PWM},0}(s)G_{\mathrm{d},0}(s) = T_{\mathrm{s}}e^{-sT_{\mathrm{d}}}$ and $G_{\mathrm{PWM},1}(s)G_{\mathrm{d},1}(s) = -T_{\mathrm{s}}e^{-sT_{\mathrm{d}}}$, which corresponds to a simple (worst-case) time delay PWM model [1, 53, 55], the dynamics of $(Y_{\mathrm{fc}}G_{\mathrm{PWM}}G_{\mathrm{d}})'(s)$ become $T_{\mathrm{s}}/l_{\mathrm{fc}}e^{-(4s+\frac{r_{\mathrm{fc}}}{l_{\mathrm{fc}}})\frac{T_{\mathrm{s}}}{2}}/(1-e^{-(s+\frac{r_{\mathrm{fc}}}{l_{\mathrm{fc}}})T_{\mathrm{s}}})$. As can be recalculated, the expression is equivalent to the (modified) z-transform of $Y_{\mathrm{fc}}(s)T_{\mathrm{s}}e^{-sT_{\mathrm{d}}}$, written in the s-domain. Moreover, (6.10) simplifies to the classical z-transform of $Y_{\mathrm{fc}}(s)$, i.e., $\mathcal{Z}\left\{\mathcal{L}^{-1}\left\{Y_{\mathrm{fc}}(s)\right\}\right\}|_{z=e^{sT_{\mathrm{s}}}} = (1/l_{\mathrm{fc}})/(1-e^{-(s+\frac{r_{\mathrm{fc}}}{l_{\mathrm{fc}}})T_{\mathrm{s}}})$, by setting $G_{\mathrm{PWM},0}(s)G_{\mathrm{d},0}(s) = G_{\mathrm{PWM},1}(s)G_{\mathrm{d},1}(s) = 1$ and extending (6.1) by the halved jump high of $Y_{\mathrm{fc}}(t)$ at $t = 0^+$, as described in the footnote on page 59. Hence, it can be seen that the derived transform (6.10) is still in agreement with the conventional theory on digital control systems, see [39, 114, 119].

Multiple-Frequency Current Dynamics in the Laplace-Domain

Proceeding with the modeling of the converter's current dynamics and using the definition of (6.8) (or (6.10)) to solve (6.7) for the sampled current component $\boldsymbol{i}'_{\mathrm{co}}(s)$, after substituting into (6.6), $\boldsymbol{i}_{\mathrm{co},q}(s+jq\omega_{\mathrm{s}})$ can be written as

$$\boldsymbol{i}_{\mathrm{co},q}(s+jq\omega_\mathrm{s}) = \underbrace{\frac{Y_\mathrm{fc}(s+jq\omega_\mathrm{s})G_{\mathrm{PWM},q}(s)G_{\mathrm{d,q}}(s)G'_\mathrm{PR}(s)}{1+(Y_\mathrm{fc}G_\mathrm{PWM}G_\mathrm{d})'(s)G'_\mathrm{PR}(s)}}_{G_{\mathrm{cl},q}(s)} \boldsymbol{i}'_\mathrm{l}(s) + \underbrace{\frac{Y_\mathrm{fc}(s+jq\omega_\mathrm{s})G_{\mathrm{PWM},q}(s)G_{\mathrm{d,q}}(s)H'(s)}{1+(Y_\mathrm{fc}G_\mathrm{PWM}G_\mathrm{d})'(s)G'_\mathrm{PR}(s)}}_{G_{\mathrm{H},q}(s)} \boldsymbol{i}'_\mathrm{c}(s). \quad (6.11)$$

In analogy to the already specified reference transfer function $G_\mathrm{cl}(s)$ from (3.43), $G_{\mathrm{cl},q}(s) = \boldsymbol{i}_q(s+jq\omega_\mathrm{s})/\boldsymbol{i}'_\mathrm{ref}(s)|_{\boldsymbol{e}(s)=\boldsymbol{0}}$ defines the VSC's (complex) reference transfer function between $\boldsymbol{i}'_\mathrm{ref}(s)$ and the harmonic current component $\boldsymbol{i}_q(s+jq\omega_\mathrm{s})$ in the q-th sideband of the converter. In the same way, the new (complex) active damping transfer function $G_{\mathrm{H},q}(s)$ describes the VSC's dynamic behavior between the baseband components of the sampled capacitor current, $\boldsymbol{i}'_\mathrm{c}(s)$, and the current components $\boldsymbol{i}_{\mathrm{ad},q}(s+jq\omega_\mathrm{s})$ in the q-th sideband, generated by the active feed-forward. In comparison to (3.43) and (3.44), the respective transfer functions in (6.11) differ from the already introduced models only by the use of the new PWM model (6.2) in the numerators and the application of $(Y_\mathrm{fc}G_\mathrm{PWM}G_\mathrm{d})'(s)$, instead of $(Y_\mathrm{fc}G_\mathrm{PWM}G_\mathrm{d})^*(s)$ in the denominators. The effects of these differences can most easily be illustrated by the associated frequency responses. For example, considering the converter under study and neglecting any high-frequency parasitic effects, Fig. 6.5 compares the Bode plots of the converter's reference current dynamics for different PWM models in the low- and high-frequency range with the characteristics of a VSC simulation model, described in more detail in Sec. 7.1.

It can be noticed that the phase response of the new (weighted) reference current dynamics, $G_{\mathrm{cl},q}(s)/T_\mathrm{s}$, $q = 0, 1, 2, \ldots$, is (more or less) identical to the phase responses of the other models as well as the identified characteristics, whereas the magnitudes match only fairly exactly up to the frequency of the PR controller's highest resonator at $h_m\omega_\mathrm{r}$. Above this frequency, $G_{\mathrm{cl},0}(s)/T_\mathrm{s}$ first has a marginally smaller gain, but then shows a higher gain for all $\omega \gg \omega_\mathrm{crit}$ than the (primary-frequency) model (3.43), which uses a classical ZOH PWM model, such as in [53]. On the other hand, the magnitude response of the VSC's reference current dynamics

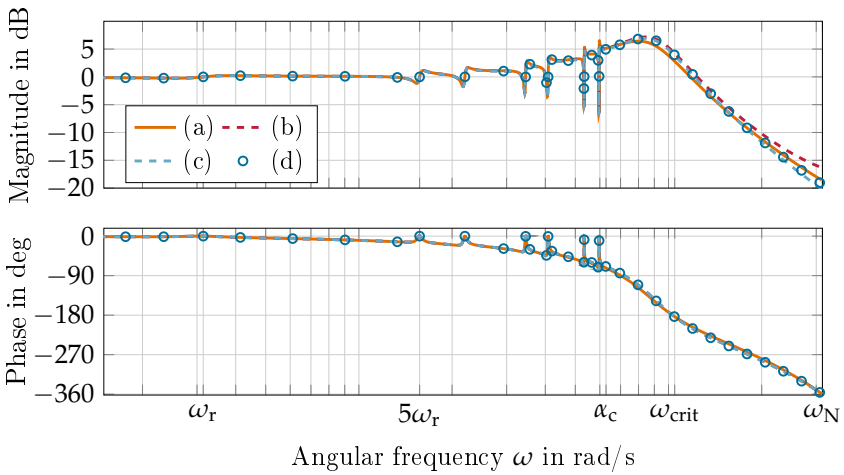

(A)

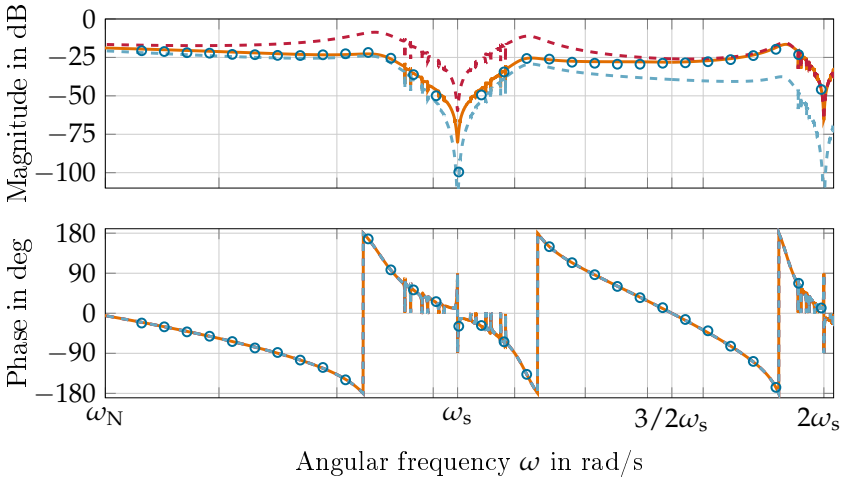

(B)

Fig. 6.5: Bode plots of the VSC's reference current dynamics, where the model implements (a) the proposed multiple-frequency PWM model, (b) a time delay PWM model, (c) a ZOH PWM model, and (d) shows the corresponding identified magnitude and phase characteristics of a simulation model with (nonlinear) single-update PWM. Subfigure (A) shows the associated characteristics for primary input signal components in the converter baseband and subfigure (B) illustrates the behaviors in the sidebands.

with time delay PWM model shows a larger gain for a wide range of frequencies, but approaches the behavior of the proposed model in the very high frequency range. A similar behavior can also be observed for the measured characteristics, which were found to be in good agreement with the Bode plot of $G_{\mathrm{cl},q}(s)/T_\mathrm{s}$, $q = 0, 1, 2, \ldots$. Hence, although there might be a larger magnitude of $G_{\mathrm{cl},q}(s)/T_\mathrm{s}$, if higher offset terms, o_q, are chosen, Fig. 6.5 demonstrates that the resulting reference current dynamics from (6.11) represent a reasonable and accurate model, which is consistent with well-known models in the literature, but is neither too conservative nor suppresses high-frequency switching harmonics too much.

Finally, reviewing the introduced signal flow model from Fig. 6.1, and given the transfer functions from (6.11) as well as the alternative sampler model (6.1), the resulting converter current dynamics for signal components within the frequency range $[(2q-1)\omega_\mathrm{N}, (2q+1)\omega_\mathrm{N}]$, $q = 0, \pm1, \pm2, \ldots$ are more generally given by

$$\begin{aligned}\boldsymbol{i}_q(s+jq\omega_\mathrm{s}) = {} & G_{\mathrm{cl},q}(s)\boldsymbol{i}'_\mathrm{ref}(s) + Y_\mathrm{fc}(s+jq\omega_\mathrm{s})\boldsymbol{e}_q(s+jq\omega_\mathrm{s}) \\ & - G_{\mathrm{cl},q}(s)\boldsymbol{i}'_\mathrm{l}(s) - G_{\mathrm{H},q}(s)\boldsymbol{i}'_\mathrm{c}(s)\end{aligned} \tag{6.12}$$

or equivalently

$$\begin{aligned}\boldsymbol{i}_q(s+jq\omega_\mathrm{s}) = {} & G_{\mathrm{cl},q}(s)\boldsymbol{i}'_\mathrm{ref}(s) + Y_\mathrm{fc}(s+jq\omega_\mathrm{s})\boldsymbol{e}_q(s+jq\omega_\mathrm{s}) - \frac{G_{\mathrm{cl,q}}(s)}{T_\mathrm{s}}\cdot \\ & \sum_{k=-\infty}^{\infty} Y_\mathrm{fc}(s+jk\omega_\mathrm{s}) \underbrace{\left(1+\frac{Y_\mathrm{c}(s+jk\omega_\mathrm{s})}{Y_\mathrm{fc}(s+jk\omega_\mathrm{s})}\frac{H'(s)}{G'_\mathrm{PR}(s)}\right)}_{\Gamma_k(s)} \boldsymbol{e}_k(s+jk\omega_\mathrm{s})\end{aligned} \tag{6.13}$$

where again, $Y_\mathrm{c}(s)$ can be replaced by $Y_\mathrm{d}(s)$, if the LCL filter topology from Fig. 3.2C is considered. As can be verified when taking the periodicity of impulse-sampled signals and systems into account [39, 114, 119], the derived dynamics (6.12) or (6.13) have also a great similarity with the converter current dynamics (3.45), which are shifted to the q-th sideband by substituting $s \mapsto s + jq\omega_\mathrm{s}$ [51, 131]. If both sides of (6.13) are weighed by $1/T_\mathrm{s}$ and the obtained model is evaluated at $q = k$, (6.13) describes the

converter's dynamics with respect to primary-frequency signal components, where $\boldsymbol{i}_q(s)/T_\mathrm{s}$, $\boldsymbol{e}_q(s)/T_\mathrm{s}$, and $\boldsymbol{i}'_\mathrm{ref}(s)$ correspond to the components of $\boldsymbol{i}_\mathrm{p}(s)$, $\boldsymbol{e}_\mathrm{p}(s)$, and $\boldsymbol{i}^*_\mathrm{ref,p}(s)$ in the q-th frequency range, respectively.

In this sense, the consistency of both models confirms the proposed multiple-frequency modeling approach. However, as emphasized above and exemplarily shown in Fig. 6.5, $G_{\mathrm{cl},q}(s)$ and $G_{\mathrm{H},q}(s)$ in (6.12) do not simply utilize the frequency-shifted version of a (low-frequency) SISO small-signal PWM model to reflect the modulator's switching harmonics, but allow to specify the q-th sideband dynamics more individually and accurately. At this point it should also be highlighted that, even though the frequency responses of the single transfer functions in (6.13) are not necessarily symmetric, the frequency response of the concatinated multiple-frequency model is causal and completely symmetric with respect to positive- and negative sequence components, as long as the individual transfer functions $G_{\mathrm{PWM},q}(s)G_{\mathrm{d,q}}(s)$ are symmetric for every $q = \pm1, \pm2, \ldots$. Under this assumption, the following analysis mainly focuses on the positive-sequence components without loss of generality [51, 131].

MIMO Converter Input Admittance

At this point, it is again to be highlighted that the so far discussed VSC disturbance dynamics are only valid, if all aliased signal components of the sampled current $\boldsymbol{i}'_\mathrm{l}$ or $\boldsymbol{i}^*_\mathrm{l}$ are disregarded. Hence, while one of the models may be considered for a simplified controller and filter design, as done in Ch. 4 and Ch. 5, they are rather unsuitable for a final system validation. But, given (6.13) and also taking the mirrored PCC voltage components, $\boldsymbol{e}_k(s+jk\omega_\mathrm{s}),\ \forall k$, into account, a more detailed MIMO input admittance model can be deduced by interpreting the input of the system as a vector of the form $\underline{\boldsymbol{e}}(s) = [\ldots, \boldsymbol{e}_{-1}(s-j\omega_\mathrm{s}), \boldsymbol{e}_0(s), \boldsymbol{e}_1(s+j\omega_\mathrm{s}), \ldots]^T$. Then, the VSC's disturbance dynamics are described by the (complex) transfer function matrix (6.14) with input $\underline{\boldsymbol{e}}(s)$ and output $\underline{\boldsymbol{i}_\mathrm{d}}(s)$ on the next page.

$$\underbrace{\begin{bmatrix} \vdots \\ \boldsymbol{i}_{\mathrm{d},q}(s+jq\omega_\mathrm{s}) \\ \vdots \\ \boldsymbol{i}_{\mathrm{d},0}(s) \\ \vdots \\ \boldsymbol{i}_{\mathrm{d},k}(s+jk\omega_\mathrm{s}) \\ \vdots \end{bmatrix}}_{\underline{\boldsymbol{i}}_\mathrm{d}(s)} = \underbrace{\begin{bmatrix} \ddots & \vdots & \ddots & \vdots & \ddots & \vdots & \iddots \\ \cdots & Y_\mathrm{fc}(s+jq\omega_\mathrm{s})\left[1-\Gamma_\mathrm{q}(s)\frac{G_{\mathrm{cl},\mathrm{q}}(s)}{T_\mathrm{s}}\right] & \cdots & -Y_\mathrm{fc}(s)\Gamma_0(s)\frac{G_{\mathrm{cl},\mathrm{q}}(s)}{T_\mathrm{s}} & \cdots & -Y_\mathrm{fc}(s+jk\omega_\mathrm{s})\Gamma_\mathrm{k}(s)\frac{G_{\mathrm{cl},\mathrm{q}}(s)}{T_\mathrm{s}} & \cdots \\ \cdots & \vdots & \ddots & \vdots & \ddots & \vdots & \cdots \\ \cdots & -Y_\mathrm{fc}(s+jq\omega_\mathrm{s})\Gamma_\mathrm{q}(s)\frac{G_{\mathrm{cl},0}(s)}{T_\mathrm{s}} & \cdots & Y_\mathrm{fc}(s)\left[1-\Gamma_0(s)\frac{G_{\mathrm{cl},0}(s)}{T_\mathrm{s}}\right] & \cdots & -Y_\mathrm{fc}(s+jk\omega_\mathrm{s})\Gamma_\mathrm{k}(s)\frac{G_{\mathrm{cl},0}(s)}{T_\mathrm{s}} & \cdots \\ \cdots & \vdots & \ddots & \vdots & \ddots & \vdots & \cdots \\ \cdots & -Y_\mathrm{fc}(s+jq\omega_\mathrm{s})\Gamma_\mathrm{q}(s)\frac{G_{\mathrm{cl},\mathrm{k}}(s)}{T_\mathrm{s}} & \cdots & -Y_\mathrm{fc}(s)\Gamma_0(s)\frac{G_{\mathrm{cl},\mathrm{k}}(s)}{T_\mathrm{s}} & \cdots & Y_\mathrm{fc}(s+jk\omega_\mathrm{s})\left[1-\Gamma_\mathrm{k}(s)\frac{G_{\mathrm{cl},\mathrm{k}}(s)}{T_\mathrm{s}}\right] & \cdots \\ \iddots & \vdots & \ddots & \vdots & \ddots & \vdots & \ddots \end{bmatrix}}_{\underline{\underline{Y_\mathrm{i}}}(s)} \underbrace{\begin{bmatrix} \vdots \\ \boldsymbol{e}_q(s+jq\omega_\mathrm{s}) \\ \vdots \\ \boldsymbol{e}_0(s) \\ \vdots \\ \boldsymbol{e}_k(s+jk\omega_\mathrm{s}) \\ \vdots \end{bmatrix}}_{\underline{\boldsymbol{e}}(s)} \tag{6.14}$$

Here, $\boldsymbol{e}_q(s+jq\omega_\mathrm{s})$, $\boldsymbol{i}_{\mathrm{d},q}(s+jq\omega_\mathrm{s})$ with $q<0$ and $\boldsymbol{e}_k(s+jk\omega_\mathrm{s})$, $\boldsymbol{i}_{\mathrm{d},k}(s+jk\omega_\mathrm{s})$ with $k>0$ represent two exemplary high-frequency input-output pairs, where one of them can be associated with the illustrated red signal flow path in Fig. 6.1. In general, the diagonal elements of the input admittance matrix $\underline{\underline{Y_\mathrm{i}}}(s)$, i.e., $\ldots, Y_{\mathrm{i},-1-1}(s), Y_{\mathrm{i},00}(s), Y_{\mathrm{i},11}(s), Y_{\mathrm{i},22}(s), \ldots$, where $Y_{\mathrm{i},qq}(s)=\boldsymbol{i}_q(s+jq\omega_\mathrm{s})/\boldsymbol{e}_q(s+jq\omega_\mathrm{s})|_{\boldsymbol{i}'_\mathrm{ref}(s)=\boldsymbol{0}}$, specify the converter's behavior on primary-frequency PCC voltage components, lying in the baseband and the sidebands of the converter. On the other hand, the non-diagonal elements of each column allow to model the effects of mirrored (complementary) voltage components, and the non-diagonal elements of each row enable to model the individual transfer functions that are related to the generation of switching harmonics. As motivated at the beginning of Sec. 6.1, the proposed modeling approach thus leads to a MIMO converter input admittance model, which can be understood as a generalization of classical and well studied quasi-analog or primary-frequency SISO models [4, 8, 53, 110, 144, 156, 158, 167].

Finally, given (6.14), a frequently found procedure in the literature for measuring the VSC's (MIMO) input admittance should be discussed. Accordingly, the (single-phase) input admittance characteristic can be identified by injecting a (real) sinusoidal voltage test signal, $e(t)=E\cdot\cos(\omega_i t)=E\cdot(e^{i\omega_i t}+e^{-i\omega_i t})/2$, at the synthetic PCC and measuring the resulting converter output current, while setting $i'_\mathrm{ref}=0$ (or $i^*_\mathrm{ref}=0$). After waiting for the system to be in the steady state and performing a Fast Fourier Transformation (FFT) of the input and output signals, the frequency response of the VSC's input admittance at ω_i is calculated by $|i_\mathrm{d}(\omega_i)|\,/\,|e(\omega_i)|\cdot e^{j\left(\phi_{i_\mathrm{d}(\omega_i)}-\phi_{e(\omega_i)}\right)}$. The process is repeated with a different input signal frequency, where ω_i is swept over the entire frequency range of interest, see e.g., [8, 42, 53, 110]. This procedure is also the basis for the measurements shown in Fig. 4.2, Fig. 4.3, and Fig. 6.5.

Although this is a valid measurement method, it can be seen that the procedure only identifies the diagonal elements of $\underline{\underline{Y_\mathrm{i}}}(s)$, and thus, only determines the converter's behavior on primary-frequency voltage components. As in [8, 53, 110], the approach is often not adopted to measure the non-diagonal elements of (6.14), reflecting the VSC

dynamics on mirrored signal components and the dynamics of switching harmonics in the sidebands of the converter. Nevertheless, the procedure can simply be extended by identifying all the current components $|i_{\mathrm{d},q}| \cdot e^{j\phi_{i_{\mathrm{d},q}(\omega_i)}}$, $q = 0, 1, 2, \ldots$ for a given test signal, $|e_k(\omega_i)| \cdot e^{j\phi_{e_k(\omega_i)}}$, $k = 0, 1, 2, \ldots$, and taking the model's symmetry with respect to positive- and negative-sequence components into account [42]. But, it should be emphasized that such a measurement is only reasonable, if the test signal is directly injected at the terminals of the converter side filter (at the synthetic PCC) and if there are no other filter parts in feedback [53]. This ensures that no current harmonics are fed back over the synthetic grid impedance $\tilde{Z}_{\mathrm{g}} \neq 0$, resulting in superimposed voltage components at the input of the VSC that distort the identification.

6.3 Multiple-Frequency Model

Analog to the description of the grid-converter system from Sec. 2.2.2, the closed-loop system dynamics can be derived from the converter's MIMO input admittance model (6.14) plus the relation between the synthetic PCC voltage vector $\underline{\boldsymbol{e}}(s)$ and the corresponding converter current vector $\underline{\boldsymbol{i}}(s) = [\ldots, \boldsymbol{i}_{-1}(s-j\omega_{\mathrm{s}}), \boldsymbol{i}_0(s), \boldsymbol{i}_1(s+j\omega_{\mathrm{s}}), \ldots]^T$. Following the MIMO modeling idea, the voltage $\underline{\boldsymbol{e}}(s)$ seen by the converter can be expressed as

$$\underline{\boldsymbol{e}}(s) = \underbrace{\begin{bmatrix} \vdots \\ \tilde{\boldsymbol{v}}_{\mathrm{g},q}(s+jq\omega_{\mathrm{s}}) \\ \vdots \\ \tilde{\boldsymbol{v}}_{\mathrm{g},0}(s) \\ \vdots \\ \tilde{\boldsymbol{v}}_{\mathrm{g},k}(s+jk\omega_{\mathrm{s}}) \\ \vdots \end{bmatrix}}_{\underline{\tilde{\boldsymbol{v}}}_{\mathrm{g}}(s)} - \underbrace{\begin{bmatrix} \ddots & \vdots & \ddots & \vdots & \ddots & \vdots & \iddots \\ \cdots & \tilde{Z}_{\mathrm{g}}(s+jq\omega_{\mathrm{s}}) & \cdots & 0 & \cdots & 0 & \cdots \\ \cdots & \vdots & \ddots & \vdots & \ddots & \vdots & \cdots \\ \cdots & 0 & \cdots & \tilde{Z}_{\mathrm{g}}(s) & \cdots & 0 & \cdots \\ \cdots & \vdots & \ddots & \vdots & \ddots & \vdots & \cdots \\ \cdots & 0 & \cdots & 0 & \cdots & \tilde{Z}_{\mathrm{g}}(s+jk\omega_{\mathrm{s}}) & \cdots \\ \iddots & \vdots & \ddots & \vdots & \ddots & \vdots & \ddots \end{bmatrix}}_{\underline{\underline{\tilde{Z}}}_{\mathrm{g}}(s)} \underline{\boldsymbol{i}}(s), \tag{6.15}$$

assuming that the (synthetic) grid voltage can also be separated into an infinite number of signals, where each $\tilde{v}_{\mathrm{g},k}(t), \forall k$ predominantly contains positive- or negative-sequence components within the frequency ranges $[(2k-1)\omega_\mathrm{N}, (2k+1)\omega_\mathrm{N}]$ or $[(-2k-1)\omega_\mathrm{N}, (-2k+1)\omega_\mathrm{N}]$, see Sec. 6.1.2. Then, substituting (6.15) into (6.14) and taking into account that $\underline{\boldsymbol{i}}(s) = \underline{\boldsymbol{i}_\mathrm{d}}(s) + \underline{G_\mathrm{cl}}(s)\,\boldsymbol{i}'_\mathrm{ref}(s)$, where the column vector $\underline{G_\mathrm{cl}}(s) = [\ldots, G_{\mathrm{cl},-1}(s), G_{\mathrm{cl},0}(s), G_{\mathrm{cl},1}(s), \ldots]^T$ collects all individual reference transfer functions, the MIMO closed-loop grid-converter dynamics are given by

$$\begin{aligned}\underline{\boldsymbol{i}}(s) &= \left[\underline{\underline{I}} + \underline{\underline{Y_\mathrm{i}}}(s)\underline{\underline{\tilde{Z}_\mathrm{g}}}(s)\right]^{-1}\underline{G_\mathrm{cl}}(s)\,\boldsymbol{i}'_\mathrm{ref}(s) + \left[\underline{\underline{I}} + \underline{\underline{Y_\mathrm{i}}}(s)\underline{\underline{\tilde{Z}_\mathrm{g}}}(s)\right]^{-1}\underline{\underline{Y_\mathrm{i}}}(s)\,\underline{\tilde{\boldsymbol{v}}_\mathrm{g}}(s) \\ &= \frac{\mathrm{adj}\left(\underline{\underline{I}} + \underline{\underline{Y_\mathrm{i}}}(s)\underline{\underline{\tilde{Z}_\mathrm{g}}}(s)\right)}{\det\left(\underline{\underline{I}} + \underline{\underline{Y_\mathrm{i}}}(s)\underline{\underline{\tilde{Z}_\mathrm{g}}}(s)\right)}\left(\underline{G_\mathrm{cl}}(s)\,\boldsymbol{i}'_\mathrm{ref}(s) + \underline{\underline{Y_\mathrm{i}}}(s)\,\underline{\tilde{\boldsymbol{v}}_\mathrm{g}}(s)\right) \qquad (6.16)\end{aligned}$$

where $\underline{\underline{I}}$ denotes the identity matrix. As can be seen, (6.16) is similar to (2.8), but represents a multivariable system, where each entry of the resulting (complex) transfer function matrix defines the system's input-output behavior from a distinct frequency range to another. In general, the numerators of the individual transfer functions of the matrix simply result from a multiplication and summation of different entries of the matrix $\underline{\underline{I}} + \underline{\underline{Y_\mathrm{i}}}(s)\underline{\underline{\tilde{Z}_\mathrm{g}}}(s)$ and the vector $\underline{G_\mathrm{cl}}(s)$ or the matrices $\underline{\underline{I}} + \underline{\underline{Y_\mathrm{i}}}(s)\underline{\underline{\tilde{Z}_\mathrm{g}}}(s)$ and $\underline{\underline{Y_\mathrm{i}}}(s)$, respectively. On the other hand, while the denominator of the quasi-analog system (2.8) is just given by $1 + Y_\mathrm{i}^c(s)\tilde{Z}_\mathrm{g}(s)$, the common denominator of the single transfer functions from (6.16), and thus, the system's characteristic equation has to be calculated by means of a complicated matrix inversion or an evaluation of $\det\left(\underline{\underline{I}} + \underline{\underline{Y_\mathrm{i}}}(s)\underline{\underline{\tilde{Z}_\mathrm{g}}}(s)\right)$.

However, if the modeling and analysis is focused on a certain frequency range, (6.16) can again be simplified to a SISO system by interpreting the effects of all other voltage vector elements with signal components outside the selected frequency range as disturbances. To do so, the input and output vectors $\underline{b_k} = [\ldots, 0, 0, 1, 0, 0, \ldots]^T$ and $\underline{c_q}^T = [\ldots, 0, 0, 1, 0, 0, \ldots]$, where k and q define the location of the non-zero element in $\underline{b_k}$ and $\underline{c_q}^T$, respectively, can be utilized to specify the frequency range of interest.

Then, the converter's dynamics between the reference current, $\boldsymbol{i}'_{\mathrm{ref}}(s)$, as well as the k-th synthetic grid voltage component, $\tilde{\boldsymbol{v}}_{\mathrm{g},k}(s+jk\omega_{\mathrm{s}})$, and the converter's output current in the q-th frequency range, $\boldsymbol{i}_q(s+jq\omega_{\mathrm{s}})$, are given by

$$\begin{aligned}\boldsymbol{i}_q(s+jq\omega_{\mathrm{s}}) = &\underline{c_q}^T \left[\underline{\underline{I}} + \underline{\underline{Y_{\mathrm{i}}}}(s)\underline{\underline{\tilde{Z}_{\mathrm{g}}}}(s)\right]^{-1} \underline{G_{\mathrm{cl}}}(s)\, \boldsymbol{i}'_{\mathrm{ref}}(s) \\ &+ \underline{c_q}^T \left[\underline{\underline{I}} + \underline{\underline{Y_{\mathrm{i}}}}(s)\underline{\underline{\tilde{Z}_{\mathrm{g}}}}(s)\right]^{-1} \underline{\underline{Y_{\mathrm{i}}}}(s)\underline{b_k}\, \tilde{\boldsymbol{v}}_{\mathrm{g},k}(s+jk\omega_{\mathrm{s}}) + \boldsymbol{d}(s),\end{aligned} \tag{6.17}$$

summarizing all other influences of the voltage components $\tilde{\boldsymbol{v}}_{\mathrm{g},k\pm1}(s+j(k\pm1)\omega_{\mathrm{s}}), \tilde{\boldsymbol{v}}_{\mathrm{g},k\pm2}(s+j(k\pm2)\omega_{\mathrm{s}}), \ldots$ in the complex space vector $\boldsymbol{d}(s)$. In particular, considering that the VSC's LCL filter effectively suppresses above Nyquist frequency components from the grid side, i.e., $|\tilde{\boldsymbol{v}}_{\mathrm{g}}(j\omega)| = \left|(\tilde{Z}_{\mathrm{g}}(j\omega)\tilde{Y}_{\mathrm{fg}}(j\omega))\boldsymbol{v}_{\mathrm{g}}(j\omega)\right| \approx 0,\ \forall\, |\omega| > \omega_{\mathrm{N}}$, and that consequently $\tilde{\boldsymbol{v}}_{\mathrm{g},0}(s) = \tilde{\boldsymbol{v}}_{\mathrm{g}}(s)$ and $\boldsymbol{d}(s) \approx \boldsymbol{0}$, for $q = k = 0$, (6.17) describes the dynamics of the illustrated grid-converter system from Fig. 6.1. In this special case, which is also in accordance with the EN 50388-2 standard [6], allowing to omit above Nyquist frequency signal components when assessing the behavior of active-front-ends [42, 110], the resulting control block diagram of the VSC's disturbance dynamics is in some ways similar to that from San et al. in [116] and has the structure shown in Fig. 6.6.

It might be noticed that the deduced control block diagram from Fig. 6.6 is also comparable to the motivating signal flow model from Fig. 6.1, but specifies the depicted blocks by means of their (complex) transfer functions in more detail. In this context, the sampler blocks at the input of the reference dynamics as well as the active damping dynamics from Fig. 6.1 are combined and modeled by the transformation (6.1), representing an infinite sum of the form $1/T_{\mathrm{s}} \cdot \sum_{k=-\infty}^{\infty} Y_{\mathrm{fc}}(s+jk\omega_{\mathrm{s}})\Gamma_k(s)\boldsymbol{e}_k(s+jk\omega_{\mathrm{s}})$, see (6.13). Accordingly, the sampled signals are used to generate the baseband current component $\boldsymbol{i}_{\mathrm{co},0}$ and all the harmonic components, $\boldsymbol{i}_{\mathrm{co},k}, k = \pm1, \pm2, \ldots$, which, in combination with the current $\boldsymbol{i}_{\mathrm{l},k}, k = \pm1, \pm2, \ldots$ in the respective frequency range yield the individual VSC output current components $\boldsymbol{i}_{\mathrm{d},k}, k = 0, \pm1, \pm2, \ldots$. If, in addition, $\tilde{\boldsymbol{v}}_{\mathrm{g},0}(s) = \tilde{\boldsymbol{v}}_{\mathrm{g}}(s)$ and

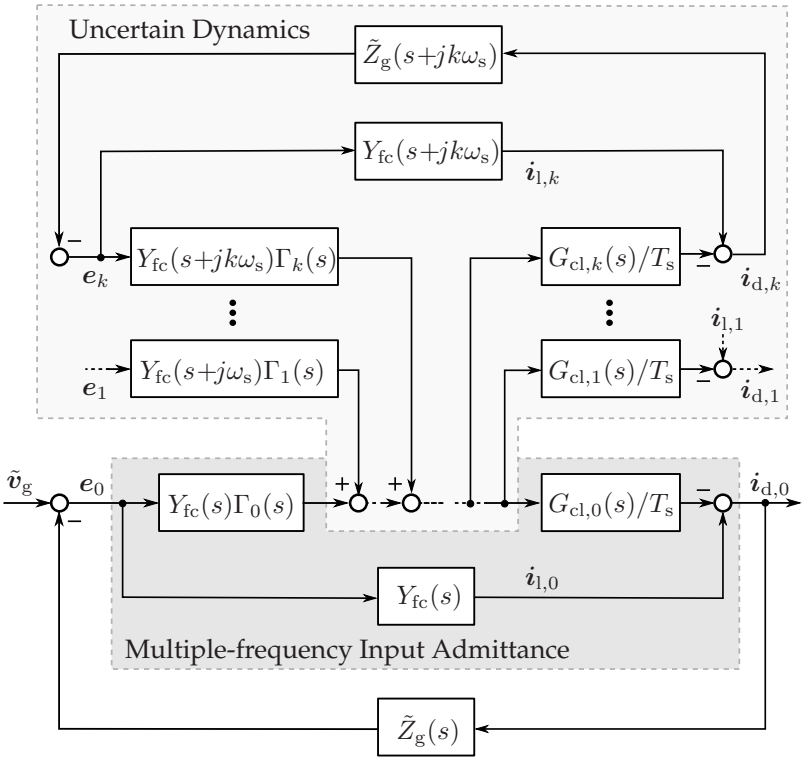

Fig. 6.6: Normalized control block diagram of the disturbance dynamics of a digitally current-controlled grid-connected converter with (optional) active damping filter under consideration of PWM harmonics and aliasing effects.

$\boldsymbol{d}(s) = \boldsymbol{0}$, the baseband dynamics of the grid-converter system can be represented by the illustrated block diagram.

Uncertain Dynamics and Multiple-Frequency Input Admittance

As shown in Fig. 6.6, the cascaded feedback of the VSC's high-frequency switching harmonics can basically be interpreted as a frequency-dependent (dynamic) uncertainty, $\Delta_0(s)$, which multiplicatively affects the baseband dynamics of the active part of the converter. Following this

observation and using simple rules from block-diagram analysis [10,119], the highlighted uncertain dynamics from Fig. 6.6 can be described by

$$\Delta_0(s) = \frac{1}{1 - \frac{1}{T_\mathrm{s}} \sum_{\substack{k=-\infty \\ k\neq 0}}^{\infty} \Gamma_k(s) G_{\mathrm{cl},k}(s) \frac{G_\mathrm{LCL}(s+jk\omega_\mathrm{s})}{\tilde{Y}_\mathrm{fg}(s+jk\omega_\mathrm{s})}} \tag{6.18}$$

where $G_\mathrm{LCL}(s)/\tilde{Y}_\mathrm{fg}(s) = \tilde{Z}_\mathrm{g}(s)Y_\mathrm{fc}(s)/(1+\tilde{Z}_\mathrm{g}(s)Y_\mathrm{fc}(s))$ is the effective (synthetic) impedance in the feedback path of the individual sideband components. Then, presupposing that (6.18) converges, it is proposed to define the VSC's new, and more accurate SISO input admittance as

$$Y_{\mathrm{m},0}(s) = \left.\frac{\boldsymbol{i}_0(s)}{\tilde{\boldsymbol{v}}_\mathrm{g}(s) - \tilde{Z}_\mathrm{g}(s)\boldsymbol{i}_0(s)}\right|_{\boldsymbol{i}'_\mathrm{ref}(s)=\boldsymbol{0}} = Y_\mathrm{fc}(s)\left[1 - \Gamma_0(s)\Delta_0(s)\frac{G_{\mathrm{cl},0}(s)}{T_\mathrm{s}}\right] \tag{6.19}$$

where, as a result, the disturbance dynamics of the closed-loop grid-converter system from (6.17) for $q = k = 0$ and with $\tilde{\boldsymbol{v}}_{\mathrm{g},0}(s) = \tilde{\boldsymbol{v}}_\mathrm{g}(s)$ and $\boldsymbol{d}(s) = 0$ can equivalently, but more simply be expressed as

$$\boldsymbol{i}_{\mathrm{d},0}(s) = \underline{c_0}^T \left[\underline{\underline{I}} + \underline{\underline{Y_\mathrm{i}}}(s)\underline{\underline{\tilde{Z}_\mathrm{g}}}(s)\right]^{-1} \underline{\underline{Y_\mathrm{i}}}(s)\,\underline{b_0}\,\tilde{\boldsymbol{v}}_\mathrm{g}(s) = \underbrace{\frac{Y_{\mathrm{m},0}(s)}{1 + Y_{\mathrm{m},0}(s)\tilde{Z}_\mathrm{g}(s)}}_{Y_{\mathrm{t},0}(s)}\,\tilde{\boldsymbol{v}}_\mathrm{g}(s). \tag{6.20}$$

Thereby, the converter's disturbance dynamics again take the form of the corresponding dynamics of the simplified closed-loop system description (2.8) from the background chapter. Based on the suggested terminology from [53], the admittance $Y_{\mathrm{m},0}(s)$ should be referred to as the converter's multiple-frequency input admittance and $Y_{\mathrm{t},0}(s)$ as the converter's total input admittance, seen from the (normalized synthetic) grid voltage $\tilde{\boldsymbol{v}}_\mathrm{g}(s) = (\tilde{Z}_\mathrm{g}(s)\tilde{Y}_\mathrm{fg}(s))\boldsymbol{v}_\mathrm{g}(s)$. It is however to be emphasized that even though the chosen terminology is the same, the multiple-frequency input admittance models differ and should not be confused. While Harnefors et al. basically use the term in [53] to denote the converter's input admittance that is related to the quotient $\boldsymbol{i}_0(s)/\boldsymbol{e}_0(s)$, where $\tilde{Z}_\mathrm{g}(s) = 0$

(and $\Delta_0(s) = 1$), throughout this thesis, the multiple-frequency input admittance $Y_{\mathrm{m},0}(s)$ is associated to the input admittance $\boldsymbol{i}_0(s)/\boldsymbol{e}_0(s)$, where $\boldsymbol{e}_0(s) = \tilde{\boldsymbol{v}}_\mathrm{g}(s) - \tilde{Z}_\mathrm{g}(s)\boldsymbol{i}_0(s)$. In comparison to the input admittance model from [53] or those from Sec. 3.4, $Y_{\mathrm{m},0}(s)$ represents an extension of commonly found input admittance models in the literature. More precisely, it takes mirrored components of the measured voltage at the VSC's terminals with respect to a specific synthetic grid impedance, $\tilde{Z}_\mathrm{g}(s)$, into account. As was to be expected, (6.18) and (6.19) also make clear that the influence of aliasing effects on the converter dynamics can only be assessed for a certain grid impedance and that it is not possible to make any generally valid statements on the VSC's multiple-frequency input admittance $Y_{\mathrm{m},0}(s)$ or the total input admittance $Y_{\mathrm{t},0}(s)$. The system modeling and analysis becomes even more complicated if it is considered that Z_g is usually unknown and that the (actual) effective grid impedance continually varies due to permanent changes of the power network [30,86,153].

Nevertheless, it can practically be assumed that the grid predominantly shows a (resistive-) inductive behavior and that possibly emerging grid resonances usually act within a well limited frequency range [17,19,86,91]. Hence, also taking the low-pass characteristic of the converter's LCL filter in the high-frequency range into account, it can typically be supposed that (6.18) converges for realistic grid impedances, Z_g. In fact, using the multiple-frequency PWM model (6.2), where $G_{\mathrm{PWM},0}(s)G_{\mathrm{d},0}(s)$ specifies all even and $G_{\mathrm{PWM},1}(s)G_{\mathrm{d},1}(s)$ all odd sideband harmonics and applying a similar approach to the one given in the Appendix A.4, it can be verified that a solution exists and the sum representation in (6.18) can be reformulated into an explicit equation, as long as $G_\mathrm{LCL}(s)/(\tilde{Y}_\mathrm{fg}(s)Z_\mathrm{c}(s))$ has a denominator at least one degree higher in s than the numerator, see also [114]. This approach for the calculation of (6.18) is however not pursued further here, since $\Delta_0(s)$ is still influenced by other unmodelled effects, such as nonlinear PWM effects [64, 129], and it is therefore to be expected that the actually effective uncertainty in (6.19) can almost never be determined exactly. But, in most applications this is no major problem and a simpler model of $\Delta_0(s)$ should usually be sufficient to estimate the influence of aliased signal components. In

particular, it should again be considered that most mirrored components have an ever decreasing effect for higher sidebands. Thus, since $G_{\mathrm{LCL}}(s)/(\tilde{Y}_{\mathrm{fg}}(s)Z_{\mathrm{c}}(s))$ usually has (at least) a pole excess of one, it is suggested to approximate the dynamic uncertainty $\Delta_0(s)$ by evaluating the sum in (6.18) only with a small number of summands, instead of aiming for an exact calculation. As has been confirmed by a variety of simulative tests, this approach also leads to appropriate results, even if a more complex grid impedance is supposed, e.g., resulting from a transmission line modeling by one or multiple Π-segments [141, 166] or an interconnection of multiple grid-connected converters as in [11, 88, 141].

In addition, a closer look at the effective (non-active) impedance in the feedback path of the sideband components in (6.18) shows that $G_{\mathrm{LCL}}(s)/\tilde{Y}_{\mathrm{fg}}(s)$ approaches a simple second-order lag element in scenarios where no dominant resonances above the Nyquist frequency appear. By setting $Z_{\mathrm{g}}(s) = 0$, the impedance $G_{\mathrm{LCL}}(s)/\tilde{Y}_{\mathrm{fg}}(s)$ shows a gain of approximately $L_{\mathrm{fg}}/(L_{\mathrm{fg}} + L_{\mathrm{fc}}) < 1$ for $s = 0$ and a resonance at

$$\omega_{\mathrm{r,G_{LCL},max}} \approx \sqrt{\frac{L_{\mathrm{fc}} + L_{\mathrm{fg}}}{L_{\mathrm{fc}} L_{\mathrm{fg}} C_{\mathrm{c}}}}, \tag{6.21}$$

whereas for $|Z_{\mathrm{g}}(s)| \to \infty$, the impedance $G_{\mathrm{LCL}}(s)/\tilde{Y}_{\mathrm{fg}}(s)$ has approximately a gain of one for $s = 0$ and a resonance at

$$\omega_{\mathrm{r,G_{LCL},min}} \approx \sqrt{\frac{1}{L_{\mathrm{fc}} C_{\mathrm{c}}}} < \omega_{\mathrm{r,G_{LCL},max}}. \tag{6.22}$$

It can be seen that although the gain at $s = 0$ rises, the resulting resonance is more and more shifted to lower and usually less critical frequencies if $|Z_{\mathrm{g}}(s)|$ increases, see also the Bode plot of $G_{\mathrm{LCL}}(s)$ in Fig. 3.3. Therefore, the greatest influence of mirrored switching harmonics near the Nyquist frequency can be expected when the converter is connected to a stiff grid, i.e., when Z_{g} is close to zero. The authors of [125] come to (more or less) the same conclusion and use (6.21) and (6.22) for the design of LCL filters with resonance frequencies above the Nyquist frequency. In some ways, this finding also corresponds to the well known facts on the decoupling

and attenuation effect of large (line) inductors from classical literature on power systems [77, 91]. Hence, if no (or little) knowledge about the connected power network exists, but it can be assumed that no significant resonances above the Nyquist frequency occur, it is proposed to again approximate $\Delta_0(s)$ by evaluating (6.18) with a small number of summands and set $Z_\mathrm{g} = 0$. For instance, focusing on the harmonics in the first sideband, i.e., $k = \pm 1$, and additionally neglecting all resistive and parasitic components in the converter output filter [38], the dynamics of the uncertainty $\Delta_0(s)$ in (6.19) can be estimated by

$$\Delta_0(s) \approx \frac{1 + (Y_\mathrm{fc} G_\mathrm{PWM} G_\mathrm{d})'(s) G'_\mathrm{PR}(s)}{1 + (Y_\mathrm{fc} G_\mathrm{PWM} G_\mathrm{d})'(s) G'_\mathrm{PR}(s) - G'_\mathrm{PR}(s) G_{\Delta,\mathrm{PR}}(s) - H'(s) G_{\Delta,\mathrm{H}}(s)} \tag{6.23}$$

where

$$G_{\Delta,\mathrm{PR}}(s) = \frac{G_{\mathrm{PWM},1}(s) G_{\mathrm{d},1}(s)/T_\mathrm{s} \cdot 2s(s^2 + \omega^2_{\mathrm{r},\mathrm{G_{LCL}},\max} - 3\omega_\mathrm{s}^2)}{l_\mathrm{fc}^2 c_\mathrm{c} (s^2+\omega_\mathrm{s}^2)(s^2+(\omega_\mathrm{s}-\omega_{\mathrm{r},\mathrm{G_{LCL}},\max})^2)(s^2+(\omega_\mathrm{s}+\omega_{\mathrm{r},\mathrm{G_{LCL}},\max})^2)}, \tag{6.24}$$

$$G_{\Delta,\mathrm{H}}(s) = \frac{G_{\mathrm{PWM},1}(s) G_{\mathrm{d},1}(s)/T_\mathrm{s} \cdot 2s(s^2 + \omega^2_{\mathrm{r},\mathrm{G_{LCL}},\max} + \omega_\mathrm{s}^2)}{l_\mathrm{fc}(\omega_\mathrm{s}^4 - 2\omega_\mathrm{s}^2(\omega^2_{\mathrm{r},\mathrm{G_{LCL}},\max} - s^2) + (s^2 + \omega_{\mathrm{r},\mathrm{G_{LCL}},\max})^2)}. \tag{6.25}$$

If the actively damped converter under study is considered, Fig. 6.7 exemplarily depicts some representative frequency responses of the estimated uncertainty $\Delta_0(s)$ for different grid impedances. Given Fig. 6.7A, it can be noticed that the dashed light blue and the dash-dotted blue approximations exactly coincide and only differ mainly from the more accurate (orange) estimate in the frequency range near and above the frequency ω_crit. As already discussed, mirrored signal components are better attenuated with an increase of the effective grid inductance, l_g, which confirms that it is advantageous to set $Z_\mathrm{g} = 0$ for a rough (worst-case) approximation of the aliasing effects if no prior knowledge about the grid is available. But, Fig. 6.7B makes clear that this approximation only gives reasonable results, if there are no (significant) resonances in the effective grid impedance above the Nyquist frequency ω_N. In the illustrated example,

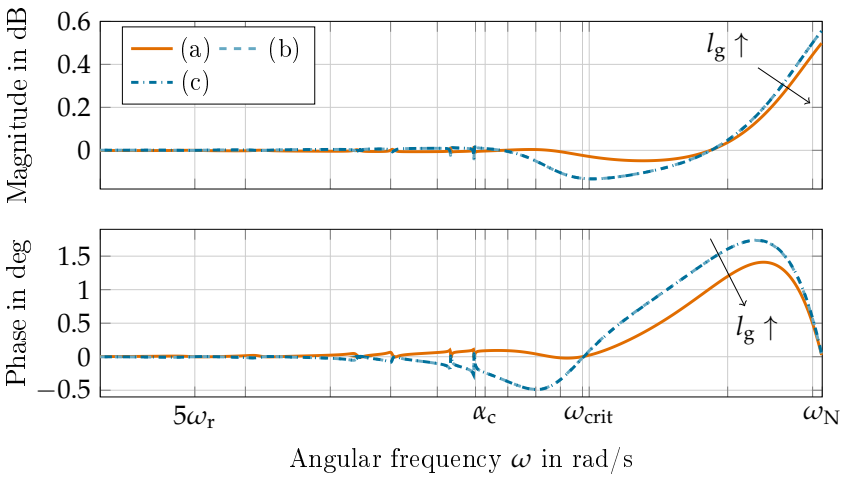

(A)

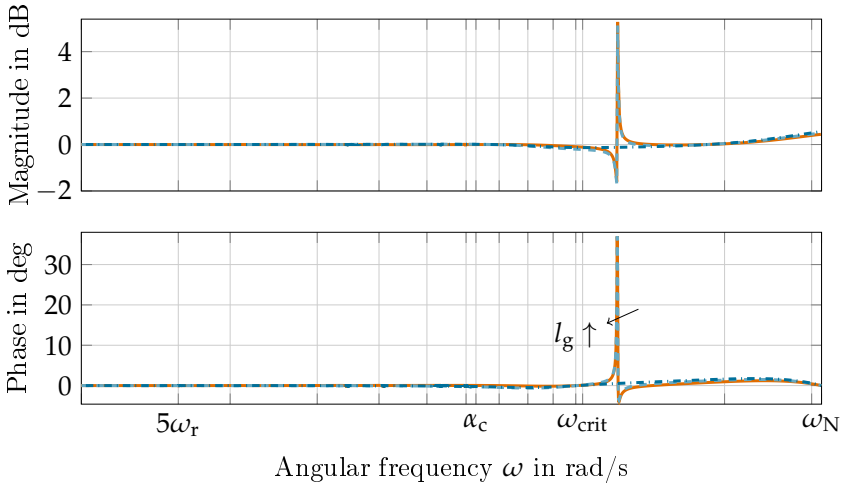

(B)

Fig. 6.7: Bode plots of the estimated dynamic uncertainty $\Delta_0(s)$, where (a) evaluates (6.18) with $k = \pm 1, \pm 2, \pm 3$, (b) evaluates (6.18) with $k = \pm 1$, and (c) uses the approximation (6.23) with (6.24) and (6.25). In both subfigures, the converter is equipped with an undamped LCL filter, where, in subfigure (A), the VSC is connected to a stiff grid with $Z_g(s) = 0$, and in subfigure (B), the VSC is connected to a resistive-inductive grid, where $\tilde{Z}_g(s)$ has an above Nyquist frequency resonance at $\omega_{r,\tilde{Z}_g,2} \approx 50492 \, \frac{\text{rad}}{\text{s}}$.

a damped Π-segment is used to model a transmission line between the converter and the grid [141,166]. If $Z_\mathrm{g} = 0$, this results in a synthetic grid impedance $\tilde{Z}_\mathrm{g}(s)$, which is similar to that shown in Fig. 3.4, whereas the resonance of the LCL filter is shifted to $\omega_{\mathrm{r},\tilde{Z}_\mathrm{g},1} \approx 10165\,\frac{\mathrm{rad}}{\mathrm{s}}$ and an additional resonance emerges at $\omega_{\mathrm{r},\tilde{Z}_\mathrm{g},2} \approx 50492\,\frac{\mathrm{rad}}{\mathrm{s}} > \omega_\mathrm{N} \approx 31416\,\frac{\mathrm{rad}}{\mathrm{s}}$. While the former resonance in $\tilde{Z}_\mathrm{g}(s)$ is ignored by the summation in (6.18), the latter causes a mirrored resonance in the corresponding dynamic uncertainty $\Delta_0(s)$ at $12152\,\frac{\mathrm{rad}}{\mathrm{s}} \approx \omega_\mathrm{s} - \omega_{\mathrm{r},\tilde{Z}_\mathrm{g},2} = 12340\,\frac{\mathrm{rad}}{\mathrm{s}} < \omega_\mathrm{N}$. Here, it should however be noticed that this is only a rough estimate, since the exact location of the mirrored resonance in $\Delta_0(s)$ depends on all resonances in $\tilde{Z}_\mathrm{g}(s)$ from $\omega = 0$ to $\omega \to \infty$. But, it can generally be observed that each resonance in $Z_\mathrm{g}(s)$ above ω_N also leads to a resonance in the synthetic grid impedance $\tilde{Z}_\mathrm{g}(s)$ (and in the effective impedance $G_\mathrm{LCL}(s)/\tilde{Y}_\mathrm{fg}(s)$ in (6.18)), which in turn causes a mirrored resonance in $\Delta_0(s)$.

Since it can be assumed that the dynamic uncertainty $\Delta_0(s)$ shows a rather moderate and well bounded magnitude and phase response in most applications, the influence of $\tilde{Z}_\mathrm{g}$ on the converter's input admittance can usually be expected to be quite low, see e.g., the Bode plots of the estimated multiple-frequency input admittance $Y_{\mathrm{m},0}(s)$ in Fig. 6.8. But, on the other hand, it can finally also be confirmed that the mirroring of above Nyquist frequency (grid) resonances might lead to stability problems in some special scenarios, especially when the grid has a low inherent damping. In the end, the discussed example validates the latest findings from [53], where, in contrast to initial research, Harnefors et al. come to the conclusion that the effective input admittance of a digitally-controlled converter is not independent of the connected grid, but is affected by the (synthetic) grid impedance.

6.4 Passivity Assessment and Implications on the Stability

Similar to the SISO closed-loop system (2.8), the MIMO closed-loop grid-converter system (6.16) is asymptotically stable, if all roots of the system's characteristic equation lie in the complex left half plane. While in the SISO case, this can be assessed relatively easily by evaluating the open-loop

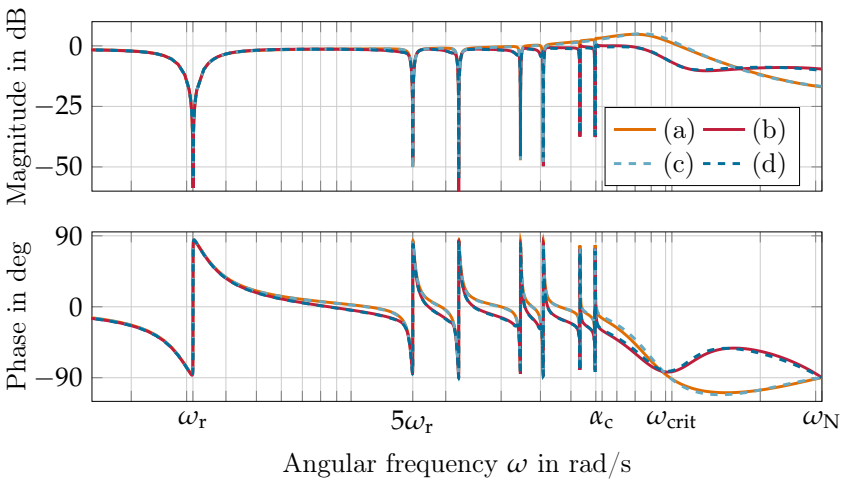

(A)

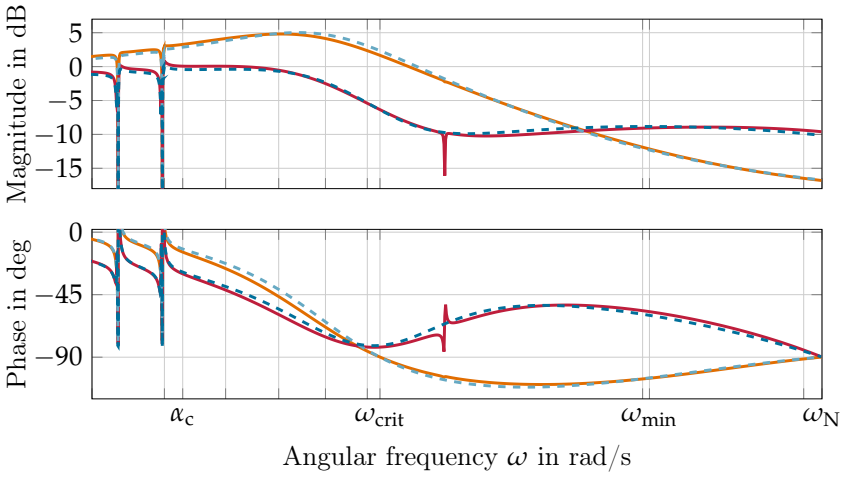

(B)

Fig. 6.8: Bode plots of the VSC's (a), (b) estimated multiple-frequency input admittance model $Y_{\mathrm{m},0}(s)$, and (c), (d) primary-frequency input admittance model $Y_{\mathrm{i,p}}(s)$, where the converter implements an undamped LCL filter and (a), (c) no active damping and (b), (d) a capacitor current feed-forward. In subfigure (A), the VSC is connected to a stiff grid with $Z_\mathrm{g}(s) = 0$, and in subfigure (B), the VSC is connected to a resistive-inductive grid, where $\tilde{Z}_\mathrm{g}(s)$ has an above Nyquist frequency resonance at $\omega_{\mathrm{r},\tilde{Z}_\mathrm{g},2} \approx 50492\,\frac{\mathrm{rad}}{\mathrm{s}}$.

system's Nyquist curve, as done in e.g., [8, 57, 89, 123, 140, 143, 156, 171], the MIMO case requires an application of the multivariable Nyquist stability criterion [51, 121]. More precisely, since the transfer function matrix of the open-loop system $\underline{\underline{Y}}_{\mathrm{i}}(s)\underline{\underline{\tilde{Z}}}_{\mathrm{g}}(s)$ only consists of the series and parallel connection of stable systems, the digitally current-controlled grid-connected converter is asymptotically stable, if the Nyquist plot of $\det(\underline{\underline{I}} + \underline{\underline{Y}}_{\mathrm{i}}(s)\underline{\underline{\tilde{Z}}}_{\mathrm{g}}(s))$ does not pass through nor encircle the origin of the complex s-plane for all $s = j\omega$, $\omega \in (-\infty, \infty)$ [51, 121]. Hence, unlike the SISO case, the stability in the MIMO case is defined by the eigenvalues of the open-loop transfer function matrix, which can generally only be calculated with increased effort.

This increase in complexity and the associated difficulties similarly occur in the passivity assessment of the converter's MIMO admittance model (6.14). The passivity properties of the transfer function matrix $\underline{\underline{Y}}_{\mathrm{i}}(s)$ cannot simply be analyzed by evaluating every single matrix element, $Y_{\mathrm{i},qk}(s)$, describing the VSC disturbance dynamics between the synthetic PCC voltage input component $\boldsymbol{e}_k(s + jk\omega_{\mathrm{s}})$, $k = 0, \pm 1, \pm 2, \ldots$ and the output current component $\boldsymbol{i}_{\mathrm{d},q}(s + jq\omega_{\mathrm{s}})$, $q = 0, \pm 1, \pm 2, \ldots$. Instead, the MIMO passivity criteria from Sec. 2.1.1 should be considered, which, as can be seen, would still require to calculate and to assess the eigenvalues of a matrix. At this point it should also be reviewed that input signal components above the Nyquist frequency are automatically misinterpreted as low-frequency signals, which cause the converter to actively generate current components at the mirrored frequencies. From this point of view it becomes clear that the input admittance matrix in (6.14) always shows entries with non-passive behavior, making a full passivation of $\underline{\underline{Y}}_{\mathrm{i}}(s)$ for all frequency components rather impossible. For this reason, a detailed passivity assessment of the converter's MIMO input admittance $\underline{\underline{Y}}_{\mathrm{i}}(s)$ should not be pursued further here.

Passivity of the VSC's Multiple-Frequency Input Admittance

Regarding the EN 50388-2 [6] and focusing on input and output signal components up to the Nyquist frequency, where $\tilde{\boldsymbol{v}}_{\mathrm{g},0}(s) \approx \tilde{\boldsymbol{v}}_{\mathrm{g}}(s)$, the

previous section showed that the closed-loop grid-converter system again simplifies to a SISO system. Hence, given Fig. 6.6 and noticing that the associated SISO disturbance dynamics (6.20) principally have the same structure as the simplified disturbance dynamics from (2.8), it turns out that all the subsequent considerations can readily be applied to the more accurate grid-converter model $Y_{\mathrm{t},0}(s)$. This particularly includes the proposed passivity assessment and filter design methods from Ch. 5. It should only be kept in mind that, unlike the SISO admittance models from Sec. 3.4 or that presented in [53], the converter's multiple-frequency input admittance model $Y_{\mathrm{m},0}(s)$ from (6.19) also depends on the synthetic grid impedance. Therefore, all investigations are always related to a certain $\tilde{Z}_{\mathrm{g}}(s)$. In many cases, however, this is not a major issue. As explained and exemplarily demonstrated in Sec. 6.3, it can typically be assumed that the dynamic uncertainty $\Delta_0(s)$, and thus, the mirrored signal components influence the converter's behavior only marginally, as long as the grid shows a well inherent damping and the LCL filter is designed so that its resonance frequency is well below the Nyquist frequency. As a result, the (exact) passivity indices of the VSC's effective input admittance should usually be close to the passivity indices of $Y_{\mathrm{m},0}(s)$ with $\Delta_0(s) = 1$, lying within a more or less narrow uncertainty band around IFP $\left\{Y_{\mathrm{m},0}(j\omega)|_{\Delta_0(s)=1}\right\}$ or OFP $\left\{Y_{\mathrm{m},0}(j\omega)|_{\Delta_0(s)=1}\right\}$. Fig. 6.9 illustrates this basic idea using the IFP index of the inherent converter conductance under study.

This interpretation of the effect of mirrored signal components shows that the converter's effective, but generally not exactly known input admittance can be rendered passive almost independently of the power system by demanding a feed-forward filter design that robustly passivates the VSC's input admittance model. For this purpose, the control system literature contains not only the well-known passivity theory from the background chapter [14, 74, 169], but also more general techniques for a robust passivation of uncertain systems, see e.g., [14, 73, 92]. However, since the existing methods typically require to transform the given uncertainty into an unstructured additive, multiplicative or feedback uncertainty, the class of uncertainties that has to be considered may become

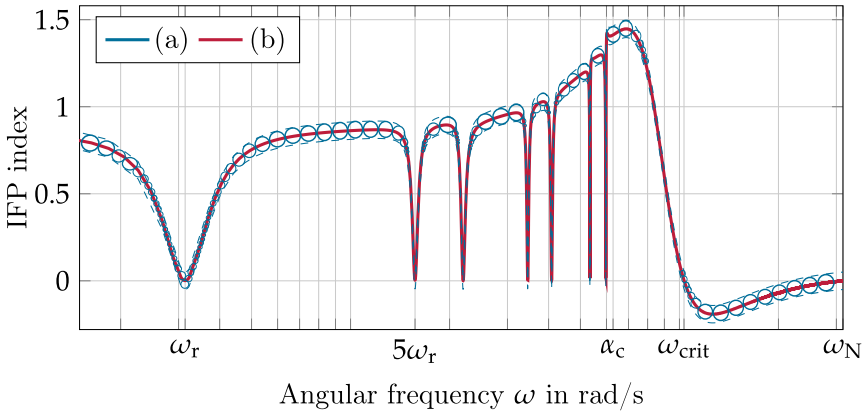

Fig. 6.9: IFP index of the converter's effective inherent input admittance, which interprets aliasing effects by (a) a well bounded uncertainty that perturbs (b) the nominal IFP index of $Y_{\mathrm{m},0}(s)$ with $\Delta_0(s) = 1$.

excessively large. Moreover, as revealed in [73], robust design methods often result in rather conservative sufficient passivation conditions and the deduced active filter (if there is any complying with the passivation conditions) is likely to produce unnecessarily large control actions in frequency regions, where the converter's input admittance is already inherently passive. These drawbacks make robust passivation methods like those proposed in [14, 73, 92] less suitable for the practical application to the grid-connected converter system of Fig. 6.6. Therefore, in order to overcome the disadvantages and not to be forced to use unrealistic worst-case approximations, which mostly lead to over-conservative designs, it is suggested to still perform an active damping filter design according to the ideas of Sec. 5.3, but considering the following aspects.

Similar to the approach from Sec. 5.3.1, a simplified active feed-forward filter design criterion that takes aliasing effects into account can be derived from the IFP index of $Y_{\mathrm{m},0}(s)$. In particular, given the definition of the converter's multiple-frequency input admittance (6.19), IFP $\{Y_{\mathrm{m},0}(j\omega)\}$ can be decomposed into

$$\begin{aligned}\mathrm{IFP}\left\{Y_{\mathrm{m},0}(j\omega)\right\} = &\,\mathrm{IFP}\left\{Y_{\mathrm{fc}}(j\omega)\right\} \\ &- \mathrm{IFP}\left\{Y_{\mathrm{fc}}(j\omega)\Gamma_0(j\omega)\Delta_0(j\omega)G_{\mathrm{cl},0}(j\omega)/T_{\mathrm{s}}\right\}. \end{aligned} \tag{6.26}$$

Reviewing the findings from Sec. 5.1.1 and again assuming that the converter-side filter resistance is negligible, i.e., $r_{\mathrm{fc}} \approx 0$, and thus, $\mathrm{IFP}\left\{Y_{\mathrm{fc}}(j\omega)\right\} \approx 0$ and $\arg\left\{Y_{\mathrm{fc}}(j\omega)\right\} \approx -\pi/2$, an evaluation of (6.26) shows that the multiple-frequency input admittance is passive, if

$$-180^\circ \leq \arg\left\{\Gamma_0(j\omega)\right\} + \arg\left\{\Delta_0(j\omega)\right\} + \arg\left\{G_{\mathrm{cl},0}(j\omega)/T_{\mathrm{s}}\right\} \leq 0^\circ, \forall\omega \in [0, \omega_{\mathrm{N}}]. \tag{6.27}$$

If it is considered that $\Gamma_0(s)$ is identical to $\Gamma(s)$ and $G_{\mathrm{cl},0}(s)/T_{\mathrm{s}} \approx G_{\mathrm{cl}}(s)/T_{\mathrm{s}}$ in the low-frequency range up to the Nyquist frequency, it can be noticed that the passivity condition (6.27) differs from condition (5.24) more or less only in the additional term $\arg\left\{\Delta_0(j\omega)\right\}$ in (6.27). In this context, (6.27) simultaneously defines the class of uncertainties, which might perturb the model of the VSC primary-frequency input admittance from Sec. 3.4.2 without leading to a negative converter conductance. As usual when dealing with sufficient passivity criteria for SISO systems [14, 25], the passivity condition (6.27) does not make any further demands on the amplitude of the dynamic uncertainty $\Delta_0(s)$, but only on the phase response, $\arg\left\{\Delta_0(j\omega)\right\}$. This makes clear that all basic active feed-forward filter design guidelines from Sec. 5.3 can directly be adopted, where, in addition, also the (estimated) phase response of the dynamic uncertainty (6.18) should be taken into account.

Although (6.18) depends on the grid impedance $Z_{\mathrm{g}}(s)$ as well as the utilized feed-forward filter $H(z)$, and therefore no general statements can be made, the exemplary Bode plots of $\Delta_0(s)$ in Fig. 6.7 provide useful information from which some fundamental design recommendations can be derived. Observing Fig. 6.7, it can be seen that it becomes especially important that $\Gamma_0(s)$ does not show a sudden phase change from 0° to 180° at ω_{crit}, but implements a phase response that increases sufficiently moderate between ω_{crit} and ω_{N}. This avoids that a possibly emerging resonance or phase lead of $\Delta_0(s)$ raises the phase response of

$\Gamma_0(s)\Delta_0(s)G_{\mathrm{cl},0}(s)/T_\mathrm{s}$ in the high-frequency range above $0°$, and thus, probably yields a non-passive region in $Y_{\mathrm{m},0}(s)$. From this point of view and with regard to the findings from Sec. 5.3.2 and Sec. 5.3.3, it is strongly recommended not to adopt a purely proportional damping filter as suggested in [4, 57, 156]. Instead, a more advanced capacitor current feed-forward filter should be used, which allows to implement a phase lag between ω_crit and ω_N, e.g., the proposed filter (5.38) with a sufficiently large damping ratio δ. If more damping at the Nyquist frequency is required, it is still proposed to increase the converter-side filter resistance, r_fc, keeping the resulting losses in mind.

Moreover, it has been shown through a number of tests that the dynamic uncertainty $\Delta_0(s)$ tends to introduce an unwanted phase lead near the specified resonance frequencies, $h_i\omega_\mathrm{r}, \forall h_i \in h$, which might also lead to some non-passive regions in the low-frequency range. This effect should be suppressed in the filter $H(z)$ by implementing a band-stop at every $h_i\omega_\mathrm{r}$, e.g., by using the suggested preceding filter $G_\mathrm{PR}(z)/G_\mathrm{PRH}(z)$ in (5.38). It might also be an advantage to reduce the PR controller's integral gains, k_{I,h_i}, either by increasing the resonator's associated cut-off frequencies ω_{c,h_i} or by choosing other weightings $\gamma_{h_1} \geq \ldots \geq \gamma_{h_m}$, which both generally improve the passivity (or stability) properties of the converter, but weaken the VSC's capabilities to compensate for harmonics [3,4]. Certainly, the structure and parameterization of the active damping filter can further be enhanced and concretized by taking prior knowledge about the grid impedance Z_g into account and should be tested thoroughly after each design. But, if the discussed guidelines are followed, the influence of (previously unmodeled) aliasing effects on the passivation of the converter's input admittance can effectively be counteracted and it can largely be avoided that $Y_{\mathrm{m},0}(s)$ shows any non-passive regions in the complete frequency range of interest up to the Nyquist frequency.

Given a well damped grid with no significant above Nyquist frequency resonances and using (6.23) to approximate the (actual) dynamic uncertainty $\Delta_0(s)$, Fig. 6.10 demonstrates that the proposed capacitor current feed-forward filter (5.38) with the parameters from Tab. 5.2 already renders the converter's input admittance models robustly passive, i.e.,

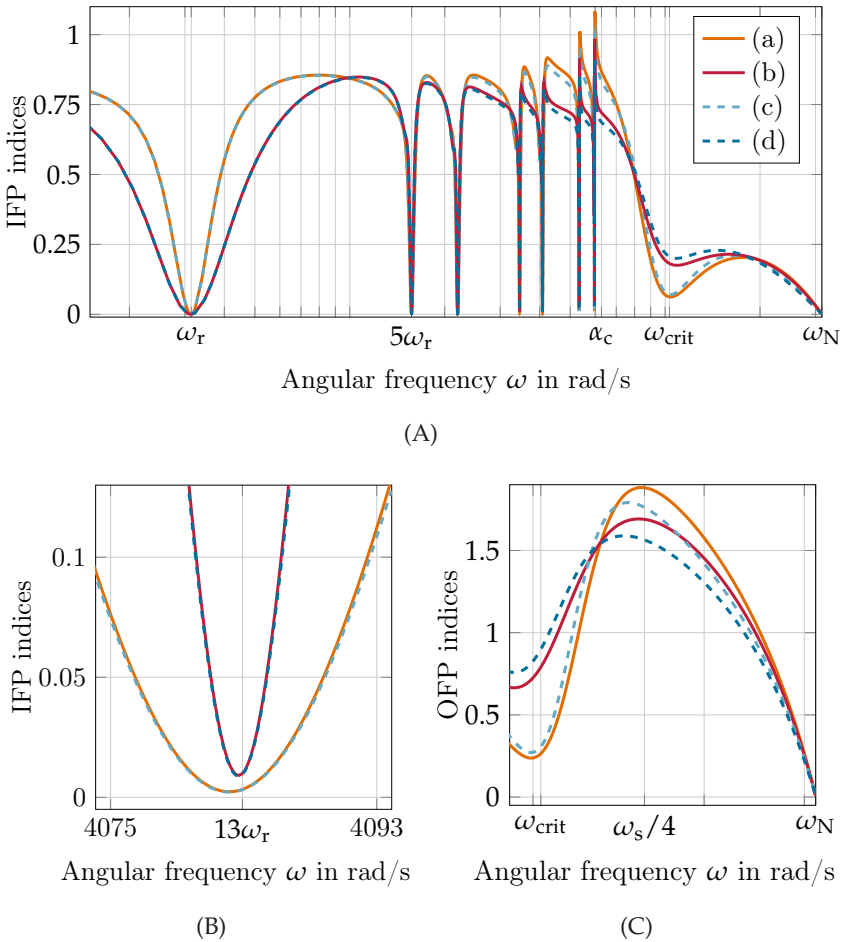

Fig. 6.10: Passivity indices of the VSC's (a), (b) estimated multiple-frequency input-admittance model $Y_{m,0}(s)$ with $Z_g = 0$, and (c), (d) primary-frequency input admittance model $Y_{i,p}(s)$, where the converter under study is equipped with an undamped LCL filter and implements the proposed active capacitor current feed-forward filter (5.38) using (a), (c) the parameters from Tab. 5.2 and (b), (d) an alternative, more robust parameterization. Subfigure (A) shows the IFP indices of the converters' admittances in the complete frequency range of interest, (B) shows a detailed section of the systems' IFP indices near $13\,\omega_r$, and (C) illustrates the systems' OFP indices in the high-frequency range.

$\mathrm{IFP}\{Y_{\mathrm{i,p}}(j\omega)\} > 0, \forall\omega \in [0,\omega_{\mathrm{N}}]$ and $\mathrm{IFP}\left\{Y_{\mathrm{m},0}(j\omega)|_{Z_{\mathrm{g}}=0}\right\} > 0, \forall\omega \in [0,\omega_{\mathrm{N}}]$.

Compared to $\mathrm{IFP}\{Y_{\mathrm{i,p}}(j\omega)\}$ and $\mathrm{OFP}\{Y_{\mathrm{i,p}}(j\omega)\}$, the passivity indices of the estimated multiple-frequency input admittance show higher values near ω_{N}, but marginally lower values in the frequency range near the critical frequency ω_{crit}. Nevertheless, it can be assumed that a perturbation by a more significant dynamic uncertainty $\Delta_0(s)$, which is, e.g., caused by an above Nyquist frequency resonance in $Z_{\mathrm{g}}(s)$, is unlikely to lead to a lack of passivity. If at all, there exists only a certain risk in the frequency ranges near the frequency ω_{crit} and the PR controller's resonance frequencies, $h_i\omega_{\mathrm{r}}, \forall h_i \in h$. But, if it is still desired that the converter's input admittance shows a more robust behavior for frequencies above $5\,\omega_{\mathrm{r}}$ [6] and a higher feed-forward action can be tolerated, the design can be adapted, for example, by increasing the feed-forward filter's damping ratio from $\delta = 0.1$ to $\delta = 0.2$ and additionally decrease the prioritization of high-frequency harmonics to e.g., $\gamma_1 = 1, \gamma_5 = \gamma_7 = 0.2, \gamma_{11} = \gamma_{13} = 0.06, \gamma_{17} = \gamma_{19} = 0.02$. The corresponding (red and dashed blue) passivity indices in Fig. 6.10 illustrate the VSC's beneficial passivity properties in the high- as well as low-frequency range and also demonstrate the easy plug-and-play feature of the suggested design approach.

Stability of the Closed-Loop Grid-Converter System

Since a sufficiently robust passivation of the converter's primary-frequency input admittance model mostly also results in a strictly passive multiple-frequency input admittance, it can directly be concluded that the actively damped closed-loop grid-converter system is asymptotically stable, if the (synthetic) grid impedance is passive [14, 25, 74]. Estimating $\Delta_0(s)$ by (6.18) with $k = \pm 1$, this can also be verified by the exemplary Nyquist plots of the open-loop grid-converter system in Fig. 6.11. If the converter is connected to a purely inductive grid, the Nyquist curves of $Y_{\mathrm{m},0}(s)\tilde{Z}_{\mathrm{g}}(s)$ and $Y_{\mathrm{i,p}}(s)\tilde{Z}_{\mathrm{g}}(s)$ are largely similar to each other, see Fig. 6.11A and Fig. 6.11B. Since no curve crosses or encircles the critical point $(-1 + j0)$ for all $\omega \in [0,\omega_{\mathrm{N}}]$, and thus, the shown systems satisfy

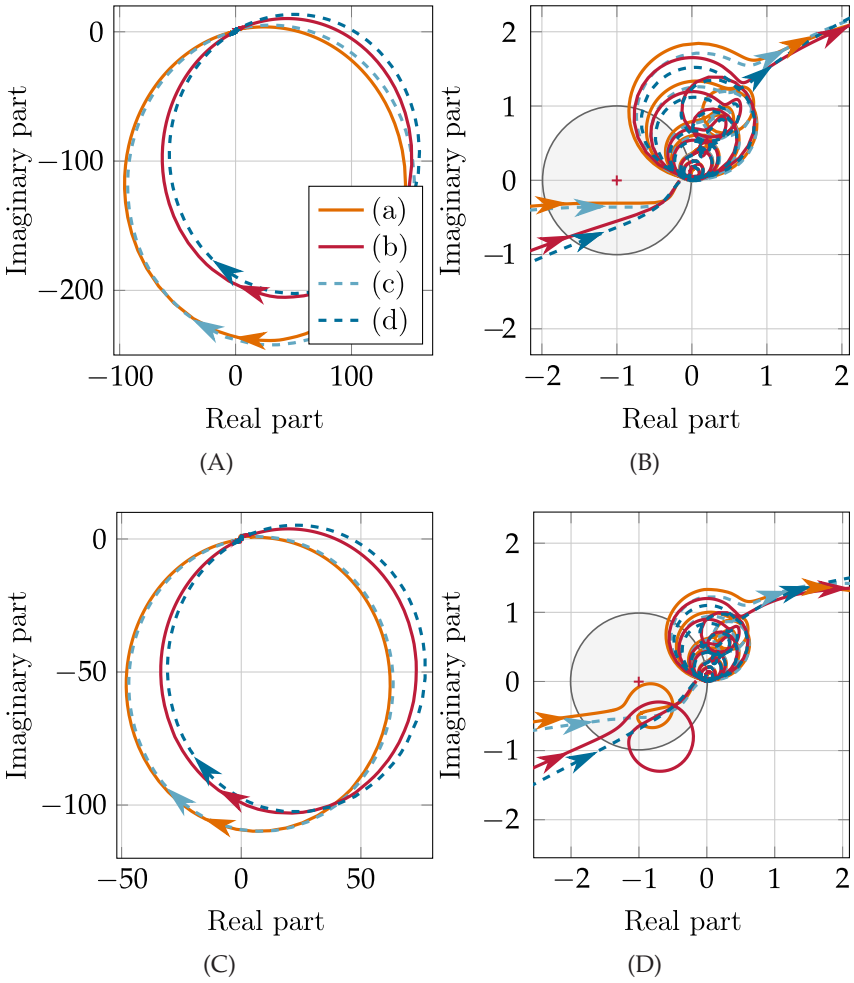

Fig. 6.11: Nyquist plots of the open-loop grid-converter system using (a), (c) the estimated multiple-frequency input admittance model and (b), (d) the primary-frequency input admittance model, where the VSC is equipped with an undamped LCL filter and implements the proposed active capacitor current feed-forward filter (5.38) with (a), (c) the parameters from Tab. 5.2 and (b), (d) an alternative, more robust parameterization. Subfigures (A), (C) and subfigures (B), (D) show the complete and detailed plots for $\omega \in [0, \omega_{\mathrm{N}}]$, respectively, where the VSC is connected (A), (B) to an inductive grid with $Z_{\mathrm{g}}(s) = l_{\mathrm{g}} s$, $l_{\mathrm{g}} = 64.95\,\mu\mathrm{s}$, and (C), (D) to a resistive-inductive grid, where $\tilde{Z}_{\mathrm{g}}(s)$ has an above Nyquist frequency resonance at $\omega_{\mathrm{r},\tilde{\mathrm{Z}}_{\mathrm{g}},2} \approx 50492\,\frac{\mathrm{rad}}{\mathrm{s}}$.

the SISO Nyquist stability criterion [10, 39, 98, 119], it can be concluded with high probability that the VSC can safely be operated on a grid with predominant resistive-inductive character. Hereby, a more robust converter passivation with the modified filter parameters $\delta = 0.2$ and $\gamma_1 = 1, \gamma_5 = \gamma_7 = 0.2, \gamma_{11} = \gamma_{13} = 0.06, \gamma_{17} = \gamma_{19} = 0.02$ leads to a higher stability measure, specified by the system's phase margin or the system's sensitivity peak, i.e., the inverse of the minimum distance between the Nyquist curve and the point $(-1 + j0)$ [10, 119]. Regarding the findings from Sec. 6.3, this can also be assumed to be true for any other passive grid impedance having no significant resonance above the Nyquist frequency.

On the other hand, Fig. 6.11D demonstrates that the Nyquist curves of $Y_{\mathrm{m},0}(s)\tilde{Z}_{\mathrm{g}}(s)$ and consequently also the passivity assessment may differ, if the connected (synthetic) grid impedance shows one or multiple resonances above ω_{N}. While the model which uses the primary-frequency input admittance does not detect any potential stability issues at all, the proposed multiple-frequency model allows to accurately predict the effects of a mirrored above Nyquist frequency resonance. As can be seen, there might occur loops that yield an encirclement of the critical point $(-1 + j0)$. Nevertheless, for the converter test-system and the chosen filter parameterizations, it is likely that both suggested designs result in an asymptotically stable (more or less robust) total input admittance $Y_{\mathrm{t},0}(s)$. If required, the actively damped VSC can be complemented by a passive damping scheme, which in most cases further improves the converter's stability properties, see Fig. 5.15.

Finally, the examples demonstrate that a sufficiently robust passivation of the converter system typically ensures that the SISO Nyquist stability criterion is satisfied for all $\omega \in [0, \omega_{\mathrm{N}}]$, even if an (unexpected) resonance or changes in the grid impedance might cause a worsening of the passivity properties of $Y_{\mathrm{m},0}(s)$. Furthermore, in view of unmodeled dissipative effects and the decreasing gains of all active grid components near and above the Nyquist frequency, it is rather unlikely that grid resonances lead to a critical expansion of the Nyquist curves in the very high-frequency range, resulting in a destabilization of the power system. This

finding differs from the results of most recent research. Although it may be beneficial to aim for a passive converter input admittance above the Nyquist frequency, as recommended in [53], this chapter has shown that the most important aspect for the system stability is still the (robust) passivation of the input admittance in the low-frequency range up to ω_{N}.

7 Simulation and Verification

In this chapter, the theoretical findings on the modeling and passivation of the VSC's input admittance from the previous chapters are verified by detailed computer simulations. After introducing the utilized simulation model and test procedure, Sec. 7.2 summarizes the most important results from several studies. This includes the measurement and comparison of the IFP index of different VSC input admittances and the discussion of the converter's transient behavior in scenarios where the grid shows (multiple) below and/or above Nyquist frequency resonances.

7.1 Simulation Setup and Test Procedure

For the simulation of the closed-loop grid-converter system, a model of the single-phase converter circuit from Fig. 3.1 is implemented in MATLAB/SIMULINK. The model uses the ODE45 explicit Runge-Kutta based variable step solver with enabled zero-crossing detection option and limited maximum step size of $T_\mathrm{s}/40$. For simplicity, emerging switching losses and the high-frequency (parasitic) dynamic behavior of specific semiconductor switches is not taken into account and a single-update PWM with triangular carrier, as illustrated in Fig. 3.6, is used to generate the converter output voltage V_c. In order to ensure that the converter's sampling and control cycle is perfectly synchronized with the (continuous) carrier signal of the nonlinear modulator, the simulation model implements a triggered subsystem to conditionally run the digital part of the hybrid sampled-data system. This includes the digital realization of the multifrequency PR controller shown in Fig. 3.11 as well as different digital active feed-forward filters. The control output V_ref is delayed by a time delay of length $T_\mathrm{c} = T_\mathrm{s}$ to model the analog-to-digital conversion and computation time of practical systems. Since a constant DC link

voltage is assumed throughout the thesis, the model does not include the (nonlinear) dynamics of the DC link [2] nor any outer loops, such as a reference current calculator plus PLL, or an outer voltage and power control loop. The inputs of the model are the digital reference current I^*_{ref} and the continuous grid voltage V_{g}.

Where not otherwise noted, the simulation model implements the already introduced converter test-system parameters from Tab. 3.1, the parameters of an undamped LCL filter from Tab. 3.2, and the PR current controller parameters from Tab. 4.1. As demonstrated by the theoretical analysis of Sec. 4.3, the resulting grid-converter system will probably generate poorly damped or increasing oscillations without additional damping scheme. This is because the resonance of the synthetic grid impedance $\tilde{Z}_{\mathrm{g}}(s)$ at $\omega_{\mathrm{r},\tilde{\mathrm{Z}}_{\mathrm{g}}} \approx 1/\sqrt{L_{\mathrm{fg}}C_{\mathrm{c}}} \approx 11910\,\frac{\mathrm{rad}}{\mathrm{s}}$ falls within the frequency range between $\omega_{\mathrm{crit}} \approx 10324\,\frac{\mathrm{rad}}{\mathrm{s}}$ and $\omega_{\mathrm{N}} = 31415.9\,\frac{\mathrm{rad}}{\mathrm{s}}$, where the converter inherently shows a negative conductance. To still simulate (at least at the beginning) a stable operation of the grid-converter system, the MATLAB/SIMULINK model either implements an optimized LCL filter or initially activates the synthetic PCC voltage feed-forward filter (5.31) or the capacitor current feed-forward filter (5.38).

Input Admittance Measurements

Based on the principle procedures from [8,42,53,110], in the following, the converter's effective input admittances are measured by a voltage test-signal injection at the point of the grid voltage (and not at the PCC). As explained in Sec. 6.3, this ensures that all aliasing effects of high-frequency switching harmonics are captured and $Y_{\mathrm{m},0}(s)$ can accurately be identified. Hereby, $I_{\mathrm{ref}}(kT_{\mathrm{s}}) = 0,\ k = 0,1,2,\ldots$ and $V_{\mathrm{g}}(t)$ defines a real sinusoidal of the form $V_{\mathrm{g}}(t) = E_{\mathrm{b}}/4 \cdot \sin(\omega_i t)$, which frequency ω_i is swept from $100\,\frac{\mathrm{rad}}{\mathrm{s}}$ to immediately below ω_{N}. The relatively low test-signal amplitude and the resulting low degree of extinction is chosen to guarantee that VSC's reference voltage always keeps within the normal operation range of the PWM, i.e., $0 < V_{\mathrm{ref}}(kT_{\mathrm{s}}) < V_{\mathrm{DC}}/2,\ k = 0,1,2,\ldots$. After waiting 1000 periods each time until the converter current $I(t)$ is in the steady

state, the last 53 periods are used to perform an FFT and to calculate the normalized magnitude and phase characteristics of the VSC's total input admittance seen from the grid, $Y_{\mathrm{t},0}(j\omega_i) = |I(\omega_i)|\, Z_\mathrm{b}/(E_\mathrm{b}/4) \cdot e^{j\phi_{I(\omega_i)}}$. Then, given (6.20) and taking into account that $Y_{\mathrm{t},0}(s)$ is defined with respect to the normalized synthetic grid voltage $\tilde{\boldsymbol{v}}_\mathrm{g}(s) = \tilde{Z}_\mathrm{g}(s)\tilde{Y}_\mathrm{fg}(s)\boldsymbol{v}_\mathrm{g}(s)$, the frequency response of the converter's effective (multiple-frequency) input admittance at each frequency sample ω_i is obtained by

$$Y_{\mathrm{m},0}(j\omega_i) = \frac{Y_{\mathrm{t},0}(j\omega_i)}{\tilde{Y}_\mathrm{fg}(j\omega_i)\tilde{Z}_\mathrm{g}(j\omega_i) - Y_{\mathrm{t},0}(j\omega_i)\tilde{Z}_\mathrm{g}(j\omega_i)/Z_\mathrm{b}} \tag{7.1}$$

where the frequency responses of $\tilde{Y}_\mathrm{fg}(j\omega_i)$ and $\tilde{Z}_\mathrm{g}(j\omega_i)$ are assumed to be exactly known from the theoretical models from Sec. 3.2.1 for the calculation. The IFP index of the measured VSC input admittance is finally specified by $\mathrm{Re}\,\{Y_{\mathrm{m},0}(j\omega_i)\}$ or $\mathrm{Re}\,\{Y_{\mathrm{t},0}(j\omega_i)\}$.

Transient Measurements

In order to illustrate the most important theoretical results and to demonstrate the potential destabilizing effect of poorly damped grid resonances, the converter simulation model is connected to a grid with different synthetic grid impedances, showing one (or more) resonances in $\tilde{Z}_\mathrm{g}(s)$. As has been found, the interconnection of the VSC via a transmission line, modeled by a single Π-segment, in combination with the resonance of the LCL filter might already yield (multiple) critical resonances in the synthetic grid impedance. Similar critical resonances also occur when modeling much complexer networks that include multiple grid-connected converters, see e.g., [11, 88, 141], but are not used here.

The exemplarily studied converter setups are shown in Fig. 7.1. While the implemented converter model is directly connected to a grid with impedance $Z_\mathrm{g}(s)$ in scenario (A), the VSC is connected to the grid via an $1.1\,\mathrm{km}$ long transmission line in scenario (B). Depending on the scenario and the system parameters, there result the (unnormalized) synthetic grid impedances shown in Fig. 7.2. The parameters of the adopted LCL filter,

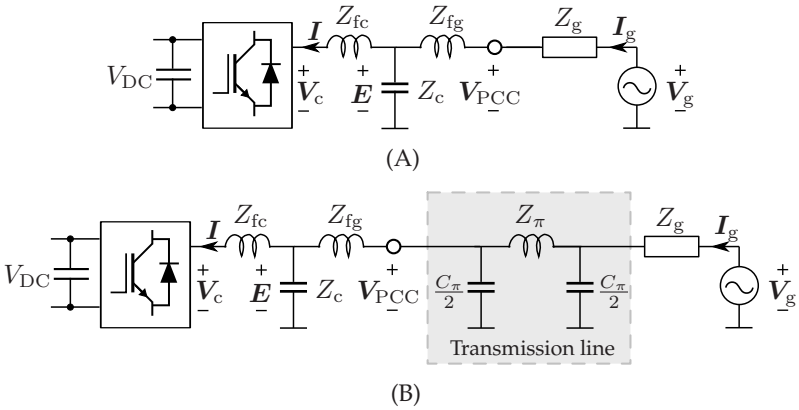

Fig. 7.1: Simplified single-phase impedance-based equivalent circuit diagram of the converter test-system setup, where the VSC implements a damped or undamped LCL filter and, in scenario (A), is directly connected to the grid and, in scenario (B), is connected to the grid over a (long) transmission line, modeled by a Π-segment.

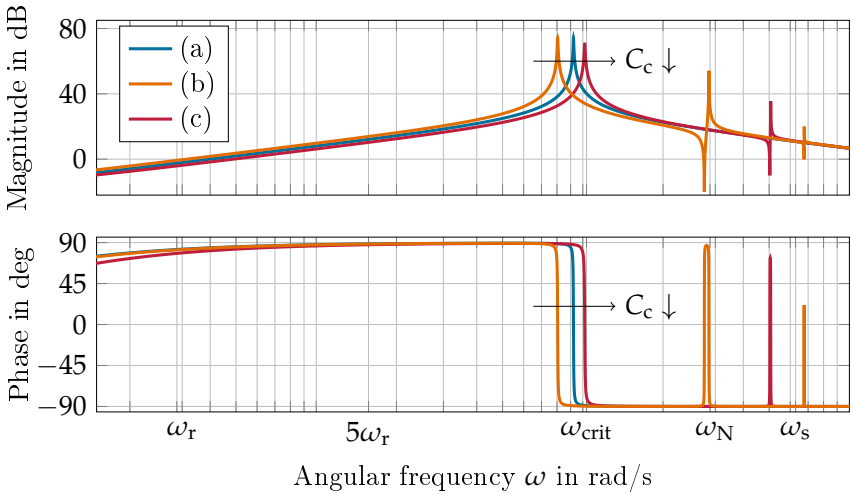

Fig. 7.2: Bode plots of $\tilde{Z}_g(s) \cdot Z_b$, resulting from the interconnection of the capacitance and grid-side inductance of an ideal LCL filter with (a) an inductive grid with $Z_g(s) = L_g s$, $L_g = 1\,\mathrm{mH}$, (b) an inductive grid with $Z_g(s) = L_g s$, $L_g = 1\,\mathrm{mH}$ plus $1.1\,\mathrm{km}$ long transmission line, and (c) a stiff grid with $Z_g(s) = 0$ plus $1.1\,\mathrm{km}$ long transmission line.

the effective (low-frequency) grid impedance and the transmission line's equivalent Π-model for the simulations are summarized in Tab. 7.1.

Table 7.1: Summary of exemplary LCL filter, grid impedance, and transmission line parameters

Parameter	Symbol	Value	Units
LCL filter parameters			
Converter-side inductor	L_{fc}	3	mH
Converter-side resistor	R_{fc}	0.2	Ω
Grid-side inductor	L_{fg}	1.5	mH
Grid-side resistor	R_{fg}	0.1	Ω
LCL filter capacitor	C_{c}	4.7 or 2.7	μF
Damping resistor	R_{d}	0, 4.16 or 0.4	Ω
Effective (low-frequency) grid impedance parameters			
Grid inductance	L_{g}	1 or 0	mH
Parameters of Π-segment [141]			
Cable inductance	L_{π}	0.48	mH/km
Cable resistance	R_{π}	0.025, 0.012 or 0	Ω/km
Cable capacitance	C_{π}	0.46	μF/km

As intended for the illustration, the principle behavior of the resulting synthetic grid impedances is similar to the behavior of $\tilde{Z}_{\mathrm{g}}(s)$ with $Z_{\mathrm{g}}(s) = 0$, shown in Fig. 3.4. If the converter test-system with (undamped) LCL filter is directly connected to the grid, $\tilde{Z}_{\mathrm{g}}(s) \cdot Z_{\mathrm{b}}$ shows a single resonance near the frequency ω_{crit}, at which the VSC's input admittance becomes inherently non-passive, whereas a connection via a single Π-segment leads either to an additional resonance at $\omega_{\mathrm{r},\tilde{\mathrm{Z}}_{\mathrm{g}},2} \approx 29128\,\frac{\mathrm{rad}}{\mathrm{s}} < \omega_{\mathrm{N}} \approx 31416\,\frac{\mathrm{rad}}{\mathrm{s}}$ and a negligible resonance at $\omega_{\mathrm{r},\tilde{\mathrm{Z}}_{\mathrm{g}},3} \approx 67665\,\frac{\mathrm{rad}}{\mathrm{s}} > \omega_{\mathrm{s}} \approx 62832\,\frac{\mathrm{rad}}{\mathrm{s}}$ or to an additional resonance at $\omega_{\mathrm{r},\tilde{\mathrm{Z}}_{\mathrm{g}},2} \approx 50492\,\frac{\mathrm{rad}}{\mathrm{s}} > \omega_{\mathrm{N}}$.

In all scenarios and independent of the system parameters or the connected synthetic grid impedance, the grid voltage $V_{\mathrm{g}}(t)$ is defined to have a sinusoidal fundamental component at $\omega_{\mathrm{r}} = 2\pi 50\,\frac{\mathrm{rad}}{\mathrm{s}} \approx 314.159\,\frac{\mathrm{rad}}{\mathrm{s}}$ with amplitude $E_{\mathrm{b}} \approx 326.6\,\mathrm{V}$, as well as harmonics of order $h = \{5, 7, 11, 13, 17, 19\}$ with $4\%, 4\%, 2\%, 2\%, 1\%, 1\%$ of the nominal grid voltage amplitude, E_{b}, respectively. In the performed transient simulations, a sampled sinusoidal of the form $I_{\mathrm{ref}}(kT_{\mathrm{s}}) = 15 \cdot \sin(\omega_r k T_{\mathrm{s}})$, $k = 0, 1, 2, \ldots$

is used as the converter's reference current. For the sake of simplicity, and to avoid the application of a PLL [5], which might (negatively) affect the simulative verification of the discussed theory, the phase offset of the converter reference current is constantly set to zero. Since, in this case, the grid current $I_{\mathrm{g}}(t)$ is generally not aligned with the PCC voltage $V_{\mathrm{PCC}}(t)$, the test-system does not provide an unit power factor, and thus, not only injects an active current component into the grid, but also more or less reactive current depending on the specific scenario. The resulting phase displacement is, however, not essential for the operation or the stability of the studied converter system, but should be considered in the reference current calculation or the power control in advanced simulations [127].

7.2 Results and Discussion

The main results of different simulative studies, including an exemplary destabilization of the grid-converter system by a below and an above Nyquist frequency grid resonance, are summarized as follows.

7.2.1 Destabilization by a Below Nyquist Frequency Resonance

To begin with, the limited damping capability and the associated risks of a passively damped converter system are demonstrated. As elaborated in Sec. 5.2.2 and shown in Fig. 5.6, the excess of the IFP index of the synthetic grid impedance $\tilde{Z}_{\mathrm{g}}(s)$ can be used to compensate for the inherent shortage of the VSC input admittance's passivity. However, a stable operation and a complete passivation of the grid-converter system can only be guaranteed by design, if the grid impedance $Z_{\mathrm{g}}(s)$ is known in advance and changes only marginally. Presupposing that $Z_{\mathrm{g}}(s) \approx 0$ and adopting the proposed optimized LCL filter topology from Fig. 3.2B with $C_{\mathrm{c}} = c_{\mathrm{c}}/Z_{\mathrm{b}} = 2.7\,\mu\mathrm{F}$ and series damping resistance $R_{\mathrm{d}} = r_{\mathrm{d}} Z_{\mathrm{b}} \approx 4.16\,\Omega$, this can also be verified by the corresponding IFP indices of the test-system's theoretical and measured total input admittance shown in Fig. 7.3.

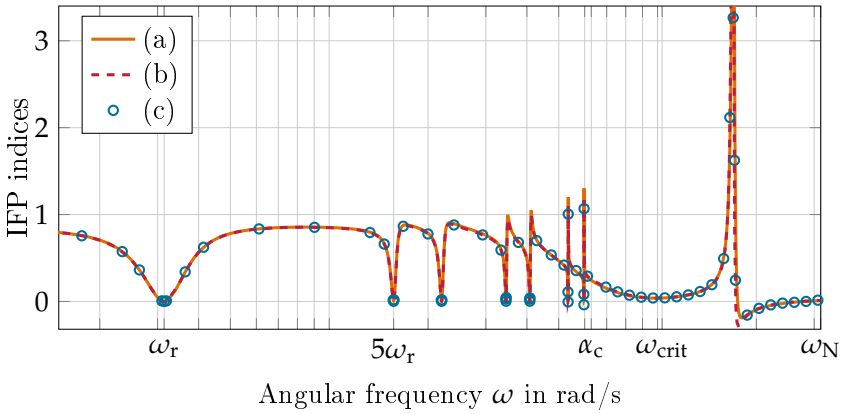

Fig. 7.3: IFP indices of different total input admittance models for the converter test-system with passive damped LCL filter and $Z_\mathrm{g}(s) = L_\mathrm{g}s$, $L_\mathrm{g} = 1\,\mathrm{mH}$, where (a) is calculated with the multiple-frequency input admittance model $Y_{\mathrm{m},0}(s)$, (b) is calculated with the primary-frequency input admittance model $Y_{\mathrm{i,p}}(s)$, and (c) shows the characteristics obtained from a simulative input admittance measurement.

It can be observed that both theoretic models match well with the measured characteristic. All total input admittances show a large excess of passivity in the frequency range above ω_crit (between $16367\,\frac{\mathrm{rad}}{\mathrm{s}}$ and $17291\,\frac{\mathrm{rad}}{\mathrm{s}}$), but, for higher frequencies, also have a (small) non-passive region near the Nyquist frequency ω_N. This lack of passivity is caused by the inaccurate estimation of the grid impedance $Z_\mathrm{g}(s)$ during the design. As indicated by the associated Nyquist plots from Fig. 5.7A and Fig. 5.7B, it is nevertheless likely that the converter can be operated safely on a (resistive-) inductive grid with similar effective low-frequency grid inductances. But, the Nyquist curves in Fig. 5.7C and Fig. 5.7D also predict that an unfavorable, poorly-damped grid resonance below the Nyquist frequency may yet destabilize the closed-loop system.

In accordance to the theory, this can also be verified by the transient simulations shown in Fig. 7.4. Here, the passive damped converter is initially connected to an inductive grid, where $Z_\mathrm{g}(s) = L_\mathrm{g}s$, $L_\mathrm{g} = 1\,\mathrm{mH}$. The digitally current-controlled converter is able to accurately track its reference

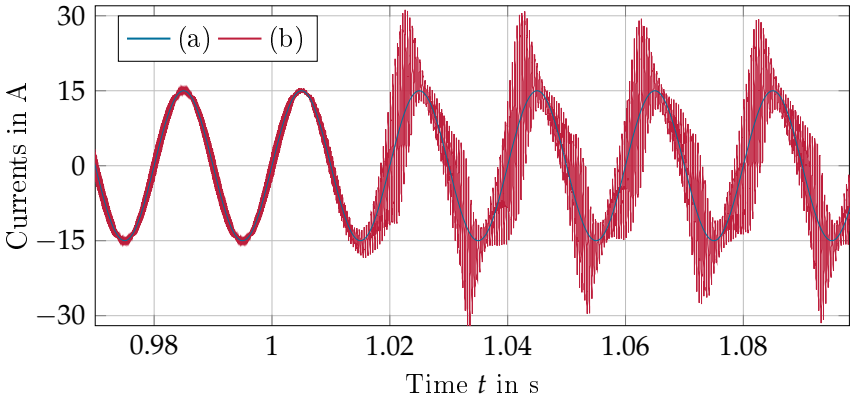

(A)

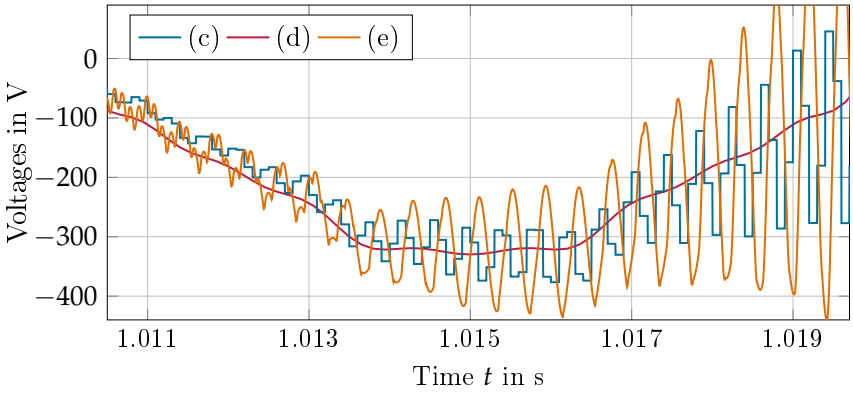

(B)

Fig. 7.4: Simulative converter responses of the passive damped VSC in case of a suddenly emerging below Nyquist frequency resonance at $t = 1\,\mathrm{s}$, where, in subfigure (A), (a) and (b) show the VSC's reference current and output current, respectively, and in subfigure (B), (c) illustrates a detailed section of the VSC's reference voltage, and (d) and (e) show the related grid and PCC voltage, respectively.

and to suppress the superimposed voltage harmonics. At $t = 1\,\mathrm{s}$, the VSC is connected to the grid over an $1.1\,\mathrm{km}$ long transmission line, yielding an additional dominant resonance in the synthetic grid impedance $\tilde{Z}_\mathrm{g}(s)$ at $\omega_{\mathrm{r},\tilde{Z}_\mathrm{g},2} \approx 29128\,\frac{\mathrm{rad}}{\mathrm{s}}$, see Fig. 7.2. Since the resonance falls within a region, where the damping effect of the LCL filter topology is minor, harmonic oscillations are from now on amplified to an inadmissibly high level.

A similar situation also arises when the grid-connected converter implements a synthetic PCC voltage feed-forward instead of an LCL filter with series passive damping resistor. In this context, Fig. 7.5 shows the measured IFP index as well as the calculated IFP indices of different total input admittance models. To be consistent with the theoretical analysis from Sec. 5.3.2, the capacitance and the damping resistance of the LCL filter are again $C_\mathrm{c} = 4.7\,\mu\mathrm{F}$ and $R_\mathrm{d} = 0\,\Omega$, respectively, and the parameters of the implemented feed-forward filter (5.31) are those from Tab. 5.2, where $\omega_\delta = 0$.

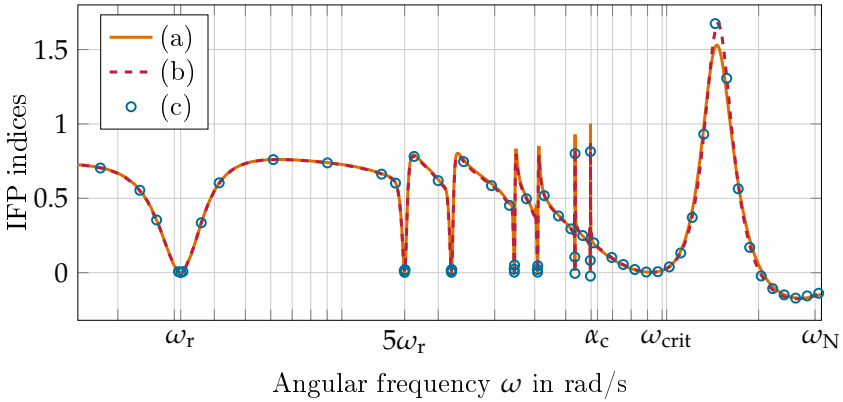

Fig. 7.5: IFP indices of different total input admittance models for the converter test-system with active synthetic PCC voltage feed-forward and $Z_\mathrm{g}(s) = L_\mathrm{g} s$, $L_\mathrm{g} = 1\,\mathrm{mH}$, where (a) is calculated with $Y_{\mathrm{m},0}(s)$, (b) is calculated with $Y_{\mathrm{i,p}}(s)$, and (c) shows the characteristics obtained from a simulative input admittance measurement.

As can be verified, the basic evolution of the closed-loop system's IFP index is comparable to that shown in Fig. 7.3. Again, the measured total

VSC input admittance shows a large excess of IFP above ω_{crit}, but also has a (more significant) shortage of IFP in the high-frequency range near the Nyquist frequency. Hereby, the identified IFP index is similar to the theoretically calculated indices, but tends to better comply with the IFP index of the total input admittance which utilizes the primary-frequency model $Y_{\mathrm{i,p}}(s)$. In this scenario, the influence of aliasing effects are negligible and the visible discrepancy is mainly caused by the nonlinear, but less pessimistic character of the PWM. If necessary, a better compliance can be achieved by adapting the parameters of the suggested multiple-frequency small-signal PWM model (6.2), e.g., by tuning the even duty cycles $D_{0,q}$ or the odd offset terms o_q, see Fig. 6.3. However, it can be assumed that both models reflect the real behavior of the converter disturbance dynamics well enough in the critical frequency range to provide an accurate stability assessment.

In particular, reviewing the conclusion from Sec. 5.3.2, it is again likely that the converter can safely be operated on a grid with (predominant) resistive-inductive behavior. But, on the other hand, the VSC might get destabilized by a below Nyquist frequency resonance, which falls within the region where the conductance of the actively damped converter shows a lack of passivity, see Fig. 5.11. This agrees with the results of the simulation shown in Fig. 7.6. Here, the converter with activated synthetic PCC voltage feed-forward is initially connected to an inductive grid with $Z_{\mathrm{g}}(s) = L_{\mathrm{g}}s$, $L_{\mathrm{g}} = 1\,\mathrm{mH}$ and at $t = 1\,\mathrm{s}$, the VSC is connected to the grid over an $1.1\,\mathrm{km}$ long transmission line. As predicted by the associated open-loop system's Nyquist plots in Fig. 5.11, the first grid connection yields a stable closed-loop system, while the latter causes the converter to leave its stable operation range. Analogous to the previous simulation of a passively damped converter, high-frequency harmonics are unacceptably amplified, resulting in superimposed oscillations with increasing amplitude in the converter output current. Hence, it can finally be confirmed by simulation that a digitally current-controlled grid-connected converter with passive damping or synthetic PCC voltage feed-forward leaves room for a destabilization by an unfavorable below Nyquist frequency resonance in the synthetic grid impedance $\tilde{Z}_{\mathrm{g}}(s)$.

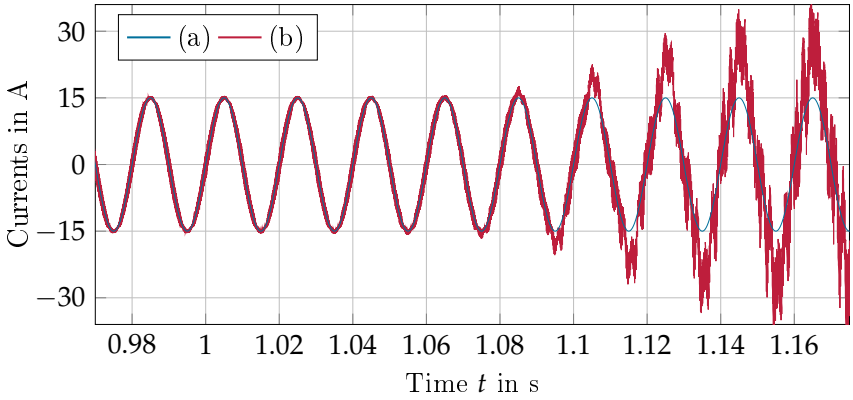

(A)

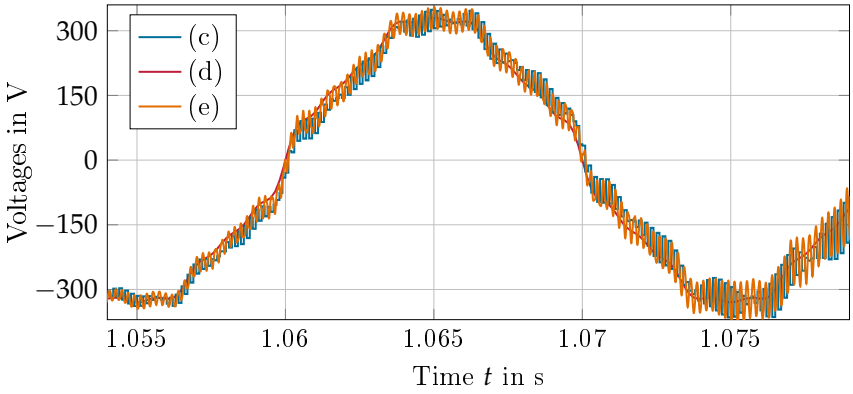

(B)

Fig. 7.6: Simulative converter responses of the VSC with active synthetic PCC voltage feed-forward in case of a suddenly emerging below Nyquist frequency resonance at $t = 1\,\mathrm{s}$, where, in subfigure (A), (a) and (b) show the VSC's reference current and output current, respectively, and in subfigure (B), (c) illustrates a detailed section of the VSC's reference voltage, and (d) and (e) show the related grid and PCC voltage, respectively.

7.2.2 Destabilization by an Above Nyquist Frequency Resonance

In order to avoid any non-passive region in the VSC input admittance up to the Nyquist frequency, Sec. 5.3.3 discusses the application and design of an active capacitor current feed-forward. Using the proposed digital filter (5.38), it was concluded that a system destabilization by poorly damped below Nyquist frequency resonances can effectively be prevented. Although this is in accordance with the results of the literature, as e.g., [4, 57, 60, 156, 157], Sec. 6.4 reveals that above Nyquist frequency resonances may still pose a risk for the system stability. As can be expected from the exemplary Bode plots of the converter's multiple-frequency input admittance model in Fig. 6.8B, the mirroring of grid resonances can lead to frequency regions, where the system's phase response falls below $-90°$. As a consequence, there might result one or multiple unwanted non-passive regions in the converter conductance.

This also becomes clear by observing the theoretical and measured IFP indices of the test-system's effective input admittance, shown in Fig. 7.7. This time, the measured IFP samples of the simulation model coincide better with the IFP indices of the theoretical multiple-frequency model than with the primary-frequency input admittance model from Sec. 3.4.2. While IFP $\{Y_{\mathrm{i,p}}(j\omega)\}$ only reflects the passivity properties of the converter's disturbance dynamics for primary-frequency input signal components, IFP $\{Y_{\mathrm{m},0}(j\omega)\}$ also takes the influence of the synthetic grid impedance on the VSC into account. As predicted by the estimate of the dynamic uncertainty $\Delta_0(s)$ in Fig. 6.7B, in this example, the mirroring of the above Nyquist frequency resonance in $\tilde{Z}_{\mathrm{g}}(s) \cdot Z_{\mathrm{b}}$ causes a distinct resonance in the IFP index of the converter's input admittance at approximately $\omega_{\mathrm{s}} - \omega_{\mathrm{r},\tilde{\mathrm{Z}}_{\mathrm{g}},2} \approx 12152\,\frac{\mathrm{rad}}{\mathrm{s}} < \omega_{\mathrm{N}}$. But, although a resonance has been proven to occur by the measurement, the introduced damping of the feed-forward filter is just sufficient to avoid a non-passive region in $Y_{\mathrm{m},0}(s)$. As indicated by the associated (solid orange) Nyquist curve of the open-loop grid-converter system in Fig. 6.11C and Fig. 6.11D, the closed-loop system can thus be assumed to be asymptotically stable despite the grid resonance. However, as can also be imagined from

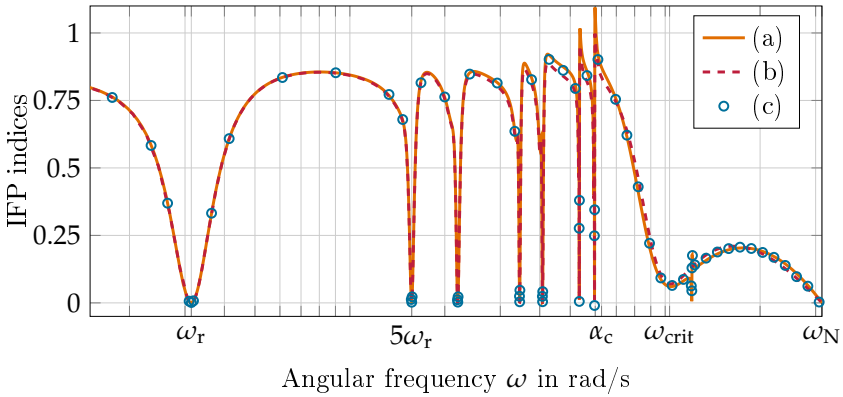

Fig. 7.7: IFP indices of different input admittance models for the converter test-system with active capacitor current feed-forward and above Nyquist frequency resonance in $\tilde{Z}_\mathrm{g}(s)$, where (a) corresponds to the estimated multiple-frequency input admittance model $Y_{\mathrm{m},0}(s)$, (b) to the primary-frequency input admittance model $Y_{\mathrm{i,p}}(s)$, and (c) shows the characteristics obtained from a simulative input admittance measurement.

Fig. 6.11D, a worse damped grid resonance or a less well designed active feed-forward filter may result in an encirclement of the point $(-1 + j0)$ by the Nyquist curve of $Y_{\mathrm{m},0}(s)\tilde{Z}_\mathrm{g}(s)$.

For instance, if the feed-forward filter's damping ratio is reduced from $\delta = 0.1$ to e.g., $\delta = 0.05$ (still ensuring that IFP $\{Y_{\mathrm{i,p}}(j\omega)\} > 0, \forall\omega \in [0, \omega_\mathrm{N}]$), and, additionally, the cable resistance of the modeled transmission line is lowered from $R_\pi = 0.025\,\Omega/\mathrm{km}$ [141] to e.g., $R_\pi = 0.012\,\Omega/\mathrm{km}$, Fig. 7.8 shows the corresponding open-loop system's Nyquist curves using the primary-frequency as well as the multiple-frequency model. Similar to the scenarios in Fig. 6.11, the Nyquist plots of the primary-frequency model indicate that the converter can safely be operated on the grid at any time, even if a poorly damped grid resonance above the Nyquist frequency occurs. On the contrary, the Nyquist curves of the proposed multiple-frequency model in Fig. 7.8 predict that it is rather uncritical to operate the VSC on a stiff grid, but the closed-loop system may be desta-

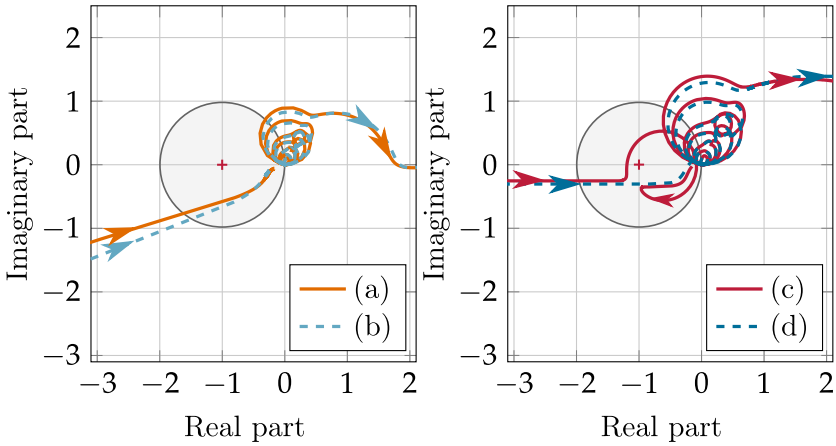

Fig. 7.8: Detailed Nyquist plots of the open-loop grid-converter system using (a), (c) $Y_{\mathrm{m},0}(s)$ and (b), (d) $Y_{\mathrm{i,p}}(s)$, where the VSC is equipped with an undamped LCL filter and implements an active capacitor current feed-forward with $\delta = 0.05$. In subfigure (A), the VSC is connected to a stiff grid with $Z_{\mathrm{g}}(s) = 0$, and in subfigure (B), the VSC is connected to a resistive-inductive grid, where $\tilde{Z}_{\mathrm{g}}(s)$ has an above Nyquist frequency resonance at $\omega_{\mathrm{r},\tilde{Z}_{\mathrm{g}},2} \approx 50492\,\frac{\mathrm{rad}}{\mathrm{s}}$.

bilized if the grid shows an unfavorable resonance above the Nyquist frequency.

And in fact, the latter behavior can also be observed in the transient simulations from Fig. 7.9 and Fig. 7.10. At the beginning, the converter is connected to a stiff grid with $Z_{\mathrm{g}}(s) = 0$, showing that the implemented capacitor current feed-forward filter with $\delta = 0.05$ still introduces enough damping at the LCL filter's resonance frequency to stabilize the grid-converter system. At $t = 1\,\mathrm{s}$, the VSC is connected to the grid over an $1.1\,\mathrm{km}$ long transmission line with low inherent damping. At first view, the converter still injects the desired current to the grid and the system seems to still operate in a stable way. However, if a small high-frequency disturbance with amplitude $0.02E_{\mathrm{b}} \approx 6.5\,\mathrm{V}$ and frequency $\omega_{\mathrm{d}} = 12125\,\frac{\mathrm{rad}}{\mathrm{s}}$ is added to the grid voltage $V_{\mathrm{g}}(t)$ at $t = 1.16\,\mathrm{s}$, the converter system begins

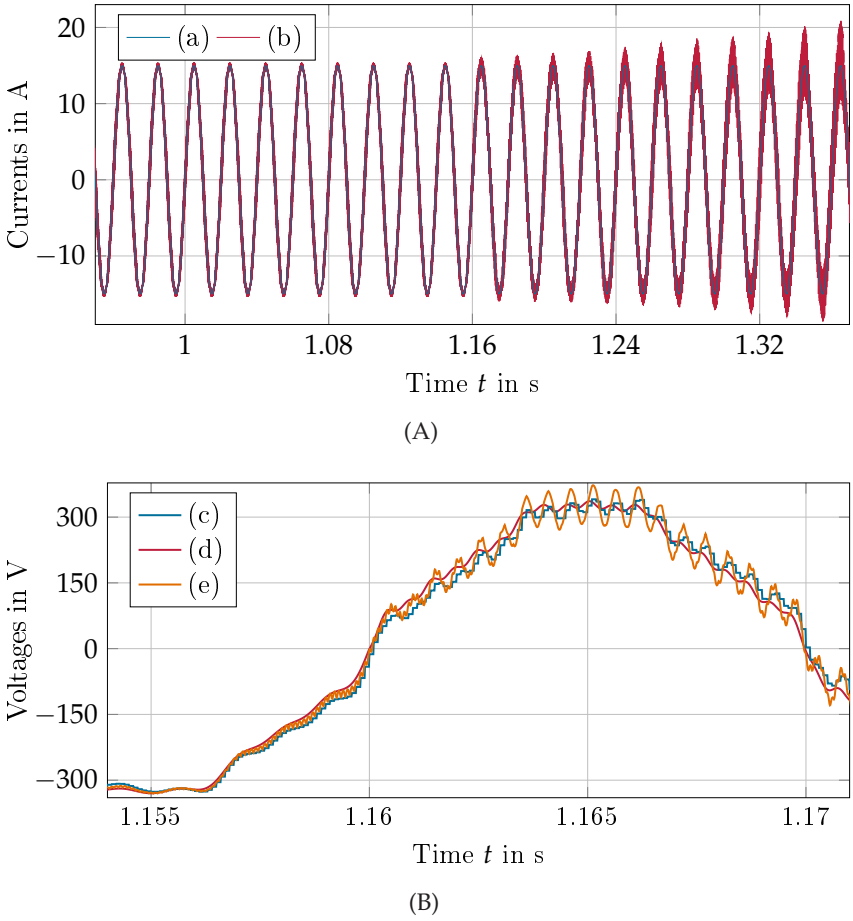

Fig. 7.9: Simulative converter responses of the VSC with ill-designed active capacitor current feed-forward in case of a suddenly emerging above Nyquist frequency resonance at $t = 1\,\mathrm{s}$ and an additional small high-frequency voltage disturbance at $t = 1.16\,\mathrm{s}$. In subfigure (A), (a) and (b) show the VSC's reference current and output current, respectively, and in subfigure (B), (c) illustrates a detailed section of the VSC's reference voltage, and (d) and (e) show the related grid and PCC voltage, respectively.

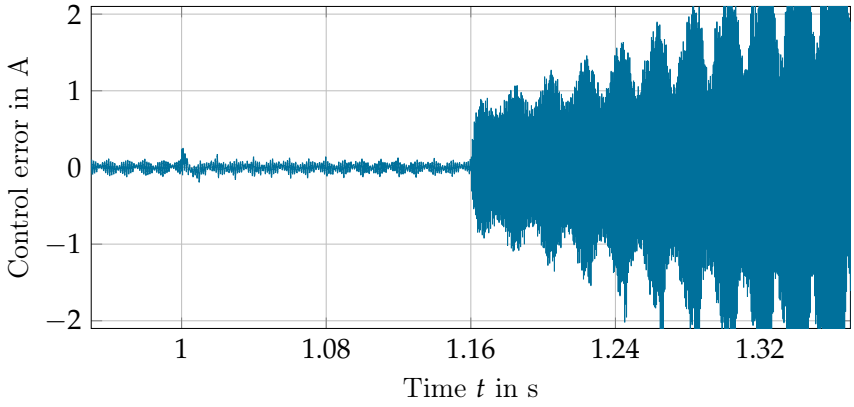

(A)

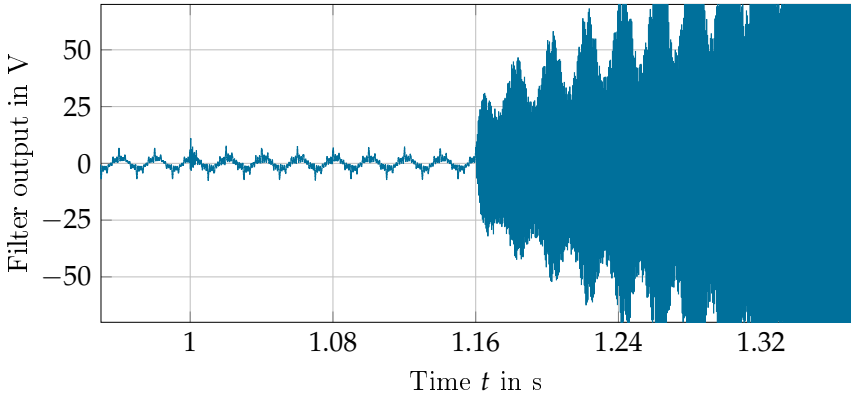

(B)

Fig. 7.10: Simulative converter responses of the VSC with ill-designed active capacitor current feed-forward in case of a suddenly emerging above Nyquist frequency resonance at $t = 1\,\mathrm{s}$ and an additional small high-frequency voltage disturbance at $t = 1.16\,\mathrm{s}$. Subfigure (A) shows the control error $I^*_{\mathrm{ref}}(t) - I^*(t)$ and subfigure (B) illustrates the output of the active feed-forward filter $H(z)$.

to leave its stable operation range. Since the active filter is not able to provide sufficient damping, the converter output current and the PCC voltage are superimposed by exponentially growing oscillations, predominantly having the frequency of the mirrored grid resonance. The destabilizing effect of the grid resonance in combination with a small disturbance is also particularly visible in the control error and the output signal of the capacitor current feed-forward filter $H(z)$ in Fig. 7.10.

Finally, the theory and the accuracy of the proposed multiple-frequency converter model from Ch. 6 are verified by the input admittance measurement and the transient simulations. Moreover, although the discussed example may be constructed, the simulation results confirm the warnings of recent literature, that even a very small and narrow lack of passivity in the converter's input admittance can be sufficient to produce critical oscillations, which may threaten the power system stability [8, 55–57]. But, due to a number of unmodelled dissipation effects, e.g., caused by parasitic winding resistances or copper and iron losses, which naturally damp resonances [35, 38, 110], it must be admitted that a converter destabilization by an above Nyquist frequency resonance should be unlikely in most scenarios. The proper damping of mirrored grid resonances can, however, still play a role in grids that have a low inherent damping or implement a great number of grid-connected power converters with different sampling and switching frequencies, see also the conclusion of Harnefors et al. in [53].

7.2.3 Robust Stabilization in case of Below and Above Nyquist Frequency Resonances

If the likelihood of a system destabilization by below or above Nyquist frequency grid resonances is to be minimized, it is recommended to aim for a robust converter passivation by an active filter and additionally to implement a passive damping scheme. As explained in Sec. 6.4, a robust passivation can, for example, be achieved by increasing the damping ratio δ of the active feed-forward filter (5.38). In doing so, the IFP index of the VSC's input admittance near the frequency ω_{crit} can be raised, with-

out producing any unwanted power losses, see Fig. 6.10. A disadvantage of this method, however, is that the higher gain of $H(z)$ in the low and medium frequency range also amplifies some mirrored harmonics more strongly. Depending on the specific scenario and parameter settings, this causes certain above Nyquist frequency resonances to have more negative influence on the converter's disturbance dynamics in the baseband, while others have less. But, as can be verified by the beneficial stability measures of the exemplary open-loop system's Nyquist plots from Fig. 6.11, it can mostly be assumed that a higher damping ratio δ also yields a stable, more robust closed-loop grid-converter system. In order to further reduce the influence of aliasing effects, it is advantageous to damp the differentiation action of the output filter's capacitance, and thus, to limit the amplification of high-frequency harmonics in the synthetic grid voltage, used by the active feed-forward. From a practical point of view, the digital control should therefore be complemented by a passive damping scheme [4].

For example, implementing an LCL filter with a series damping resistance of $R_\mathrm{d} = 0.4\,\Omega$ and using the suggested capacitor current feed-forward filter with the more robust parameterization from Sec. 6.4, i.e., setting $\delta = 0.2$ and further decreasing the prioritization of the harmonics, $\gamma_i, \forall i > 1$, Fig. 7.11 shows the IFP indices of the test-system's conductance. As in the previous scenario, the primary-frequency model does not allow to detect the influence of the mirrored grid resonance, whereas the estimated multiple-frequency model, taking harmonics in the first sideband into account, gives a relatively accurate approximation of the identified IFP index. Compared to the IFP indices from Fig. 7.7, Fig. 7.11 clearly demonstrates the beneficial passivity properties if the converter is equipped with a damped LCL filter and implements the proposed, more robust PR controller and feed-forward filter parameters. The only disadvantage is the emerging minor non-passive region of the VSC's input admittance near the Nyquist frequency, which, however, is of less importance due to the low magnitude of $Y_{\mathrm{m},0}(s)$ and the good damping capabilities of the LCL filter in this frequency range. As intended by the robust passivation, the mirrored grid resonance at approximately $12152\,\frac{\mathrm{rad}}{\mathrm{s}}$ affects the IFP index

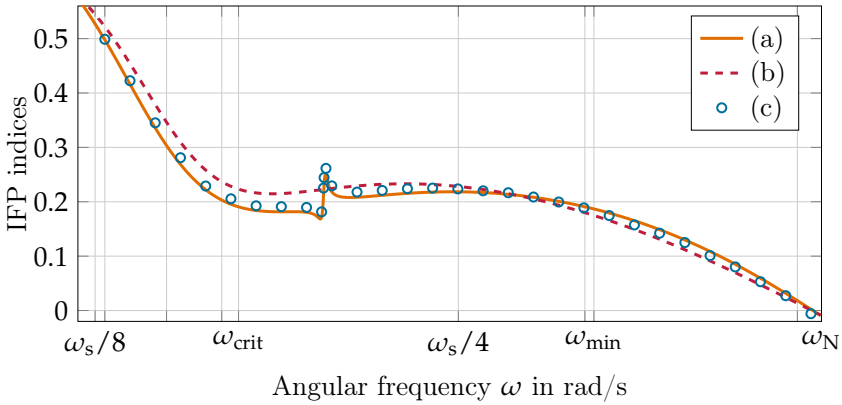

Fig. 7.11: Detailed IFP indices of different input admittance models for the converter test-system with damped LCL filter plus robust active capacitor current feed-forward and above Nyquist frequency resonance in $\tilde{Z}_g(s)$, where (a) corresponds to $Y_{m,0}(s)$, (b) to $Y_{i,p}(s)$, and (c) shows the characteristics obtained from a simulative input admittance measurement.

of the VSC's effective input admittance much less than with the previously selected parameterization. Consequently, it can be assumed that even a less damped above Nyquist frequency grid resonance or a superposition of multiple resonances does not lead to a lack of passivity in IFP $\{Y_{m,0}(j\omega)\}$ in the frequency range up to just below ω_N, and thus, not to a risk for the closed-loop system stability.

Reducing the damping of the modeled resonances in Fig. 7.2 by setting the transmission line's resistance R_π to zero, the Nyquist plots in Fig. 7.12 also indicate that it is highly unlikely that stability issues occur with the more robust design. All Nyquist curves, either constructed with the primary-frequency or the multiple-frequency model, show a large stability measure, even if the grid has a nearly undamped resonance below or above the Nyquist frequency with a magnitude of approximately $54\,\mathrm{dB}$ or $45\,\mathrm{dB}$, respectively. The robustness of the stabilization can also be observed in the transient measurement shown in Fig. 7.13 and Fig. 7.14.

Similar to the presented simulation from the previous section, the converter with active plus passive damping is initially connected to a stiff

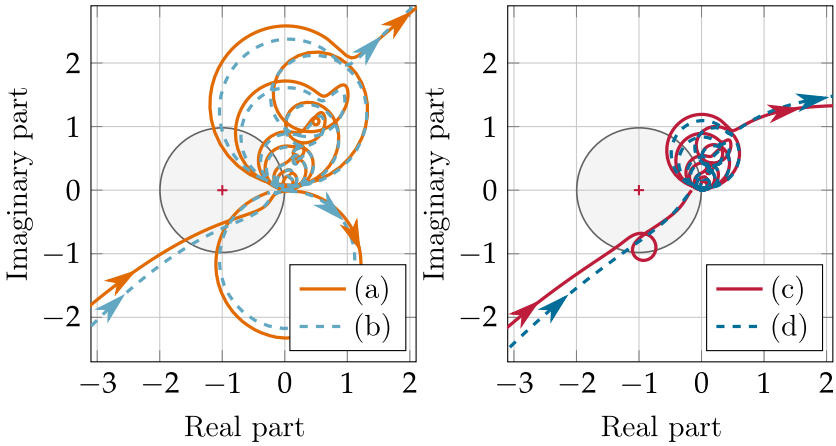

Fig. 7.12: Detailed Nyquist plots of the open-loop grid-converter system using (a), (c) the estimated multiple-frequency input admittance model $Y_{\mathrm{m},0}(s)$ and (b), (d) the primary-frequency input admittance model $Y_{\mathrm{i,p}}(s)$, where the VSC is equipped with a damped LCL filter and implements an active capacitor current feedforward with $\delta = 0.2$. In subfigure (A), the VSC is connected to a grid, where $\tilde{Z}_{\mathrm{g}}(s)$ has a near Nyquist frequency resonance at $\omega_{\mathrm{r},\tilde{Z}_{\mathrm{g}},2} \approx 29128\,\frac{\mathrm{rad}}{\mathrm{s}} < \omega_{\mathrm{N}}$, and in subfigure (B), $\tilde{Z}_{\mathrm{g}}(s)$ has an above Nyquist frequency resonance at $\omega_{\mathrm{r},\tilde{Z}_{\mathrm{g}},2} \approx 50492\,\frac{\mathrm{rad}}{\mathrm{s}}$.

grid with $Z_{\mathrm{g}}(s) = 0$. As before, the LCL filter resonance is sufficiently damped and the digitally current-controlled converter accurately tracks its reference and suppresses the superimposed voltage harmonics. At $t = 1\,\mathrm{s}$, the VSC is connected to an inductive grid over an $1.1\,\mathrm{km}$ long transmission line, yielding a nearly undamped below Nyquist frequency resonance at $\omega_{\mathrm{r},\tilde{Z}_{\mathrm{g}},2} \approx 29128\,\frac{\mathrm{rad}}{\mathrm{s}}$ in $\tilde{Z}_{\mathrm{g}}(s)$. As can be seen, the converter can deal with the new synthetic grid impedance and continuous to operate without causing a substantial variation in the output current. This does not change if the converter is connected to the grid via a synthetic grid impedance with a nearly undamped above Nyquist frequency resonance at $t = 1.16\,\mathrm{s}$. The control error becomes smaller again and reaches a similar (averaged) magnitude as if the converter were directly

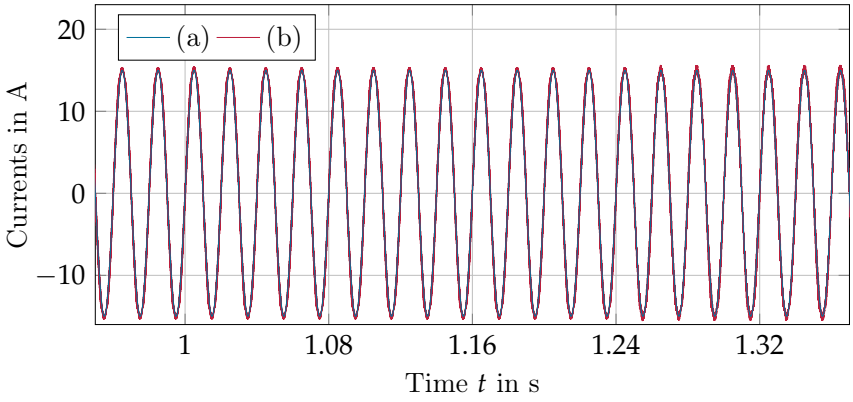

(A)

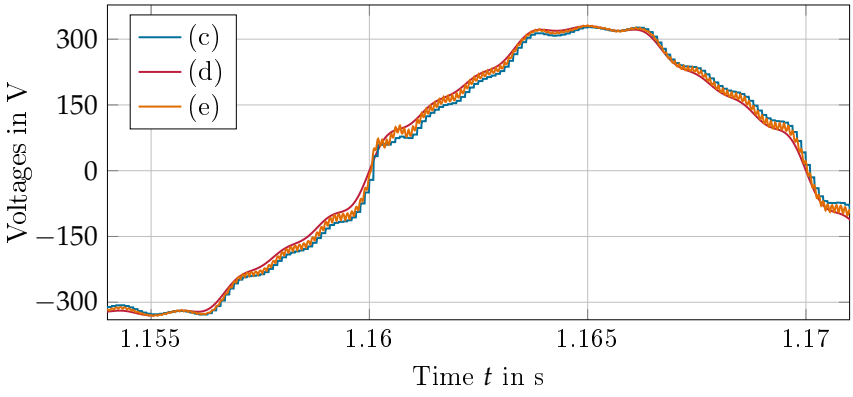

(B)

Fig. 7.13: Simulative converter responses of the robustly passivated VSC in case of a suddenly emerging below Nyquist frequency resonance at $t = 1\,\mathrm{s}$, an above Nyquist frequency resonance at $t = 1.16\,\mathrm{s}$ and an additional small high-frequency voltage disturbance at $t = 1.25\,\mathrm{s}$. In subfigure (A), (a) and (b) show the VSC's reference current and output current, respectively, and in subfigure (B), (c) illustrates a detailed section of the VSC's reference voltage, and (d) and (e) show the related grid and PCC voltage, respectively.

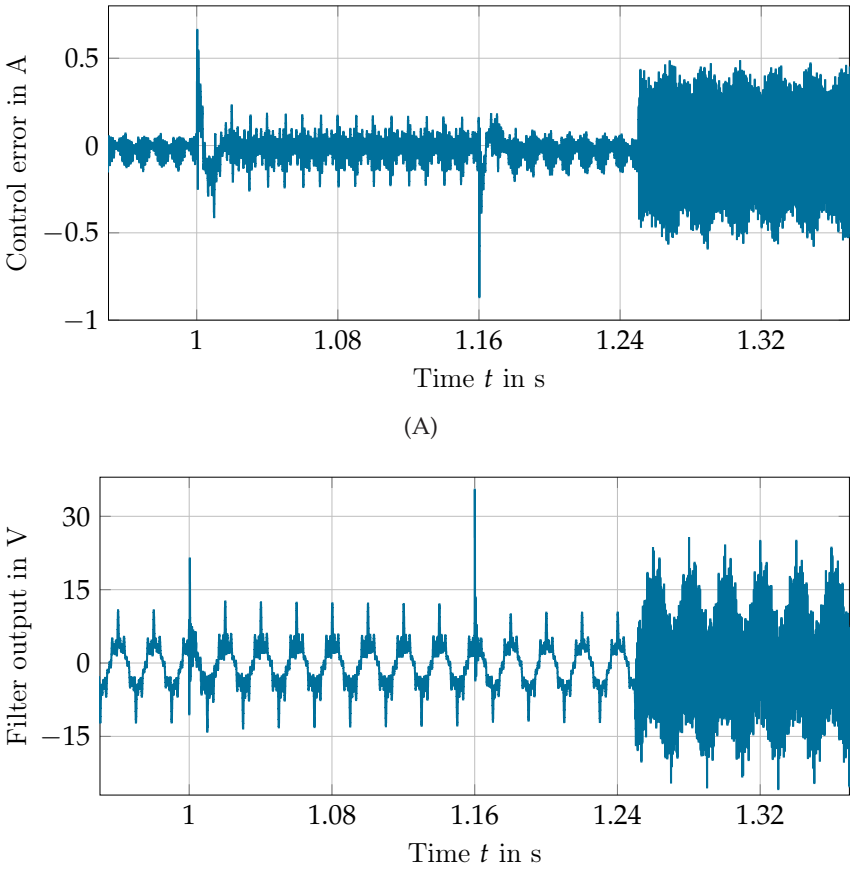

Fig. 7.14: Simulative converter responses of the robustly passivated VSC in case of a suddenly emerging below Nyquist frequency resonance at $t = 1\,\mathrm{s}$, an above Nyquist frequency resonance at $t = 1.16\,\mathrm{s}$ and an additional small high-frequency voltage disturbance at $t = 1.25\,\mathrm{s}$. Subfigure (A) shows the control error $I^*_{\mathrm{ref}}(t) - I^*(t)$ and subfigure (B) illustrates the output of the active feed-forward filter $H(z)$.

connected to a stiff grid, see Fig. 7.14A. But, in contrast to the case where the active feed-forward filter is ill-designed and the damping ratio is set to $\delta = 0.05$, an additional disturbance of the grid voltage with an amplitude of $0.02E_\mathrm{b} \approx 6.5\,\mathrm{V}$ and a frequency of $\omega_\mathrm{d} = 12125\,\frac{\mathrm{rad}}{\mathrm{s}}$ does not lead to a destabilization of the grid-converter system. Even though a sudden increase in the control error and the output voltage of the capacitor current feed-forward can be noticed, the (steady-state) converter output current worsens only marginally, showing a minor overlaid oscillation of approximately $0.1\,\mathrm{A}$ at $12125\,\frac{\mathrm{rad}}{\mathrm{s}}$. As predicted in theory, this directly demonstrates the positive effect of an increased damping ratio δ in combination with a (small) damping resistance R_d and verifies that a robust passivation of the VSC's multiple-frequency input admittance typically eliminates the risk of destabilizing poorly damped grid resonances.

8 Conclusion and Outlook

Faced with recurring stability problems that have been associated with the excitation of poorly damped grid resonances by power electronic-based energy systems, this thesis thoroughly reviewed the modeling and the controller plus filter design of digitally current-controlled grid-connected converters. After introducing the most important components involved with the current control, i.e, the VSC's output filter, the PWM plus computational delay, and the digital current controller, it was explained why most present SISO converter models are only partially suitable for the analysis and the harmonic stability assessment. While still commonly used quasi-analog models neglect all effects of the digital control, the latest VSC models typically reflect some, but not all PWM and aliasing effects. In particular, they typically do not consider the influence of switching harmonics, which appear as high-frequency signal components in the synthetic PCC voltage or in the LCL filter's capacitor current used for active damping. Nevertheless, as was argued at the beginning of the thesis and later verified by simulation, the proposed primary-frequency model, which is almost identical to the so called multiple-frequency model in the literature, accurately reflects the converter behavior if no dominant grid resonances above the Nyquist frequency occur.

Using the model for an initial design, it was again shown that our already proposed design approach for multifrequency PR current controllers from [3] can readily be applied for the parameterization, without leading to critical interactions between neighboring resonators. To avoid a destabilization by resonances near the specified harmonic frequencies to be suppressed by the PR controller, it is advisable to aim for rather moderate integral gains instead of demanding a too high disturbance rejection capability. In addition, it confirms that the resonance

frequency of the highest compensator should be limited to well below the frequency where the phase response of the open-loop system crosses $-180°$. But, even in compliance with these guidelines, it shows that it is still very unlikely that the closed-loop grid-converter system can be operated safely without additional damping scheme. Depending on the total time delay, the converter-side filter resistance, and the current controller specifications, the converter's input admittance inherently shows a non-passive region for frequencies above roughly $f_\mathrm{s}/6$ up to the Nyquist frequency f_N. Hereby, the passivity indices of the VSC's primary-frequency model largely match those of the quasi-analog model and only shows a marginally greater lack of passivity. Therefore, both models allow a relatively good (initial) estimation of the passivity and stability properties of the VSC.

As an analysis of different passive damping strategies has shown, it is however rather difficult to compensate for the VSC's negative damping by adding dissipative elements to the LCL filter. On the one hand, increased losses have to be accepted and on the other hand the introduced damping is strongly dependent on the continually varying grid impedance. In the end, the implementation of a passive damping scheme certainly represents a suitable method to damp the LCL filter's resonance, but it can generally not be guaranteed that the VSC's negative conductance interacts with poorly damped grid resonances, possibly leading to critical harmonic oscillations. This situation can also occur in a similar way when using the synthetic PCC voltage as feed-forward quantity. While much of the literature comes to the conclusion that an active PCC voltage feed-forward is capable to remove the non-passive region of the VSC's input admittance, it cannot be assumed that this is true in practical applications. This can be reasoned by the fact that the digital implementation of the required differentiating part of the active filter is never feasible in an optimal way. Hence, although possibly emerging non-passive regions near and at the specified PR controller resonance frequencies can effectively be counteracted by a series band-stop filter, the digital filter realization still causes a significant lack of passivity in the high-frequency range near f_N. But, as theoretically derived and verified by simulation,

the feed-forward of the LCL filter's capacitor current allows to render the converter's primary-frequency input admittance model passive in the complete frequency range up to the Nyquist frequency. As an alternative to our method from [4], this thesis proposes another, even more intuitive approach for the active filter design. It also becomes clear why a purely proportional filter may stabilize the closed-loop system, but it is beneficial to use the Tustin approximation of a lead-lag element, which makes the passivation more robust against modeling uncertainties.

At this point, however, it must be considered that the VSC model used for the analysis and controller plus filter design only reflects the converter's behavior for primary-frequency signal components and does not allow to take mirrored signal components of the sampled synthetic PCC voltage or capacitor current into account. Since, to the best of the author's knowledge, a complete model was missing in the literature, the final part of the thesis concentrated on the development of a suitable extension. As a result and in addition to an alternative sampler model, a new multiple-frequency small-signal PWM model was proposed, allowing to accurately describe the converter's behavior in the baseband as well as in its sidebands. It was shown that the derived theory is similar to the well known theory on digital control systems, but can be understood as a generalization, where the mathematical description of the introduced sampling process becomes the discrete Laplace transform in certain cases. The VSC's resulting multiple-frequency current dynamics therefore look very similar to the primary-frequency dynamics. But, the input admittance can now be written in form of a matrix, which can be used to construct a MIMO model of the closed-loop system, where each element reflects the behavior of the grid-converter system in a certain frequency range. If the analysis is to be focused on the low-frequency range up to the Nyquist frequency and it is assumed that the LCL filter effectively suppresses all above Nyquist frequency voltage components from the grid side, the model again simplifies to a SISO system. It can then be seen that the influence of mirrored high-frequency switching harmonics can principally be interpreted as a dynamic uncertainty, which affects the baseband dynamics of the primary-frequency input admittance

model of the converter. Among others, the uncertainty mainly depends on the implemented active feed-forward, but even more importantly, also on the synthetic grid impedance. Hence, with the derived SISO multiple-frequency model, it finally becomes possible to predict the effects of above Nyquist frequency grid resonances on the converter's effective input admittance.

As a result, it can be concluded that the mirroring of a grid resonance can lead to a worsening of the converter's passivity properties or even to a lack of passivity within a limited frequency range. However, even though the risk may increase in grids with a low inherent damping or in grids with a large number of (ill-designed) grid-connected VSCs, a threatening of the system stability can effectively be counteracted by a robust converter passivation. As demonstrated by example, this can be achieved by a proper parameterization of the proposed active capacitor current feed-forward filter in combination with a passive damping scheme that physically limits the amplification of high-frequency signal components. At the end, the theory and the proposed design recommendations are verified by a variety of computer simulations.

Based on the summarized findings, further research can concentrate on extending the theory of the presented alternative sampler model and multiple-frequency PWM model. Besides the better reflection of very high-frequency switching harmonics, the analysis of other digital PWM schemes might also be advanced. Moreover, in addition to switching harmonics which represent aliases of the PWM's reference input voltage, also other sideband harmonics or interharmonics can be incorporated. In this regard, a combination with more advanced nonlinear analyzing methods, such as the describing function method, might also bring further insights into the generation of undamped or exponentially increasing oscillations caused by the nonlinear PWM. Furthermore the next step would be the passivity assessment of the VSC's multiple-frequency input admittance including outer control loops, such as the DC-link voltage control or the PLL. And finally, in view of the methods and results of the presented work, initial research using quasi-analog models should be reviewed with respect to the effects of digital control.

A Appendix

A.1 IFP Indices of SISO Feedback-Systems

In this section, a standard feedback interconnection of two linear, asymptotically stable SISO systems according to Fig. A.1 should be considered.

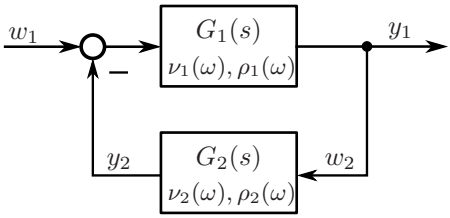

Fig. A.1: Feedback interconnection of (passive) subsystems.

Suppose that the passivity indices for the system in the forward-path and feedback-path are given by IFP $\{G_1(j\omega)\} = \nu_1(\omega)$, OFP $\{G_1(j\omega)\} = \rho_1(\omega)$ and IFP $\{G_2(j\omega)\} = \nu_2(\omega)$, OFP $\{G_2(j\omega)\} = \rho_2(\omega)$, respectively. Thus, the systems' frequency responses and their inverses can be expressed as $G_1(j\omega) = \nu_1(\omega) + j\mathrm{Im}\{G_1(j\omega)\}$, $G_1^{-1}(j\omega) = \rho_1(\omega) + j\mathrm{Im}\{G_1^{-1}(j\omega)\}$, and $G_2(j\omega) = \nu_2(\omega) + j\mathrm{Im}\{G_2(j\omega)\}$, $G_2^{-1}(j\omega) = \rho_2(\omega) + j\mathrm{Im}\{G_2^{-1}(j\omega)\}$. Then, given the closed-loop transfer function

$$G_{\mathrm{cl}}(s) = \frac{y_1(s)}{w_1(s)} = \frac{G_1(s)}{1 + G_1(s)G_2(s)} = \frac{1}{G_1^{-1}(s) + G_2(s)}, \tag{A.1}$$

after substituting and rearranging, the IFP index of $G_{\mathrm{cl}}(s)$ is given by

$$\begin{aligned}\mathrm{IFP}\{G_{\mathrm{cl}}(j\omega)\} &= \frac{\rho_1(\omega) + \nu_2(\omega)}{\left[\rho_1(\omega) + \nu_2(\omega)\right]^2 + \left[\mathrm{Im}\left\{G_1^{-1}(j\omega)\right\} + \mathrm{Im}\left\{G_2(j\omega)\right\}\right]^2} \\ &= \left[\rho_1(\omega) + \nu_2(\omega)\right] \left|G_{\mathrm{cl}}(j\omega)\right|^2 . \end{aligned} \tag{A.2}$$

Observing (A.2), the closed-loop system is (strictly) passive, if the passivity indices satisfy the necessary and sufficient condition that $\rho_1(\omega) + \nu_2(\omega) \geq 0$, $\forall\omega \in \mathbb{R}$. This verifies the passivity theorem of [74,94,169], that a shortage of OFP, i.e., $\rho_1(\omega) < 0$, can be compensated for by an excess of IFP, i.e., $\nu_2(\omega) \geq |\rho_1(\omega)|$, from the frequency-domain perspective.

Moreover, the closed-loop transfer function can also be expressed as

$$G_{\mathrm{cl}}(s) = \frac{y_1(s)}{w_1(s)} = \frac{G_1(s)}{1 + G_1(s)G_2(s)} = \frac{G_1(s)G_2^{-1}(s)}{G_2^{-1}(s) + G_1(s)}, \tag{A.3}$$

which yields the IFP index

$$\begin{aligned}\mathrm{IFP}\left\{G_{\mathrm{cl}}(j\omega)\right\} = &\frac{\nu_1(\omega)\rho_2(\omega)\left[\nu_1(\omega) + \rho_2(\omega)\right]}{\left[\nu_1(\omega) + \rho_2(\omega)\right]^2 + \left[\mathrm{Im}\left\{G_1(j\omega)\right\} + \mathrm{Im}\left\{G_2^{-1}(j\omega)\right\}\right]^2} \\ &+ \frac{\nu_1(\omega)\mathrm{Im}^2\left\{G_2^{-1}(j\omega)\right\} + \rho_2(\omega)\mathrm{Im}^2\left\{G_1(j\omega)\right\}}{\left[\nu_1(\omega) + \rho_2(\omega)\right]^2 + \left[\mathrm{Im}\left\{G_1(j\omega)\right\} + \mathrm{Im}\left\{G_2^{-1}(j\omega)\right\}\right]^2}.\end{aligned} \tag{A.4}$$

As can be seen, $\nu_1(\omega) + \rho_2(\omega) \geq 0$, $\forall\omega \in \mathbb{R}$ does not necessarily imply passivity of the closed-loop system. On the other hand, $\nu_1(\omega) \geq 0$ and $\rho_2(\omega) \geq 0$ represents a sufficient condition for passivity of $G_{\mathrm{cl}}(s)$.

A.2 Analytic Description of the Single-Update PWM

This section develops an analytic description for the pulse-width pattern of the digital pulse-width modulator from Section 3.2.2 in more detail.

The derivation is based on the periodic representation of a repeating pulse sequence, as illustrated in Fig. A.2. The shown pulse sequence $S_{\mathrm{p}}(t)$ can be expressed by the Fourier-series [28]

$$S_{\mathrm{p}}(t) = \frac{c}{T_{\mathrm{cp}}} + \frac{2}{\pi}\sum_{k=1}^{\infty}\frac{1}{k}\sin\left(k\pi\frac{c}{T_{\mathrm{cp}}}\right)\cos\left(k\frac{2\pi}{T_{\mathrm{cp}}}t\right) \tag{A.5}$$

where c is the pulse width, T_{cp} is the cycle time, and c/T_{cp} represents the duty-cycle.

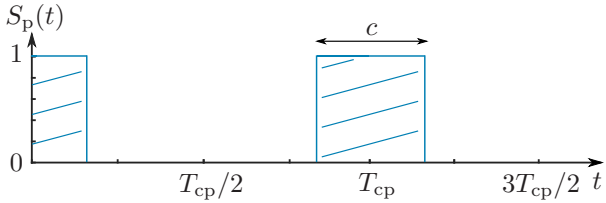

Fig. A.2: Time waveform of repeating pulse sequence with pulse width c and cycle time T_cp.

In the following, a sinusoidal reference input signal of the form $V_\mathrm{ref}(t) = V_\mathrm{DC}/2 + a_\mathrm{m} V_\mathrm{DC}/2 \sin(\omega_\mathrm{r} t + \phi_\mathrm{r})$ is considered, where $0 \leq a_\mathrm{m} \leq 1$ is the signal's amplitude modulation index and $\omega_\mathrm{r} = 2\pi/T_\mathrm{r}$ and ϕ_r represents the angular frequency and phase shift, respectively. After passing $V_\mathrm{ref}(t)$ though a ZOH circuit, the resulting staircase signal $\overline{V}_\mathrm{ref}(t)$ is compared to a triangular carrier signal $S_\mathrm{c}(t)$, which generates the PWM output $V_\mathrm{c}(t)$, as illustrated in Fig. A.3.

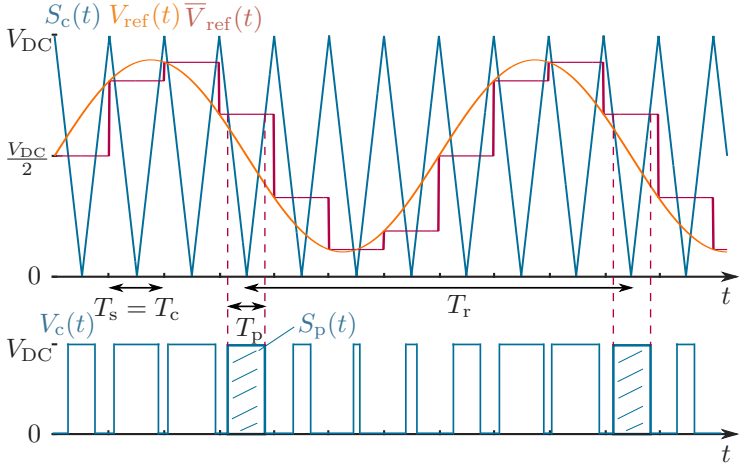

Fig. A.3: Exemplary pulse-width pattern of a digital single-update PWM with a sinusoidal reference input, where $T_\mathrm{r} = 7T_\mathrm{s}$.

As can be seen, the resulting PWM pulse-width pattern $V_\mathrm{c}(t)$ can be understood as a concatenation of weighted and time-shifted repeating pulse sequences $S_\mathrm{p}(t)$ with different pulse widths. Reviewing that

$T_\mathrm{p}(t)/T_\mathrm{c} = \overline{V}_\mathrm{ref}(t)/V_\mathrm{DC}$ and noticing that the pulse sequence's cycle time corresponds to the lowest common multiple of the input signal's cycle time and the sampling time, i.e., $T_\mathrm{cp} = \mathrm{lcm}(T_\mathrm{r}, T_\mathrm{s})$, the duty-cycle c/T_cp of the q-th pulse can be described by

$$\left.\frac{c}{T_\mathrm{cp}}\right|_q = \frac{T_\mathrm{p}(t = qT_\mathrm{s})}{\mathrm{lcm}(T_\mathrm{r}, T_\mathrm{s})} = \frac{1}{\mathrm{lcm}(T_\mathrm{r}, T_\mathrm{s})}\frac{T_\mathrm{s}}{2}\left(1 + a_\mathrm{m}\sin(\omega_\mathrm{r} q T_\mathrm{s} + \phi_\mathrm{r})\right). \quad \text{(A.6)}$$

Given (A.5), each repeating PWM pulse segment can be expressed as

$$S_\mathrm{p}|_q(t) = V_\mathrm{DC}\left[\left.\frac{c}{T_\mathrm{cp}}\right|_q + \frac{2}{\pi}\sum_{k=1}^{\infty}\frac{1}{k}\sin\left(k\pi\left.\frac{c}{T_\mathrm{cp}}\right|_q\right)\cos\left(k\frac{2\pi}{T_\mathrm{cp}}\left(t - qT_\mathrm{s} - \frac{1}{2}T_\mathrm{s}\right)\right)\right] \quad \text{(A.7)}$$

and the resulting PWM pulse-width pattern is given by

$$\begin{aligned} V_\mathrm{c}(t) = V_\mathrm{DC}\Bigg[&\sum_{q=1}^{\frac{\mathrm{lcm}(T_\mathrm{r},T_\mathrm{s})}{T_\mathrm{s}}}\frac{T_\mathrm{s}}{2\,\mathrm{lcm}(T_\mathrm{r}, T_\mathrm{s})} + \frac{T_\mathrm{s}}{\mathrm{lcm}(T_\mathrm{r}, T_\mathrm{s})}\frac{a_\mathrm{m}}{2}\sin(\omega_\mathrm{r} q T_\mathrm{s} + \phi_\mathrm{r}) \\ &+ \frac{2}{\pi}\sum_{k=1}^{\infty}\frac{1}{k}\sin\Bigg(\frac{k\pi T_\mathrm{s}}{2\,\mathrm{lcm}(T_\mathrm{r}, T_\mathrm{s})} + \frac{k\pi T_\mathrm{s}}{\mathrm{lcm}(T_\mathrm{r}, T_\mathrm{s})}\frac{a_\mathrm{m}}{2}\sin(\omega_\mathrm{r} q T_\mathrm{s} + \phi_\mathrm{r})\Bigg) \cdot \\ &\cos\left(\frac{k2\pi}{\mathrm{lcm}(T_\mathrm{r}, T_\mathrm{s})}\left(t - qT_\mathrm{s} - \frac{1}{2}T_\mathrm{s}\right)\right)\Bigg]. \end{aligned} \quad \text{(A.8)}$$

Since the first sum counts over an integer multiple of the input signal's cycle time, the term $(T_\mathrm{s} a_\mathrm{m})/(2\mathrm{lcm}(T_\mathrm{r}, T_\mathrm{s}))\sum_{q=1}^{\mathrm{lcm}(T_\mathrm{r},T_\mathrm{s})/T_\mathrm{s}}\sin(q\omega_\mathrm{r} T_\mathrm{s} + \phi_\mathrm{r})$ vanishes and it can be noticed that $T_\mathrm{s}/(2\,\mathrm{lcm}(T_\mathrm{r}, T_\mathrm{s}))\sum_{q=1}^{\mathrm{lcm}(T_\mathrm{r},T_\mathrm{s})/T_\mathrm{s}} 1 = 1/2$. In addition, to further simplify (A.8), the properties of the Bessel function of the first kind, $J_\mathrm{n}(x)$, can be used [64], i.e.,

$$\begin{aligned} &\sin\left(\frac{k\pi T_\mathrm{s}}{2\,\mathrm{lcm}(T_\mathrm{r}, T_\mathrm{s})} + \frac{k\pi T_\mathrm{s}}{\mathrm{lcm}(T_\mathrm{r}, T_\mathrm{s})}\frac{a_\mathrm{m}}{2}\sin(\omega_\mathrm{r} q T_\mathrm{s} + \phi_\mathrm{r})\right) \\ &\quad = \sum_{n=-\infty}^{\infty} J_\mathrm{n}\left(\frac{k\pi T_\mathrm{s}}{\mathrm{lcm}(T_\mathrm{r}, T_\mathrm{s})}\frac{a_\mathrm{m}}{2}\right)\sin\left(n\left(\omega_\mathrm{r} q T_\mathrm{s} + \phi_\mathrm{r}\right) + \frac{T_\mathrm{s}}{2\,\mathrm{lcm}(T_\mathrm{r}, T_\mathrm{s})}\right), \end{aligned} \quad \text{(A.9)}$$

and thus, (A.8) becomes

$$V_{\mathrm{c}}(t) = V_{\mathrm{DC}}\Bigg[\frac{1}{2} + \frac{2}{\pi}\sum_{k=1}^{\infty}\sum_{n=-\infty}^{\infty}\sum_{q=1}^{\frac{\mathrm{lcm}(T_{\mathrm{r}},T_{\mathrm{s}})}{T_{\mathrm{s}}}}\frac{1}{k}\,J_{\mathrm{n}}\left(\frac{k\pi T_{\mathrm{s}}}{\mathrm{lcm}(T_{\mathrm{r}},T_{\mathrm{s}})}\frac{a_{\mathrm{m}}}{2}\right)\cdot \sin\left(n\left(\omega_{\mathrm{r}}qT_{\mathrm{s}}+\phi_{\mathrm{r}}\right)+\frac{T_{\mathrm{s}}}{2\,\mathrm{lcm}(T_{\mathrm{r}},T_{\mathrm{s}})}\right)\cdot \cos\left(\frac{k2\pi}{\mathrm{lcm}(T_{\mathrm{r}},T_{\mathrm{s}})}\left(t-qT_{\mathrm{s}}-\frac{1}{2}T_{\mathrm{s}}\right)\right)\Bigg]. \quad \text{(A.10)}$$

Equation (A.10) describes the resulting pulse-width pattern from Fig. A.3 entirely and can be evaluated for different sampling and cycle times $T_{\mathrm{s}}, T_{\mathrm{r}}$ as well as for various amplitude modulation indices, a_{m}.

If reference input signals are considered, where the cycle time T_{r} is an integer multiple of the sampling time T_{s}, (A.10) can be simplified by taking the periodicity of the sinusoidal input signal into account. After applying the addition theorems and the trigonometric identities

$$\cos(k\omega_{\mathrm{r}}t-a)-\cos(k\omega_{\mathrm{r}}t-b) = 2\sin\left(\frac{(a-b)}{2}\right)\sin\left(k\omega_{\mathrm{r}}t-\frac{(a+b)}{2}\right) \quad \text{(A.11)}$$

$$\cos(k\omega_{\mathrm{r}}t-a)+\cos(k\omega_{\mathrm{r}}t-b) = 2\cos\left(\frac{(a-b)}{2}\right)\cos\left(k\omega_{\mathrm{r}}t-\frac{(a+b)}{2}\right) \quad \text{(A.12)}$$

where a, b are some constants, (A.10) can be decomposed into

$$V_{\mathrm{c}}(t) = V_{\mathrm{DC}}\Bigg[\frac{1}{2} + \frac{2}{\pi}\sum_{k=1}^{\infty}\sum_{n=-\infty}^{\infty}\frac{1}{k}\,J_{\mathrm{n}}\left(k\,a_{\mathrm{m}}\frac{\pi}{2}\frac{T_{\mathrm{s}}}{T_{\mathrm{r}}}\right)\cdot \Bigg[\left(1+2\sum_{q=1}^{\lceil\frac{1}{2}\frac{T_{\mathrm{r}}}{T_{\mathrm{s}}}-1\rceil}\cos\left(qn\omega_{\mathrm{r}}T_{\mathrm{s}}+n\phi_{\mathrm{r}}\right)\cos\left(k\omega_{\mathrm{r}}\left(qT_{\mathrm{s}}-\frac{1}{2}T_{\mathrm{r}}\right)\right)\right)\cdot \sin\left(k\pi\frac{1}{2}\frac{T_{\mathrm{s}}}{T_{\mathrm{r}}}\right)\cos\left(k\omega_{\mathrm{r}}\left(t-\frac{T_{\mathrm{s}}+T_{\mathrm{r}}}{2}\right)\right)+ \left(2\sum_{q=1}^{\lceil\frac{1}{2}\frac{T_{\mathrm{r}}}{T_{\mathrm{s}}}-1\rceil}\sin\left(qn\omega_{\mathrm{r}}T_{\mathrm{s}}+n\phi_{\mathrm{r}}\right)\sin\left(k\omega_{\mathrm{r}}\left(qT_{\mathrm{s}}-\frac{1}{2}T_{\mathrm{r}}\right)\right)\right)\cdot \cos\left(k\pi\frac{1}{2}\frac{T_{\mathrm{s}}}{T_{\mathrm{r}}}\right)\sin\left(k\omega_{\mathrm{r}}\left(t-\frac{T_{\mathrm{s}}+T_{\mathrm{r}}}{2}\right)\right)\Bigg]\Bigg] \quad \text{(A.13)}$$

where $\lceil\cdot\rceil$ rounds the respective argument to the next positive integer. Now, disregarding the phase shift, $\phi_\mathrm{r} = 0$, and evaluating the two sums

$$d_\mathrm{s}(k,n) = 2 \sum_{q=1}^{\lceil \frac{1}{2}\frac{T_\mathrm{r}}{T_\mathrm{s}}-1 \rceil} \sin\Big(qn\omega_\mathrm{r}T_\mathrm{s}\Big) \sin\left(k\omega_\mathrm{r}\left(qT_\mathrm{s}-\frac{1}{2}T_\mathrm{r}\right)\right), \tag{A.14}$$

$$d_\mathrm{c}(k,n) = 1 + 2 \sum_{q=1}^{\lceil \frac{1}{2}\frac{T_\mathrm{r}}{T_\mathrm{s}}-1 \rceil} \cos\Big(qn\omega_\mathrm{r}T_\mathrm{s}\Big) \cos\left(k\omega_\mathrm{r}\left(qT_\mathrm{s}-\frac{1}{2}T_\mathrm{r}\right)\right), \tag{A.15}$$

it shows that

$$d_\mathrm{s}(k,n) = \begin{cases} \frac{1}{2}\frac{T_\mathrm{r}}{T_\mathrm{s}} & \text{if } k \neq q\frac{T_\mathrm{r}}{T_\mathrm{s}},\ q \in \mathbb{N}_{>0} \text{ and } n = k + p\frac{T_\mathrm{r}}{T_\mathrm{s}},\ p \in \mathbb{Z} \\ -\frac{1}{2}\frac{T_\mathrm{r}}{T_\mathrm{s}} & \text{if } k \neq q\frac{T_\mathrm{r}}{T_\mathrm{s}},\ q \in \mathbb{N}_{>0} \text{ and } n = -k + p\frac{T_\mathrm{r}}{T_\mathrm{s}},\ p \in \mathbb{Z} \\ 0 & \text{else} \end{cases}, \tag{A.16}$$

$$d_\mathrm{c}(k,n) = \begin{cases} \frac{1}{2}\frac{T_\mathrm{r}}{T_\mathrm{s}} & \text{if } k \neq q\frac{T_\mathrm{r}}{T_\mathrm{s}},\ q \in \mathbb{N}_{>0} \text{ and } n = \pm k + p\frac{T_\mathrm{r}}{T_\mathrm{s}},\ p \in \mathbb{Z} \\ \frac{T_\mathrm{r}}{T_\mathrm{s}} & \text{if } k = q\frac{T_\mathrm{r}}{T_\mathrm{s}},\ q \in \mathbb{N}_{>0} \text{ and } n = k + p\frac{T_\mathrm{r}}{T_\mathrm{s}},\ p \in \mathbb{Z} \\ 0 & \text{else} \end{cases}. \tag{A.17}$$

Thus, given (A.16) and (A.17) and using the sinc-function $\mathrm{sinc}(x) = \sin(x)/x$, the PWM output $V_\mathrm{c}(t)$ from (A.13) can finally be simplified to

$$\begin{aligned} V_\mathrm{c}(t) = \overbrace{\frac{1}{2}V_\mathrm{DC}}^{\text{DC offset}} + \overbrace{\frac{2}{\pi}V_\mathrm{DC} \sum_{\substack{k=1 \\ k\neq q\frac{T_\mathrm{r}}{T_\mathrm{s}} \\ q\in\mathbb{N}_{>0}}}^{\infty} \sum_{\substack{n=\pm k+p\frac{T_\mathrm{r}}{T_\mathrm{s}} \\ p\in\mathbb{Z}}}^{\infty} J_\mathrm{n}\left(k\,a_\mathrm{m}\frac{\pi}{2}\frac{T_\mathrm{s}}{T_\mathrm{r}}\right) \frac{d_\mathrm{s}(k,n)}{k} \cdot}^{\text{fundamental component and sideband harmonics}} \\ \sin\left(k\omega_\mathrm{r}\left(t - \frac{T_\mathrm{s}}{2} + d_\mathrm{s}(k,n)\frac{T_\mathrm{s}^2}{2T_\mathrm{r}}\right)\right) + \\ \underbrace{V_\mathrm{DC} \sum_{\substack{k=q\frac{T_\mathrm{r}}{T_\mathrm{s}} \\ q\in\mathbb{N}_{>0}}}^{\infty} \sum_{\substack{n=k+p\frac{T_\mathrm{r}}{T_\mathrm{s}} \\ p\in\mathbb{Z}}}^{\infty} J_\mathrm{n}\left(k\,a_\mathrm{m}\frac{\pi}{2}\frac{T_\mathrm{s}}{T_\mathrm{r}}\right) \mathrm{sinc}\left(k\pi\frac{1}{2}\frac{T_\mathrm{s}}{T_\mathrm{r}}\right) \sin\left(k\omega_\mathrm{r}\left(t-\frac{T_\mathrm{s}}{2}\right)+\frac{\pi}{2}\right)}_{\text{carrier harmonics}}. \end{aligned} \tag{A.18}$$

As can be observed, the pulse-width pattern of the digital single-update PWM is composed of three parts, namely, a DC component, the fundamental component with sideband harmonics and carrier harmonics. To illustrate the analytic description (A.18) with a simple example, Fig. A.4 shows the (calculated) PWM output in case of a single sinusoidal input voltage and Fig. A.5 shows the resulting (normalized) amplitude spectra of $V_\mathrm{c}(t)/(a_\mathrm{m}/2)$ for two different amplitude modulation indices.

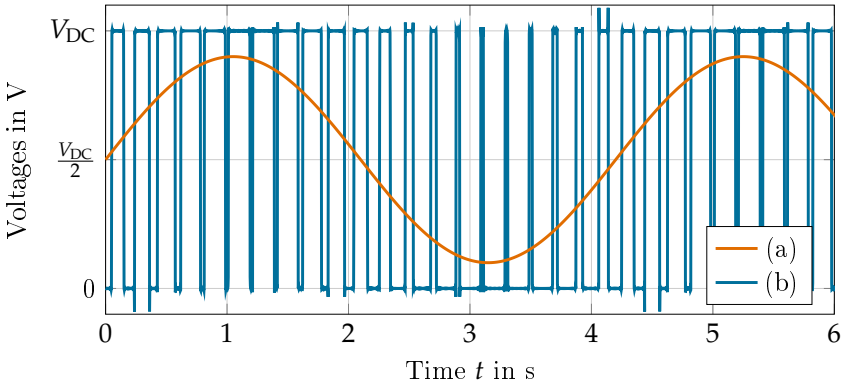

Fig. A.4: Waveforms of (a) the reference voltage $V_\mathrm{ref}(t)$ and (b) the resulting (calculated) PWM output voltage $V_\mathrm{c}(t)$, where $T_\mathrm{r}/T_\mathrm{s} = 21$, $a_\mathrm{m} = 0.8$, and $k = \{1, \ldots, 10000\}$, $n = \{-10000, \ldots, 10000\}$.

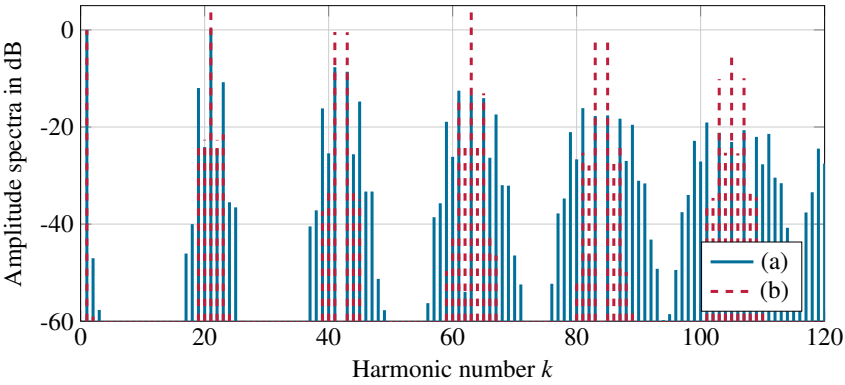

Fig. A.5: Theoretic normalized spectra of the PWM output voltage, where $T_\mathrm{r}/T_\mathrm{s} = 21$ and (a) $a_\mathrm{m} = 0.8$ and (b) $a_\mathrm{m} = 0.2$.

A.3 Derivation of the Plant Dynamics in the Discrete z-Domain

Referring to standard literature on digital control systems, as e.g., [39, 119], it is well known how to calculate the (common) z-transform of the plant dynamics, $Y_{\mathrm{fc}}(s)$, from (3.5) which are preceded by a ZOH-element plus computational delay, i.e.,

$$\begin{aligned}(Y_{\mathrm{fc}}G_{\mathrm{ZOH}}G_{\mathrm{d}})(z) &= \mathcal{Z}\left\{\mathcal{L}^{-1}\left\{\frac{1/l_{\mathrm{fc}}}{s+r_{\mathrm{fc}}/l_{\mathrm{fc}}}\frac{1-e^{-sT_{\mathrm{s}}}}{s}e^{-sT_{\mathrm{c}}}\right\}\right\}\\ &= \frac{z-1}{z}\mathcal{Z}\left\{\mathcal{L}^{-1}\left\{\frac{1/l_{\mathrm{fc}}}{s(s+r_{\mathrm{fc}}/l_{\mathrm{fc}})}e^{-sT_{\mathrm{c}}}\right\}\right\}. \end{aligned} \tag{A.19}$$

If a symmetrically sampled single-update PWM with $T_{\mathrm{c}} = T_{\mathrm{s}}$ is considered, (A.19) becomes

$$(Y_{\mathrm{fc}}G_{\mathrm{ZOH}}G_{\mathrm{d}})(z) = \frac{1}{r_{\mathrm{fc}}}\frac{(1-e^{-\frac{r_{\mathrm{fc}}}{l_{\mathrm{fc}}}T_{\mathrm{s}}})}{z(z-e^{-\frac{r_{\mathrm{fc}}}{l_{\mathrm{fc}}}T_{\mathrm{s}}})}. \tag{A.20}$$

Similarly, it is also possible to define the z-transform of the plant, which is preceded by the proposed PWM model $G_{\mathrm{PWM}}(s)$ from (3.23) plus a computational delay. In particular, again focusing on a single-update PWM, the plant's discretized dynamics can be obtained by evaluating

$$\begin{aligned}(Y_{\mathrm{fc}}G_{\mathrm{PWM}}G_{\mathrm{d}})(z) &= \mathcal{Z}\left\{\mathcal{L}^{-1}\left\{\frac{1/l_{\mathrm{fc}}}{s+r_{\mathrm{fc}}/l_{\mathrm{fc}}}\frac{1-e^{-sD_0T_{\mathrm{s}}}}{sD_0}e^{-s\left(\left(\frac{1-D_0}{2}\right)T_{\mathrm{s}}+T_{\mathrm{c}}\right)}\right\}\right\}\\ &= \frac{z^{-2}}{D_0l_{\mathrm{fc}}}\mathcal{Z}\left\{\mathcal{L}^{-1}\left\{\frac{e^{s\left(1-\frac{1-D_0}{2}\right)T_{\mathrm{s}}}}{s(s+r_{\mathrm{fc}}/l_{\mathrm{fc}})}-\frac{e^{-s\left(D_0-\left(1-\frac{1-D_0}{2}\right)\right)T_{\mathrm{s}}}}{s(s+r_{\mathrm{fc}}/l_{\mathrm{fc}})}\right\}\right\}. \end{aligned} \tag{A.21}$$

To solve (A.21), the (more general) approach from [1] can be followed. Defining the auxiliary variable $q = (1-\frac{1-D_0}{2}) = \frac{1+D_0}{2}$, $\frac{1}{2} \leq q \leq 1$, it becomes clear that the inverse Laplace transform of the first term in (A.21) represents a time-shifted impulse response of the form

$$g_{\mathrm{q}}(t) = \mathcal{L}^{-1}\left\{\frac{e^{s\left(1-\frac{1-D_0}{2}\right)T_{\mathrm{s}}}}{s(s+r_{\mathrm{fc}}/l_{\mathrm{fc}})}\right\} = -\frac{l_{\mathrm{cf}}}{r_{\mathrm{fc}}}\left(e^{-\frac{r_{\mathrm{fc}}}{l_{\mathrm{fc}}}(t+qT_{\mathrm{s}})}-1\right), \tag{A.22}$$

which z-transform can be derived to be [1, 39, 119]

$$\begin{aligned}\mathcal{Z}\left\{g_{\mathrm{q}}(kT_{\mathrm{s}})\right\} &= \sum_{k=-\infty}^{\infty} g_{\mathrm{q}}(kT_{\mathrm{s}})z^{-k} = -\frac{l_{\mathrm{cf}}}{r_{\mathrm{fc}}}\sum_{k=-\infty}^{\infty}\left(e^{-\frac{r_{\mathrm{fc}}}{l_{\mathrm{fc}}}(k+q)T_{\mathrm{s}}}-1\right)z^{-k} \\ &= -\frac{l_{\mathrm{cf}}}{r_{\mathrm{fc}}}\left(\sum_{k=-\infty}^{\infty} e^{-q\frac{r_{\mathrm{fc}}}{l_{\mathrm{fc}}}T_{\mathrm{s}}}\left(\frac{e^{-\frac{r_{\mathrm{fc}}}{l_{\mathrm{fc}}}T_{\mathrm{s}}}}{z}\right)^k - \sum_{k=-\infty}^{\infty}\left(\frac{1}{z}\right)^k\right).\end{aligned} \tag{A.23}$$

If only right-sided signals are considered, the geometric series in (A.23) converge, where with $\sum_{k=0}^{\infty}(a/x)^k = x/(x-a)$ for all $|a/x| < 1$, (A.23) simplifies to

$$\mathcal{Z}\left\{g_{\mathrm{q}}(kT_{\mathrm{s}})\right\} = -\frac{l_{\mathrm{cf}}}{r_{\mathrm{fc}}}\left(\frac{z\,e^{-q\frac{r_{\mathrm{fc}}}{l_{\mathrm{fc}}}T_{\mathrm{s}}}}{z-e^{-\frac{r_{\mathrm{fc}}}{l_{\mathrm{fc}}}T_{\mathrm{s}}}} - \frac{z}{z-1}\right). \tag{A.24}$$

Analog to the specification of $g_{\mathrm{q}}(t)$ in (A.22) and the derivation of its z-transformed from (A.24), the z-transform of the second term in (A.21) can be calculated by replacing the auxiliary variable q with a new auxiliary variable, $v = -(D_0 - (1 - \frac{1-D_0}{2})) = \frac{1-D_0}{2}$, $0 \leq v \leq \frac{1}{2}$. Then, combining both z-transforms according to (A.21) yields the plant's common z-transform $(Y_{\mathrm{fc}}G_{\mathrm{PWM}}G_{\mathrm{d}})(z)$, which is given by

$$(Y_{\mathrm{fc}}G_{\mathrm{PWM}}G_{\mathrm{d}})(z) = \frac{1}{D_0 r_{\mathrm{fc}}}\frac{e^{-\frac{1-D_0}{2}\frac{r_{\mathrm{fc}}}{l_{\mathrm{fc}}}T_{\mathrm{s}}} - e^{-\frac{1+D_0}{2}\frac{r_{\mathrm{fc}}}{l_{\mathrm{fc}}}T_{\mathrm{s}}}}{z\left(z-e^{-\frac{r_{\mathrm{fc}}}{l_{\mathrm{fc}}}T_{\mathrm{s}}}\right)}. \tag{A.25}$$

As can be verified, (A.25) simplifies to (A.20), if $D_0 = 1$, and is also equivalent to the (modified) z-transform of $Y_{\mathrm{fc}}(s)T_{\mathrm{s}}e^{-sT_{\mathrm{d}}}$ for $D_0 = 0$, which shows that $(Y_{\mathrm{fc}}G_{\mathrm{PWM}}G_{\mathrm{d}})(z)$ from (A.25) can be understood as a generalization of classical plant plus PWM models in the z-domain.

A.4 Alternative Representation of the Discretized Plant Dynamics using the Multiple-Frequency PWM Model

Given the VSC's converter-side filter admittance, $Y_{\mathrm{fc}}(s)$ from (3.5), and applying the transformation (6.1) on the filter dynamics which are preceded by the piece-wise defined multiple-frequency PWM plus computational delay model (6.2), the (discretized) plant dynamics seen by the converter are defined to be

$$(Y_{\mathrm{fc}}G_{\mathrm{PWM}}G_{\mathrm{d}})'(s) = \frac{1}{T_{\mathrm{s}}}\sum_{q=-\infty}^{\infty} Y_{\mathrm{fc}}(s+jq\omega_{\mathrm{s}})G_{\mathrm{PWM,q}}(s)G_{\mathrm{d,q}}(s) \quad \text{(A.26)}$$

where an extension can be avoided if the adopted PWM model has a sufficient low-pass characteristic. Then, regarding the special case where the transfer functions $G_{\mathrm{PWM,q}}(s)G_{\mathrm{d,q}}(s), \forall q$ are represented by the same transfer functions, $G_{\mathrm{PWM},0}(s)G_{\mathrm{d},0}(s)$ and $G_{\mathrm{PWM},1}(s)G_{\mathrm{d},1}(s)$ for all even and odd q, respectively, (A.26) can be decomposed into

$$\begin{aligned}(Y_{\mathrm{fc}}G_{\mathrm{PWM}}G_{\mathrm{d}})'(s) = {} & G_{\mathrm{PWM},0}(s)G_{\mathrm{d},0}(s)\,\frac{1}{T_{\mathrm{s}}}\sum_{\substack{q=-\infty\\ q\text{ even}}}^{\infty} Y_{\mathrm{fc}}(s+jq\omega_{\mathrm{s}}) \\ & + G_{\mathrm{PWM},1}(s)G_{\mathrm{d},1}(s)\,\frac{1}{T_{\mathrm{s}}}\sum_{\substack{q=-\infty\\ q\text{ odd}}}^{\infty} Y_{\mathrm{fc}}(s+jq\omega_{\mathrm{s}}). \quad \text{(A.27)}\end{aligned}$$

Adopting the substitution $q = 2k$ plus $\tilde{\omega}_{\mathrm{s}} = 2\omega_{\mathrm{s}}$ with $\tilde{T}_{\mathrm{s}} = T_{\mathrm{s}}/2$ and following the calculation of the discrete Laplace transform of a first-order lag element via Laplace transforms from [114], the first sum in (A.27) can be written as an explicit equation of the form

$$\frac{1}{T_{\mathrm{s}}}\sum_{\substack{q=-\infty\\ q\text{ even}}}^{\infty} Y_{\mathrm{fc}}(s+jq\omega_{\mathrm{s}}) = \frac{1}{2\tilde{T}_{\mathrm{s}}}\sum_{k=-\infty}^{\infty} Y_{\mathrm{fc}}(s+jk\tilde{\omega}_{\mathrm{s}}) = \frac{1}{4\,l_{\mathrm{fc}}}\frac{1+e^{-(s+\frac{r_{\mathrm{fc}}}{l_{\mathrm{fc}}})\frac{T_{\mathrm{s}}}{2}}}{1-e^{-(s+\frac{r_{\mathrm{fc}}}{l_{\mathrm{fc}}})\frac{T_{\mathrm{s}}}{2}}}. \quad \text{(A.28)}$$

As can be verified, (A.28) represents the Laplace-domain representation of the z-transformed of $(Y_{\mathrm{fc}}(s) - 1/(2l_{\mathrm{fc}}))/2$ using half the sampling time, i.e., $[((z/l_{\mathrm{fc}})/(z - e^{-\frac{r_{\mathrm{fc}}}{l_{\mathrm{fc}}}\tilde{T}_{\mathrm{s}}}) - 1/(2l_{\mathrm{fc}}))/2]|_{z=e^{s\tilde{T}_{\mathrm{s}}}}$. This can also directly be deduced from (A.27), by substituting $q = 2k$, $\tilde{\omega}_{\mathrm{s}} = 2\omega_{\mathrm{s}}$ and taking into account that $\mathcal{L}^{-1}\{Y_{\mathrm{fc}}(s)\}$ shows a jump discontinuity at $t = 0$ with $Y_{\mathrm{fc}}(0^+) = 1/l_{\mathrm{fc}}$. According to the footnote on page 59, the discrete Laplace transform of $Y_{\mathrm{fc}}(s)$ with sampling time $\tilde{T}_{\mathrm{s}}$ is then defined by $Y^*_{\mathrm{fc}}(s) = 1/\tilde{T}_{\mathrm{s}} \sum_{k=-\infty}^{\infty} Y_{\mathrm{fc}}(s + jk\tilde{\omega}_{\mathrm{s}}) + 1/(2l_{\mathrm{fc}})$.

Similar to the derivation of (A.28), the second sum in (A.27) can be reformulated, adopting the substitution $q = 2k-1$ and $\tilde{\omega}_{\mathrm{s}} = 2\omega_{\mathrm{s}}$, which results in

$$\frac{1}{T_{\mathrm{s}}} \sum_{\substack{q=-\infty \\ q \text{ odd}}}^{\infty} Y_{\mathrm{fc}}(s+jq\omega_{\mathrm{s}}) = \frac{1}{2\tilde{T}_{\mathrm{s}}} \sum_{k=-\infty}^{\infty} Y_{\mathrm{fc}}(s-j\omega_{\mathrm{s}}+jk\tilde{\omega}_{\mathrm{s}}) = \frac{1}{4\,l_{\mathrm{fc}}} \frac{1 - e^{-(s+\frac{r_{\mathrm{fc}}}{l_{\mathrm{fc}}})\frac{T_{\mathrm{s}}}{2}}}{1 + e^{-(s+\frac{r_{\mathrm{fc}}}{l_{\mathrm{fc}}})\frac{T_{\mathrm{s}}}{2}}} \tag{A.29}$$

noticing that $e^{-(s-j\omega_{\mathrm{s}})\tilde{T}_{\mathrm{s}}} = e^{-s\tilde{T}_{\mathrm{s}}+j\pi} = -e^{-s\frac{T_{\mathrm{s}}}{2}}$. Alternatively, (A.29) might again directly be deduced from (A.27) by substituting $q = 2k - 1$ and evaluating the resulting z-transformed of $(Y_{\mathrm{fc}}(s) - 1/(2l_{\mathrm{fc}}))/2$ with half the sampling time at $z = e^{(s-j\omega_{\mathrm{s}})\tilde{T}_{\mathrm{s}}} = -e^{s\frac{T_{\mathrm{s}}}{2}}$.

Hence, considering the special case (A.27), where $G_{\mathrm{PWM},0}(s)G_{\mathrm{d},0}(s)$ and $G_{\mathrm{PWM},1}(s)G_{\mathrm{d},1}(s)$ are used to specify the transfer functions for all even and odd sideband components, respectively, with (A.28) and (A.29), the discretized plant dynamics seen by the converter are given by

$$\begin{aligned}(Y_{\mathrm{fc}}G_{\mathrm{PWM}}G_{\mathrm{d}})'(s) = &\frac{G_{\mathrm{PWM},0}(s)G_{\mathrm{d},0}(s)}{4\,l_{\mathrm{fc}}} \frac{1 + e^{-(s+\frac{r_{\mathrm{fc}}}{l_{\mathrm{fc}}})\frac{T_{\mathrm{s}}}{2}}}{1 - e^{-(s+\frac{r_{\mathrm{fc}}}{l_{\mathrm{fc}}})\frac{T_{\mathrm{s}}}{2}}} \\ &+ \frac{G_{\mathrm{PWM},1}(s)G_{\mathrm{d},1}(s)}{4\,l_{\mathrm{fc}}} \frac{1 - e^{-(s+\frac{r_{\mathrm{fc}}}{l_{\mathrm{fc}}})\frac{T_{\mathrm{s}}}{2}}}{1 + e^{-(s+\frac{r_{\mathrm{fc}}}{l_{\mathrm{fc}}})\frac{T_{\mathrm{s}}}{2}}}.\end{aligned} \tag{A.30}$$

The adopted procedure for the calculation of $(Y_{\mathrm{fc}}G_{\mathrm{PWM}}G_{\mathrm{d}})'(s)$ can also be applied in a similar way, if the transfer functions $G_{\mathrm{PWM,q}}(s)G_{\mathrm{d,q}}(s), \forall q$ are to be defined more individually.

Own Publications

[1] Hans, F., M. Oeltze and W. Schumacher: *A modified ZOH model for representing the small-signal PWM behavior in digital DC-AC converter systems*. In *45th Annu. Conf. IEEE Ind. Electron. Soc. (IECON 2019)*, Lisbon, Portugal, Oct. 14–17, 2019. IEEE.

[2] Hans, F. and W. Schumacher: *Simplified small-signal modelling of grid-connected voltage source converters for transient grid studies*. In *20th Eur. Conf. Power Electron. Appl. (EPE'18 ECCE Europe)*, Riga, Latvia, Sept. 17–21, 2018. IEEE.

[3] Hans, F., W. Schumacher, S.-F. Chou and X. Wang: *Design of multifrequency proportional-resonant current controllers for voltage-source converters*. IEEE Trans. Power Electron., 35(12):13573–13589, Dec. 2020.

[4] Hans, F., W. Schumacher, S.-F. Chou and X. Wang: *Passivation of current-controlled grid-connected VSCs using passivity indices*. IEEE Trans. Ind. Electron., 66(11):8971–8980, Nov. 2019.

[5] Hans, F., W. Schumacher and L. Harnefors: *Small-signal modeling of three-phase synchronous reference frame phase-locked loops*. IEEE Trans. Power Electron., 33(7):5556–5560, July 2018.

References

[6] Aeberhard, M., M. Meyer and C. Courtois: *The new standard EN 50388-2 Part 2 - Stability and harmonics*. Elektrische Bahnen, 12(1):28–35, 2014.

[7] Ainsworth, J.: *Harmonic instability between controlled static convertors and a.c. networks*. Proc. Instit. Electr. Eng., 114(7):949–957, July 1967.

[8] Akhavan, A., H. R. Mohammadi, J. C. Vasquez and J. M. Guerrero: *Passivity-based design of plug-and-play current-controlled grid-connected inverters*. IEEE Trans. Power Electron., 35(2):2135–2150, Feb. 2020.

[9] Al-Alaoui, M. A.: *Novel approach to analog-to-digital transforms*. IEEE Trans. Circuits Syst. I, Reg. Papers, 54(2):338–350, Feb. 2007.

[10] Åström, K. J. and R. M. Murray: *Feedback systems: an introduction for scientists and engineers*. Princeton university press, 2010.

[11] Bai, H., X. Wang and F. Blaabjerg: *Passivity enhancement in renewable energy source based power plant with paralleled grid-connected VSIs*. IEEE Trans. Ind. Appl., 53(4):3793–3802, July/Aug. 2017.

[12] Bakhshizadeh, M. K., X. Wang, F. Blaabjerg, J. Hjerrild, Ł. Kocewiak, C. L. Bak and B. Hesselbæk: *Couplings in phase domain impedance modeling of grid-connected converters*. IEEE Trans. Power Electron., 31(10):6792–6796, Oct. 2016.

[13] Balasubramanian, A. K. and V. John: *Analysis and design of split-capacitor resistive-inductive passive damping for LCL filters in grid-connected inverters*. IET Power Electron., 6(9):1822–1832, Nov. 2013.

[14] Bao, J. and P. L. Lee: *Process control: the passive systems approach*. Springer Science & Business Media, 2007.

[15] Bartels, W., F. Ehlers, K. Heidenreich, R. Huttner, H. Kuhn, T. Meyer, T. Kumm, J. Salzmann, H. Schafer and K. Weck: *Tech-*

nical guideline: generating plants connected to the medium-voltage network. Technical Guideline of BDEW, 2008.

[16] Beres, R. N.: *Optimal design of passive power filters for grid-connected voltage-source converters*. Ph. D. dissertation, Fac. Eng. Sc., Aalborg University, Denmark, 2016.

[17] Beres, R. N., X. Wang, M. Liserre, F. Blaabjerg and C. L. Bak: *A review of passive power filters for three-phase grid-connected voltage-source converters*. IEEE J. of Emerg. Sel. Topics Power Electron., 4(1):54–69, Mar. 2016.

[18] Bevrani, H., A. Ghosh and G. Ledwich: *Renewable energy sources and frequency regulation: survey and new perspectives*. IET Renew. Power Gener., 4(5):438–457, Sept. 2010.

[19] Bienholz, M. and G. Griepentrog: *Wide-band impedance measurement for converter impedance determination in LV-grids*. In *20th Eur. Conf. Power Electron. Appl. (EPE'18 ECCE Europe)*, Riga, Latvia, Sept. 17–21, 2018. IEEE.

[20] Blaabjerg, F., R. Teodorescu, M. Liserre and A. V. Timbus: *Overview of control and grid synchronization for distributed power generation systems*. IEEE Trans. Ind. Electron., 53(5):1398–1409, Oct. 2006.

[21] Blasko, V. and V. Kaura: *A novel control to actively damp resonance in input LC filter of a three-phase voltage source converter*. IEEE Trans. Ind. Appl., 33(2):542–550, Mar./Apr. 1997.

[22] Bojoi, R., L. R. Limongi, F. Profumo, D. Roiu and A. Tenconi: *Analysis of current controllers for active power filters using selective harmonic compensation schemes*. IEEJ Trans. Electric. and Electron. Eng., 4(2):139–157, Feb. 2009.

[23] Bottrell, N. and T. C. Green: *Comparison of current-limiting strategies during fault ride-through of inverters to prevent latch-up and wind-up*. IEEE Trans. Power Electron., 29(7):3786–3797, July 2014.

[24] Bottrell, N., M. Prodanovic and T. C. Green: *Dynamic stability of a microgrid with an active load*. IEEE Trans. Power Electron., 28(11):5107–5119, Nov. 2013.

[25] Brogliato, B., R. Lozano, B. Maschke and O. Egeland: *Dissipative systems analysis and control*, vol. 3. Springer Nature Switzerland AG, 2020.

[26] Buchhagen, C., M. Greve, A. Menze and J. Jung: *Harmonic stability-practical experience of a TSO*. In *15th Wind Integr. Workshop*, Vienna, Austria, Nov. 15–17, 2016. energynautics.

[27] Busada, C. A., S. G. Jorge, A. E. Leon and J. A. Solsona: *Current controller based on reduced order generalized integrators for distributed generation systems*. IEEE Trans. Ind. Electron., 59(7):2898–2909, July 2012.

[28] Butzer, P. L. and R. J. Nessel: *Fourier analysis and approximation, Vol. 1*. Reviews in Group Representation Theory, Part A (Pure and Applied Mathematics Series, Vol. 7), 1971.

[29] Castilla, M., J. Miret, J. Matas, L. G. De Vicuña and J. M. Guerrero: *Control design guidelines for single-phase grid-connected photovoltaic inverters with damped resonant harmonic compensators*. IEEE Trans. Ind. Electron., 56(11):4492–4501, Nov. 2009.

[30] Cespedes, M. and J. Sun: *Adaptive control of grid-connected inverters based on online grid impedance measurements*. IEEE Trans. Sustain. Energy, 5(2):516–523, Apr. 2014.

[31] Cespedes, M. and J. Sun: *Impedance modeling and analysis of grid-connected voltage-source converters*. IEEE Trans. Power Electron., 29(3):1254–1261, Mar. 2014.

[32] Chen, G.: *Stability of nonlinear systems*. In *Encyclopedia of RF and Microwave Engineering*, pp. 4881–4896. Wiely, New York, USA, 2004.

[33] Chou, S.-F., X. Wang and F. Blaabjerg: *Passivity-based LCL Filter Design of Grid-Connected VSCs with Converter Side Current Feedback*. In *2018 Int. Power Electron. Conf. (IPEC-Niigata 2018-ECCE Asia)*, Niigata, Japan, May 20–24, 2018. IEEE.

[34] Corradini, L., W. Stefanutti and P. Mattavelli: *Analysis of multisampled current control for active filters*. IEEE Trans. Ind. Appl., 44(6):1785–1794, Nov./Dec. 2008.

[35] Dannehl, J., M. Liserre and F. W. Fuchs: *Filter-based active damping of voltage source converters with LCL filter*. IEEE Trans. Ind. Electron., 58(8):3623–3633, Aug. 2011.

[36] Dennetiere, S., H. Saad, Y. Vernay, P. Rault, C. Martin and B. Clerc: *Supporting energy transition in transmission systems: an operator's experience using electromagnetic transient simulation*. IEEE Power Energy Mag., 17(3):48–60, May/June 2019.

[37] Enslin, J. H. and P. J. Heskes: *Harmonic interaction between a large number of distributed power inverters and the distribution network*. IEEE Trans. Power Electron., 19(6):1586–1593, Nov. 2004.

[38] Franke, W.-T., J. Dannehl, F. W. Fuchs and M. Liserre: *Characterization of differential-mode filter for grid-side converters*. In *35th Annu. Conf. IEEE Ind. Electron. Soc. (IECON 2009)*, Porto, Portugal, Nov. 3–5, 2009. IEEE.

[39] Franklin, G. F., J. D. Powell and M. L. Workman: *Digital control of dynamic systems*, vol. 3. Addison-wesley Reading, MA, 1998.

[40] FRAUNHOFER ISE: *Interaktive Grafiken zu Stromproduktion und Börsenstrompreisen in Deutschland*. `https://www.energy-charts.de`. Accessed: Aug. 24, 2020.

[41] Freijedo, F. D., D. Dujic and J. A. Marrero-Sosa: *Design for passivity in the z-domain for LCL grid-connected converters*. In *42nd Annu. Conf. IEEE Ind. Electron. Soc. (IECON 2016)*, Florence, Italy, Oct. 23–26, 2016. IEEE.

[42] Freijedo, F. D., M. Ferrer and D. Dujic: *Multivariable high-frequency input-admittance of grid-connected converters: modeling, validation and implications on stability*. IEEE Trans. Ind. Electron., 66(8):6505 – 6515, Aug. 2019.

[43] Ghoshal, A. and V. John: *High-accuracy multi-rate implementation of resonant integrator using FPGA*. IET Power Electron., 10(3):348–356, Mar. 2017.

[44] Gu, K. and S.-I. Niculescu: *Survey on recent results in the stability and control of time-delay systems*. J. Dyn. Sys., Meas., Control, 125(2):158–165, June 2003.

[45] Guerrero, J. M., C. González-Moral, D. Fernández, D. Reigosa, C. Rivas and F. Briz: *Realizable references anti-windup implementation for parallel controllers in multiple reference frames*. In *2018 IEEE Energy Conv. Congr. Expo. (ECCE)*, Portland, OR, USA, Sept. 23–27, 2018. IEEE.

[46] Guiver, C., H. Logemann and M. R. Opmeer: *Transfer functions of infinite-dimensional systems: positive realness and stabilization*. Math. Control Signals and Syst., 29(4):20, Dec. 2017.

[47] Guo, X.-Q., W.-Y. Wu and H.-R. Gu: *Phase locked loop and synchronization methods for grid-interfaced converters: a review*. Przeglad Elektrotechniczny, 87(4):182–187, 2011.

[48] H2020 PROJECT MIGRATE WEBSITE: *Migrate Deliverable 1.1, Report on systemic issues*. `https://www.h2020-migrate.eu/downloads.html`. Accessed: Nov. 09, 2020.

[49] Han, Y., M. Yang, H. Li, P. Yang, L. Xu, E. A. A. Coelho and J. M. Guerrero: *Modeling and stability analysis of LCL-type grid-connected inverters: a comprehensive overview*. IEEE Access, 7:114975–115001, Aug. 2019.

[50] Harnefors, L.: *Implementation of resonant controllers and filters in fixed-point arithmetic*. IEEE Trans. Ind. Electron., 56(4):1273–1281, Apr. 2009.

[51] Harnefors, L.: *Modeling of three-phase dynamic systems using complex transfer functions and transfer matrices*. IEEE Trans. Ind. Electron., 54(4):2239–2248, Aug. 2007.

[52] Harnefors, L., M. Bongiorno and S. Lundberg: *Input-admittance calculation and shaping for controlled voltage-source converters*. IEEE Trans. Ind. Electron., 54(6):3323–3334, Dec. 2007.

[53] Harnefors, L., R. Finger, X. Wang, H. Bai and F. Blaabjerg: *VSC input-admittance modeling and analysis above the Nyquist frequency for passivity-based stability assessment*. IEEE Trans. Ind. Electron., 64(8):6362–6370, Aug. 2017.

[54] Harnefors, L. and H.-P. Nee: *Model-based current control of AC machines using the internal model control method*. IEEE Trans. Ind. Appl.,

34(1):133–141, Jan./Feb. 1998.

[55] Harnefors, L., X. Wang, A. G. Yepes and F. Blaabjerg: *Passivity-based stability assessment of grid-connected VSCs - an overview*. IEEE J. of Emerg. Sel. Topics Power Electron., 4(1):116–125, Mar. 2016.

[56] Harnefors, L., A. G. Yepes, A. Vidal and J. Doval-Gandoy: *Passivity-based stabilization of resonant current controllers with consideration of time delay*. IEEE Trans. Power Electron., 29(12):6260–6263, Dec. 2014.

[57] Harnefors, L., A. G. Yepes, A. Vidal and J. Doval-Gandoy: *Passivity-based controller design of grid-connected VSCs for prevention of electrical resonance instability*. IEEE Trans. Ind. Electron., 62(2):702–710, Feb. 2015.

[58] Harnefors, L., A. G. Yepes, A. Vidal and J. Doval-Gandoy: *Multifrequency current control with distortion-free saturation*. IEEE J. of Emerg. Sel. Topics Power Electron., 4(1):37–43, Mar. 2016.

[59] Harnefors, L., A. G. Yepes, A. Vidal and J. Doval-Gandoy: *Reduction of saturation-induced distortion and antiwindup in multifrequency current control*. In *17th Eur. Conf. Power Electron. Appl. (EPE'15 ECCE-Europe)*, Geneva, Switzerland, Sept. 8–10, 2015. IEEE.

[60] Harnefors, L., L. Zhang and M. Bongiorno: *Frequency-domain passivity-based current controller design*. IET Power Electron., 1(4):455–465, Dec. 2008.

[61] Hazell, P. and J. Flower: *Theoretical analysis of harmonic instability in a.c.-d.c. convertors*. Proc. Instit. Electr. Eng., 117(9):1869–1878, Sept. 1970.

[62] Hoffmann, N., F. W. Fuchs, M. P. Kazmierkowski and D. Schröder: *Digital current control in a rotating reference frame - Part I: system modeling and the discrete time-domain current controller with improved decoupling capabilities*. IEEE Trans. Power Electron., 31(7):5290–5305, July 2016.

[63] Holmes, D., T. Lipo, B. McGrath and W. Kong: *Optimized design of stationary frame three phase AC current regulators*. IEEE Trans. Power Electron., 24(11):2417–2426, Nov. 2009.

[64] Holmes, D. G. and T. A. Lipo: *Pulse width modulation for power converters: principles and practice*, vol. 18. John Wiley & Sons, 2003.

[65] Hou, P., E. Ebrahimzadeh, X. Wang, F. Blaabjerg, J. Fang and Y. Wang: *Harmonic stability analysis of offshore wind farm with component connection method*. In *43rd Annu. Conf. IEEE Ind. Electron. Soc. (IECON 2017)*, Beijing, China, Oct. 29–Nov. 1, 2017. IEEE.

[66] Hu, H., H. Tao, F. Blaabjerg, X. Wang, Z. He and S. Gao: *Train-network interactions and stability evaluation in high-speed railways - Part I: phenomena and modeling*. IEEE Trans. Power Electron., 33(6):4627–4642, June 2018.

[67] Husev, O., C. Roncero-Clemente, E. Makovenko, S. P. Pimentel, D. Vinnikov and J. Martins: *Optimization and implementation of the proportional-resonant controller for grid-connected inverter with significant computation delay*. IEEE Trans. Ind. Electron., 67(2):1201–1211, Feb. 2020.

[68] IEEE Standards Coordinating Committee 21 on Fuel Cells, Photovoltaics, Dispersed Generation, and Energy Storage: *IEEE Application Guide for IEEE Std 1547(TM), IEEE Standard for Interconnecting Distributed Resources With Electric Power Systems*. IEEE, New York, NY, USA, Apr. 2009.

[69] International Energy Agency - Photovoltaic Power Systems Programme: *Annual Reports*. `https://iea-pvps.org/annual-reports/`. Accessed: Aug. 24, 2020.

[70] International Energy Agency - Wind Technology Collaboration Programme: *Annual Reports*. `https://community.ieawind.org/publications/ar`. Accessed: Aug. 24, 2020.

[71] Kapetanovic, T., B. M. Buchholz, B. Buchholz and V. Buehner: *Provision of ancillary services by dispersed generation and demand side response–needs, barriers and solutions*. e & i Elektrotechnik und Informationstechnik, 125(12):452–459, Dec. 2008.

[72] Karttunen, J., S. Kallio, P. Peltoniemi and P. Silventoinen: *Transforming dynamic system models between two-axis reference frames rotating at different angular frequencies*. In *16th Eur. Conf. Power Electron.*

Appl. (EPE'14 ECCE Europe), Lappeenranta, Finland, Aug. 26–28, 2014. IEEE.

[73] Kelkar, A. and S. Joshi: *Robust passification and control of non-passive systems*. In *1998 American Control Conf. (ACC)*, Philadelphia, PA, USA, June 24–26, 1998. IEEE.

[74] Khalil, H. K.: *Nonlinear systems: Pearson new international edition*, vol. 3. Pearson, 2014.

[75] Kottenstette, N., M. J. McCourt, M. Xia, V. Gupta and P. J. Antsaklis: *On relationships among passivity, positive realness, and dissipativity in linear systems*. Automatica, 50(4):1003–1016, Apr. 2014.

[76] Kroutikova, N., C. A. Hernandez-Aramburo and T. C. Green: *State-space model of grid-connected inverters under current control mode*. IET Electr. Power Appl., 1(3):329–338, May 2007.

[77] Kundur, P., N. J. Balu and M. G. Lauby: *Power system stability and control*, vol. 7. McGraw-hill New York, 1994.

[78] Kundur, P., J. Paserba, V. Ajjarapu, G. Andersson, A. Bose, C. Canizares, N. Hatziargyriou, D. Hill, A. Stankovic, C. Taylor et al.: *Definition and classification of power system stability IEEE/CIGRE joint task force on stability terms and definitions*. IEEE Trans. Power Syst., 19(3):1387–1401, Aug. 2004.

[79] Lawrence, R. and S. Middlekauff: *The new guy on the block*. IEEE Ind. Appl. Mag., 11(1):54–59, Jan./Feb. 2005.

[80] Li, C.: *Unstable operation of photovoltaic inverter from field experiences*. IEEE Trans. Power Del., 33(2):1013–1015, Apr. 2018.

[81] Li, Y., Y. Gu and T. C. Green: *Interpreting Frame Transformations in AC Systems as Diagonalization of Harmonic Transfer Functions*. IEEE Trans. Circuits Syst. I, Reg. Papers, 67(7):2481–2491, July 2020.

[82] Limongi, L. R., R. Bojoi, G. Griva and A. Tenconi: *Digital current-control schemes*. IEEE Ind. Electron. Mag., 3(1):20–31, Mar. 2009.

[83] Lipnicki, P.: *Smart grids: general review of synchronization techniques*. Informatyka, Automatyka, Pomiary w Gospodarce I Ochronie Środowiska, 3(3):18–23, July 2013.

[84] Liserre, M., F. Blaabjerg and S. Hansen: *Design and control of an LCL-filter-based three-phase active rectifier*. IEEE Trans. Ind. Appl., 41(5):1281–1291, Sept./Oct. 2005.

[85] Liserre, M., A. Dell'Aquila and F. Blaabjerg: *Stability improvements of an LCL-filter based three-phase active rectifier*. In *2002 IEEE 33rd Annu. Power Electron. Special. Conf.*, vol. 4, Cairns, Qld., Australia, June 23–27, 2002. IEEE.

[86] Liserre, M., R. Teodorescu and F. Blaabjerg: *Stability of photovoltaic and wind turbine grid-connected inverters for a large set of grid impedance values*. IEEE Trans. Power Electron., 21(1):263–272, Jan. 2006.

[87] Liu, T., J. Liu, Z. Liu and Z. Liu: *A study of virtual resistor-based active damping alternatives for LCL resonance in grid-connected voltage source inverters*. IEEE Trans. Power Electron., 35(1):247–262, Jan. 2020.

[88] Lu, M., Y. Yang, B. Johnson and F. Blaabjerg: *An interaction-admittance model for multi-inverter grid-connected systems*. IEEE Trans. Ind. Electron., 34(8):7542–7557, Aug. 2019.

[89] Lumbreras, D., E. L. Barrios, A. Urtasun, A. Ursúa, L. Marroyo and P. Sanchis: *On the stability of advanced power electronic converters: the generalized Bode criterion*. IEEE Trans. Power Electron., 34(9):9247–9262, Sept. 2019.

[90] Ma, J., X. Wang, F. Blaabjerg, L. Harnefors and W. Song: *Accuracy analysis of the zero-order hold model for digital pulse width modulation*. IEEE Trans. Power Electron., 33(12):10826–10834, Dec. 2018.

[91] Machowski, J., J. Bialek and J. Bumby: *Power system dynamics: stability and control*, vol. 2. John Wiley & Sons, 2008.

[92] Manjarekar, N. S., R. N. Banavar and A. G. Kelkar: *Robust passification using norm bounded uncertainty models*. In *2003 IEEE Conf. Control Appl. (CCA 2003)*, Istanbul, Turkey, June 23–25, 2003. IEEE.

[93] Mattavelli, P.: *Synchronous-frame harmonic control for high-performance AC power supplies*. IEEE Trans. Ind. Appl., 37(3):864–872, May/June 2001.

[94] McCourt, M. J.: *Dissipativity theory for hybrid systems with applications to networked control systems*. Ph. D. dissertation, Coll. Eng., University of Notre Dame, Indiana, USA, 2013.

[95] Möllerstedt, E. and B. Bernhardsson: *Out of control because of harmonics - an analysis of the harmonic response of an inverter locomotive*. IEEE Control Syst. Mag., 20(4):70–81, Aug. 2000.

[96] Pan, D., X. Ruan, C. Bao, W. Li and X. Wang: *Capacitor-current-feedback active damping with reduced computation delay for improving robustness of LCL-type grid-connected inverter*. IEEE Trans. Power Electron., 29(7):3414–3427, July 2014.

[97] Parker, S. G., B. P. McGrath and D. G. Holmes: *Regions of active damping control for LCL filters*. IEEE Trans. Ind. Appl., 50(1):424–432, Jan./Feb. 2014.

[98] Pekař, L., R. Matušů, P. Dostálek and J. Dolinay: *The Nyquist criterion for LTI time-delay systems*. In *Proc. 13th WSEAS Int. Conf. Aut. Control, Mod. Sim. (ACMOS'11)*, pp. 80–85, May 2011.

[99] Pekař, L. and R. Prokop: *Some observations about the RMS ring for delayed systems*. In *17th Int. Conf. Process Control*, Štrbské Pleso, Slovakia, June 9–12, 2009. Institute of Information Engineering, Automation and Mathematics, FCFT STU Bratislava.

[100] Pena-Alzola, R., M. Liserre, F. Blaabjerg, R. Sebastián, J. Dannehl and F. W. Fuchs: *Analysis of the passive damping losses in LCL-filter-based grid converters*. IEEE Trans. Power Electron., 28(6):2642–2646, June 2013.

[101] Phadke, A. G. and J. H. Harlow: *Generation of abnormal harmonics in high-voltage AC-DC power systems*. IEEE Trans. Power App. Syst., PAS-87(3):873–883, Mar. 1968.

[102] Pogaku, N., M. Prodanovic and T. C. Green: *Modeling, analysis and testing of autonomous operation of an inverter-based microgrid*. IEEE Trans. Power Electron., 22(2):613–625, Mar. 2007.

[103] Poznyak, A. S.: *Advanced mathematical tools for automatic control engineers: deterministic techniques*, vol. 1. Elsevier, 2008.

[104] Prodanovic, M. and T. C. Green: *Control and filter design of three-phase inverters for high power quality grid connection*. IEEE Trans. Power Electron., 18(1):373–380, Jan. 2003.

[105] Raats, W.: *Small-signal analysis of asymmetrical regular sampled PWM control loops*. M. Sc. Thesis, Electr. Electron. Eng., Stellenbosch University, Stellenbosch, Western Cape, South Africa, 2017.

[106] Rasvan, V., S.-I. Niculescu and R. Lozano: *Input-output passive framework for delay systems*. In *39th IEEE Conf. Decision and Control (CDC)*, Sydney, NSW, Australia, Dec. 12–15, 2000. IEEE.

[107] Richter, S. A. and R. W. De Doncker: *Digital proportional-resonant (PR) control with anti-windup applied to a voltage-source inverter*. In *14th Eur. Conf. Power Electron. Appl. (EPE 2011)*, Birmingham, UK, Aug. 30–Sept. 1, 2011. IEEE.

[108] Rocabert, J., A. Luna, F. Blaabjerg and P. Rodriguez: *Control of power converters in AC microgrids*. IEEE Trans. Power Electron., 27(11):4734–4749, Nov. 2012.

[109] Rockhill, A., M. Liserre, R. Teodorescu and P. Rodriguez: *Grid-filter design for a multimegawatt medium-voltage voltage-source inverter*. IEEE Trans. Ind. Electron., 58(4):1205–1217, Apr. 2011.

[110] Rodriguez-Diaz, E., F. D. Freijedo, J. M. Guerrero, J.-A. Marrero-Sosa and D. Dujic: *Input-admittance passivity compliance for grid-connected converters with an LCL filter*. IEEE Trans. Ind. Electron., 66(2):1089–1097, Feb. 2019.

[111] Rodriguez-Diaz, E., F. D. Freijedo, J. C. Vasquez and J. M. Guerrero: *Analysis and comparison of notch filter and capacitor voltage feed-forward active damping techniques for LCL grid-connected converters*. IEEE Trans. Power Electron., 34(4):3958–3972, Apr. 2019.

[112] Rogalla, S., F. Ackermann, N. Bihler, H. Moghadam and O. Stalter: *Source-driven and resonance-driven harmonic interaction between PV inverters and the grid*. In *2016 IEEE 43rd Photovoltaic Special. Conf. (PVSC)*, Portland, OR, USA, June 5–10, 2016. IEEE.

[113] Roldán-Pérez, J., E. J. Bueno, R. Peña-Alzola and A. Rodríguez-Cabero: *All-pass-filter-based active damping for VSCs with LCL filters*

connected to weak grids. IEEE Trans. Power Electron., 33(11):9890–9901, Nov. 2018.

[114] Rosenwasser, E. N. and B. Lampe: *Computer controlled systems: analysis and design with process-orientated models*. Springer Science & Business Media, 2000.

[115] Rygg, A., M. Molinas, C. Zhang and X. Cai: *On the equivalence and impact on stability of impedance modeling of power electronic converters in different domains*. IEEE Trans. Emerg. Sel. Topics Power Electron., 5(4):1444–1454, Dec. 2017.

[116] San, G., W. Zhang, R. Luo, X. Guo, H. Xin, E. Tedeschi and M. Malinowski: *Small-signal multi-frequency model for grid-connected inverter system with PWM effect*. CSEE J. Power Energy Syst., 6(2):307–317, June 2020.

[117] San-Sebastian, J., I. Etxeberria-Otadui, A. Rujas, J. A. Barrena and P. Rodriguez: *Optimized LCL filter design methodology applied to MV grid-connected multimegawatt VSC*. In *2012 IEEE Energy Convers. Congr. Expo. (ECCE)*, Raleigh, NC, USA, Sept. 15–20, 2012. IEEE.

[118] Schröder, D. et al.: *Elektrische Antriebe - Regelung von Antriebssystemen*, vol. 2. Berlin, Heidelberg, New York: Springer, 2009.

[119] Schumacher, W.: *Umdruck zur Vorlesung Grundlagen der Regelungstechnik*. Technische Universität Braunschweig, Institut für Regelungstechnik, 2014.

[120] Shuai, Z., Y. Li, W. Wu, C. Tu, A. Luo and Z. J. Shen: *Divided DQ small-signal model: A new perspective for the stability analysis of three-phase grid-tied inverters*. IEEE Trans. Ind. Electron., 66(8):6493–6504, Aug. 2019.

[121] Skogestad, S. and I. Postlethwaite: *Multivariable feedback control: analysis and design*, vol. 2. Wiley New York, 2007.

[122] Sun, J.: *Small-signal methods for AC distributed power systems–a review*. IEEE Trans. Power Electron., 24(11):2545–2554, Nov. 2009.

[123] Sun, J.: *Impedance-based stability criterion for grid-connected inverters*. IEEE Trans. Power Electron., 26(11):3075–3078, Nov. 2011.

[124] Sun, J., G. Wang, X. Du and H. Wang: *A theory for harmonics created by resonance in converter-grid systems*. IEEE Trans. Power Electron., 34(4):3025–3029, Apr. 2019.

[125] Tang, Y., W. Yao, P. C. Loh and F. Blaabjerg: *Design of LCL filters with LCL resonance frequencies beyond the Nyquist frequency for grid-connected converters*. IEEE J. of Emerg. Sel. Topics Power Electron., 4(1):3–14, Mar. 2016.

[126] Teodorescu, R., F. Blaabjerg, M. Liserre and P. C. Loh: *Proportional-resonant controllers and filters for grid-connected voltage-source converters*. IEE Proc. - Electr. Power Appl., 153(5):750–762, Sept. 2006.

[127] Teodorescu, R., M. Liserre and P. Rodriguez: *Grid converters for photovoltaic and wind power systems*, vol. 29. John Wiley & Sons, 2011.

[128] Testa, A., M. Akram, R. Burch, G. Carpinelli, G. Chang, V. Dinavahi, C. Hatziadoniu, W. Grady, E. Gunther, M. Halpin et al.: *Interharmonics: theory and modeling*. IEEE Trans. Power Del., 22(4):2335–2348, Oct. 2007.

[129] Toit Mouton, H. du, B. McGrath, D. G. Holmes and R. H. Wilkinson: *One-dimensional spectral analysis of complex PWM waveforms using superposition*. IEEE Trans. Power Electron., 29(12):6762–6778, Dec. 2014.

[130] Tomaszewski, E. and J. Jiangy: *An anti-windup scheme for proportional resonant controllers with tuneable phase-shift in voltage source converters*. In *2016 IEEE Power Energy Soc. General Meeting (PESGM)*, Boston, MA, USA, July 17–21, 2016. IEEE.

[131] Troeng, O., B. Bernhardsson and C. Rivetta: *Complex-coefficient systems in control*. In *2017 American Control Conf. (ACC)*, Seattle, WA, USA, May 24–26, 2017. IEEE.

[132] Tsili, M. and S. Papathanassiou: *A review of grid code technical requirements for wind farms*. IET Renew. Power Gener., 3(3):308–332, Sept. 2009.

[133] VandeSype, D. M., K. DeGusseme, F. M. DeBelie, A. P. VandenBossche and J. A. Melkebeek: *Small-signal z-domain analysis of dig-*

itally controlled converters. IEEE Trans. Power Electron., 21(2):470–478, Mar. 2006.

[134] VDE: *Power Generation Systems Connected to the Low-Voltage Distribution Network - Technical Minimum Requirements for the Connection to and Parallel Operation With Low-Voltage Distribution Networks*. VDE-AR-N 4105:2011-08, Verband der Elektrotechnik Elektronik Informationstechnik e.V., 2011.

[135] Vesti, S., T. Suntio, J. Oliver, R. Prieto and J. Cobos: *Impedance-based stability and transient-performance assessment applying maximum peak criteria*. IEEE Trans. Power Electron., 28(5):2099–2104, May 2013.

[136] Von Appen, J., M. Braun, T. Stetz, K. Diwold and D. Geibel: *Time in the sun: the challenge of high PV penetration in the German electric grid*. IEEE Power Energy Mag., 11(2):55–64, Mar./Apr. 2013.

[137] Walton, K. and J. Marshall: *Direct method for TDS stability analysis*. IEE Proc. D-Control Theory and Appl., 134(2):101–107, Mar. 1987.

[138] Wang, T. C., Z. Ye, G. Sinha and X. Yuan: *Output filter design for a grid-interconnected three-phase inverter*. In *IEEE 34th Annu. Conf. Power Electron. Special. (PESC'03)*, Acapulco, Mexico, June 15–19, 2003. IEEE.

[139] Wang, X., R. Beres, F. Blaabjerg and P. C. Loh: *Passivity-based design of passive damping for LCL-filtered voltage source converters*. In *2015 IEEE Energy Conv. Congr. Expo. (ECCE)*, Montreal, QC, Canada, Sept. 20–24, 2015. IEEE.

[140] Wang, X. and F. Blaabjerg: *Harmonic stability in power electronic-based power systems: concept, modeling, and analysis*. IEEE Trans. on Smart Grid, 10(3):2858–2870, May 2019.

[141] Wang, X., F. Blaabjerg and P. C. Loh: *Passivity-based stability analysis and damping injection for multiparalleled VSCs with LCL filters*. IEEE Trans. Power Electron., 32(11):8922–8935, Nov. 2017.

[142] Wang, X., F. Blaabjerg and P. C. Loh: *Virtual RC damping of LCL-filtered voltage source converters with extended selective harmonic compensation*. IEEE Trans. Power Electron., 30(9):4726–4737, Sept. 2015.

[143] Wang, X., F. Blaabjerg and W. Wu: *Modeling and analysis of harmonic stability in an AC power-electronics-based power system*. IEEE Trans. Power Electron., 29(12):6421–6432, Dec. 2014.

[144] Wang, X., L. Harnefors and F. Blaabjerg: *Unified impedance model of grid-connected voltage-source converters*. IEEE Trans. Power Electron., 33(2):1775–1787, Feb. 2018.

[145] Wang, X., Y. W. Li, F. Blaabjerg and P. C. Loh: *Virtual-impedance-based control for voltage-source and current-source converters*. IEEE Trans. Power Electron., 30(12):7019–7037, Dec. 2015.

[146] Wang, X., X. Ruan, S. Liu and C. K. Tse: *Full feedforward of grid voltage for grid-connected inverter with LCL filter to suppress current distortion due to grid voltage harmonics*. IEEE Trans. Power Electron., 25(12):3119–3127, Dec. 2010.

[147] Wang, Y.: *Stability assessment of inverter-fed power systems*. Ph. D. dissertation, Fac. Eng. Sc., Aalborg University, Denmark, 2017.

[148] Wen, B., D. Boroyevich, R. Burgos, P. Mattavelli and Z. Shen: *Analysis of DQ small-signal impedance of grid-tied inverters*. IEEE Trans. Power Electron., 31(1):675–687, Jan. 2016.

[149] Wen, B., D. Boroyevich, P. Mattavelli, Z. Shen and R. Burgos: *Influence of phase-locked loop on input admittance of three-phase voltage-source converters*. In *28th Annu. IEEE Appl. Power Electron. Conf. Expo. (APEC)*, Long Beach, CA, USA, Mar. 17–21, 2013. IEEE.

[150] Wen, B., D. Dong, D. Boroyevich, R. Burgos, P. Mattavelli and Z. Shen: *Impedance-based analysis of grid-synchronization stability for three-phase paralleled converters*. IEEE Trans. Power Electron., 31(1):26–38, Jan. 2016.

[151] Wereley, N. M.: *Analysis and control of linear periodically time varying systems*. Ph. D. dissertation, Dept. of Aeronautics and Astronautics, Massachusetts Institute of Technology, 1991.

[152] Wu, W., Y. He, T. Tang and F. Blaabjerg: *A new design method for the passive damped LCL and LLCL filter-based single-phase grid-tied inverter*. IEEE Trans. Ind. Electron., 60(10):4339–4350, Oct. 2013.

[153] Wu, W., Y. Liu, Y. He, H. S.-H. Chung, M. Liserre and F. Blaabjerg: *Damping methods for resonances caused by LCL-filter-based current-controlled grid-tied power inverters: An overview*. IEEE Trans. Ind. Electron., 64(9):7402–7413, Sept. 2017.

[154] Xia, M., P. J. Antsaklis and V. Gupta: *Passivity analysis of human as a controller*. Technical report of the ISIS group at the University of Notre Dame, ISIS-2014-002, 2014.

[155] Xia, M., P. J. Antsaklis and V. Gupta: *Passivity indices and passivation of systems with application to systems with input/output delay*. In *53rd IEEE Conf. Decision and Control (CDC)*, Los Angeles, CA, USA, Dec. 15–17, 2014. IEEE.

[156] Xie, C., K. Li, J. Zou and J. M. Guerrero: *Passivity-based stabilization of LCL-type grid-connected inverters via a general admittance model*. IEEE Trans. Power Electron., 35(6):6636–6648, June 2020.

[157] Xin, Z., P. C. Loh, X. Wang, F. Blaabjerg and Y. Tang: *Highly accurate derivatives for LCL-filtered grid converter with capacitor voltage active damping*. IEEE Trans. Power Electron., 31(5):3612–3625, May 2016.

[158] Yang, D., X. Ruan and H. Wu: *Impedance shaping of the grid-connected inverter with LCL filter to improve its adaptability to the weak grid condition*. IEEE Trans. Power Electron., 29(11):5795–5805, Nov. 2014.

[159] Yang, D., X. Wang and F. Blaabjerg: *Sideband harmonic instability of paralleled inverters with asynchronous carriers*. IEEE Trans. Power Electron., 33(6):4571–4577, June 2018.

[160] Yepes, A. G., F. D. Freijedo, J. Doval-Gandoy, Ó. López, J. Malvar and P. Fernandez-Comesana: *Effects of discretization methods on the performance of resonant controllers*. IEEE Trans. Power Electron., 25(7):1692–1712, July 2010.

[161] Yepes, A. G., F. D. Freijedo, O. López and J. Doval-Gandoy: *High-performance digital resonant controllers implemented with two integrators*. IEEE Trans. Power Electron., 26(2):563–576, Feb. 2011.

[162] Yepes, A. G., F. D. Freijedo, Ó. Lopez and J. Doval-Gandoy: *Analysis and design of resonant current controllers for voltage-source converters*

by means of Nyquist diagrams and sensitivity function. IEEE Trans. Ind. Electron., 58(11):5231–5250, Nov. 2011.

[163] Yoon, C., X. Wang, C. L. Bak and F. Blaabjerg: *Stabilization of multiple unstable modes for small-scale inverter-based power systems with impedance-based stability analysis*. In *2015 IEEE Appl. Power Electron. Conf. Expo. (APEC)*, Charlotte, NC, USA, Mar. 15–19, 2015. IEEE.

[164] Yuan, X., W. Merk, H. Stemmler and J. Allmeling: *Stationary-frame generalized integrators for current control of active power filters with zero steady-state error for current harmonics of concern under unbalanced and distorted operating conditions*. IEEE Trans. Ind. Appl., 38(2):523–532, Mar./Apr. 2002.

[165] Yue, X., X. Wang and F. Blaabjerg: *Review of small-signal modeling methods including frequency-coupling dynamics of power converters*. IEEE Trans. Power Electron., 34(4):3313–3328, Apr. 2019.

[166] Zhang, S., S. Jiang, X. Lu, B. Ge and F. Z. Peng: *Resonance issues and damping techniques for grid-connected inverters with long transmission cable*. IEEE Trans. Power Electron., 29(1):110–120, Jan. 2014.

[167] Zhang, X., J. W. Spencer and J. M. Guerrero: *Small-signal modeling of digitally controlled grid-connected inverters with LCL filters*. EEE Trans. Ind. Electron., 60(9):3752–3765, Sept. 2013.

[168] Zhou, J. Z., H. Ding, S. Fan, Y. Zhang and A. M. Gole: *Impact of short-circuit ratio and phase-locked-loop parameters on the small-signal behavior of a VSC-HVDC converter*. IEEE Trans. Power Del., 29(5):2287–2296, Oct. 2014.

[169] Zhu, F., M. Xia and P. J. Antsaklis: *Passivity analysis and passivation of feedback systems using passivity indices*. In *2014 American Control Conf. (ACC)*, Portland, OR, USA, June 4–6, 2014. IEEE.

[170] Zmood, D. N. and D. G. Holmes: *Stationary frame current regulation of PWM inverters with zero steady-state error*. IEEE Trans. Power Electron., 18(3):814–822, May 2003.

[171] Zou, C., B. Liu, S. Duan and R. Li: *Influence of delay on system stability and delay optimization of grid-connected inverters with LCL filter*. IEEE Trans. Ind. Informat., 10(3):1775–1784, Aug. 2014.